



UNIVERSITÀ DEGLI STUDI DI TRIESTE

UNIVERSITÀ DEGLI STUDI DI UDINE

XXXII CICLO DEL DOTTORATO DI RICERCA IN

INGEGNERIA CIVILE-AMBIENTALE E ARCHITETTURA

**THE ROLE OF ROAD PAVEMENTS IN THE
PHENOMENON OF URBAN HEAT ISLAND**

**IL RUOLO DELLE PAVIMENTAZIONI STRADALI NEL
FENOMENO DELL'ISOLA DI CALORE URBANO**

Settore scientifico-disciplinare: ICAR/04 - STRADE, FERROVIE E AEROPORTI

**DOTTORANDO
ANDREA BALIELLO**

**COORDINATORE
PROF. STEFANO SORACE**

**SUPERVISORE DI TESI
PROF. MARCO PASETTO**

**CO-SUPERVISORE DI TESI
PROF. NICOLA BALDO**

ANNO ACCADEMICO 2018/2019



UNIVERSITÀ DEGLI STUDI DI TRIESTE

UNIVERSITÀ DEGLI STUDI DI UDINE

XXXII CICLO DEL DOTTORATO DI RICERCA IN

INGEGNERIA CIVILE-AMBIENTALE E ARCHITETTURA

**THE ROLE OF ROAD PAVEMENTS IN THE
PHENOMENON OF URBAN HEAT ISLAND**

**IL RUOLO DELLE PAVIMENTAZIONI STRADALI NEL
FENOMENO DELL'ISOLA DI CALORE URBANO**

Settore scientifico-disciplinare: **ICAR/04 - STRADE, FERROVIE E AEROPORTI**

**DOTTORANDO
ANDREA BALIELLO**

**COORDINATORE
PROF. STEFANO SORACE**

**SUPERVISORE DI TESI
PROF. MARCO PASETTO**

**CO-SUPERVISORE DI TESI
PROF. NICOLA BALDO**

ANNO ACCADEMICO 2018/2019



A sculpture of a post-human breathing... from the last tree on Earth.

Melting men by Brazilian Artist, Nele Azevedo, Berlin.

Index

Abstract	5
Declaration	7
Acknowledgements	8
List of figures	9
List of tables	15
List of abbreviations	17
List of symbols	18
Introduction	21
Chapter 1. Urban Heat Island	23
1.1. General introduction	23
1.2. Historical background	25
1.3. Urban heat island	26
1.3.1. UHI composition	26
1.3.2. UHI causes, impacts and effects	30
1.4. The role of road pavements	39
Chapter 2. Theory of Heat Transfer	43
2.1. Generalities	43
2.1.1. Physics of radiation	43
2.1.2. Radiative properties of real objects	49
2.1.3. Solar and atmospheric radiations	54
2.2. Road pavement concerns	60
2.2.1. Micro-climate of urban areas	60
2.2.2. Heat mechanisms of road pavements	66
Chapter 3. Literature Review	75
3.1. Heat mitigation	75
3.1.1. Real-scale experiences	75
3.1.2. Small-scale experiences	83
3.2. Heat management	88
Chapter 4. Work Activity	95
4.1. Research objective	95
4.2. Work approach	96
4.3. Chromatic evaluation	97
4.4. Thermal assessment	102
4.4.1. Preliminary considerations	102
4.4.2. Laboratory activity	104
4.4.3. In-field experimentation	109
4.5. Mechanical characterization	110
4.5.1. Multi-scale approach	110
4.5.2. Rheological characterization	111
4.5.2.1. Viscosity	112

4.5.2.2. Stiffness characteristics	113
4.5.2.3. Fatigue resistance	117
4.5.2.4. Permanent deformation resistance	120
4.5.3. Characteristics of blends	122
4.5.3.1. Adhesion properties	122
4.5.4. Performance of mixtures	123
4.5.4.1. Mechanical strength	123
4.5.4.2. Stiffness	124
4.5.4.3. Fatigue life	125
4.5.4.4. Rutting resistance	125
4.5.4.5. Surface characteristics	125
4.5.4.6. Durability	125
Chapter 5. Experimental Results	129
5.1. Binders and mastics	129
5.1.1. Materials and plan	129
5.1.2. Chromatic evaluation	133
5.1.3. Rheological characterization	136
5.1.3.1. Viscosity	136
5.1.3.2. Stiffness characteristics	138
5.1.3.3. Fatigue resistance	148
5.1.3.4. Permanent deformation resistance	151
5.2. Loose blends	155
5.2.1. Materials	155
5.2.2. Adhesion properties	156
5.3. Mixtures	158
5.3.1. Materials	158
5.3.1.1. Conventional asphalt mixtures	158
5.3.1.2. Resin-based mixtures	160
5.3.1.3. Oxide-colored mixtures	163
5.3.1.4. Surface-treated mixtures	165
5.3.2. Mixture's testing plan	168
5.3.3. Chromatic evaluation	169
5.3.4. Thermal assessment	171
5.3.4.1. Laboratory activity	171
5.3.4.2. In-field experimentation	181
5.3.5. Mechanical characterization	191
5.3.5.1. Mechanical strength	191
5.3.5.2. Stiffness	192
5.3.5.3. Fatigue life	200
5.3.5.4. Rutting resistance	202
5.3.5.5. Surface characteristics	203
5.3.5.6. Durability	205
Chapter 6. Outline and Discussion	209
6.1. Thermal correlations	209
6.1.1. Chromatic-thermal correlations	209
6.1.2. Thermal responses	210

6.2. Numerical computation	214
6.2.1. Alternative scenarios	214
6.2.2. Mitigation efficacy	222
6.3. Multi-scale performance of materials	227
6.4. Discussion	231
Chapter 7. Further Aspects	235
7.1. Thermal-optimized roads: related aspects	235
7.1.1. Infrastructure-landscape integration	235
7.1.2. Traffic calming and road safety	238
7.1.3. Night and tunnel lighting	242
7.2. Thermal-optimized roads: related aspects	243
7.2.1. Thermal comfort	243
7.2.2. Visual comfort	246
7.3. Guidelines for thermal-optimized roads	248
7.4. Preliminary cost estimation	251
Conclusions	255
Recommendations for Future Works	259
Bibliography	261

Abstract

The thesis aims at proposing a comprehensive study concerning the role of road pavements with respect to the phenomenon of the urban heat island that are generated within the anthropized areas, i.e. all the dynamics that determine a sensible increase of the urban temperatures with respect to that recorded in the surrounding rural environments.

More specifically, the core of the research concerns an extensive experimental activity aimed at evaluating different construction solutions to obtain thermal-optimized road pavements. Such solutions consist of clear or colored road pavements made with non-black surfaces and are manufactured with different techniques. Therefore, the main purpose of the whole research regards the definition of advices, indications and guidelines for the production of road pavements able to mitigate the urban heat island and prevent an excessive increase of the urban temperatures.

Laboratory and outside activities were scheduled to identify the chromatic characteristics and monitor the thermal properties and responses of the selected technologies. Using a multi-scale approach (from binders to mixtures), an advanced mechanical characterization of the materials was also proposed to assess their suitability since each alternative must ensure adequate standards from functional, safety and durability points of view.

A back calculation based on all the collected data permitted the evaluation of the efficacy of the proposed technologies in mitigating the urban heat.

Finally, further aspects involved in the use of thermal-optimized pavements, but not directly related to thermal concerns, were also studied: mainly, such aspect regarded the infrastructure-landscape integration of clear or colored surfaces, their possible use as traffic calming measures (and the related road safety matter), their repercussions on the nightly artificial illumination or that needed within the road tunnels. Furthermore, some efforts were

also spent in order to investigate their impacts with respect to the human comfort (thermal and visual ones) and the human health.

Principal findings of the research stated that some technologies (clear mixtures containing synthetic transparent resins and valuable clear aggregates) were effectively able to contain the temperatures reached during the direct solar exposition (more intense in the summer). The most effective material was useful to lower the maximum reached temperature of about 18 °C with respect to that of a traditional black mixture conventionally employed as wearing courses in urban roads (assumed as reference).

Declaration

The work described in this thesis was conducted at the University of Padova, Department of Civil, Environmental and Architectural Engineering between November 2016 and November 2019. I declare that the work is my own and has not been submitted for a degree of another University.

Acknowledgements

I would like to thank all those who have provided the assistance, advice, encouragement and funding without which this research would not have been possible. I wish, particularly, to thank the following persons and organizations:

- Professor Marco Pasetto and Nicola Baldo, my supervisor and co-supervisor, for their guidance and advice throughout the research period notwithstanding their own heavy workload.
- The Department of Civil, Environmental and Architectural Engineering (ICEA) of the University of Padova that provided the logistic and technical support for the development of the work undertaken in this thesis.
- The Department of Engineering and Architecture of the University of Trieste, the Department of Civil and Environmental Engineering of the University of Udine, and in particular Ph.D. commission, that provided all the financial and organizing support during all the Ph.D. research duration.
- My colleagues in Department ICEA, Emiliano Pasquini and Giovanni Giacomello for their assistance in developing all the work done, specifically for the help given during the theoretical and experimental activities done and the writing of the thesis.

List of Figures

- 1.1. Examples of LST distribution in northern China: 5th September 2006 (a), 23th August 2007 (b), 12th August 2009 (c), 15th August 2010 (d)
- 1.2. Scheme of spatial distribution of UHI typologies
- 1.3. UHI scheme: example of temperature trends on surface and atmosphere
- 1.4. Evapotranspiration and infiltration in rural and urban areas
- 1.5. Cool roof as a solution to enhance the reflected solar radiation
- 1.6. Anthropogenic heat flux statistics: 2005 record (a) and 2040 projection (b)
- 1.7. Global factors influencing the formation of UHI
- 1.8. Urban surface energy budget
- 1.9. Environmental-related deaths recorded worldwide in year 2000
- 1.10. Temperatures change across the world (1906–2005)
- 1.11. Emissions of CO₂ recorded across the world (2010)
- 1.12. Projection of global mean temperature increases under different emission scenarios (2046–2200)
- 1.13. Ground energetic balance for a rural area during day-time (a) and night-time (b)
- 1.14. Ground energetic balance for an urban area
- 2.1. Type of electromagnetic radiations (a) and characteristics of visible spectrum (b)
- 2.2. Monochromatic radiative power for selected temperatures
- 2.3. Black body emission: radiative powers for surface unity
- 2.4. Monochromatic emissivity vs. wavelength: approximation with step function
- 2.5. Variability of total and monochromatic emissivities vs. wavelength (a) and temperature (b)
- 2.6. Reflection geometry (a) and α coefficient vs. temperature of radiation source (b)
- 2.7. Characteristics of solar radiation
- 2.8. Spectrum of solar radiation outside and inside the atmosphere (a) and colors of solar light perceived on the Earth's surface
- 2.9. Convention used to indicate the azimuth sign
- 2.10. Solar and surface angles for a tilted surface
- 2.11. Graphic relationships for angle's calculation (northern hemisphere)
- 2.12. Solar diagram for the city of Padova (Italy)
- 2.13. Vapor pressure curve vs. atmospheric temperature
- 2.14. Wind canalization (Venturi effect): conceptual scheme (a) and real application (b)
- 2.15. Wind behavior: overpassing of short buildings (a), trapping on ground areas (b) and reinforcing due to tall constructions (c)
- 2.16. Radiation variety among the urban context
- 2.17. Solutions to intercept the reflected radiation
- 2.18. Radiative properties of common construction materials
- 2.19. General radiative balance on a surface exposed to solar radiations
- 2.20. General radiative balance for road pavements (during summertime)

-
- 2.21. Examples of albedo for urban construction materials
 - 2.22. Maximum pavement temperature vs. absorptivity (for different emissivities)
 - 2.23. Maximum pavement temperature vs. conductivity (for different wind convections)
 - 2.24. Maximum hourly solar radiation vs. latitude (normal and horizontal surface)
 - 2.25. Yearly trends of hourly solar radiation for different latitudes
 - 2.26. Gradients between maximum pavement and air temperatures vs. latitude
 - 3.1. Schematic representation of the studied pavement [3.1]
 - 3.2. Heat (left) and stiffness (right) distribution through the depth of pavement layers [3.1]
 - 3.3. Model results about the temporal distribution of the pavement temperatures [3.3]
 - 3.4. Picture of the pervious pavement (left) and the conventional rigid one (right) [3.10]
 - 3.5. Schematic view of the pervious pavement (left) and the rigid one (right) [3.10]
 - 3.6. Comparison of measured and predicted mid-depth pavement temperatures [3.12]
 - 3.7. Cross-section detail of pavement sensor filling materials [3.15]
 - 3.8. Real-scale application of flexible pavements for winter climate [3.17]
 - 3.9. Trial sections for the analysis of pavement thermal responses [1.18]
 - 3.10. Survey area for the analysis of pavement thermal responses [3.23]
 - 3.11. Experimental scenario set up to monitor the laboratory samples [3.26]
 - 3.12. Details of the equipment used to monitor laboratory samples [3.27]
 - 3.13. Slabs tested in the laboratory and in external environment [3.28]
 - 3.14. Scheme of the modeled structure [3.30]
 - 3.15. In-field measurement performed for the model validation [3.30]
 - 3.16. Scheme of the layers composing the studied pavement [3.31]
 - 3.17. Laboratory heating of asphalt concrete slabs carried out with infrared lamps [3.32]
 - 3.18. Surface temperature for different voids: dry (left) and wet (right) condition [3.32]
 - 3.19. Bottom temperature for different voids: dry (left) and wet (right) condition [3.32]
 - 3.20. Scheme of the three-dimension modeled structure [3.36]
 - 3.21. Scheme of the slabs prepared in the laboratory [3.36]
 - 3.22. Slabs' construction details [3.36]
 - 3.23. Scheme of the pavement equipped with the steel bars [3.37]
 - 3.24. Simulation: heat flux distribution for a given steel bar's configuration [3.37]
 - 3.25. Laboratory samples produced to validate the numerical simulations [3.37]
 - 3.26. Rutting curves: conventional (CS), literature (G-BHIS) and designed (SB-BHIS-1,2) structures [3.37]
 - 3.27. Schematic view of an instrumented laboratory sample [3.40]
 - 3.28. Example of thermal distribution inside a sample: filament's pitch of 150 mm [3.40]
 - 4.1. Acquisition chamber: top (a) and side (b) views
 - 4.2. Color back analysis: determination of RGB dominant color of a binder sample
 - 4.3. Color back analysis: calculation example of the colored portion (mix surfaces)
 - 4.4. Human eye functioning: R-G-B receptor cones
 - 4.5. RGB and HSL models represented in a tridimensional space
 - 4.6. Determination of material emissivity: preliminary calibration phases
 - 4.7. Determination of material albedo: image processing phases
 - 4.8. Typical emission spectra of artificial lamps
 - 4.9. Experimental equipment and set up: side (a) and front (b) views
-

-
- 4.10. Analysis tools implemented in elaboration software (a); example of recordings (b)
 - 4.11. Images of monitoring activities performed in the laboratory
 - 4.12. Set up for heat release study: schematic representation (a) and image (b)
 - 4.13. Example of output images and data
 - 4.14. Outside set up: acquisition phases (a, b); images of materials tested (c, d)
 - 4.15. OKTA scale: levels and standard symbols (a); example of cloud cover levels (b, c)
 - 4.16. Flow curves (τ vs. $\dot{\gamma}$): examples of possible rheological behaviors
 - 4.17. Stiffness investigation: applied loads for AS (γ vs. t) (a) and TS (T vs. t) (b) tests
 - 4.18. Model of stiffness master curve (G^* vs. ω_r)
 - 4.19. Model of phase angle master curve (δ vs. ω_r)
 - 4.20. Loads applied on LAS phases – 1st: FS (f vs. t) (a); 2nd: AS (γ vs. n) (b)
 - 4.21. Damage evolution: integrity (C vs. D) (a) and integrity loss (C_0-C vs. D) (b)
 - 4.22. Example of n -cycle (creep-recovery): γ vs. t
 - 4.23. Stripping results: example of DIP output
 - 5.1. Scheme of the planned experimental protocol
 - 5.2. Viscosity: η of binders in unaged (a) RTFO-aged (b) and PAV-aged (c) condition
 - 5.3. Flow curves of binders (τ vs. γ)
 - 5.4. Projections of η with respect to mixing and compaction temperature ranges
 - 5.5. AS binders' results: G^* vs. γ (a) and isochronal plots, γ vs. τ (b)
 - 5.6. AS binders' results: G' , G'' vs. γ for B and S: unaged (a) and PAV-aged (b) condition
 - 5.7. AS: G^* vs. γ and LVE trends at different T for B (a), B-OX-R (b) and B-OX-G (c)
 - 5.8. B and S mastics at unaged and PAV-aged condition: G^* vs. γ (a) and γ vs. τ (b)
 - 5.9. TS results: temperature dependency (G^* vs. T) of the studied binders
 - 5.10. Black diagrams (δ vs. G^*) of binders B (a), S (b), B-OX-R (c) and B-OX-G (d)
 - 5.11. Cole-Cole plots (G'' vs. G') of binders B (a), S (b), B-OX-R (c) and B-OX-G (d)
 - 5.12. G^* (a) and δ (b) vs. ω for binder B: experimental data and master curves
 - 5.13. G^* (a) and δ (b) vs. ω for binder S: experimental data
 - 5.14. G^* (a) and δ (b) vs. ω for binder B-OX-R: experimental data
 - 5.15. G^* (a) and δ (b) vs. ω for binder B-OX-G: experimental data
 - 5.16. G^* (a) and δ (b) vs. ω for mastic B-Lf: experimental data
 - 5.17. G^* (a) and δ (b) vs. ω for mastic B-Sf: experimental data
 - 5.18. G^* (a) and δ (b) vs. ω for mastic S-Lf: experimental data
 - 5.19. G^* (a) and δ (b) vs. ω for mastic S-Sf: experimental data
 - 5.20. Binder's LAS results: fatigue law – γ vs. N (a) and shear stress evolution – τ vs. γ (b)
 - 5.21. γ evolution on time: binder B (a), S (b), B-OX-R (c) and B-OX-G (d)
 - 5.22. $R\%$ for binders at T of 58, 64, 70, 76 °C and τ of 0.1 (a) and 3.2 kPa (b)
 - 5.23. J_{nr}/J_{TOT} for binders at T of 58, 64, 70, 76 °C and τ of 0.1 (a) and 3.2 kPa (b)
 - 5.24. $R\%$ for mastics at T of 58, 64, 70, 76 °C and τ of 3.2 (a) and 10 kPa (b)
 - 5.25. J_{nr}/J_{TOT} for mastics at T of 58, 64, 70, 76 °C and τ of 0.1 (a) and 3.2 kPa (b)
 - 5.26. Example of stripping results: DIP output (original samples before AST)
 - 5.27. Example of stripping results: DIP output (composite samples after AST)
 - 5.28. Selected gradation for BL mixture
 - 5.29. Optimization of BL mixture: stability, flow (a), Marshall quotient and voids (b)
 - 5.30. Limestone aggregate (left) and example of produced slab (BL mixture – right)
-

-
- 5.31. Selected gradation for SL (a), SW (b), SY (c) and SP (d) mixtures
 - 5.32. Optimization of SL mixture: stability, flow (a), Marshall quotient and voids (b)
 - 5.33. Limestone aggregate (left) and SL slab (right)
 - 5.34. White marble aggregate (left) and SW slab (right)
 - 5.35. Yellow-Siena marble aggregate (left) and SY slab (right)
 - 5.36. Coral-pink stone aggregate (left) and SP slab (right)
 - 5.37. Marshall results for oxide fully-colored BL-based mixtures: stability (a) and flow (b)
 - 5.38. Red oxide-pigment (left) and BL(oxR) slab (right)
 - 5.39. Green oxide-pigment (left) and BL(oxG) slab (right)
 - 5.40. White oxide-pigment (left) and BL(oxW) slab (right)
 - 5.41. Yellow oxide-pigment (left) and BL(oxY) slab (right)
 - 5.42. Red slabs painted with resin (left) or mortar (right)
 - 5.43. Green slabs painted with resin (left) or mortar (right)
 - 5.44. Yellow slabs painted with resin (left) or mortar (right)
 - 5.45. Blue slabs painted with resin (left) or mortar (right)
 - 5.46. Scheme of experimental plan (mixture-scale)
 - 5.47. Inside thermal monitoring (BL): reliability of T_{max} for lighting (a) and darkening (b) periods
 - 5.48. Lighting (a) and darkening (b) periods (inside BL vs. S-based mixes)
 - 5.49. Lighting (a) and darkening (b) periods (inside BL vs. oxide-pigmented mixes)
 - 5.50. Lighting (a) and darkening (b) periods (inside BL vs. r- surface-treated mixes)
 - 5.51. Lighting (a) and darkening (b) periods (inside BL vs. m- surface-treated mixes)
 - 5.52. Temperature gradient from reference BL: S-based (a), oxide-pigmented (b), r- surface-treated (c) and m- surface-treated (d) mixes
 - 5.53. Maximum temperature peaks (at 5.5 h) normalized on reference BL
 - 5.54. Temperature distribution on slab depth (BL vs. S-based vs. oxide-pigmented mixes)
 - 5.55. Temperature recordings on slab depth (BL vs. S-based vs. oxide-pigmented mixes)
 - 5.56. Temperature distribution on slab depth (BL vs. m- and r- surfaced-treated mixes)
 - 5.57. Temperature recordings on slab depth (BL vs. S-based vs. oxide-pigmented mixes)
 - 5.58. Isotherms (25 °C) at $t = 0$ and 30 min.: BL vs. S-based (a) and oxide-pigmented (b)
 - 5.59. Isotherms (25 °C) at $t = 0$ and 30 min.: BL vs. r- (a) and m- (b) treated mixes
 - 5.60. Air temperature distribution vs. distance from slab (at 0 min): BL vs. S-based (a), oxide-pigmented (b), r- (c) and m- (d) surface-treated mixtures
 - 5.61. Air temperature distribution above BL (a) and SW (b) slabs (at 0 min)
 - 5.62. SVF calculation (direct irradiation periods – 5.5 h)
 - 5.63. Irradiation (a) and shading (b) periods (outside BL vs. S-based mixes)
 - 5.64. Irradiation (a) and shading (b) periods (outside BL vs. oxide-pigmented mixes)
 - 5.65. Irradiation (a) and shading (b) periods (outside BL vs. r- surface-treated mixes)
 - 5.66. Irradiation (a) and shading (b) periods (outside BL vs. m- surface-treated mixes)
 - 5.67. Summary of outside thermal results: temperature evolution of mixtures' surfaces
 - 5.68. Temperature gradient from air: BL vs. S-based (a), oxide-pigmented (b), r- surface-treated (c) and m- surface-treated (d) mixes
 - 5.69. Temperature peaks (at 5.5 h) recorded outside
 - 5.70. Maximum temperature mitigation with respect to reference BL.
 - 5.71. ITSM results: results: BL vs. S-based (a) and oxide-pigmented (b) mixtures.
-

-
- 5.72. Black diagram (a), Cole-Cole plot (b), master curves of E^* (c) and δ (d) of BL
 - 5.73. Black diagram (a), Cole-Cole plot (b), master curves of E^* (c) and δ (d) of SL
 - 5.74. Black diagram (a), Cole-Cole plot (b), master curves of E^* (c) and δ (d) of SW
 - 5.75. Black diagram (a), Cole-Cole plot (b), master curves of E^* (c) and δ (d) of SY
 - 5.76. Black diagram (a), Cole-Cole plot (b), master curves of E^* (c) and δ (d) of SP
 - 5.77. Black diagram (a), Cole-Cole plot (b), master curves of E^* (c) and δ (d) of BL(oxR)
 - 5.78. Black diagram (a), Cole-Cole plot (b), master curves of E^* (c) and δ (d) of BL(oxG)
 - 5.79. Black diagram (a), Cole-Cole plot (b), master curves of E^* (c) and δ (d) of BL(oxW)
 - 5.80. Black diagram (a), Cole-Cole plot (b), master curves of E^* (c) and δ (d) of BL(oxY)
 - 5.81. Comparison of E^* master curves: BL vs. S-based (a) and oxide-pigmented (b) mixes
 - 5.82. Comparison of δ master curves: BL vs. S-based (a) and oxide-pigmented (b) mixes
 - 5.83. Fatigue curves (failure plotted against initial strain): BL vs. S-based (a) and oxide-pigmented (b) mixtures
 - 5.84. RLA tests results: BL vs. S-based (a) and oxide-pigmented (b) mixtures
 - 5.85. Example of DIP: evaluation of residual coating before (a) and after (b) abrasion – BL(rY) mixture
 - 5.86. Results of fuel resistance: BL(rR) mixture before (a) and after (b) the treatment
 - 5.87. Results of fuel resistance: BL(mR) mixture before (a) and after (b) the treatment
 - 5.88. Results of fuel resistance: BL(rG) mixture before (a) and after (b) the treatment
 - 5.89. Results of fuel resistance: BL(mG) mixture before (a) and after (b) the treatment
 - 6.1. Correlation between conductivity and hue (a), saturation (b) and lightness (c)
 - 6.2. Absorbed, released and net rates of heat flow calculated
 - 6.3. Gradients (from reference BL) of temperatures vs. net rates of heat flow
 - 6.4. Gradients (from reference BL) of temperatures vs. net rate of heat flow (grouped by mixture typology)
 - 6.5. Plot of q_{net} vs. k, ρ (mathematical fitting)
 - 6.6. Plot of q_{sun} for each mixture and selected scenario
 - 6.7. Plot of q_{cnd} for each mixture and selected scenario
 - 6.8. Plot of q_{cny} for each mixture and selected scenario
 - 6.9. Plot of q_{em} for each mixture and selected scenario
 - 6.10. Plot of q_{net} for each mixture and selected scenario
 - 6.11. Representation of a (a), b (b), c (c) and d (d) coefficients for the different scenarios
 - 7.1. Piazza del Campo square (Siena, Italy): example of red block pavement
 - 7.2. Colored asphalt pavement in a naturalistic context in Texas
 - 7.3. Red road pavements located in Utah
 - 7.4. Clear road pavements located in Japan
 - 7.5. Residential driveway made with red asphalt concrete
 - 7.6. Colored cycling track: example of blue asphalt concrete
 - 7.7. Colored cycling track: example of green texturized pavement
 - 7.8. Example of red-painted pedestrian crossing
 - 7.9. Colored pavement to assign priority to emergency vehicles
 - 7.10. Colored pavement to assign priority to taxis and busses
 - 7.11. Black asphalt concrete (left) vs. clear mixture (right) paved in the tunnel [7.1]
 - 7.12. Thermal balance: heat exchange between the human body and the environment
-

-
- 7.13. Adapted thermal balance: human-environment heat exchange
 - 7.14. Heat “strain” vs. environmental heat stress [7.28]
 - 7.15. Air temperature evolution (left) and obtained physiological quantities (right) [7.29]
 - 7.16. Reflectance and visual properties of different kinds of pavements [7.40]

List of Tables

- 1.1. Comparison between features of SUHI and AUHI
- 2.1. Function $f\lambda$: radiative emission of black body
- 2.2. Possible assumptions for theorization of surface emissivity
- 2.3. Direct vs. diffused solar radiation in function of weather conditions
- 2.4. Thermal parameters of main construction materials
- 2.5. Literature-based results about thermal responses of white pavements & asphalts
- 2.6. Literature-based results about surface temperatures of different paving materials
- 4.1. Technical specifications of utilized halogen lamp
- 4.2. Scheme of adopted multi-scale approach
- 5.1. Basic properties of studied binders
- 5.2. Basic properties of utilized fillers
- 5.3. Morphological compositions of fillers
- 5.4. Mastic's composition and test program
- 5.5. Scheme of the rheological protocol
- 5.6. Chromatic results of binders
- 5.7. Chromatic results of fillers
- 5.8. Chromatic results of mastics
- 5.9. AS binders' results: LVE limits at 34 °C (unaged samples)
- 5.10. Elaboration details for the construction of B master curves
- 5.11. LAS calculated parameters
- 5.12. Binder's $G^* \cdot \sin\delta$ as a function of T (AASHTO PG classification)
- 5.13. Binder's J_{nr} and $J_{nr-diff}$ as a function of T (AASHTO PG classification)
- 5.14. Composition (by weight) of binder-aggregate loose blends
- 5.15. AST results about binder-aggregate loose blend's adhesion
- 5.16. Basic properties of La aggregate (referred to different stockpiles)
- 5.17. Marshall tests and optimization details
- 5.18. Basic properties of La, Wa, Ya and Pa aggregates (referred to different stockpiles)
- 5.19. Marshall tests and optimization details
- 5.20. Summary of mixtures' compositions
- 5.21. Mechanical testing (mixture-scale)
- 5.22. Results of chromatic evaluation at mixture-scale
- 5.23. Radiative properties (emissivity and albedo) determine for each mixture
- 5.24. Mixture conductivity determined along slab thickness
- 5.25. Environmental characteristics: air temperature recorded outside
- 5.26. Environmental characteristics: OKTA cloud coverage recorded outside
- 5.27. Environmental characteristics: relative humidity recorded outside
- 5.28. Environmental characteristics: wind speed recorded outside (from North-East)
- 5.29. Heating and cooling speeds provided by the different mixtures

-
- 5.30. ITS results (25 °C): BL vs. S-based and oxide-pigmented mixtures
 - 5.31. Fatigue results: law parameters and stress related to 106 cycles (σ_6)
 - 5.32. RLA test results: final axial strain, creep rate and creep modulus of mixtures
 - 5.33. Mean texture depth and permeability results for surface-treated mixtures
 - 5.34. Pendulum test values for surface-treated mixtures
 - 5.35. Water sensitivity expressed in ITSR
 - 5.36. Resistance to abrasion for r- surface-treated mixtures
 - 5.37. Resistance to abrasion for m- surface-treated mixtures
 - 6.1. Details used for the heat flow balance calculation
 - 6.2. Single components of the heat flow balance
 - 6.3. Computation scenarios: description
 - 6.4. Computation scenarios: combination of parameters
 - 6.5. Scenario's parameters
 - 6.6. Computation results: incoming rate of heat flow for each mix and scenario
 - 6.7. Computation results: outgoing rate of heat flow for each mix and scenario
 - 6.8. Computation results: net rate of heat flow for each mix and scenario
 - 6.9. Parameters of the selected scenarios
 - 6.10. Mitigation efficacy: q_{net} reduction with respect to reference BL
 - 6.11. Fitting parameters of Equation 6.1 (radiative properties vs. thermal responses)
 - 7.1. Physiological parameters vs. different air temperature sets (extracted from [7.27])
 - 7.2. Cost estimations for paved surfaces – upper layer rehabilitation (extracted from [1.77])
 - 7.3. Cost estimations for paved surfaces – full-depth rehabilitation (extracted from [1.77])

List of Abbreviations

<i>4PB</i> : four point bending	<i>LAS</i> : linear amplitude sweep
<i>AHF</i> : anthropogenic heat flux	<i>LST</i> : land surface temperature
<i>AS</i> : amplitude sweep	<i>LVDT</i> : linear variable displacement transducer
<i>AST</i> : Ancona stripping test	<i>LVE</i> : linear visco-elastic
<i>AUHI</i> : atmospheric urban heat island	<i>MSCR</i> : multiple stress creep recovery
<i>BLUHI</i> : boundary layer urban heat island	<i>PAV</i> : pressure-ageing-vessel
<i>CLUHI</i> : canopy layer urban heat island	<i>RGB</i> : red-green-blue color model
<i>DIP</i> : digital image processing	<i>RLA</i> : repeated load axial
<i>DSR</i> : dynamic shear rheometer	<i>RTFO</i> : rolling-thin-film-oven
<i>DV</i> : dynamic viscosity	<i>SUHI</i> : surface urban heat island
<i>ET</i> : evapotranspiration	<i>SVF</i> : sky view factor
<i>FAR</i> : floor area ratio	<i>TS</i> : temperature sweep
<i>FS</i> : frequency sweep	<i>TTSP</i> : time temperature superposition principle
<i>HSL</i> : hue-saturation-lightness color model	<i>UHI</i> : urban heat island
<i>IPCC</i> : intergovernmental panel on climate change	<i>UV</i> : ultraviolet
<i>IR</i> : infrared	<i>VECD</i> : visco-elastic continuum damage
<i>ITS</i> : indirect tensile strength	<i>WLF</i> : Williams-Landel-Ferry
<i>ITSM</i> : indirect tensile stiffness modulus	
<i>ITSR</i> : indirect tensile strength ratio	

List of Symbols

$\dot{\gamma}$: shear rate	G : incident radiation
A : area	G' : storage elastic stiffness modulus
A : fatigue law parameter	G'' : loss viscous stiffness modulus
A : geometry factor (rheometer)	G_0^* : initial complex modulus (binder fatigue)
a_T : horizontal shift factor	G_{abs} : absorbed radiation
AZ : azimuth	$G_{d,pav}$: diffused radiation on pavement
B : blue (RGB model)	$G_{D,pav}$: direct radiation on pavement
B : fatigue law parameter	G_d : diffused solar radiation
b : intercept of $G'-\omega$ curve (binder fatigue)	G_D : direct solar radiation
b_T : vertical shift factor	$G_{D\perp}$: direct solar radiation (perpendicular)
C : integrity parameter (binder fatigue)	G_e^* : glassy complex stiffness modulus
C : sensible heat loss (human)	G_{Earth} : terrestrial radiation
c : speed of light	$G_{em,pav}$: energy emitted by pavement
C_0 : fit-coefficient (binder fatigue)	G_g^* : equilibrium complex stiffness modulus
c_0 : speed of light on absolute vacuum	G_i^* : complex modulus at time i (binder fatigue)
C_1, C_2 : math constant (emissive power)	$G_{in,pav}$: input energy on pavement
C_1 : fit parameters (master curve)	$G_{net,pav}$: net energy on pavement
C_1 : fit-coefficient (binder fatigue)	$G_{out,cnd}$: conductive energy on pavement
C_2 : fit parameters (master curve)	$G_{out,env}$: convective energy on pavement
C_2 : fit-coefficient (binder fatigue)	$G_{out,pav}$: output energy on pavement
c_p : specific heat	G_{ref} : reflected radiation
c_t : thermal capacity	G_s : energy from sun reaching Earth
D : damage parameter (binder fatigue)	G_{sky} : atmospheric radiation
d : depth	G_{sun} : incident solar radiation
d : thickness	G_{tr} : transmitted radiation
D_f : damage at failure (binder fatigue)	H : building height
E^* : complex modulus (beam)	H : hue (HSL model)
e : quantum energy	h : mean specimen thickness (mix stiffness)
E : total emissive power	h : Planck constant
E : latent heat loss (human)	h_e : average convective heat transfer coefficient
$E_{n,0-\lambda}$: emissive power (on wavelength interval)	hr : hour angle
E_n : creep modulus (mix rutting)	I : dual-value function (master curve)
E_n : radiative power (for surface unit)	ITS_{dry} : dry indirect tensile strength
$E_{n\lambda}$: monochromatic emissive power	ITS_{wet} : wet indirect tensile strength
E_{sun} : radiation power emitted by sun	J_{nr}/J_{TOT} : creep compliance ratio
f : frequency	J_{nr} : non-recoverable creep compliance
F : peak value of load (mix stiffness)	$J_{nr-diff}$: difference of creep compliance at different stress
F_{load} : thermal load applied to humans	J_{TOT} : total creep compliance
f' : generic experimental frequency	k : Boltzmann constant
f_c : creep rate (mix rutting)	k : shape parameter (master curve)
f_c : crossover frequency	k : thermal conductivity
f_d : location frequency (master curve)	L : average distance sun-Earth
f_λ : radiative function	L : lightness (HSL model)
$f_{\lambda 1-\lambda 2}$: radiative function (on wavelength interval)	m : relative mass of air
G^* : shear complex stiffness modulus	m : slope of $G'-\omega$ curve (binder fatigue)
G : green (RGB model)	

<i>max</i> : maximum value of RGB tern	<i>u_n</i> : cumulative perm. deformation (mix rutting)
<i>M</i> : metabolic heat rate	<i>UR</i> : relative humidity
<i>M_d</i> : recorded torque (rheometer) <i>α</i> : absorptivity	<i>W</i> : building width
<i>m_d</i> : shape parameter (master curve)	<i>W</i> : mechanical workload (human)
<i>m_e</i> : shape parameter (master curve)	<i>z</i> : amplitude of horizontal strain (mix stiffness)
<i>min</i> : minimum value of RGB tern	<i>z</i> : depth
<i>MTD</i> : mean texture depth	<i>z</i> : zenith-radiation direction angle
<i>n</i> : cycles	<i>α</i> : parameter of undamaged material (binder fatigue)
<i>n</i> : refractive index	<i>β</i> : South meridian-surface normal angle
<i>N</i> : total cycle number (binder fatigue)	<i>γ</i> : strain
<i>n_{day}</i> : day number	<i>γ</i> : sun elevation
<i>N_f</i> : number of cycles to failure (fatigue)	<i>δ</i> : phase angle
<i>p</i> : air pressure	<i>δ_m</i> : phase angle at location frequency
<i>P</i> : pavement horizontal drainability	<i>ΔQ_A</i> : heat coming from the neat advection
<i>p_s</i> : saturation pressure	<i>ΔQ_S</i> : heat stored by the pavements
<i>PTV</i> : pendulum test value	<i>δ_{sun}</i> : solar declination
<i>Q*</i> : net radiation at ground level	<i>ΔT</i> : temperature gradient
<i>Q_E</i> : turbulent latent heat flux	<i>ε</i> : emissivity
<i>Q_F</i> : anthropogenic heat flux	<i>ε₀</i> : initial deformation (rutting)
<i>Q_{FH}</i> : anthropogenic heat flux (stationary)	<i>ε₀</i> : strain amplitude (mix stiffness)
<i>Q_{FM}</i> : anthropogenic heat flux (metabolic)	<i>ε₁</i> : deformation at creep removal (rutting)
<i>Q_{FV}</i> : anthropogenic heat flux (vehicles)	<i>ε₁₀</i> : final deformation (rutting)
<i>Q_G</i> : conduction heat flux from bottom layer	<i>ε_n</i> : axial deformation (mix rutting)
<i>Q_H</i> : turbulent sensible heat flux	<i>ε_R</i> : pseudo-strain
<i>R%</i> : percent recovery	<i>ε_θ</i> : emissivity (to perpendicular)
<i>R</i> : red (RGB model)	<i>ε_λ</i> : monochromatic emissivity
<i>R</i> : rheological index (upper)	<i>η</i> : dynamic viscosity
<i>R</i> : rough surface	<i>θ</i> : angle of emission (to perpendicular)
<i>r</i> : sun radius	<i>λ</i> : wavelength
<i>R'</i> : rheological index (lower)	<i>λ_m</i> : thermal diffusivity
<i>R_d</i> : shape parameter (master curve)	<i>ν</i> : Poisson's ratio
<i>R_{net}</i> : net solar radiation (thermal comfort)	<i>ν</i> : vapor pressure of air
<i>S</i> : saturation (HSL model)	<i>ρ</i> : albedo
<i>S</i> : smooth surface	<i>ρ₀</i> : density at reference temperature
<i>SH</i> : solar hour	<i>ρ_i</i> : generic density
<i>SRI</i> : solar reflectance index	<i>ρ_m</i> : material density
<i>T</i> : temperature	<i>ρ_{urb}</i> : urban albedo
<i>t</i> : time	<i>σ</i> : axial stress
<i>T₀</i> : reference temperature	<i>σ</i> : Stefan-Boltzmann constant
<i>T_{air}</i> : air temperature	<i>τ</i> : coefficient of transmission
<i>T_{amb}</i> : ambient temperature	<i>τ</i> : shear stress
<i>T_d</i> : temperature at depth d	<i>τ_a</i> : transmission coefficient for mass unit
<i>T_i</i> : generic experimental temperature	<i>Φ</i> : local latitude
<i>t_i</i> : specimen thickness (mix rutting)	<i>Ψ</i> : tilt angle
<i>T_m</i> : average surface temperature	<i>ω</i> : angular frequency
<i>T_{max}</i> : maximum temperature	<i>ω_i</i> : generic experimental angular frequency
<i>T_{sky}</i> : sky temperature	<i>ω_r</i> : reduced angular frequency
<i>T_{src}</i> : temperature of incident radiation source	
<i>T_{sun}</i> : temperature of sun	
<i>T_{surf}</i> : surface temperature	
<i>U</i> : average daily wind speed	

Introduction

The present thesis concerns the study of the role of road pavements with respect to the phenomenon of the Urban Heat Island (UHI). UHI are defined as urban or a metropolitan areas appreciably warmer than their surrounding rural zones. Because of the high demographic density and the severe anthropogenic activities, the largest and the most populated cities record greater temperatures at the town-heart or at the town-center, above all during the summerly good-weather, no-windy days. This fact is traduced in temperature increases up to 20 °C with respect to the surrounding pristine lands and could determine sensible impacts on humans and environment. Really, serious discomfort in humans and heat-related diseases, even deaths (above all in children, older adults and people with existing health conditions), are widely recognized to be connected to heat phenomena. Likewise, global warming due to increasing emissions, climate changes and several repercussions on vegetal and animal ecosystems are well documented.

In order to define the effective role of roads in such a complex aspect, the causes of UHI must be analyzed. First, the general lack of vegetation (plants and high-growing trees) compromises the attenuation of the superficial temperatures and the evapotranspiration; green areas are progressively replaced by the urban texture, within which the human activity, the energy-intensive buildings and the infrastructures (included the transportation systems) contribute to develop the anthropogenic warmth shaped by the direct heat generation (heating systems, stoves, fireplaces) or the indirect heat production (results of artificial lighting, transport use, industrial activities, etc.). In turn, the progressive climate changes influence the local weather, the characteristics of the wind and the cloud cover, affecting the heat island formation.

Therefore, the topic is not surprisingly of extreme actuality and interests various fields of study and research sectors, as well as several targeted policies taking place in companies, agencies, governmental and private institutions and associations. As examples, the World Health Organization, the European Environmental Agency or the Intergovernmental Panel on Climate Change, started to deal with the thematic since the last decades; in operative terms, the Kyoto Protocol, the Paris Agreement or the Horizon 2020 programs concretely fixed ad-hoc objectives about theme-related aspects (greenhouse gas emissions reduction, global warming and worldwide temperature mitigation, financial sustainability, etc.), also in view of non-comfortable future projections actually obtained.

For all these reasons, it goes without saying that also the important sector of the civil engineering is involved in the process. In fact, buildings and structures are pollution sources during the construction phases but maintain also backlashes during the in-service life (they are composed by reflective surface and low-impermeable materials and contribute to the heat concentration). Similarly, roads can constitute obstacles that obstruct the natural ground runoff and the water disposal, thus they cause the warming of the local canopy heights. Not least, it is worth noting that road surfaces generally assume a black color which concentrates the heat radiations. Moreover, in view of their great extension in the most civilized areas, road networks are mutually integrated with the building's patterns and create a composite urban texture that leads to a unique high heat-absorbing entity.

In addition, the constituent materials and their characteristics are fundamental aspects at least as much as the spatial distribution and the urban geometry concerning the transportation systems. In particular, the radiative properties of pavement materials determine the heat transfer mechanisms since they affect the absorbed radiations and that one released/emitted in the urban environment.

This is the main reason which led to the writing of the present dissertation, which regards the development of specific guidelines useful to produce thermal-optimized road pavements which, thanks to their radiative properties (linked to color and composition), could be able to limit the heat concentration within the city and mitigate the above-mentioned drawbacks involved in urban heat island phenomenon.

Chapter 1

Urban Heat Island

The present Chapter aims at introducing the Urban Heat Island (UHI) phenomenon: firstly, a preface defines and contextualizes the theme. Then, a historical background and the characteristics of UHI are detailed. Composition, causes, impacts and effects are furtherly treated to give a comprehensive description of the phenomenon. Finally, the role of road pavements in UHI is discussed.

1.1. General introduction

According to the most diffused definition, urban heat island is an urban or a metropolitan area appreciably warmer than its surrounding rural zones. In particular, within the most of the large and populated cities, the temperature at the town-heart or at the center is commonly higher than the suburban areas (centers are often several degrees warmer than the less developed zones). UHI phenomenon is more evident in the summer and winter months, especially during night-time and when wind flows are less intense. Generally, temperature differences are more significant in the evening; during the day, such temperature gradients could be between 2 and 5 °C but can raise even 20 °C after the sunset [1.1]. The UHI phenomenon is caused by several factors, mainly correlated to the high-density of people and the subsequent anthropogenic activities: urbanization realizes through the progressive substitution of lands and vegetation with built areas (productive, commercial, residential), infrastructures (roads, bridges, parking lots, etc.) and artificial installations [1.2]. Thus, serious repercussions could interest the perceived comfort and the human health, the air quality and the environmental pollution, as well as the climatic changes and the local

ecosystem it-self. Equally, the energetic performance of buildings and related economical concerns can be affected by such complex mechanism [1.3]. Conceivably, these problems are extremely actual if considering that the percentage of humans living within urban areas is continuously growing; by 2030, it has been estimated that more than the 60% of the world population will live in urbanized regions (80% in the European case) [1.4].

Therefore, UHI theme started to attract growing interest referred to recent literature production and scientific efforts, at least since the last three decades; this could be probably attributable to the actual consciousness about that global-scale environmental matters that have been demonstrated to be strongly involved in the UHI thematic. In this perspective, global warming mechanism must be surely cited; such phenomenon is intended as the complex totality of dynamics that determines tangible increases in the average atmospheric temperature of the Earth, which are responsible of effective climate changings and greenhouse gas concentrations. To this aims, several data about climate and global temperature modification have been widely measured and are available. Dating back the 1980's, some technical reports started to deal with globing warming problems [1.5, 1.6]. If possible, a significant boost in this direction was given when UHI phenomenon started to be linked to human health concerns – Word Health Organization published in 2009 a technical report about chonical diseases and mental health in urban populations due to climate change exposure [1.7]. More recently, an extensive overview about the climate change impacts, vulnerabilities and risks was produced by the European Environmental Agency [1.8]. The Intergovernmental Panel on Climate Change (IPCC) identified the human influence as the dominant cause of observed warming since the second half of the last Century [1.9]. Since 1979, global average land temperatures increased with an approximate rate of 0.25 °C per decade [1.10]. Indeed, recent model projections quantified for the 21st Century a possible increase of the global surface temperature between 1.7 and 4.8 °C [1.9]. Parallely, visible effects of such climatic changes manifested during the last 100 years; according to the IPCC [1.10], 38 heat waves (extended periods of anomalous heat) occurred in Europe during the 20th Century, 11 of which after the 1990 and 6 after the 2000. Such data could be even more alarming considering the actual projections for the next 50 years, under which future heat waves could increase in intensity and frequency [1.11]. In addition, considering also the strict connection between the UHIs and the heat-related mortality (moreover in the case of elderly people), significant costs for public health should be also hypothesized [1.12].

Considering all these reasons, the complex issue of urban heat island started to address several national and international agencies, bureaus, administrations, institutions and governors to adopt specific-focused policies; this, attempting to define fruitful strategies to face the UHI-related problems, in some cases also delivering definite measures, programs and targets to be achieved in the next future for the containing of UHI consequences. As

example, already in 1997, international treaties signed with the Kyoto Protocol [1.13] approached the theme of the global warming. More actually, Paris Agreement [1.14] dealt with greenhouse gas emissions and global warming mitigation, adaptations and finances with an approved program starting in the year 2020 (principal long-term goals aim at maintaining the increase in global average temperature below 2 °C above the pre-industrial levels and the absolute increase to 1.5 °C). In turn, Horizon 2020 financial program is now implementing European policies in the field of environmental research and innovation with the purpose to face climate-related investments. Also American associations, agencies and companies demonstrated and are still manifesting precise efforts to fight the discomforts perceived within the cities related to the demographic growth and the urbanization in general [1.15]. In the same direction is moving also the research focus: literature widely counted different contributions in the field of civil engineering dealing with the topic of UHI mitigation and the study of urban environments, thermo-resistant/low-thermal-inertia materials, buildings and infrastructures [1.16, 1.17]. Concerning road structures and pavements, successful applications and solutions are quite documented. For instances, colored, clear or transparent materials for paving, porous asphalts, special-equipped cool pavements [1.18–1.20] were reported to be suitable to reduce the heat concentration within cities. Quite pioneering studies also tried to define strategies connected to the energy harvesting and the conversion of heat collected by pavements [1.21].

1.2. Historical background

Publishing in 1818 the “The Climate of London: Deduced from Meteorological Observations”, Luke Howard was probably the first scientist to identify an abnormal heat concentration inside an urban environment [1.22]. At the beginning of 1900, the British engineer Guy Stewart Callendar identified a global warming trend and a human-caused greenhouse effect only on the basis of temperature records [1.23]. In the 1930’s, he also studied thousands of temperature stats, most from Europe and North America, and concluded that the world had warmed by about 1 °F (equal about to 0.5 °C) from 1890 to 1935 [1.24]. Furtherly, in 1965, Tony Chandler reported of London’s heat island as a mass of warm air roughly coincident with the city and closely related to wind velocities and cloud amounts as controlled by weather systems [1.25]. In 1967, a successful publication was able to demonstrate an existing relationship between the size of urban areas and the magnitude of the urban heat island; an early model was also proposed to measure the UHI intensity, incorporating variables such as the local wind speed and the population density [1.26]. Basing on these examples, the clear existence of the UHI intended as the complex phenomenon actually dealt was already demonstrated during the 19th Century.

Considering the strict dependency of UHI on the thermal and climatic characteristics of a specific area, historical meteorological data became crucial aspects during the 1900 for the

analysis of UHI mechanisms and definitely improved the specific scientific production. In parallel, demographic analysis and statistics started to be employed since historical temperature recordings seemed to strongly suggest that UHI intensity could be attributed to the increase of population, the urban development, the modification of urban surface properties and the increments of anthropogenic heat production and energy consumptions [1.27]. Further development of satellite technology and remote sensing started then to allow the objective recording of UHI characteristics, spatial and temporal distributions (above all during the second half of the 19th Century) [1.28]. More recently, modeling approaches have been widely used to define the effective growth of urban heat island and have been also utilized as starting points to propose trends and projections about the future UHI properties and severity, also in view of the well-documented climatic changes globally recorded. For instance, temperature recordings from 50 large American metropolitan areas (urban and proximate rural regions), collected between 1951 and 2000, have been utilized to demonstrate that the mean decadal rate of UHI intensification has been of about 0.05 °C [1.29]. Other researchers demonstrated the UHI intensification through long-term analysis (since the 1960's) concerning nocturnal temperature in London, especially during spring and summer (+0.131 and +0.120 °C, respectively) [1.30]. Actually, urban-correlated biases between 14 and 21% of the rise in minimum temperatures since 1895 and 6 to 9% since 1960 were found. In 2004, Kim and Baik analyzed UHI trends in the six largest cities of South Korea during the period 1973–2001 and discovered an average increase of 0.3 °C per decade of the daily maximum temperatures [1.4]. Again, American researchers in 2002 evaluated historical temperature trends (from 1900 to 2002) within the city of New York and accounted an urban heat island intensification responsible for 1/3 of the total warming experienced by the town since the year 1900 [1.31].

1.3. Urban heat island

1.3.1. UHI composition

The description of urban heat island composition can surely improve the full understanding of the aspect. Therefore, depending on the mechanisms of development, the spatial and the temporal horizons, different concepts of UHI can be defined.

The **Surface Urban Heat Island** (SUHI) regards the urban surfaces affected by higher temperatures with respect to those involved in rural areas. Such dynamic typically manifests through the entire day but boosts during the sun-exposed periods; averagely, difference reaching 10–15 °C during sunshine hours and 5–10°C during dark hours can be detected. Being influenced by the degree of sun exposure, SUHI intensity is strictly dependent on the season of the year. Irradiated building surfaces and pavements during summer could reach temperatures 25–50 °C greater than the ambient one, whereas humid or shaded spaces

typical of countryside fair differ in terms of heating. The fundamental parameter used to measure SUHI is the Land Surface Temperature (LST) generally recorded by radiometers on board of aircraft or satellites [1.32–1.34]. In particular, many researches established a strict connection between SHUI conformation and elements such as the urban area size, the building's concentration, the street geometry, the traffic volume, the human activities, the population density, as long as the presence of impervious surfaces [1.35–1.37]. Main indicators considered in different studies concerned the population, the economy and the involved space. SUHI temporal variation pattern could be a little different with respect to that of the global UHI [1.38]. The maximum value of SUHI is usually reached certain time after the recorded maximum UHI peak [1.39]. This is verified because the mechanisms that contribute to the formation of UHI and SUHI are quite different [1.40]. Commonly, UHI is mainly caused by the difference in radiative cooling rate between urban and rural regions at night, while SUHI is mainly governed by the difference in radiative surface heating during the day-time (inside and outside of the urban area). However, the response of SUHI varies also in function of the climate background and the land cover [1.41]. For instance, Figure 1.1 reports some examples of LST distributions in an area of the northern China, derived from Landsat TM images collected among different years (from 2006 to 2010) [1.42].

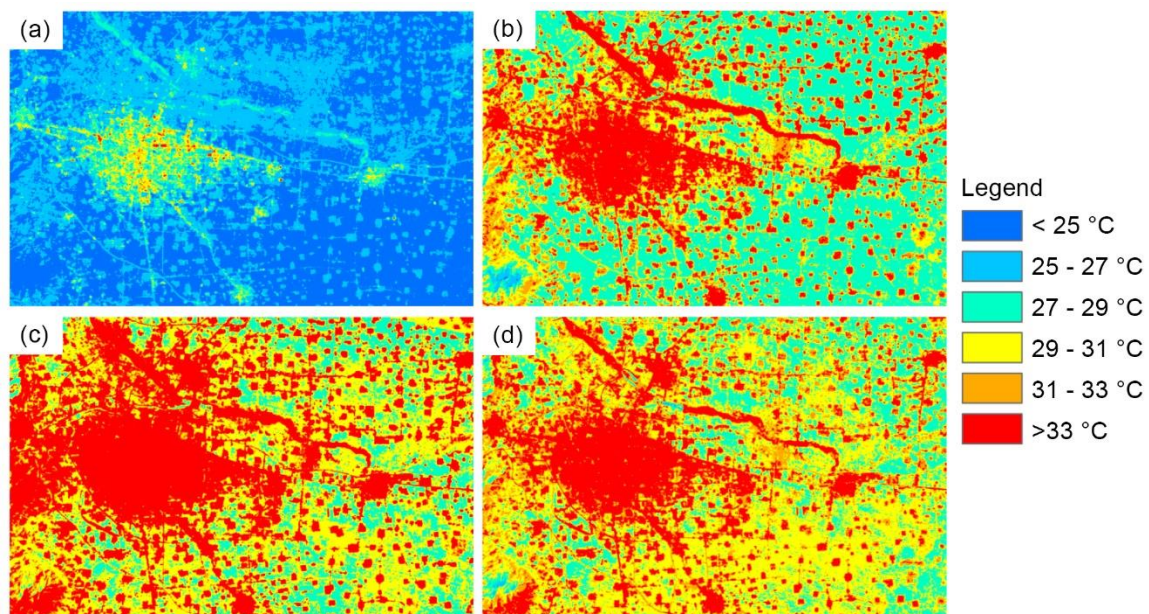


Figure 1.1. Examples of LST distribution in northern China: 5th September 2006 (a), 23th August 2007 (b), 12th August 2009 (c), 15th August 2010 (d).

A close relationship between the land surface temperature and the near surface air temperature is generally demonstrated, thus the SUHI is a reliable indicator of the **Atmospheric Urban Heat Island (AUHI)** phenomenon, defined as the higher air temperature in cities with respect to the that of the country. Therefore, AUHIs are based on air temperature, which is usually measured though thermometers installed at field sites or

with ad-hoc-equipped vehicles [1.43, 1.44]. For this reason, characterization of AUHI is more suitable to identify the UHI local causes, commonly characterized by spatial and temporal variations [1.45–1.47]. Climate factors such as wind (speed, typology, temperature, direction, etc.) and cloudiness often change in a few times and interact with the urban environment. All its elements have been widely studied analyzing UHI; it is ascertained that the urban forms affect the urban microclimate [1.48, 1.49], even to the point that the relationship between urban shape and climatology has been proposed as a focus point in urban planning and design practices [1.50, 1.51]. For instance, the Sky View Factor (SVF) has been generally considered a crucial parameter useful to describe the urban spaces [1.52]; SVF is referred to the ratio between the radiation received by a planar surface and the radiation emitted by the entire hemispheric environment (it owns dimensionless values that range from 0 to 1) [1.53–1.55]. Given the importance of SVF in determining the radiation on urban surfaces (being at the ground-level, road pavements could probably be one of the urban portions mostly affected by obstacles), several studies tried to optimize its calculation: traditional techniques aim at projecting the surrounding building geometries onto a hemisphere located at the measuring point and computing the ratio of blocked to unblocked parts of the sky. Otherwise, considering the particular complexity in evaluating SVF inside the urban spaces (moreover with particular landscapes counting skyscrapers and high buildings), specific models and software have been proposed [1.56–1.59].

More specifically, AUHI can be subdivided in two further portions.

The **Canopy Layer Urban Heat Island** (CLUHI) interests the segment of AUHI contained between the ground level and the medium height of buildings and directly influences the perceived comfort and the human health. For these reasons, canopy layer urban heat islands are the most studied concerns. Generally, CLUHI assumes the greater importance towards the night-time because urban surfaces employ a certain time to release the heat (a substantial delay occur between the solar exposure and the heat release) [1.60]. As obvious, CLUHI and SUHI (canopy layer and surface UHI) develop strong interactions since they are merged together and constitute the volume interested by all the urban “things”.

Contrarily, the **Boundary Layer Urban Heat Island** (BLUHI) influences the superior layers of the atmosphere, starting above the CLUHI and interesting the space up to the line at which heating effect disappears (up to about 1.5 km) [1.61]. As conceivable, the strict determination of the boundary layer height, as well as the measurement of variables within the BLUHI, could represent stringent challenges, above all in the higher atmospheric portion. Because of such constrains, literature started to deal with specific modelling to estimate the boundary layer properties [1.62, 1.63] also considering that a crucial role is covered by the efficacy in measuring the surface UHI processes which occur at land level [1.64]. Further interest in BLUHIs is justified by associated air-pollution concerns [1.65].

As summary, Figure 1.2 schematizes the spatial distribution of the distinct UHI typologies.

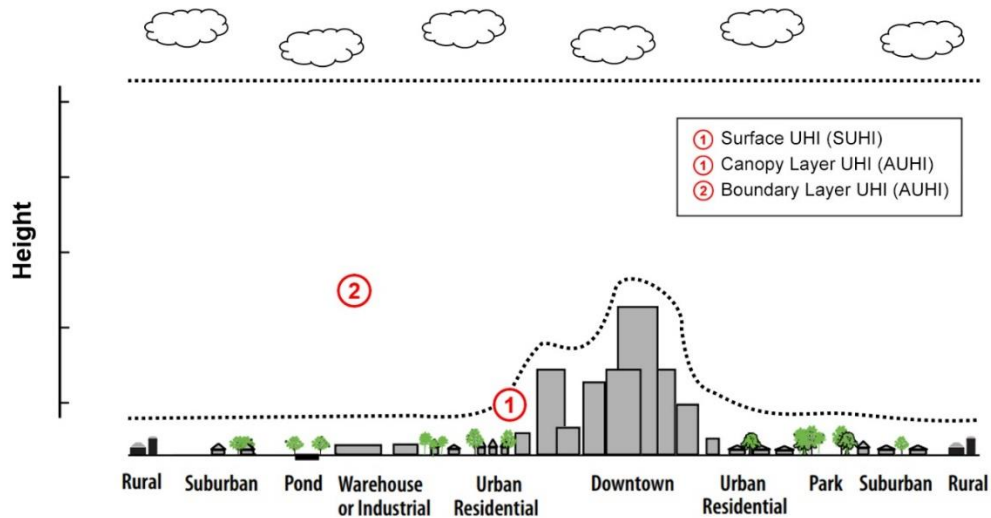


Figure 1.2. Scheme of spatial distribution of UHI typologies.

Ordinarily, monitoring of air temperatures requires the use of direct measurement methods (fixed or mobile thermometers); an overall view of surface temperatures can be provided by thermic remote detection (quantification of infrared radiations emitted) through specific satellite sensors. Collected data could be useful to produce the thermal mapping of the focus area. For further deepening, Figure 1.3 and Table 1.1 depict some features of surface and atmospheric UHI, respectively [1.66].

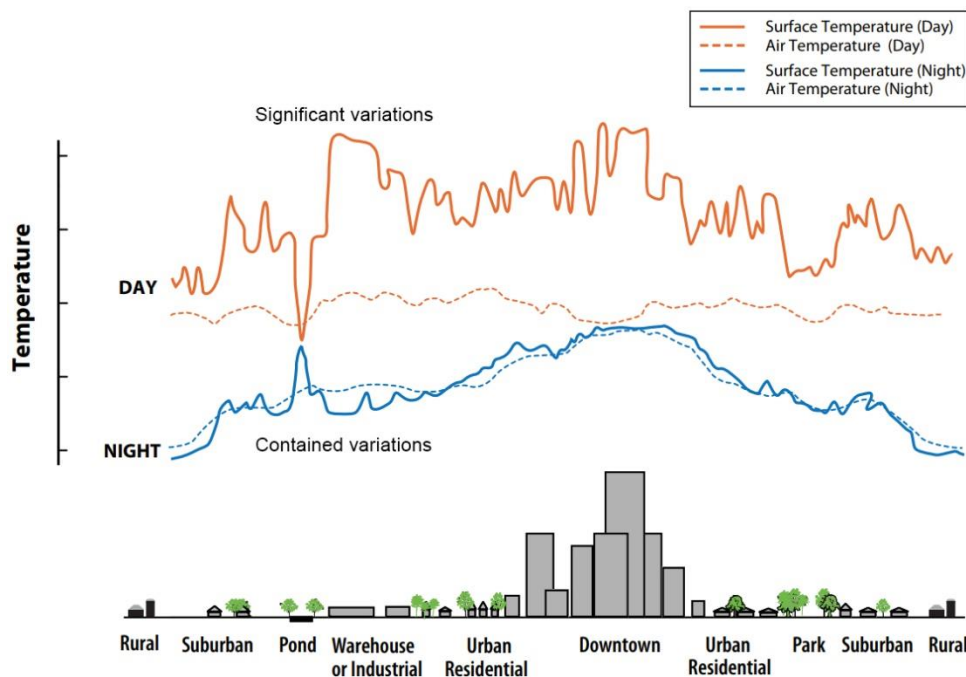

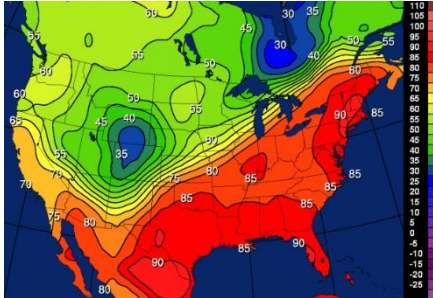


Figure 1.3. UHI scheme: example of temperature trends on surface and atmosphere.

Table 1.1. Comparison between features of SUHI and AUHI.

Feature	Surface SUHI	Atmospheric AUHI
Duration	Always present	Small/absent during day-time
Intensity peak	Day-time (summer noon)	Night-time (winter dawn)
Variations	Significant (spatial/temporal)	Contained
Analysis method	Remote sensing (indirect)	Temperature measurement (direct)
Representation	Thermal sensing	Isotherm map
Example [1.67, 1.68]		

1.3.2. UHI causes, impacts and effects

UHI phenomenon is a concern whose causes are complex and often related to multiple factors, even linked each other. As mentioned, the higher temperatures of UHI can be usually attributed to the human activity in general, as well as to the urban development and the progressive substitution of green areas and vegetation with significant amounts of high-absorbing and impermeable construction materials (moreover utilized within complex urban layouts that exacerbate the concentration and the entrapment of the solar heat).

More specifically, many urban areas lack of green coverage such as the **vegetation** [1.69]: in rural regions, open lands typically dominate the landscape, therefore plants and high-growing trees provide shade and help in attenuating the superficial temperatures, also promoting the EvapoTranspiration – ET (i.e. an important stage of the water cycle) for which the water vapor is released in the air by the soil and the tree leaves [1.70]. The evapotranspiration process helps to cool the surrounding air dissipating the ambient heat (generally, the combined effect of ET and cooling is evaluated since the two variables cannot be accounted separately) [1.71]. Some estimates indicated that, with favorable conditions, a vegetation cover of 30% is able to decrease peak temperatures by up to 6 °C [1.72]. In contrast, cities experience lower levels of ET than rural areas since they are characterized by dry and impervious surfaces (building walls, roofs, sidewalks, roads, parking lots, etc.) which usually reduce the removal of carbon dioxide and do not provide cooling shades [1.73]. Urbanization impacts on the water cycle since the impermeable surfaces affect the retained quantity of water, thus the global moisture useful to keep cool the urban areas: some authors even indicated a negligible urban ET because considerably lower than that from neighboring rural areas in view of the hydrological properties of building materials and vegetation-covered soils [1.74]. Otherwise, based on Figure 1.4,

whilst evapotranspiration and soil infiltration of rural pristine areas have been recently estimated respectively equal about to 40% and 50% of the total, urbanism significantly changes this proportion (evapotranspiration and infiltration respectively limited up to 30% and 15%), causing a surface runoff of about 55% due to the extensive presence of impermeable surfaces [1.75].

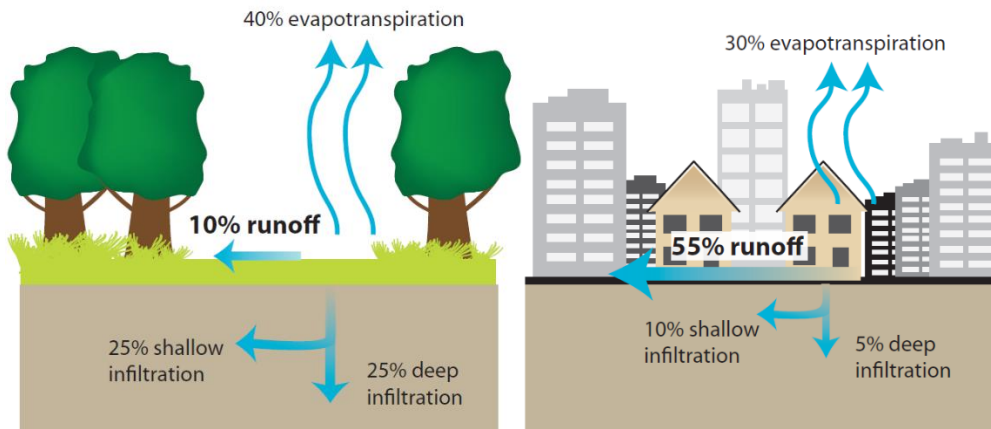


Figure 1.4. Evapotranspiration and infiltration in rural and urban areas.

Furtherly, urban heat island development is influenced by the radiative properties of the **urban materials** that, when hit by solar energy, determine the entity of reflected, adsorbed and stored radiations [1.76]. Urban surfaces (typically roofing and paving) are characterized by lower reflection coefficients than those recorded in rural settings. As a consequence, the absorbed heat increases the temperatures of the surfaces and contributes to the formation of SUHI and AUHI [1.77]. Similarly, such materials tend to exhibit specific thermal emittances that compromise a readily release of the collected heat and determine higher surface temperatures [1.78]. Another important property that influences heat island development is the heat capacity of the materials, which refers to its ability to store heat. Many constructions materials own higher heat capacities than rural ones; as a result, cities are typically more effective at storing the energy of Sun as heat within their infrastructures. Downtown metropolitan areas can absorb and store almost twice the amount of heat in comparison with their rural surroundings during the day-time [1.79]. For all these reasons, strategies to mitigate the UHI have been widely addressed to the accurate design of construction materials utilized within urban areas [1.80, 1.81]. As an example, green/cool roofs have been studied to modify the development of day-time BLUHI and govern the energy balance of the surfaces to potentially reduce the atmospheric warming [1.82, 1.83]. In this perspective, Figure 1.5 gives an estimation of the benefits achievable through the application of common-employed solutions for cool roofs [1.84]. In the case of pavements, which are thicker than roofing products and are located at the ground level, a more complex set of factors, included the radiative and thermal properties of materials, must be considered to face the UHI development [1.85, 1.86].

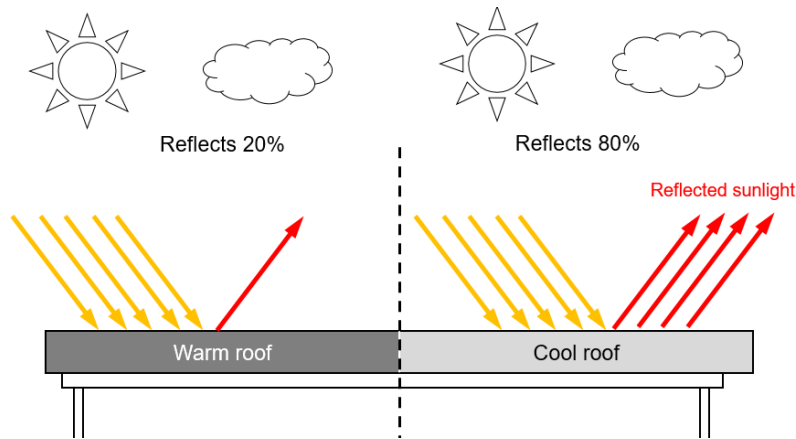


Figure 1.5. Cool roof as a solution to enhance the reflected solar radiation.

Although the UHI dependency on the time, the city extensions, the weather and the climate characteristics has been widely documented [1.87], an additional factor that influences urban heat island development, particularly during the night, is the **urban geometry**, intended as the dimensions and spacing of buildings within the city [1.88]. Residential and business zones deeply modify the wind flow and alter the solar radiation patterns, giving obstructions to the heat masses due to the presence of urban canyons [1.89–1.90]. These ones also shield the coolant process of air currents, improving the absorption of solar emissions and dampening the heat dispersion (rays bounce on the canyon surfaces); additionally, in absence of convection cooling, air pollution is able to stagnate and increase [1.91]. Moreover, urban buildings delimit roads; this fact promote the solar radiation trapping for which the reiterated glare between canyon facades increases the fraction of energy absorbed by surfaces also at the ground level [1.92]. In this perspective, several scientific efforts have been spent to understand the complex role of the urban shapes in relation with UHI characteristics and intensities; multi-disciplinary approaches useful to describe such complexity could concern several fields of study, for example the urban planning, the building design, the fluid dynamics, etc. [1.93].

Among the various factors contributing to urban heat islands, also **anthropogenic warmth** can be cited [1.94]. Heat produced by human activities contributes in developing AUHI [1.95]; it derives from various sources linked to the urban activity and the infrastructures (heating systems, stoves, fireplaces, artificial lighting, transport use, industries, etc.). Usually, anthropic heat does not interest the rural areas. Especially during winter, it can significantly boost the UHI formation [1.96]. In general, the anthropogenic heat flux Q_F can be indicated as reported in Equation 1.1, where the single components Q_{FV} , Q_{FH} , and Q_{FM} stand for the heat generated by vehicles, the heat generated by stationary sources (houses, factories) and the metabolic heat generated by humans and animals, respectively.

$$Q_F = Q_{FV} + Q_{FH} + Q_{FM} \quad (1.1)$$

For instance, the Anthropogenic Heat Flux (AHF) has been globally estimated equal to 0.028 W/m^2 in 2005, with a spatial distribution mainly concentrated in the most urbanized world areas (Figure 1.6.a); an increasing AHF trend has been estimated according to projections regarding the next decades, towards the 2040 (Figure 1.6.b) [1.97].

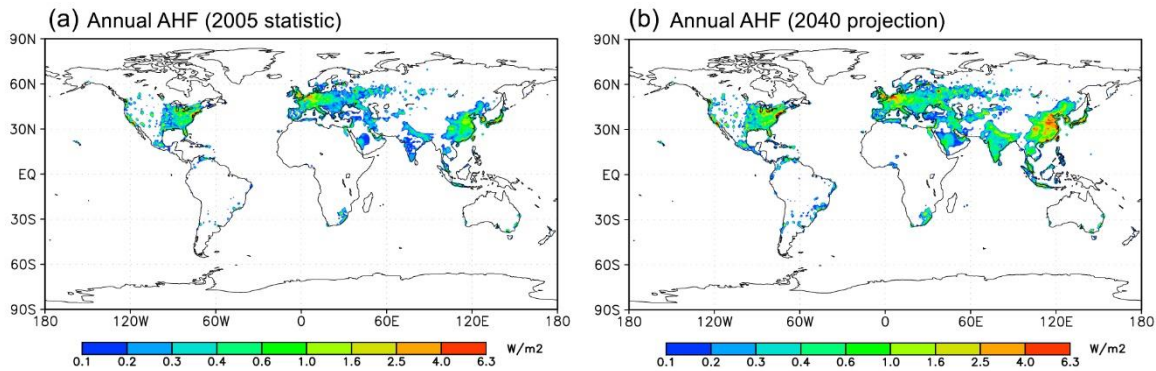


Figure 1.6. Anthropogenic heat flux statistics: 2005 record (a) and 2040 projection (b).

As mentioned, also **weather** and **location** strongly affect the urban heat island formation. Concerning weather, two primary characteristics are crucial: wind and cloud cover. In general, urban heat islands form during periods of calm winds and clear sky, because such conditions maximize the amount of solar energy reaching urban surfaces and minimize the amount of heat that can be sent away. On the contrary, strong winds and deep cloud coverage tend to avoid UHIs [1.45]. For these motivations, also orography and eventual presence of large water bodies (basins, lakes, seas, etc.) own importance (wind formation and magnitude are deeply governed by the territorial conformation) [1.98]. As a summary, Figure 1.7 summarizes all the factors contributing to the UHI formation.

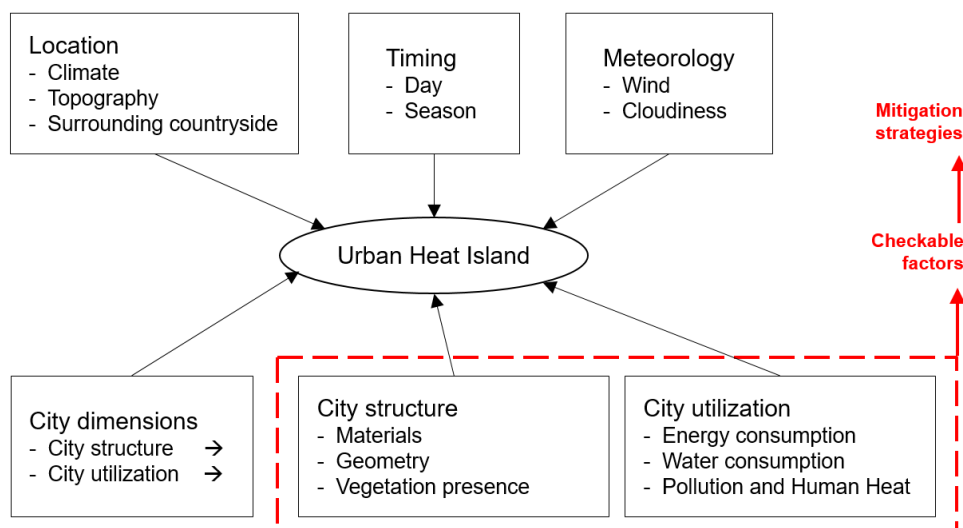


Figure 1.7. Global factors influencing the formation of UHI.

A large-scale scheme of the energy budget which quantifies the incoming and the outgoing energy flows regarding a typical urban environment is also presented in Figure 1.8 [1.75].

In particular, energy of surfaces should differ from that of rural regions because of the different land covers, the materials properties and the presence of anthropogenic heat. Short-wave and long-wave radiations are less reflected by urban materials and geometry, thus they cannot be easily released into the atmosphere and enhance the storage of heat. Sensible heat stands for the perceived temperatures, intended as gradients between surfaces and air (urban surfaces warm the air above them). Latent heat is referred to the evapotranspiration mechanisms, that are perceived as humidity (dry and impervious urban infrastructures could determine very high surface temperatures).

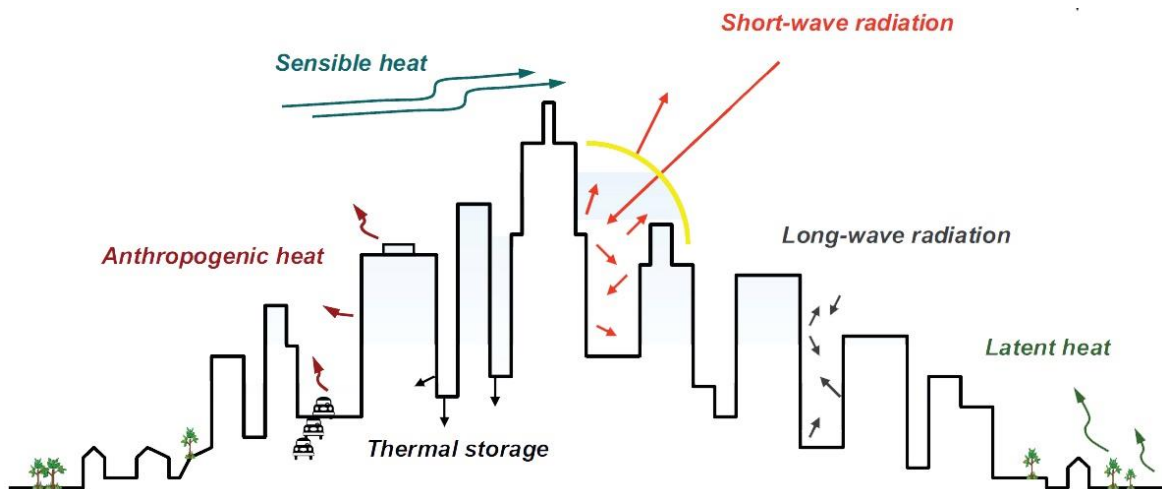


Figure 1.8. Urban surface energy budget.

For what concerning the UHI effects, one of the most debated impacts regards the human life. Essentially, the increased day-time temperatures are associated to a general discomfort perceived by humans [1.99]. This fact is surely enhanced if considering the reduced night-time cooling effect, for which humans could suffer because the UHI tend to prevent the decrease of night temperatures with respect to that happening in the rural districts [1.100]. Nevertheless, heat can directly threaten the human **health** it-self: headaches, respiratory problems, heat cramps, strokes and faints are well-known effects directly connected to the heat concentration. Absolutely, vulnerable population (children, older adults, people with existing health conditions) is at risk even of events of heat-related mortality. With the presence of extended periods of abnormally heat (the so called “heat waves”), urban heat islands can also worsen the impacts on health by favouring particular weather conditions and high humidity rates. Extreme temperatures menace individuals with pre-existing health conditions also in the case of significantly impaired cognitive functioning (e.g. Parkinson’s disease or dementia); people with diabetes, obesity, asthma, sleep deprivation or cardiovascular disorders are advised to heat exposure that, in many cases, could aggravate and intensify symptoms or cause permanent damages to organs, thus the risk of early death [1.101]. Some estimates accounted an average number of heat-related deaths that passed

from 0.6 to 1.8 per million people from the 1990 to the 2011 in the United States; in 2011, 3.5 deaths per million people were due to heat and cardiovascular disease [1.102]. One of the strongest heat waves registered in Europe, caused in 2003 over 70 000 deaths, distributed in 12 countries; among that, the majority was already at risk from heat-stroke, cardiovascular, renal, respiratory and metabolic disorders associated to high temperatures [1.103]. As an example, Figure 1.9 shows the rate of mortality related to environmental concerns in the different world countries (statistic for year 2000) [1.104].

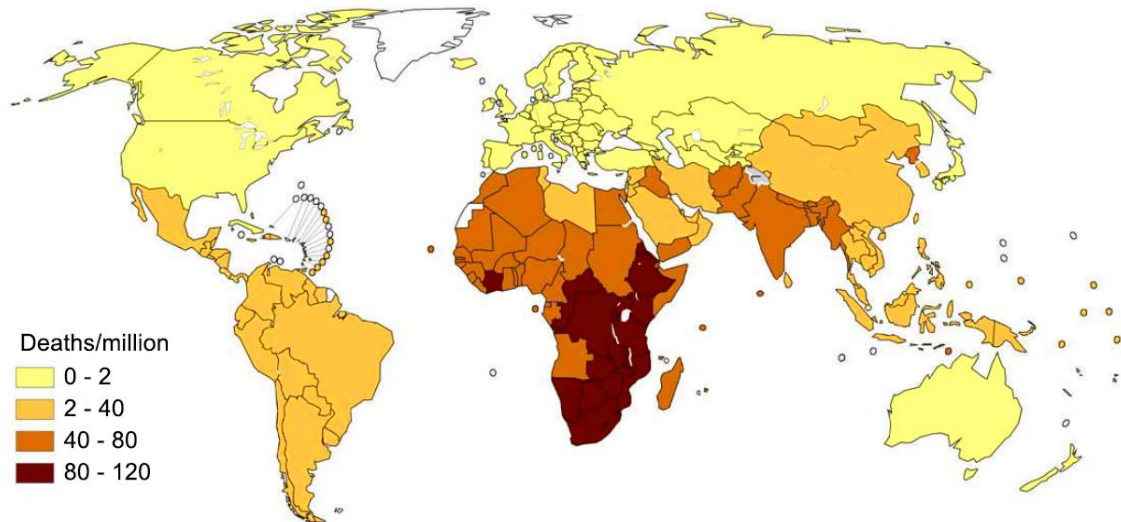


Figure 1.9. Environmental-related deaths recorded worldwide in year 2000.

Basing on such preliminary information, it could be understood that UHI consists in a complex phenomenon related to large-scale dynamics and global mechanisms referred to the climate and the environment. On the other hands, it is widely demonstrated that UHI directly impacts on such global aspects. The **global warming** is the evident effect of the world climate change that occurred over time. Despite the natural temperature variability documented since the Earth formation, the heavy responsibility of the human activity could be ascertained if considering that temperature increased by 0.6 °C just during the 20th Century, above all over lands rather than oceans [1.100]. Indeed, urban anthropogenic heat does not seem to create a direct impact upon global warming; heating of urban atmospheres exerts a slight influence upon the computation of global heat since high-populated areas cover less than the 1% of Earth's land surface; but, on the opposite way, cities are considered very intense sources of anthropogenic greenhouse gases that indirectly contribute to the global warming. The greenhouse effect consists in that processes for which the radiations due to the atmosphere warm the planet surface, determining a temperature higher than that it would be recorded without the same atmosphere [1.10]. Atmospheric gases absorb some wavelengths of energy and, with combined effects, contribute to the greenhouse effect on Earth: main actors are generally reported to be the water vapor, the carbon dioxide, the methane and the ozone [1.105]. Principally concerning the CO₂, anthropogenic activities

are responsible of the most severe emissions that strengthen the greenhouse effect [1.106]. Radiative power of atmosphere is influenced by UHI, as well as by high pollution levels; the temperature raises within the cities promote the concentration of greenhouse gases, motioning a self-feeding circle which develops a mutual cause-effect interaction [1.107]. For instance, Figure 1.10 depicts the amplitude of global warming (per billion people) caused by the different countries and measured in average temperature increments (historical data referred to the 20th Century) [1.108]; Figure 1.11 illustrates the average CO₂ emissions recorded in 2010 for each country [1.109].

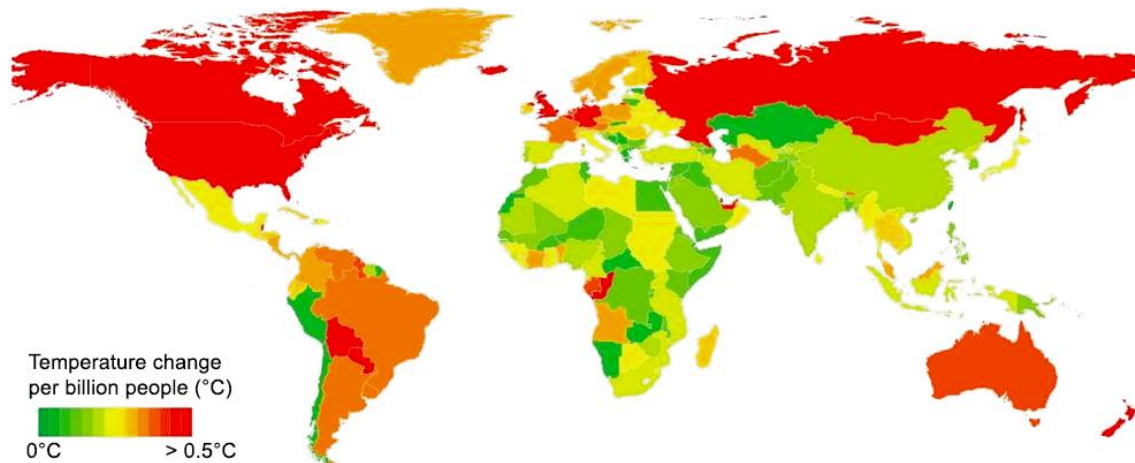


Figure 1.10. Temperatures change across the world (1906–2005).

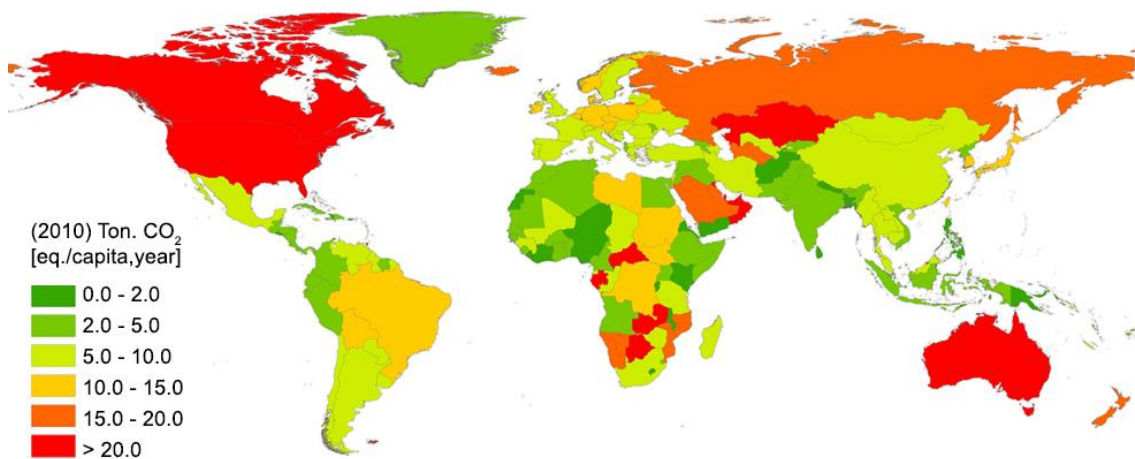


Figure 1.11. Emissions of CO₂ recorded across the world (2010).

Another interesting prospect is given in Figure 1.12, where changes in global average temperatures are projected for the future under four emissions pathways (rows of the Figure 1.12); in particular, RCP2.6, RCP4.5, RCP6.0 and RCP8.5 scenarios indicate very low, medium, medium-high and high emissions pathway, respectively (assuming a constant emission increase throughout the century) [1.9].

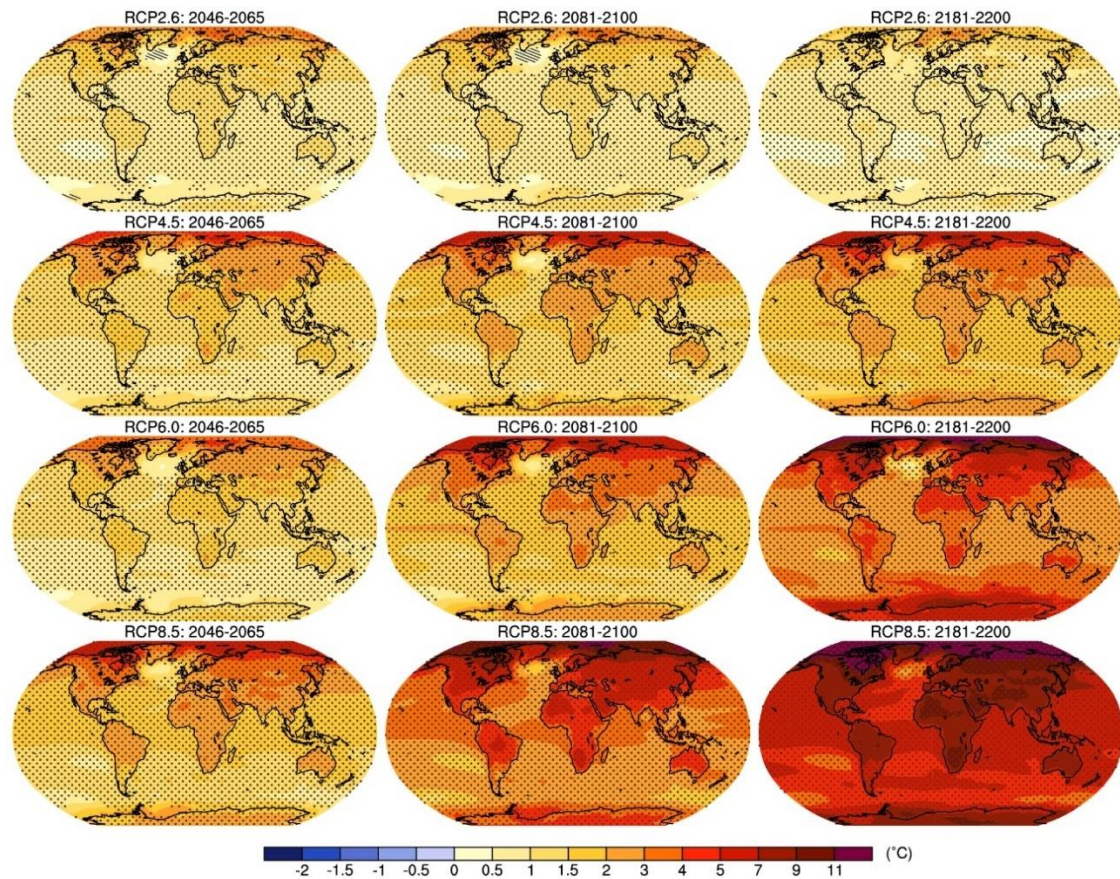


Figure 1.12. Projection of global mean temperature increases under different emission scenarios (2046–2200).

Indeed, urban heat islands also bring secondary effects on the **local climate** and the local weather conditions, influencing elements such as the cloud coverage, the fog presence, the humidity levels and the wind patterns. Moreover, hotter temperatures condition the upward movement of air masses that surround the atmosphere, thus alter the frequency and intensity of precipitation and encourage the formation of thunderstorms and intense climatic events. In fact, during the day-time, UHI experiences local low-pressure areas because of the cool air converging from the adjacent rural zones; this fact creates a framework for the contrast between cool and hot masses which could lead to the increase of the total rainfall rates in the city thanks to the ideal conditions of cloud coverage and high humidity. A visible consequence of such aspects is given by the modification of the phenology (the seasonality and the growing rate) of several plant species inserted in the urban context [1.110].

Further, impacts on **ecosystem** are also manifested in the reduction of water quality due to the higher temperatures reached by the urban surfaces (pavements, roofs, roads, etc.): this is traduced in hooter stormwater runoffs that, once drained, gain streams, rivers, ponds and lakes and tend to affects all aspects of aquatic life. Especially, increased feeding, disorientation, increased metabolism, reduced reproduction and possible mortality of many

aquatic species are affected; palpable repercussions are documented also about the decrease of the aquatic species diversity and the modification of some migrating patterns [1.111]. In analogy, UHI impacts on the animal life and the fauna. Several species request optimum temperatures to colonize and interact with their ecosystems. Adverse heat conditions could significantly reduce the availability of food, shelter and water supply; in turn, a chain reaction concerning plant and animal species could be established in the case of herbivorous (animals dependent on certain agronomic species must adapt their natural breeding seasons in order to match the plant growing patterns) [1.112]. In addition, climatic and temperature changes may also make the cities suitable environments for survival and attract animals, as well as promote the concentration of insects [1.113]. Besides, urban heat island can equally alter the natural selection process, causing a counterbalance of new set of selective forces. A typical example regards the growing existence of winter-climate species within cities and mild-climate regions, which are progressively bypassing the migrations towards their common habitat in the northern regions [1.114]. In other cases, opposite trends could be also recorded [1.115].

Parallely, **economical drawbacks** could be referred to UHI. Elevated temperatures in cities increase the energy request for cooling, especially during the summertime. Overall and peak electricity demands generally occur on hot summer weekday afternoons, when living and productive buildings utilize cooling/conditioning systems, lights and appliances (blackout are more and more frequent because of electrical overloads) [1.116]. In this perspective, certain researchers demonstrated that the demand for electricity grows of about the 2% for each Celsius degree of air temperature increase (from 20 to 25 °C) and stated that the 5–10% of the global electric energy requested is summerly spent to face the UHI effects [1.117]. As an example, predictions about electricity demand estimate that, in USA, about 260 TWh will be spent for air conditioning in view of the UHI phenomenon, i.e. more than one-and-a-half times of the consumption recorded in 2005 (160 TWh); this concern is even more interesting if considering that the same projection is equal about to 200 TWh neglecting the UHIs and the hypothesis of global temperature increase [1.118]. As a consequence, such energy supply inevitably leads to emissions of air pollutants and greenhouse gases from the power plants and the conditioning systems (further relations of the latter with the well-known damage of the stratospheric ozone layer have been verified [1.119]). In general, power plants emit pollutants (as sulfur dioxide, nitrogen oxides, particulate matter, carbon monoxide and dioxide, mercury) that have been certified to be harmful to human health and promote the formation of ground-level ozone (smog) and particulate matter (sunlight and hot weather enhance the concentration of smog) [1.120]. Economical involvements regard also energetic balance of buildings: heating and cooling are crucial in total building energy but, therefore, it must be considered that UHI intensity could deeply exert effects on building performance (outdoor temperature influences the incoming heat and cooling load). For instance, global building sector used approximately

115 exajoules in 2010, accounting for 32% of the final word energy demand. Nevertheless, commercial heating and cooling energy use is still expected to strongly increment towards the 2050, with an approximate growth of the 84% with respect to the 2010 (the 79% for residential heating and cooling) [1.121]. Not for nothing, a certain role of building envelope has been demonstrated in mitigating the power consumption for space cooling, thereby in containing the UHI effect [1.16].

1.4. The role of road pavements

An important role of road pavements in the phenomenon of urban heat island is widely recognized by the scientific community [1.122]. This occurs because the pavement thermal balance is governed by the quantity of the absorbed solar radiations which determines the heat stored into the pavement mass and the heat transmitted to the ground. Thus, the subsequent heat transferred by convection to the atmospheric air and the emitted infrared radiations influence the ambient temperature in the road proximity and contribute to the UHI intensification [1.123]. More specifically, the incoming solar radiation is partly absorbed by the pavement and partly reflected, depending on the radiative properties of the pavement materials. The reflected portion is constituted by short-wave radiation; pavement also emits long-wave radiation and loses heat to the air through convection (the net heat on pavement is the difference between that entering and leaving the structure). A notable difference between road pavements and roofs (i.e. the main horizontal surfaces of urban areas) stands in the inclusion of unbound aggregate layers in the former which add significant complexity to the modelling of thermal performance of surfaces (the porous nature of aggregates can create suction and influence the moisture content of layers) [1.124]. More specifically, the thermal balance at ground level could be analyzed within the day-time or the night-time, in the rural and urban zones, evaluating all the definite components and their influences. According to Equation 1.2, the net radiation (Q^*) must be intended as the sum of the turbulent sensible heat flux (Q_H), the turbulent latent one (Q_E) and the heat flux exchanged for conduction with the bottom layers (Q_G).

$$Q^* = Q_H + Q_E + Q_G \quad (1.2)$$

Both the norm and the sign of such components are strongly variable; they namely depend on the instant of the day, the weather conditions, the season, the soil characteristics and moisture, the air properties and the wind profile. Turbulent sensible flux depend on the temperature gradient between the ground surfaces and the air, the wind profile, the air vertical mixing and the possible wind canalization effects on the city. Latent flux is affected by the soil humidity and that of the air in the ground proximity. In the rural environment, the incoming net radiation is due to the solar irradiation during the day; it is dissipated

through the soil conduction and convective phenomena with the air (latent flux connected to evapotranspiration and sensible flux). During nighttime, the directions of the energetic fluxes are inverted. Here, the balance is realized according to the following Figure 1.13.

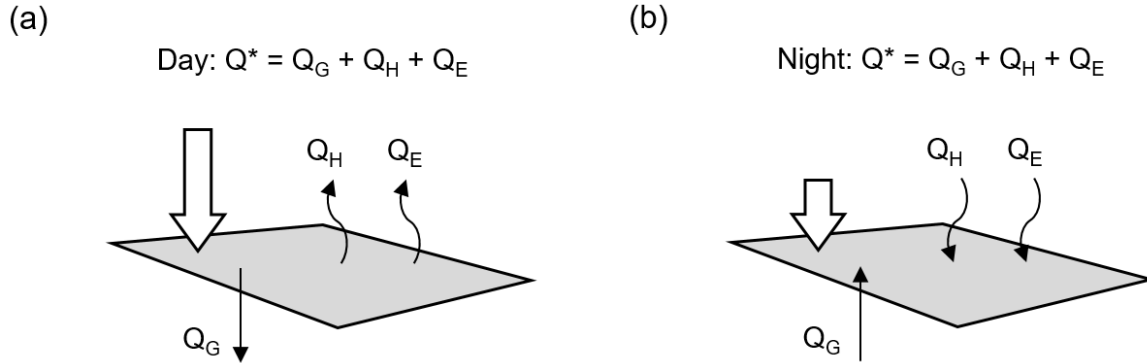


Figure 1.13. Ground energetic balance for a rural area during day-time (a) and night-time (b).

The determination of such balance in the urban areas could result more difficult in view of the general complexity of the cities. The studied zone is poorly limited (a strict delimitation is quite difficult) and the city access lines realize thermal bridging with development of turbulent phenomena. Horizontal and vertical urban surfaces are largely variable in terms of thermal performance, humidity and heat retaining capacity. City roofs own greater thermal inertia and are more impermeable with respect to rural surfaces. Such a different behavior is exemplified in Figure 1.14. During day-time, heat dispersion by ET is negligible, thus the latent heat (Q_E) is almost null (the lack of vegetation and the impermeable surfaces obstruct the water accumulation). Then, the reduced heat dispersions increased the heat retained by pavements, which result substantially hotter. During night-time, heat is dissipated in form of sensible heat (Q_H) and causes the air warming. Humidity covers a key role, since it decreases such Q_H released from pavements and increase the latent component (Q_E). As conceivable, the energetic analysis of each single urban surface must be substituted by a global balance, in particular once established a control volume (see Figure 1.8). The balance related to the defined control volume is that presented in the Equation 1.3.

$$Q^* + Q_F = Q_H + Q_E + \Delta Q_S + \Delta Q_A \quad (1.3)$$

where Q_F indicates the above-mentioned anthropogenic heat flux derived from the human activities, ΔQ_S is the heat stored by the pavements and ΔQ_A is the heat coming from the heat advection (for the control volume). ΔQ_A comes from the lateral wall and is determined by the air mass movement in the horizontal direction (when different air temperatures occur). It can be neglected analyzing central town areas (similar conditions to the surrounding areas), whereas it assumes strong importance in the urban edges (where significant diversities can be detected in the rural outer proximity).

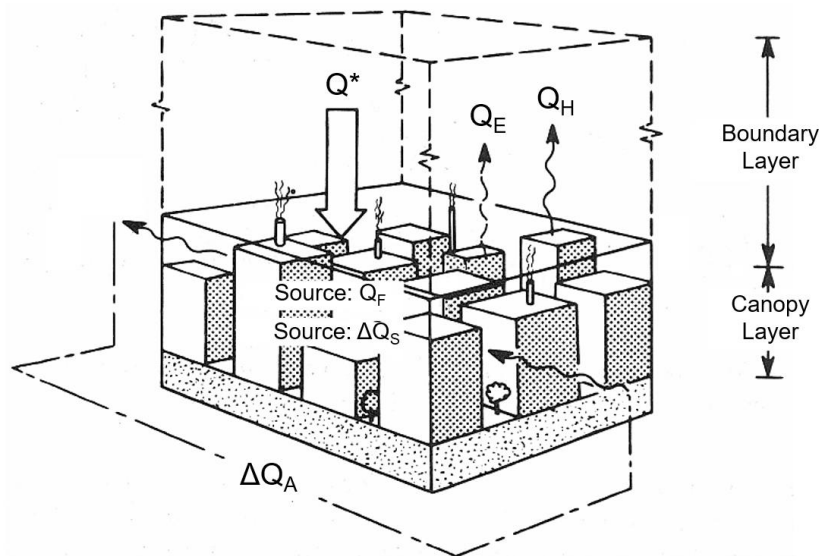


Figure 1.14. Ground energetic balance for an urban area.

In general, road thermal concerns are commonly evaluated through experimental and computational simulations, also using meso-scale remote sensing techniques or micro-scale measurement methods which involve infrared thermography and conventional temperature monitoring [1.125, 1.126]. Also satellite based analysis could be utilized to assess the surface temperature of road pavements [1.127, 1.128] since they represent effective tools to understand the spatial distribution of urban surface temperatures and evaluate at an early phase the impact of pavement materials on urban heat islands. Indeed, given some constraints related to time limitation, orbit, image resolution and interpretation, [1.129, 1.130] micro-scale measurements could provide more detailed information on the thermal conditions and processes interesting the pavements. On the basis of such techniques, several literature-based publications tried to account the magnitude of road thermal properties regarding the development of the UHI [1.131]. In general, many researches were able to conclude that road pavement could be considered one the major contributors to the development of urban heat island [1.132]. Indeed, such estimations could be very difficult if it is noted that the energy balance and the latent heat phenomena concerning road pavements are also influenced by factors such as the evaporation and the condensation (which govern the thermal regime of the pavement surfaces), the eventual effects of rain and ice, as well as the anthropogenic heat generated by the traffic during the use of the infrastructure [1.133]. Despite the complexity, successful analytical or numerical models demonstrated good degree of complexity and reliability in predicting specific thermal phenomena which may not be measured in a direct way [1.134].

A realistic and integrated evaluation could be even carried out stressing that the road system is inserted within the urban context, thus considering the effects of pavement types and thermal performance on the near surface air temperature including many environmental and

boundary parameters [1.15]. Besides the above-cited effects of traffic, street surroundings (presence of buildings, trees, attractive poles, etc.) should be taken into account also in view of the road location it-self. Thus, environmental variables including air temperature, wind, cloud cover, sun light, solar radiation, humidity level, etc., join to the specific physical parameters owned by pavements constituents [1.135]. However, as anticipated, thermal properties of objects, i.e. radiative performance of the pavement materials composing the surface layers (as well as the deeper structure which affect the ground flux of heat), are recognized among the most important aspects in preventing the UHI [1.136–1.138]. In this perspective, “cool” road pavements started to be proposed as compendium of techniques with the objective of improving the urban climate and prevent the heat island [1.86, 1.139].

Overall, “cool pavement” term is usually referred to a wide range of established and emerging materials and pavement technologies used to store less heat and lower the surface temperatures (with respect to the conventional solution) [1.140]. Some researchers believe that the most useful technique concerns the reflectivity of the pavement surface; high-reflective (clear or colored) roads allow the containing of the available heat at the surface and soften the conductive processes occurring on pavements [1.141]. Nevertheless, some authors tried to manage the aptitude of radiation emission furnished by pavements [1.142]. In some cases, convection (i.e. heat transfer from the surface to the moving air on its top) was studied in view of the speed and temperature of the above air, the pavement roughness and the total surface exposed to radiations. Pavements with low thermal conductivity (heat transmission from the pavement surface to the underlying layers) seemed to promote the heat on upper layer and avoid its storing; in turn, energy absorbed and stored within pavement (i.e. heat capacity) have been assessed considering the effects in UHI mitigation [1.123]. Different approaches examined the role of the pavement porosity since it is correlated to the degree of adsorbed solar energy [1.143]. Therefore, permeable materials with appropriate gradations and higher percentage of voids have been proposed [1.124] given their ability to insulate the ground and promote the infiltrated water to evaporate, resulting in cooler roads [1.144]. In fact, since evaporation process needs energy in changing water phase from liquid to gas, the cooling down of the surface could happen with intense repercussions on reached temperatures. Other strategies suppose also the active mechanical cooling of pavements, incorporating ad-hoc structures in the pavement, e.g. forcing water circulation [1.145] or employing thermoelectric devices to provide the cooling effect [1.146]. Also shading of pavements has been demonstrated to be effective in decreasing the surfaces heating-up (e.g. using artificial structures or vegetation) [1.147].

Based on the above considerations, the following Chapter 2 will give a focus on the radiative properties of pavement materials, describing in detail the theoretical approach needed to study the heat transfer mechanisms occurring on road pavements.

Chapter 2

Theory of Heat Transfer

The present Chapter aims at describing the theoretical approach needed to study the heat mechanisms which determine the phenomenon of Urban Heat Island. Some preliminary knowledges about the heat theory and the basic physic of such dynamics are given, deepening the topic on the basis of the aspects involved in the proximity of urban pavements. First, a general description of physical concepts about radiation is proposed. Then, radiative properties of real objects and characteristics of solar and atmospheric radiations are dealt. Finally, micro-climate interesting the urban areas, heating processes due to the road presence and specific mechanisms of heat transmission through road pavements are presented.

2.1. Generalities

2.1.1. *Physics of radiation*

Preliminary definitions of physical parameters interesting the process have to be fixed, in particular defining quantities such as the energy, the radiation, the electromagnetic wave and the thermal radiation. Some information concerning physics of colors and their perception are also given.

In physics, energy is a conservative quantity transferrable to an object in order to perform work on it, or to heat it; International System standardized unit considered for the quantification of energy is the Joule (J), which represents the energy transferred to the

subject by the work spent to move it of 1 meter against a force of intensity equal to 1 Newton.

A measure of the energy transmitted (or emitted) in the form of wave through the space or a material medium is represented by the radiation and is accounted again with the unit of Joule. Indeed, “radiation” term could be referred to the electromagnetic radiation (radio wave, microwave, infrared, visible light, ultraviolet, x-ray, gamma radiation), the particle radiation (alpha radiation, beta radiation, neutron radiation), the acoustic radiation (ultrasound, sound, seismic wave) and the gravitational radiation (gravitational wave, theoretical ripple in the curvature of space-time). Irradiation phenomenon is one of the most complex modalities of transmission of heat since it happens indistinctly on solids, liquids and gases without direct contact and occurs at the speed of light (no alterations are recorded even in the absolute vacuum). Differently from conduction or convection, irradiation between two bodies exists also crossing a separation medium cooler than the masses. Fundamentals of irradiation were demonstrated to be related to the electromagnetic waves (or electromagnetic radiations), i.e. the accelerated/electrical charges which cause the emergence of electromagnetic fields [2.1]. The wave is a vehicle of energy and travels at the speed of light c (in m/s) with a specific frequency f (in Hz) and wavelength λ (in μm) according to the formulation (Equation 2.1):

$$\lambda = \frac{c}{f} \quad (2.1)$$

where the value of c depends on the refractive index n typical of the medium (equal about to 1.0 for air and the most part of gases, to 1.5 for water and glass) according to the relation $c = c_0/n$ (c_0 is the light speed on the absolute vacuum equal to $2.998 \cdot 10^8$ m/s). In particular, frequency depends only on the radiation source (it is not affected by the crossed medium) [2.2]. More recently, electromagnetic radiation has been described as a propagation of energy packages called photon (or quanta), each of them characterized by (Equation 2.2):

$$e = h \cdot f = \frac{h \cdot c}{\lambda} \quad (2.2)$$

where e is the energy of the quantum (in J) and h is the Planck constant ($6.625 \cdot 10^{-34}$ J·s) [2.3]. Please, note that the proposed relation (Equation 2.2) defines a strict dependence of the energy on the characteristic length of the wave. Actually, the wavelength is the crucial characteristic which determines the properties of the electromagnetic radiation (existing waves range in length from $1 \cdot 10^{-10}$ to $1 \cdot 10^{10}$ μm). Based on λ , different typologies of electromagnetic radiations are distinguished according to the scheme proposed in Figure 2.1.a. Radio waves (λ from $1 \cdot 10^{10}$ to $1 \cdot 10^5$ μm , f between 300 GHz and 30 Hz) are generated by electric charges undergoing acceleration, such as time-varying electric currents.

Microwaves (λ from $1 \cdot 10^5$ to $1 \cdot 10^2 \mu\text{m}$, f between 300 GHz and 300 MHz) are reflected by metals, transmitted by glass and manifest interactions with internal energy of living molecules. Wavelengths included between $1 \cdot 10^2$ and $1 \cdot 10^{-1} \mu\text{m}$ generally identify the thermal radiations emitted because of the rotational and vibrational movements of molecules, atoms and electrons of all bodies (that, for the existence, are supposed to own temperature higher than the zero-absolute T of $0 \text{ }^\circ\text{K}$). In fact, temperature is considered an index of such internal process. Thermal radiation contains the narrow spectrum of visible light (0.40 to $0.76 \mu\text{m}$), in turn divided in well-defined color bands and generally categorized in the proximity of the following pure colors (produced by light of a single wavelength): 0.76 to $0.63 \mu\text{m}$ for red, 0.63 to $0.60 \mu\text{m}$ for orange, 0.60 to $0.54 \mu\text{m}$ for yellow, 0.54 to $0.52 \mu\text{m}$ for green, 0.52 to $0.49 \mu\text{m}$ for cyan, 0.49 to $0.44 \mu\text{m}$ for blue and 0.44 to $0.40 \mu\text{m}$ for violet (Figure 2.1.b). The upper edge of visible spectrum borders with the infrared radiation (IR) field (λ between 0.76 and $100 \mu\text{m}$), the lower one with the ultraviolet UV region (λ between 0.40 and $0.01 \mu\text{m}$). Thus, it is worth noting that the thermal radiation comprises the whole visible radiation, the entire IR region and a part of the UV band. Typically, the IR radiation is emitted by the generic body at ambient temperature; the visible radiation is emitted only when surfaces reach temperature above $800 \text{ }^\circ\text{K}$ (as example, tungsten filaments of lamps start to emit visible light only over $2000 \text{ }^\circ\text{K}$). UV radiations coming from the sun would cause severe damages to organisms without the shield effect of atmosphere (life in Earth is possible only thanks to the effect of ozone layer that filter the most part of incoming UV rays). Solar electromagnetic radiation, with common wavelengths ranging between 0.1 and $3 \mu\text{m}$, is composed for one-half by visible radiation, for the remaining part by IR and UV energies.

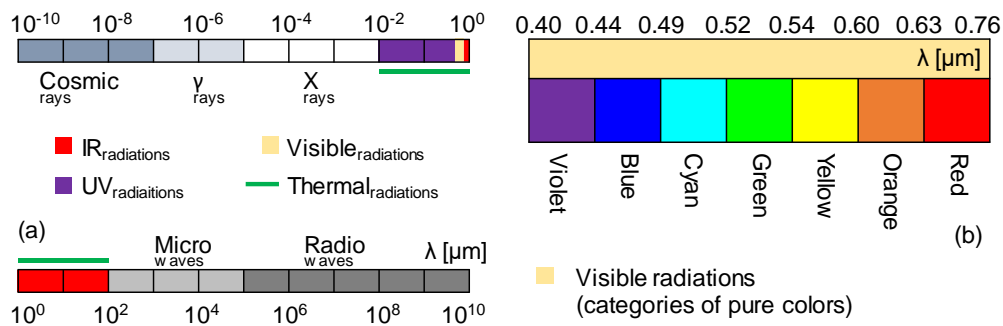


Figure 2.1. Type of electromagnetic radiations (a) and characteristics of visible spectrum (b).

Starting to consider the properties of objects subjected to electromagnetic radiations, some efforts must be spent to the understanding of matter intrinsic properties.

As anticipated, electrons, atoms and molecules of solids and fluids at temperature higher than $0 \text{ }^\circ\text{K}$ are constantly moving; for this reason, radiation emitted/absorbed by a body could be considered a volumetric phenomenon (i.e. radiation is transmitted in all the directions). However, the existence of superficial radiation could be assumed in the case of opaque (not-

transparent) solids, for which the radiation transmitted from the internal portions of the body is not allowed to gain the surface, or the incident radiation is absorbed within few microns below the external surface. Thus, it can be stated that a generic body (always hotter than 0 °K) could emit radiations in all the direction; commonly this occurs emitting a huge filed of wavelengths, depending on the body material and its surface temperature. In this sense, different radiation spectrums can be emitted by diverse objects at the same temperature; hence, an ideal body (the so-called black body) should be introduced to define a reference object to which the radiative properties of real surfaces could be compared.

The black body is a perfect emitter/absorber of radiation, i.e. an object able to emit the maximum radiation at each temperature and wavelength and to absorb the totality of incident radiation independently from the wavelength and the direction. Given the uniform radiative energy emitted in all the directions, it can be considered a “diffuse” emitter. Black body emits the radiative power (for surface unity) E_n (in W/m^2) expressed by the following Equation 2.3 [2.4]:

$$E_n = \sigma \cdot T^4 \quad (2.3)$$

where T is the absolute temperature of the surface (in °K) and σ represents the Stefan-Boltzmann constant equal to $5.67 \cdot 10^{-8} \text{ W}/(\text{m}^2 \cdot \text{K}^4)$. Considering that colors are defined by the properties of light able to leave the body surfaces (the wavelengths of the light that are reflected from them), black body should be perceived with black color. Otherwise, it must be remembered that the visible spectrum takes only a limited interval of existing wavelengths; this suggests that a strict definition of radiative characteristics cannot be based exclusively on a visible evaluation of the surfaces. Therefore, a black surface could equally represent a general body of black color (emitting limited radiations in the interval of visible light) or a black body (emitting all the radiation’s spectrum). Another example could be referred to white surfaces: the snow is perceived as white (it reflects light) but, at IR radiation results black (it absorbs the long-wave radiation). In general, colors perceived by human eye are the results of a wide merge of pure colors, so the final chromaticity of objects is function of a large wavelength combination in the range of visible spectrum; on the same way, radiative power E_n represents the sum of radiations emitted at all the wavelengths. The monochromatic emissive power of the black body $E_{n\lambda}$ expressed in $\text{W}/(\text{m}^2 \cdot \mu\text{m})$ (i.e. the radiative power for surface unit emitted at the temperature T and calculated in the proximity of a single wavelength) could be then calculated as (Equation 2.4) [2.3]:

$$E_{n\lambda} = \frac{c_1/n^2}{\lambda^5 \cdot [\exp(c_2/\lambda \cdot T) - 1]} \quad (2.4)$$

where T is expressed in $^{\circ}\text{K}$, C_1 and C_2 are constants equal to $2 \cdot \pi \cdot h \cdot c^2 = 3.742 \text{ W} \cdot \mu\text{m}^4/\text{m}^2$ and $h \cdot c/k = 1.439 \cdot 10^4 \mu\text{m} \cdot ^{\circ}\text{K}$ respectively and k is the Boltzmann constant equal to $1.3805 \cdot 10^{-23} \text{ J}/^{\circ}\text{K}$. $E_{n\lambda}$ as a function of wavelength is plotted in Figure 2.2 for some indicative temperatures. Based on the graphical relations, the typical shape of the curves indicates that:

- i) at each temperature, a $E_{n\lambda}$ peak is obtained;
- ii) emitted radiation increases with the temperature (once fixed the wavelength);
- iii) the increase of temperature corresponds to steeper and steeper trends and determines translations towards the short-wave region, thus higher temperatures involve greater radiative fractions emitted at shorter wavelengths.

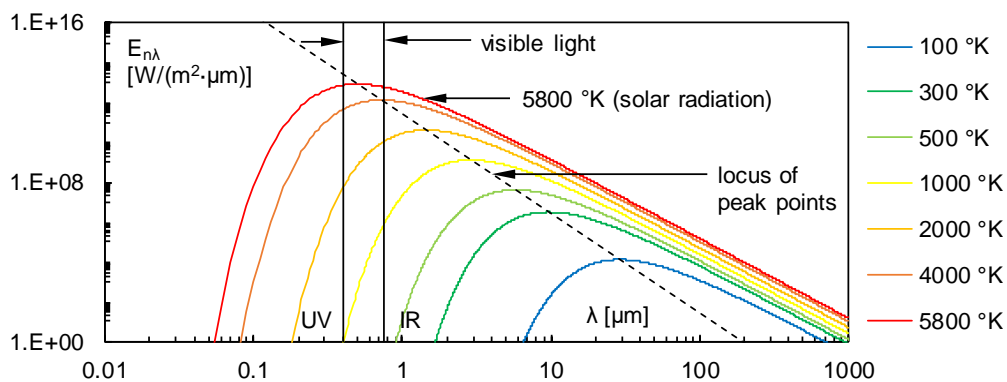


Figure 2.2. Monochromatic radiative power for selected temperatures.

It is then interesting to stress that, assuming the sun as a black body at the approximative temperature of $5800 \text{ }^{\circ}\text{K}$, peak of solar radiation is located in the region of the visible lights. At a specific temperature, the value of wavelength λ at which peak is gained can be given by the Equation 2.5 [2.5]:

$$(\lambda \cdot T)_{peak} = 2897.8 \quad (2.5)$$

In particular, peak of solar radiation is located at $0.50 \mu\text{m}$ (almost in the middle of the visible range), whereas peak of black body at ambient temperature ($\approx 298 \text{ }^{\circ}\text{K}$) occurs at $9.72 \mu\text{m}$ i.e. in the infrared region of the spectrum. This is the reason why a heating source composed by electrical resistances does not emit visible radiation suddenly after the switch on even if the IR emission start at the time zero (only when the temperature reaches about $1000 \text{ }^{\circ}\text{K}$, resistances start to assume a soft red color because the radiation begin to be located in the visible region). Thus, it is worth stressing that the color of a generic object is not linked to the emission (which occurs mainly in the IR region), unless the object temperature approaches $1000 \text{ }^{\circ}\text{K}$.

When the radiative power for unit of surface has to be referred to a range of wavelength between 0 and λ ($E_{n,0-\lambda}$), the integral of $E_{n\lambda}$ furnishes (Equation 2.6):

$$E_{n,0-\lambda} = \int_0^\lambda E_{n\lambda}(T) \cdot d\lambda \quad (2.6)$$

where $E_{n,0-\lambda}$ is expressed in W/m^2 . However, since Equation 2.6 cannot be calculated with a simple analytic approach, the radiative function of the black body f_λ (which indicates the fraction of radiation emitted at the temperature T within the wavelength from 0 to λ) can be considered introducing the Equation 2.7. Indicative values of f_λ in function of $f_\lambda \cdot T$ are presented in the following Table 2.1.

$$f_\lambda(T) = \frac{\int_0^\lambda E_{n\lambda}(T) \cdot d\lambda}{\sigma \cdot T^4} \quad (2.7)$$

Table 2.1. Function f_λ : radiative emission of black body.

$\lambda \cdot T$ [$\mu\text{m} \cdot ^\circ\text{K}$]	f_λ	$\lambda \cdot T$ [$\mu\text{m} \cdot ^\circ\text{K}$]	f_λ	$\lambda \cdot T$ [$\mu\text{m} \cdot ^\circ\text{K}$]	f_λ
200	0.000000	4200	0.51604	8500	0.874608
400	0.000000	4400	0.548796	9000	0.890029
600	0.000000	4600	0.579280	9500	0.903085
800	0.000016	4800	0.607559	10000	0.914199
1000	0.000321	5000	0.633747	10500	0.923710
1200	0.007790	5200	0.658970	11000	0.931890
1400	0.002134	5400	0.680360	11500	0.939959
1600	0.019718	5600	0.701046	12000	0.945098
1800	0.039341	5800	0.720158	13000	0.955139
2000	0.066728	6000	0.737818	14000	0.962898
2200	0.100888	6200	0.754140	15000	0.969981
2400	0.140256	6400	0.769234	16000	0.973814
2600	0.183120	6600	0.783199	18000	0.980860
2800	0.227897	6800	0.796129	20000	0.985602
3000	0.273232	7000	0.808109	25000	0.992215
3200	0.318102	7200	0.819217	30000	0.995340
3400	0.361735	7400	0.829527	40000	0.997967
3600	0.403607	7600	0.839102	50000	0.998953
3800	0.443382	7800	0.848005	75000	0.999713
4000	0.480877	8000	0.856288	100000	0.999905

Finally, radiative power for unit of surface can be associated to a defined interval of wavelengths (between λ_1 and λ_2): in this case, $f_{\lambda_1-\lambda_2}$ quantity can be used according to Equation 2.8.

$$f_{\lambda_1-\lambda_2}(T) = f_{\lambda_2}(T) - f_{\lambda_1}(T) \quad (2.8)$$

Summarizing the defined quantities for black body, Figure 2.3 schematizes as a function of wavelength: the radiative power for surface unity E_n (a), the radiative power for unit of

surface referred to the $0-\lambda$ range $E_{n,0-\lambda}$ (b) and the radiative function referred to the specific interval $\lambda_1-\lambda_2$ represented by $f_{\lambda_1-\lambda_2}$ (c).

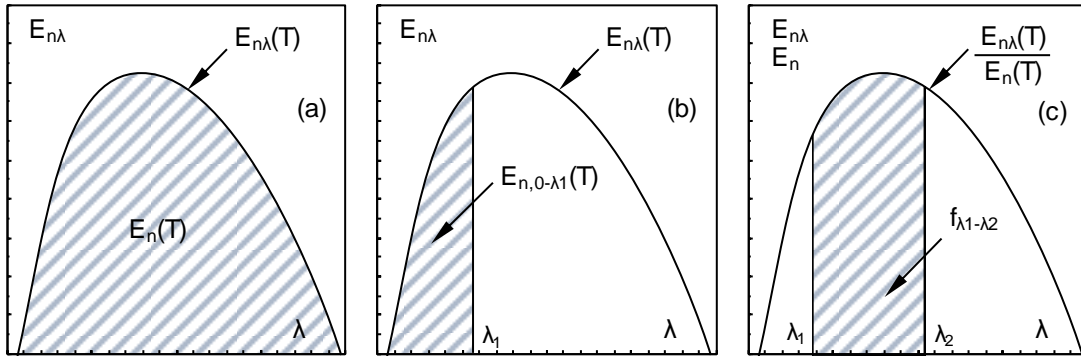


Figure 2.3. Black body emission: radiative powers for surface unity.

2.1.2. Radiative properties of real objects

The present paragraph gives a detailed description of the radiative properties of real objects in order to analyze the characteristics which determine the effective radiation absorbed and emitted by surfaces in the case of exposure to sun.

As anticipated, thermal radiation is generally considered a superficial phenomenon since the most part of real objects presents opaque surfaces.

Superficial **emissivity** ε can be defined as the ratio between the radiation emitted by the surface and the radiation emitted by the black body at the same temperature: ε value ranges from 0 to 1 and, in a certain way, indicates the tendency of the surface to approximate the ideal black body (with emissivity equal to 1). Emissivity cannot be considered an intrinsic characteristic of the material since it varies with the temperature, the wavelength and the direction of the radiation emitted by the surface. Monochromatic emissivity ε_λ can be used to indicate the emissivity at a given value of wavelength. In analogy, directional emissivity ε_θ can be employed to define the emissivity for a specific direction of emission (indicated by the angle θ formed by the emission direction and the vector perpendicular to the surface). Defining the hemispheric emissivity as the average ε in all the directions and the total emissivity as the average ε of all the wavelengths, the total hemispheric emissivity $\varepsilon(T)$ can be written as (Equation 2.9).

$$\varepsilon(T) = \frac{E(T)}{E_n(T)} = \frac{E(T)}{\sigma \cdot T^4} \quad (2.9)$$

where $E(T)$ is the total emissive power of the real surface expressed in W/m^2 . For the inverse formulation, it applies (Equation 2.10):

$$E(T) = \varepsilon(T) \cdot \sigma \cdot T^4 \quad (2.10)$$

Therefore, the emitted radiation (for the surface unit) of a real surface (at temperature T) consists in the radiation emitted by the black body multiplied by the object emissivity. Monochromatic emissivity can be calculated as (Equation 2.11):

$$\varepsilon_\lambda(T) = \frac{E_\lambda(T)}{E_{n\lambda}(T)} \quad (2.11)$$

In view of the phenomenon complexity given by the dependency of ε on several factors, some approximations are generally employed. In this perspective, some kinds of analysis suppose that real objects present grey (independent on the wavelength) and diffused (independent on the direction) surfaces. For summary, Table 2.2 schematizes all possible assumptions.

Table 2.2. Possible assumptions for theorization of surface emissivity.

Type of assumption	ε_λ	ε_θ
Real surface	\neq constant	\neq constant
Grey surface	= constant	\neq constant
Diffused surface	\neq constant	= constant
Grey and diffused surface	= constant	= constant (*)

(*) $\varepsilon = \varepsilon_\lambda = \varepsilon_\theta$

For the sake of coherence, a grey surface must emit the same radiative power of the real surface which represents; in this case, for a fixed temperature T , the areas under grey and real curves of emissions should coincide (Figure 2.4), thus the mean emissivity $\varepsilon(T)$ can be expressed by (Equation 2.12):

$$\varepsilon(T) = \frac{\int_0^\infty \varepsilon_\lambda(T) \cdot E_{n\lambda}(T) \cdot d\lambda}{\sigma \cdot T^4} \quad (2.12)$$

The integration could be simplified dividing the whole spectrum in a sufficient number of wavelength regions and hypothesizing emissivities locally constant (typical step function reported in Figure 2.4). Indeed, the mean emissivity $\varepsilon(T)$ could be developed splitting the integral in there terms (Equation 2.13) and utilizing the definition of the black body radiative functions (Equation 2.14):

$$\varepsilon(T) = \frac{\varepsilon_1 \cdot \int_0^{\lambda_1} E_{n\lambda}(T) \cdot d\lambda}{\sigma \cdot T^4} + \frac{\varepsilon_2 \cdot \int_{\lambda_1}^{\lambda_2} E_{n\lambda}(T) \cdot d\lambda}{\sigma \cdot T^4} + \frac{\varepsilon_3 \cdot \int_{\lambda_2}^\infty E_{n\lambda}(T) \cdot d\lambda}{\sigma \cdot T^4} \quad (2.13)$$

$$\varepsilon(T) = \varepsilon_1 \cdot f_{0-\lambda_1}(T) + \varepsilon_2 \cdot f_{\lambda_1-\lambda_2}(T) + \varepsilon_3 \cdot f_{\lambda_2-\infty}(T) \quad (2.14)$$

For instance, Figure 2.5 depicts some examples of total and monochromatic (normal) emissivities as functions of the wavelength (a) and the temperature (b).

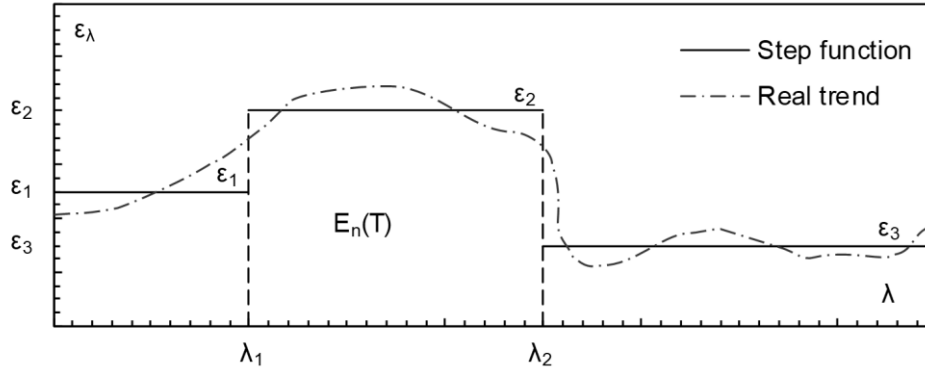


Figure 2.4. Monochromatic emissivity vs. wavelength: approximation with step function.

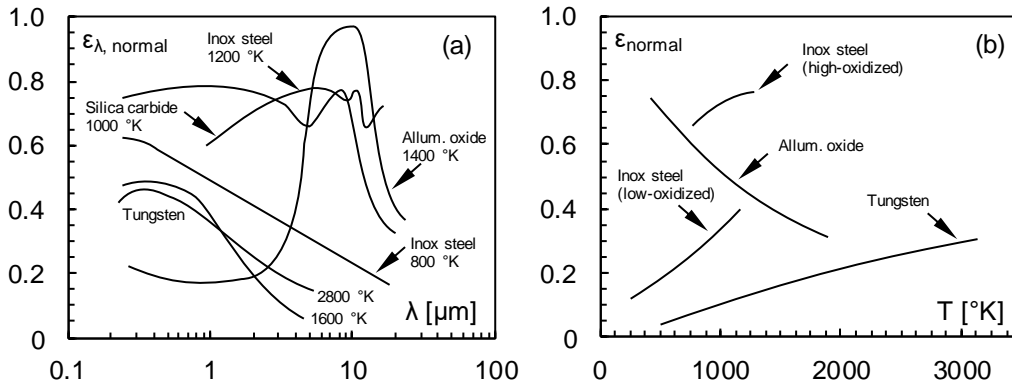


Figure 2.5. Variability of total and monochromatic emissivities vs. wavelength (a) and temperature (b).

In general, once the incident radiation G hits the object surface, energy is split in three main portions: the absorbed fraction (G_{abs}), the reflected part (G_{ref}) and the transmitted quantity (G_{tr}). In this context, three radiative properties of the surface can be defined.

The **absorptivity** α (or coefficient of absorption) is a dimensionless index of the absorbed portion and is calculated according to the Equation 2.15: it varies from 0 to 1 (indicating with 1 the total absorption of the incident radiation).

$$\alpha = \frac{G_{abs}}{G}, \quad [0 \leq \alpha \leq 1] \quad (2.15)$$

The **albedo** ρ (or coefficient of reflection) gives indications about the reflected part of radiation and, in analogy with α , ranges from 0 to 1 (1 indicates the total reflection of the incident radiation). It is calculated based on Equation 2.16.

$$\rho = \frac{G_{ref}}{G}, \quad [0 \leq \rho \leq 1] \quad (2.16)$$

The **coefficient of transmission** τ estimates the ability of transmitting the incident radiation (Equation 2.17). Once again, a dimensionless parameter (from 0 to 1) is employed.

$$\tau = \frac{G_{tr}}{G}, \quad [0 \leq \tau \leq 1] \quad (2.17)$$

Based on the first principle of the thermodynamic, the conservation of energy is realized when the total incident radiation G is equal to the sum of G_{abs} , G_{ref} and G_{tr} contributions. Then, dividing the relation for the G term, the formula becomes (Equation 2.18):

$$\frac{G_{abs}}{G} + \frac{G_{ref}}{G} + \frac{G_{tr}}{G} = \frac{G}{G} \quad \rightarrow \quad \alpha + \rho + \tau = 1 \quad (2.18)$$

Since the most part of real objects presents opaque surfaces (energy transmission is obstructed), τ term can be neglected and the Equation 2.18 can be transformed in the well-known relation $\alpha + \rho = 1$, which allows the calculation of the radiative properties of the surface using only a single parameter. In analogy with previous treatment, monochromatic contribution referred to specific direction and λ could be calculated when incident radiation is considered not-hemispheric and not-comprehensive of all wavelengths (Equation 2.19):

$$\alpha_{\lambda} = \frac{G_{abs, \lambda}}{G_{\lambda}}, \quad \rho_{\lambda} = \frac{G_{ref, \lambda}}{G_{\lambda}}, \quad \tau_{\lambda} = \frac{G_{tr, \lambda}}{G_{\lambda}} \quad (2.19)$$

Hence, the mean coefficients of absorption, reflectance and transmission of a real surface can be defined also as functions of the monochromatic coefficients (Equation 2.20):

$$\alpha = \frac{\int_0^{\infty} \alpha_{\lambda} \cdot G_{\lambda} \cdot d\lambda}{\int_0^{\infty} G_{\lambda} \cdot d\lambda}, \quad \rho = \frac{\int_0^{\infty} \rho_{\lambda} \cdot G_{\lambda} \cdot d\lambda}{\int_0^{\infty} G_{\lambda} \cdot d\lambda}, \quad \tau = \frac{\int_0^{\infty} \tau_{\lambda} \cdot G_{\lambda} \cdot d\lambda}{\int_0^{\infty} G_{\lambda} \cdot d\lambda} \quad (2.20)$$

In general, reflection (Figure 2.6.a) is considered specular in the case of smooth surfaces (reflection angle equal to incident one) or diffused in the case of rough surfaces (uniform reflection in all the directions). Differently from the other ones, absorptivity should be considered bi-directional (it should depend on the directions of incident and reflected radiations), otherwise, the assumption is generally omitted for the simplicity of calculation. Moreover, it must be specified that α is the unique radiative property actually not affected by the surface temperature, but only dependent on the T of the incident radiation source (T_{src}). Figure 2.6.b depicts the α coefficients of some materials as a function of the temperature of the radiation source; in this case it is interesting to note that a significant decrease of α with the increase of such temperature is typical of clear materials.

Additionally, these trends could be taken into account also for the albedo coefficient if considering the above-mentioned $\alpha + \rho = 1$ relation.

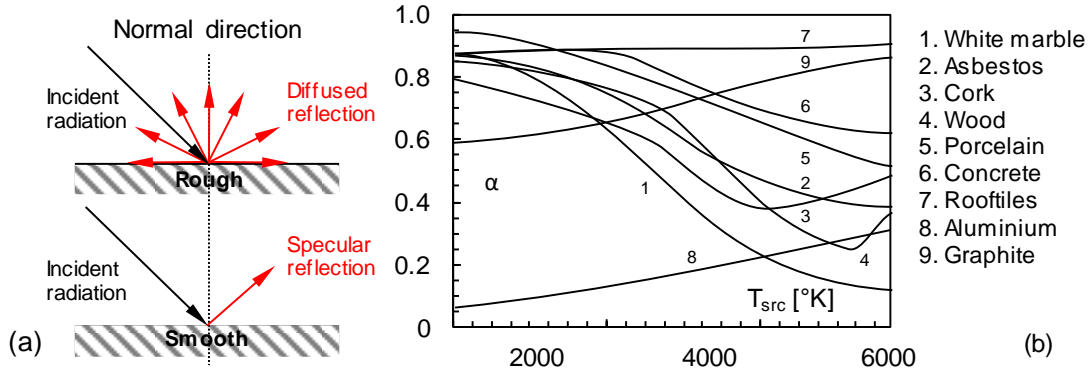


Figure 2.6. Reflection geometry (a) and α coefficient vs. temperature of radiation source (b).

Examining a surface with finite dimensions (with area A , temperature T and absorptivity α) contained in a huge isothermal cavity (with dimensions sufficient to avoid the influence due to the radiative properties of the surface), the above-explained theoretic approach could schematize the surface as a real object and the cavity as an hypothetical black body. In this case, the radiation incident on the surface coincides with the radiation emitted by the black body (Equation 2.21).

$$G = E_n(T) = \sigma \cdot T^4 \quad (2.21)$$

In turn, the radiations absorbed (G_{abs}) and emitted (G_{em}) by the surface are given by the Equations 2.22 and 2.23, respectively.

$$G_{abs} = \alpha \cdot G = \alpha \cdot \sigma \cdot T^4 \quad (2.22)$$

$$G_{em} = \varepsilon \cdot G = \varepsilon \cdot \sigma \cdot T^4 \quad (2.23)$$

In view of the thermal equilibrium, the net radiative power (i.e. the difference between absorbed and emitted radiation) must be null (Equation 2.24) [2.6].

$$A \cdot \varepsilon \cdot \sigma \cdot T^4 = A \cdot \alpha \cdot \sigma \cdot T^4 \quad \rightarrow \quad \varepsilon(T) = \alpha(T) \quad (2.24)$$

Therefore, the Kirchhoff formulation (Equation 2.24) states that the total hemispheric emissivity of a real surface at temperature T is equal to the total absorption coefficient for a radiation originated by a black body at the same temperature T . Once again, considerations could be drawn also in monochromatic terms (Equation 2.25):

$$\varepsilon_\lambda(T) = \alpha_\lambda(T) \quad (2.25)$$

As a consequence, relations $\varepsilon = \alpha$ and $\rho = 1 - \alpha$ permit in this case the determination of the radiative properties α , ρ , and τ of an opaque surface only dealing with one of such coefficients. Indeed, the supposition should be allowed only without significant temperature differences (lower than 100 °K) between the two entities (the surface and the black body).

2.1.3. Solar and atmospheric radiations

The paragraph presents the characteristics of the solar and the atmospheric radiations that cause the road pavement heating, developing the mechanisms of urban heat islands.

The sun is the primary source of energy. The so-called solar energy takes origin from the sun, travels on space and reaches terrestrial soil in form of electromagnetic wave after certain interactions with the atmosphere. Radiation emitted by atmospheric particles is named atmospheric radiation. Sun is a quasi-spherical star with a diameter of $1.39 \cdot 10^9$ m, a mass of about $2 \cdot 10^{30}$ kg and an average distance from the Earth equal to $1.5 \cdot 10^{11}$ m. Even if it emits continuous radiations with a power E_{sun} of about $3.8 \cdot 10^{26}$ W, only $1.7 \cdot 10^{17}$ W are enough to warm the Earth and ensure the life. Solar temperatures reach $4 \cdot 10^7$ °K in the core and $6 \cdot 10^3$ °K on the surface because of endless nuclear fusions (hydrogen atoms are transformed in helium). The effective energy which gains the Earth has been quantified in the constant value of 1353 W/m^2 (G_s) and is intended as the solar power incident on a normal surface (with respect to the radiation direction), located in the external part of the atmosphere when the sun is at the average distance from the Earth (Figure 2.7.a). The elliptical Earth's orbit affects G_s , determining a variance between 1310 W/m^2 and 1399 W/m^2 (commonly, the average value of 1353 W/m^2 is used). The experimental measurement of G_s has been used to estimate the effective temperature of the sun surface (T_{sun}). Considering L as the average distance between sun and Earth and r as the sun radius, Equation 2.26 can be written:

$$(4 \cdot \pi \cdot L^2) \cdot G_s = (4 \cdot \pi \cdot r^2) \cdot \sigma \cdot T_{sun}^4 \quad (2.26)$$

where, the left term represents the solar energy passing through a spherical surface with radius equal to L and right term corresponds to the energy leaving the solar external surface (Figure 2.7.b). Imposing the energy conservation principle, T_{sun} is estimated equal about to 5762 °K. On the basis of the emitted spectrum (Figure 2.8.a), measured immediately outside the atmosphere, sun can be considered a block body at about 5762 °K; energy which effectively gains the terrestrial surface is sensibly dispersed because of the atmospheric effects (phenomenon is mostly concentrated within a band of about 30 km from the Earth's crust).

The shield effect given by the atmosphere is mainly caused by the radiation absorption provided by gasses. Oxygen (O_2) absorption occurs around the wavelength of $0.76 \mu\text{m}$; ozone (O_3) absorbs the most part of the ultra-violet radiation (between 0.3 and $0.4 \mu\text{m}$) and a portion of the visible light; vapor (H_2O) and carbon dioxide (CO_2) retain the radiation in the infrared field (typically in the range $5\text{--}8 \mu\text{m}$ and above $13 \mu\text{m}$). Thus, the radiation which reaches the surface is mostly included in the range $0.3\text{--}2.5 \mu\text{m}$. Power is significantly reduced and depends also on the local atmospheric conditions. Further dispersion of radiation is given by the air molecules and the air-suspended dust particles (also smog gives contribution). In general, dispersion mechanisms are governed by the ratio between the particle dimension and the radiation wavelength (in fact, O_2 and O_3 disperse radiations with rather small λ with respect to their dimensions, corresponding to blue and violet colors). For this reason, perceived light on the Earth's surface (Figure 2.8.b) is characterized by the highest wavelengths of the visible spectrum (red, orange and yellow colors).

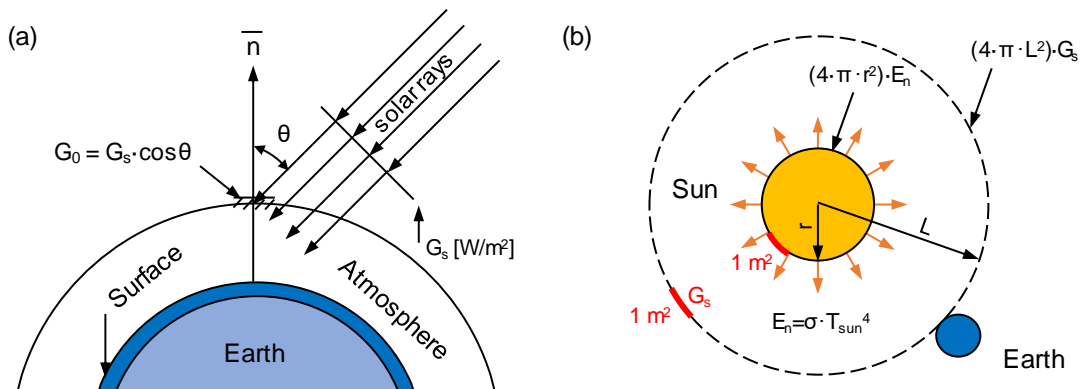


Figure 2.7. Characteristics of solar radiation.

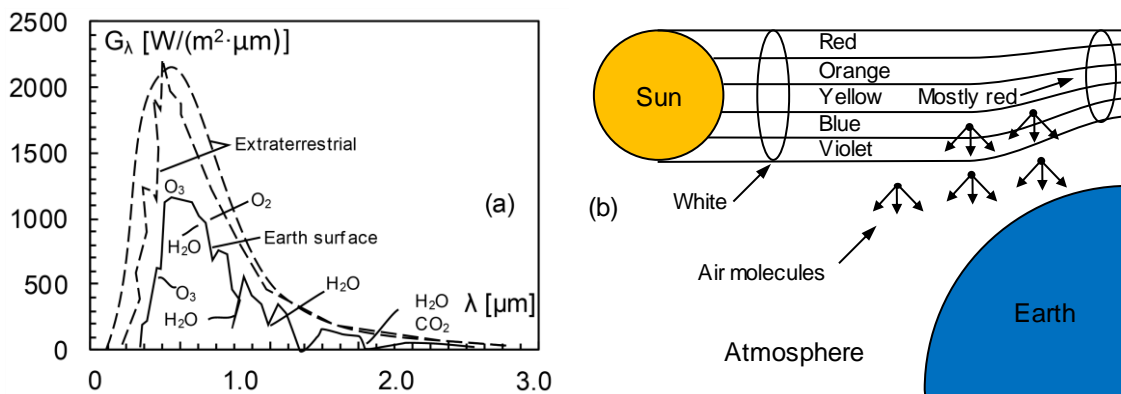


Figure 2.8. Spectrum of solar radiation outside and inside the atmosphere (a) and colors of solar light perceived on the Earth's surface.



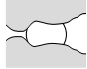





The solar energy incident on terrestrial surface is composed by a direct (D) and a diffused (d) part. The radiation which gains the surface without being absorbed or dispersed by atmosphere is the direct solar radiation G_D ; the dispersed radiation reaches the surface uniformly from all the direction and is named diffused solar radiation (G_d). Thus, the total

incident solar radiation G_{sun} (on time and temperature units) of a horizontal surface is (Equation 2.27):

$$G_{sun} = G_D + G_d = G_{D\perp} \cdot \cos(\theta) + G_d \quad (2.27)$$

where G quantities are expressed in W/m^2 , $G_{D\perp}$ indicates the perpendicular direct radiation and θ is the angle of incidence (formed by solar radiation with the direction normal to the surface). Table 2.3 give indication about $G_{D\perp}$ and G_d as a function of whether conditions (radiation assumed perpendicular to the surface).

Table 2.3. Direct vs. diffused solar radiation in function of weather conditions.

Radiation	Clear sky	Fog	Half cloudy	Yellow sun	White sun	Just visible sun	Intense fog	Cloudy
								
$G_{sun} [\text{W/m}^2]$	1000	600	500	400	300	200	100	50
$G_{D\perp}$	90%	50%	70%	50%	40%	0%	0%	0%
G_d	10%	50%	30%	50%	60%	100%	100%	100%

According to literature, a specific relation for the quantification of $G_{D\perp}$ can be also proposed (Equation 2.28) [2.7]:

$$G_{D\perp} = G_s \cdot \tau_a \cdot m \quad (2.28)$$

where G_s is the above-defined solar constant (in W/m^2), τ_a indicates the transmission coefficient for unit air mass and m is the relative mass of air, defined as the ratio of the actual path length to the shortest possible path. The transmission coefficient τ_a varies with the seasonality (higher in winter) because of the different water vapor content in the air and with the conditions of the sky (ranging from 0.81 on a clear day to 0.62 on a cloudy one). The relative mass of air (m) is generally approximated to the quantity $1/[\cos(z)]$, with z indicating the angle between the zenith and direction of the radiations. z depends on the local latitude Φ , the time of the day, and the solar declination according to the following Equation 2.29.

$$\cos(z) = \sin(\Phi) \cdot \sin(\delta_{sun}) + \cos(\delta_{sun}) \cdot \cos(hr) \cdot \cos(\Phi) \quad (2.29)$$

where hr stands for the hour angle indicative of the time (i.e. the angle needed to rotate the Earth obtaining the local meridian directly under the sun) and δ_{sun} is the solar declination. In the case of a not-horizontal surfaces, θ angle must be corrected (Equation 2.30) considering the tilting angle with respect to the horizontal (typical example of tilted roofs):

$$\cos(\Phi) = \cos|z - \Psi| - \sin(z) \cdot \sin(\Psi) + \sin(z) \cdot \Psi \cdot \sin|AZ - \beta| \quad (2.30)$$

where Ψ is the tilt angle, AZ is the azimuth of the sun and β is the angle formed by the South meridian and the normal to the surface measured westward along the horizon. For the AZ calculation, Equation 2.31 could be used.

$$AZ = \arcsin[\cos(\delta_{sun}) \cdot \sin(hr) / \cos(\gamma)] \quad (2.31)$$

Where γ is the sun elevation. The azimuth sign is established basing on the convention explained within Figure 2.9.

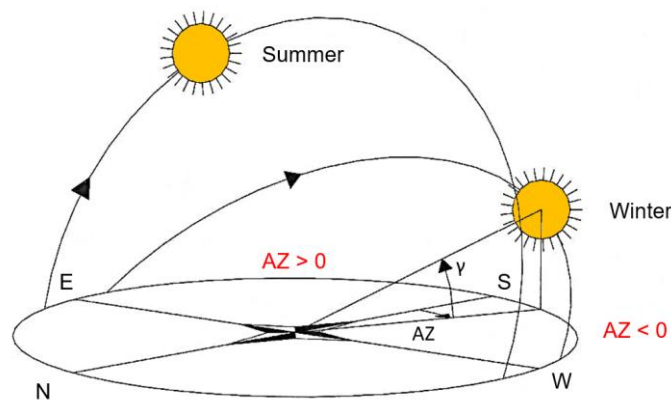


Figure 2.9. Convention used to indicate the azimuth sign.

The formulations used to calculate the solar declination δ_{sun} and the hour angle hr are those presented in Equation 2.32 and Equation 2.33, respectively.

$$\delta_{sun} = (23.45)^\circ \cdot \text{sen}[(360^\circ/365) \cdot (n_{day} - 81)] \quad (2.32)$$

where n_{day} is the day number (starting from the 1st of January, considered equal to 1).

$$hr = (12 - SH) \cdot 15 \quad (2.33)$$

where SH is the solar hour. Figure 2.10 summarizes the solar and surface angles for a tilted surface, whereas Figure 2.11 reports graphic relationships from which the values of the required angles can be obtained for the northern hemisphere [2.8].

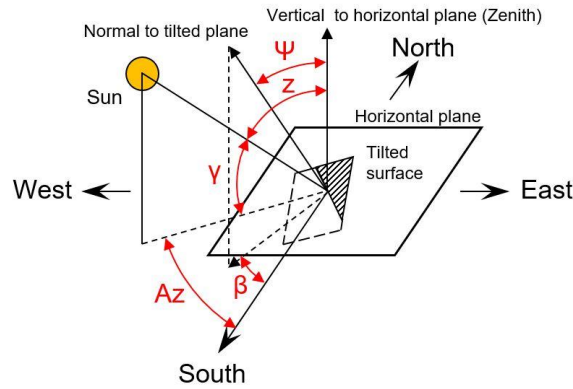


Figure 2.10. Solar and surface angles for a tilted surface.

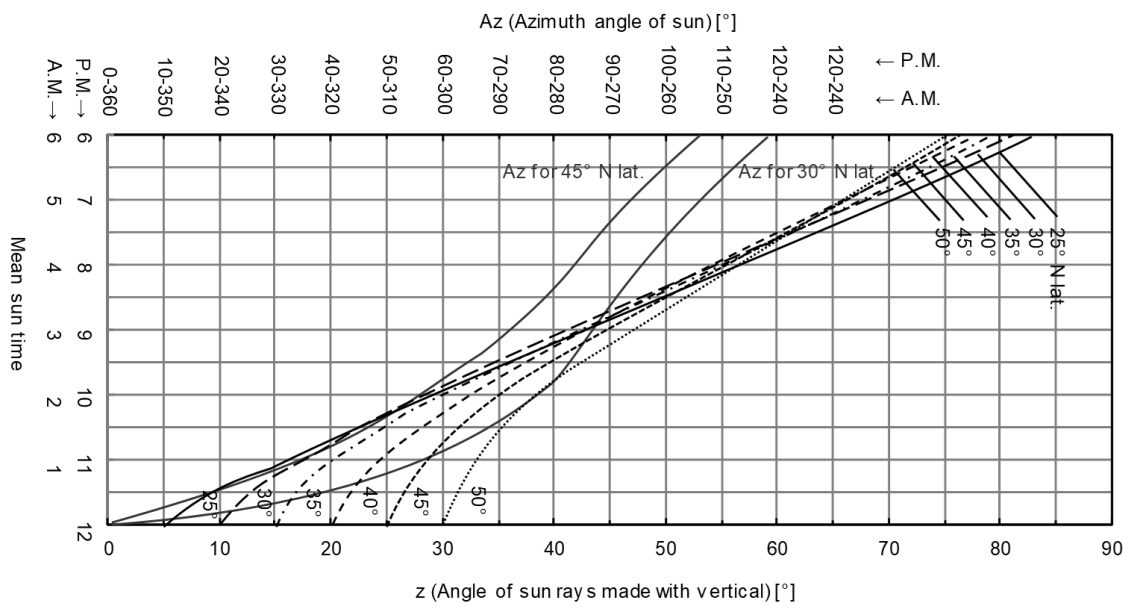


Figure 2.11. Graphic relationships for angle's calculation (northern hemisphere).

Knowing the above-defined variables, it is possible to obtain the solar diagram for a singular location (also used to estimate the shadings); as an example, Figure 2.12 presents the solar diagram for the city of Padova [2.9] (located in the northern part of Italy), i.e. the location which guested the experimentation presented in such dissertation.

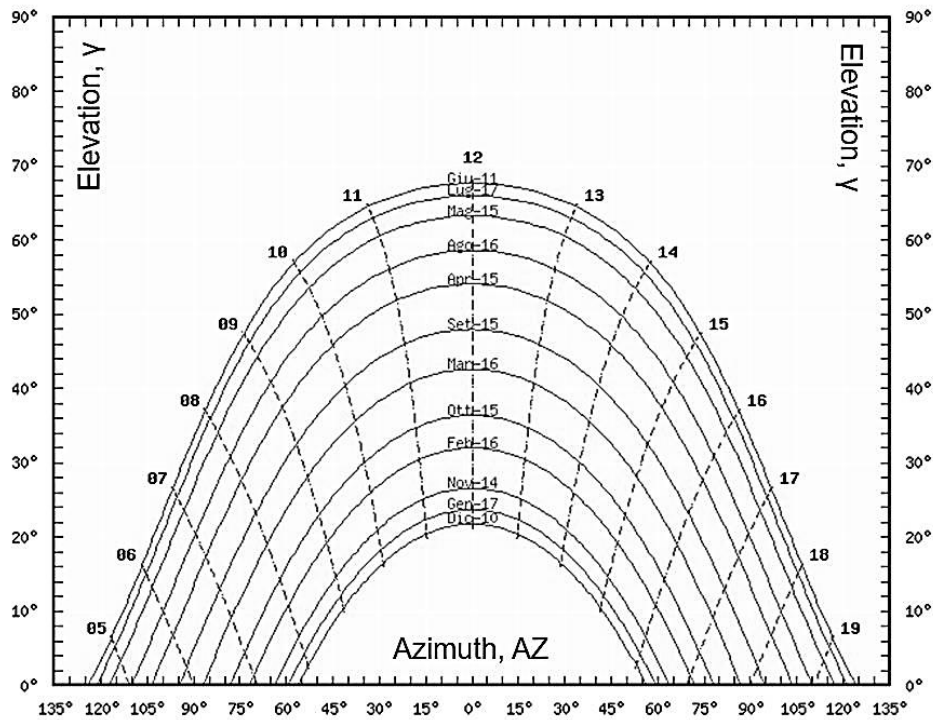


Figure 2.12. Solar diagram for the city of Padova (Italy).

Despite the above-described characteristics of the atmospheric absorption (scattering effects due to air molecules), radiative balance generally considers the atmosphere as an ideal black body, whose radiation emitted towards the surface (G_{sky} , in W/m^2) can be accounted as (Equation 2.34):

$$G_{sky} = \sigma \cdot T_{sky}^4 \quad (2.34)$$

using the temperature of the sky (T_{sky}), which depends on the atmospheric conditions (commonly from 230 °K to 285 °K) and is similar to the ambient temperature T_{amb} . In turn, a specific empirical approach [2.10] proposes the use of the following experimental formula to calculate the value of G_{sky} (Equation 2.35):

$$G_{sky} = \{0.77 - 0.28 \cdot 10^{-(0.074 \cdot \nu)}\} \cdot \sigma \cdot T_{amb}^4 \quad (2.35)$$

where ν is the vapor pressure of the air (in mmHg) given as a function of T_{amb} . Basing on literature [2.11], Figure 2.13 depicts the trend of ν in function of T_{amb} .

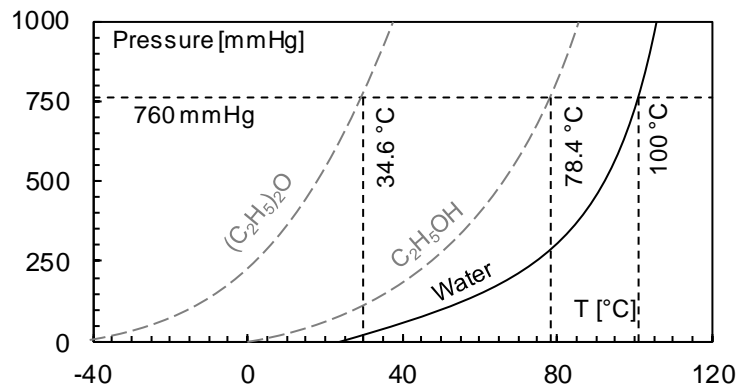


Figure 2.13. Vapor pressure curve vs. atmospheric temperature.

2.2. Road pavement concerns

2.2.1 Micro-climate of urban areas

Micro-climate of urban areas can be defined as a set of local atmospheric conditions characterized by significant variability within space and time (inhomogeneous conditions perceived by humans at distance of about 150 m) [2.12]. The environmental variability is function of several parameters (air temperature, solar radiation, relative humidity and wind speed) and is in turn deeply affected by the urban area conformation and asset: for instance, one need only think that air temperature can range from about 30 °C to 40–45 °C just moving of few meters, passing from a sun-exposed to a shadowed zone (typical temperature ranges after midday of a sunny day of summer season). The opaque surfaces, wide-diffused in the urban context, reflect and absorb solar radiation mainly depending on their albedo and their surface texture. However, the radiative response of an urban site is not linked only to the solar radiation because of the thermal radiations re-emitted by objects and their combination with radiations of surrounding elements (atmospheric, astral and terrestrial radiations). Re-emitted radiations generally present wavelengths between 0 and 10 μm , included in IR region of spectrum closer and farther from the visible light. The re-emitted radiation conditions the temperature of object surfaces according to the albedo value; thus, during a summer day with a clear sky, surfaces with different albedo values could reach significantly different temperatures. Otherwise, given the complexity of the urban context, such statement must be honed combining all the effects interesting the heat transfer.

In this perspective, **wind** is one of the most important components that determine the local micro-climate because it is able to reduce the temperature variability and it exercises a strong dissipative effect of the heat collected by humans and buildings. Wind is generated by the pressure differences in the atmosphere that are responsible of the generation of air mass movements. Turbulences (function of the wind speed and the object's rugosity) are able to modify the cooling power of the wind (the more the turbulence, the more the ability

of the wind to excise heat). Wind is an extremely variable phenomenon in terms of intensity and direction (based on seasonality, but also of daily period). In general, intensity is higher in the afternoon and weaker in the morning. Cooling effect perceived by human is governed by the heat exchange and the evaporation between the air molecules and the skin: in this sense, wind is a crucial parameter in determining the human comfort. The undisturbed flux of wind can be modified by each element included in the urban environment (buildings, infrastructures, vegetation, etc.). Overall, an accurate evaluation of wind effects is difficult and requests specific fluid-dynamics simulations: otherwise, some constructive indications have been ascertained. Effects of wind are commonly managed selecting object dimensions, collocations, orientations, proximity and porosity: as example, a denser windbreak owns a greater effect on wind speed but a smaller area of influence. Also local topography could have influence. Trees are the most effective elements in modifying the wind direction and velocity. As obvious, deciduous plants are useful only during summer period, evergreen plants act during all the year. Different height of trees and shrubs must be managed to influence the wind in different height bands; for examples, shrubs are more effective than trees if employed to manage wind speed in an urban area which include seats (e.g. areas dedicated to transport waiting). Obstruction and filtration of wind are generally needed in winter, whereas deviation and canalization (for the wind speed increase) are preferred during summer since the objective is to promote the air flows and provide the cooling effect on the populated areas (Venturi effect). Figure 2.14 concerns the wind canalization (a) and an application of the Venturi effect (b) realized with a specific building shape (Antel Building, Montevideo, Uruguay). Buildings affect wind speed in function of the wind direction and the road alignment. In the case of the tradition urban texture composed by orthogonal meshes, wind could blow parallelly to one of the main axes: the decrease of wind velocity should be negligible in the concordant direction (only friction with building surfaces) and significant in the perpendicular one (barrier effect against buildings). When wind blows with a diagonal direction with respect to the orthogonal mesh, serious influence is gained by building height. Medium-height constructions (height/width equal about to 2) determine a windward area with higher wind speed than that of a leeward one [2.13]. Figure 2.15 exemplifies possible conformations of buildings and the corresponding wind behavior.

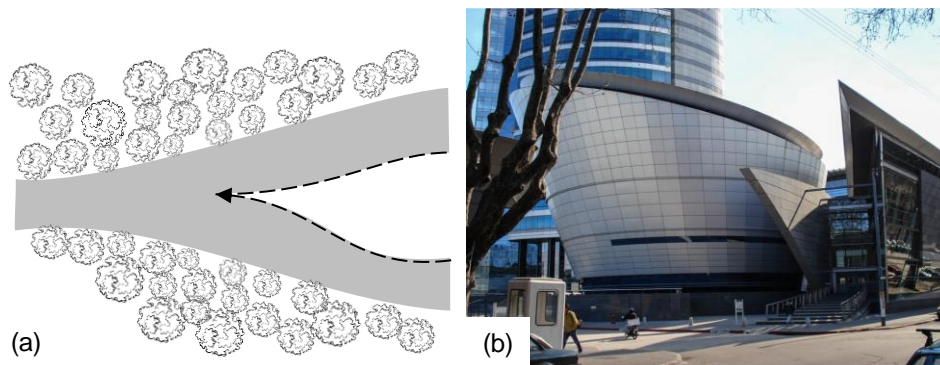


Figure 2.14. Wind canalization (Venturi effect): conceptual scheme (a) and real application (b).

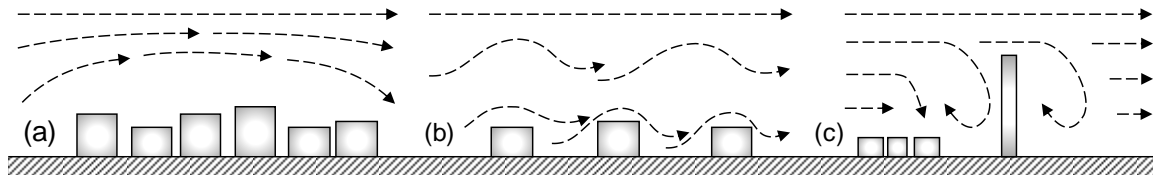


Figure 2.15. Wind behavior: overpassing of short buildings (a), trapping on ground areas (b) and reinforcing due to tall constructions (c).

The **air temperature** is a function of the solar radiation; locally, it is influenced by the heat derived by the movements of the big oceanic currents and the closeness of water masses that mitigate the daily and annual fluctuations because of the high thermal inertia. The daily trend of air temperature is strictly dependent on the state of the sky: clouds intercept the infrared radiation emitted from the terrestrial surface and govern the general radiative balance between soil and atmosphere: in this perspective, it is worth noting that the thermal excursion (day vs. night) is generally greater in presence of clear-sky daytime. The control of the air temperature involves certain difficulties since, in general, big air masses must be moved in order to obtain appreciable results. A part of literature indicates some strategies able to cool the air temperature, mainly consisting in the creation of natural barriers to protect the urban environment and prevent the global blending of air (confinement of air masses in the proximity of the city allows a better control). This is generally realized employing elements such as fences, water sheets, trees, or creating discontinuity through height gradients, but always preserving the concept of open urban space. As known, the intense presence of vegetation promotes the cooling sensation because of the decrease of the air temperature due to evaporation (even of 2–3 °C) and provides a subsequent abatement of the soil temperature (shadow given by trees contributes to enhance the mechanism) [2.13].

Really, the mitigation of the air temperature could be effective (when relative humidity remains constant) or connected to evaporation phenomena. The atmospheric **humidity** consists in the water vapor contained in the air and is generated for the major part by the oceanic evaporation. Even if it represents a tiny part of the entire water in Earth (about the 0.001%), it is crucial for the global water cycle occurring between oceans and dry land and the vegetation life. Starting from values of pressure, relative humidity UR (in percentage) is the parameter commonly utilized (Equation 2.36):

$$UR = \frac{p}{p_s} \cdot 100 \quad (2.36)$$

where p_s is the saturation pressure of vapor at temperature T at which pressure p is recorded. It expresses the ratio between the vapor quantity in the air and the vapor quantity needed to the condensation (at the same temperature). Vapor pressure commonly remains constant

within the time of the day, whereas UR varies significantly since is linked to the dry bulb temperature. Higher UR is typical of dawn, when the air temperature reaches the minimum values, and vice-versa for sunset. Daily fluctuation of relative humidity is more pronounced during the summer. During long period of consecutive good-weather days partial pressure of vapor remains more or less constant. UR is used also because it is connected to the evaporation speed: its increase corresponds to a decrement of such velocity (net evaporation equal to 0 in presence of UR at 100% because of the dynamic equilibrium between evaporation and condensation phenomena).

After the definition of some indicative parameters involved in the constitution of urban micro-climate, solar radiation must be analyzed also in view of the local characteristics of the city. One of the most effective strategies to achieve the thermal comfort concerns the control of such radiation (e.g. to shields the direct solar exposure and protect the most sensible environments). Contextualizing the effects of solar and atmospheric radiations, Figure 2.16 depicts a useful scheme referred to the urban ambient.

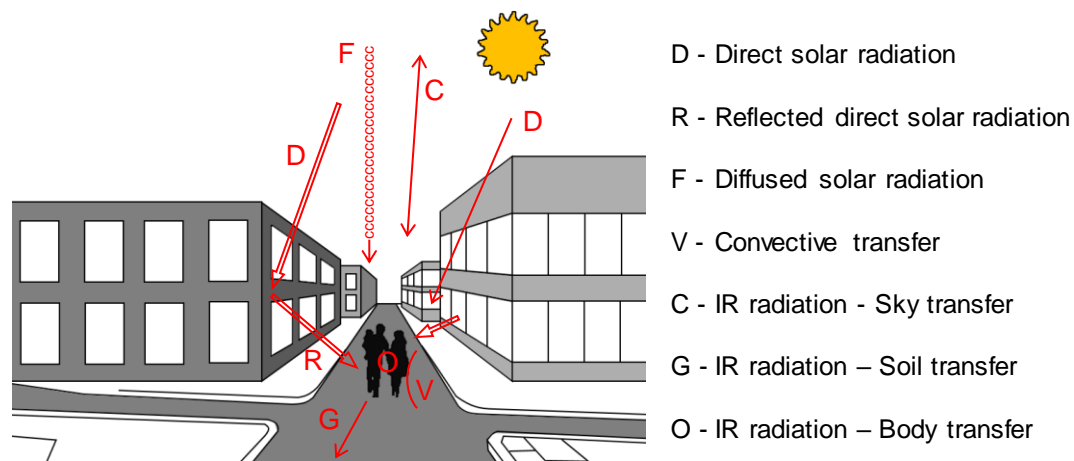


Figure 2.16. Radiation variety among the urban context.

A successful screening from solar effects must consider the variability of sun position during the day. The interception of direct radiation often is not enough to prevent discomfort, thus also reflected radiation from pavements has to be managed; in this regard, Figure 2.17 illustrates possible solutions such as a plant barrier able to avoid the reflective effect of pavement (a), a pavement surface with a low albedo/reflective coefficient (b) and the insertion of a vertical element (as example shrubs) in the lower zone of incidence (c). ambient. Indeed, the interception of the reflected radiation (linked to the SVF) can be considered a secondary problem with respect to the direct exposure since it causes a marginal discomfort rate.

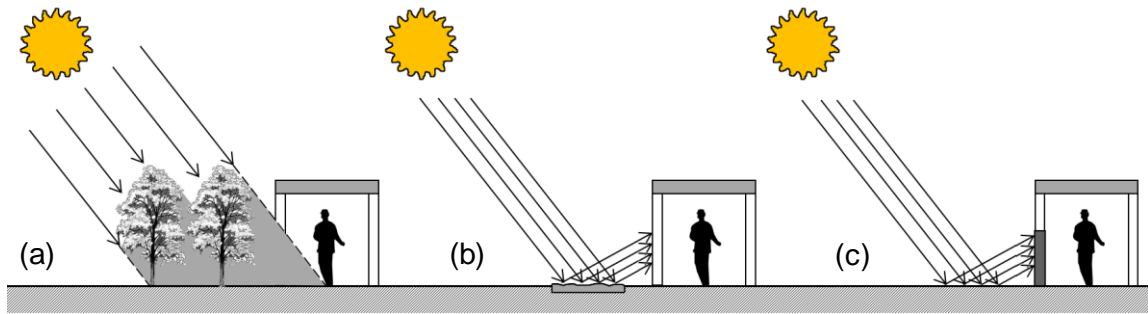


Figure 2.17. Solutions to intercept the reflected radiation.

In general, the control of the city temperatures cannot neglect the temperature reduction of all the urban surfaces. Then, materials are crucial as long as the urban morphology, above all in presence of urban canyons. Thermal radiation interesting Sun-exposed materials is partly accumulated and partly re-emitted (particularly during the night) in function of the radiative characteristics of objects. Unlucky, the so-called “cool materials” (materials with radiative properties able to contain the urban temperature increases) are more expensive and furnish high-aesthetics impacts, thus conventional ones are generally preferred. In the case of urban space, the above-analyzed radiative properties must be extended to greater area of interest. For instance, this is the case of the global albedo ρ_{urb} , defined as the reflection coefficient owned by a specific urban area. ρ_{urb} is obviously influenced by ρ values of single surfaces: generally, it assumes low values mainly because of the high absorption of solar radiation given by the darker buildings. ρ_{urb} is important also since significant spin-offs on energetic performance of buildings have been reported in literature [2.14]. In analogy, different emissivities of various urban surfaces concur to the micro-climate definition. In this standpoint, Figure 2.18 reports some of the radiative properties of construction materials commonly found within the urban environment.

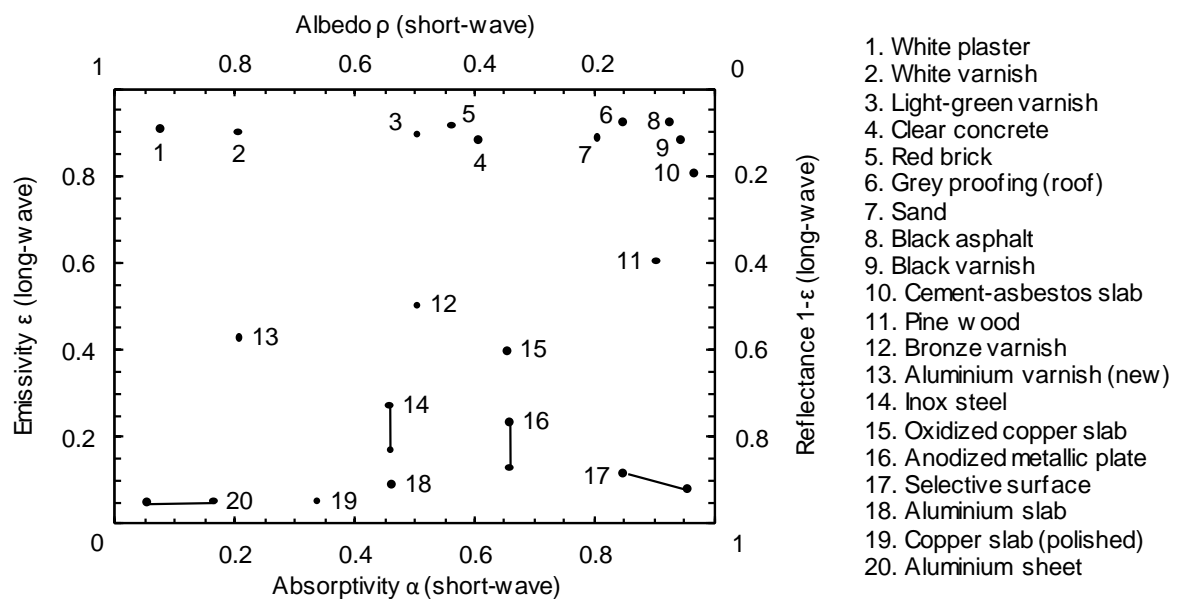


Figure 2.18. Radiative properties of common construction materials.

Other fundamental characteristics that affect the response of materials to radiations (together with α , ρ and ε) concern the aptitude to energy storing/conduction (in form of thermal radiation). Therefore, **thermal conductivity** k (in $\text{W}/\text{m}\cdot\text{K}^\circ$) is employed as an index of the aptitude in conducting heat and is considered a peculiar property of material. In analogy, the **thermal capacity** c_t of materials expresses the ability to store thermal energy and is calculated (in $\text{J}/\text{m}^3\cdot\text{K}^\circ$) according to the Equation 2.37:

$$c_t = \rho_m \cdot c_p \quad (2.37)$$

where ρ_m represents the density (in kg/m^3) and c_p indicates the specific heat (in $\text{J}/\text{kg}\cdot\text{K}^\circ$) of material. Once fixed the specific heat, the higher the material density and the higher the heat quantity needed to increase of 1° the temperature of a unitary volume. Thus, the specific heat is related to the material aptitude in storing thermal energy with respect to the unitary mass. Then, the **thermal diffusivity** λ_m can be expressed by the ratio (Equation 2.38):

$$\lambda_m = \frac{k}{\rho_m \cdot c_p} \quad (2.38)$$

where, k , ρ_m and c_p are the above-defined quantities. λ_m represents the relation between the heat transferred for conduction and the stored heat (with reference to the unitary volume). A generic material with a high thermal conductivity (or a low thermal capacity) will exhibit high values of thermal diffusivity, indicating a quick heat propagation within the material. In general, the distribution of temperatures (T) inner a generic material (below the surface) can be defined in function of the time t as (Equation 2.39):

$$\frac{\partial^2 T}{\partial z^2} = \frac{\rho_m \cdot c_p}{k} \cdot \frac{\partial T}{\partial t} \quad (2.39)$$

where z is the considered depth. As summary, Table 2.4 reports typical values of density (ρ_m), specific heat (c_p), thermal capacity (c_t), conductivity (k) and diffusivity (λ_m) of main construction materials commonly employed within urban areas.

Despite the importance of the radiative properties of materials, it must be stressed that, in general, the temperatures of urban surfaces (included road pavements) are conditioned by the total radiative balance that accounts all the typologies of thermodynamic transfer (conduction, convection and radiation).

Table 2.4. Thermal parameters of main construction materials.

Element	ρ_m [Kg/m ³]	c_p [J/Kg·°K]	c_t [J/m ³ ·°K]	k [W/m·°K]	λ_m [m ² /s]
Aluminum	2750	880	2420000	290	0.00012
Asphalt	2245	920	2065400	0.75	$3.63 \cdot 10^{-7}$
Brick	890	840	747600	0.72	$9.63 \cdot 10^{-7}$
Concrete	2240	880	1971200	0.69	$3.5 \cdot 10^{-7}$
Copper	8930	385	3438050	390	0.000113
Glass	2500	770	1925000	1	$5.19 \cdot 10^{-7}$
Gold	320	129	41280	320	0.007752
Granite	2700	790	2133000	2.53	$1.19 \cdot 10^{-6}$
Inox steel	7500	502	3765000	17	$4.52 \cdot 10^{-6}$
Iron	7870	460	3620200	80	$2.21 \cdot 10^{-5}$
Marble	2560	832	2129920	2.57	$1.21 \cdot 10^{-6}$
Rolled steel	7850	502	3940700	52	$1.32 \cdot 10^{-5}$
Sand	1900	835	1586500	0.21	$1.32 \cdot 10^{-7}$
Silver	10490	238	2496620	460	0.000184
Soil	2000	800	1600000	0.5	$3.13 \cdot 10^{-7}$
Wood	600	1700	1020000	0.15	$1.47 \cdot 10^{-7}$

Finally, as an attempt to summarize all the combined effects of the global radiative properties of a real object, **Solar Reflectance Index SRI** parameter was proposed basing on the resultant superficial temperature of the bodies. In particular, such surface characteristics were tried to be linked to those of white and black reference materials according to the following Equation 2.40. In this manner, an estimative index of mainly the emissivity and the albedo was given; properly, the increase of *SRI* involves the reduction on surface equilibrium temperature, indicating a typical case of cool material.

$$SRI = \frac{T_{black} - T_{surface}}{T_{black} - T_{white}} \cdot 100 \quad (2.40)$$

2.2.2. Heat mechanisms of road pavements

The present paragraph is aimed at analyzing the theoretical framework useful to understand the thermal mechanisms and phenomena which interest road pavements.

In general, road pavements could be schematized as an opaque surface (real object) which, depending on the structure (multi-layer system) and the material characteristics (bituminous mixture, asphalt concrete, granular materials, etc.), can exhibit a specific ability to diffuse energy towards the deeper ground. The computing approach must start dealing with the heat balance affected by the energies absorbed and released by the pavement surface. In this perspective, general radiative balance equation (Equation 2.41) could be written as the addition of such energies (powers for the unitary surface, i.e. expressed in W/m²):

$$G_{net,pav} = G_{in,pav} - G_{out,pav} \quad (2.41)$$

where, $G_{net,pav}$ indicates the net energy which interests the pavement, $G_{in,pav}$ is the energy of global incident radiations and $G_{out,pav}$ is the total energy released/transferred out from the body. In turn, these quantities can be decomposed in singular well-defined components. $G_{in,pav}$ can be rearranged utilizing the above-defined G_D and G_d energies since pavements are subjected to direct ($G_{D,pav}$) and diffused ($G_{d,pav}$) solar radiations. In this case, $G_{in,pav}$ becomes (Equation 2.42):

$$G_{in,pav} = G_{D,pav} + G_{d,pav} = G_{D\perp} \cdot \cos(\theta) \cdot \alpha + G_d \quad (2.42)$$

where, absorptivity α is the intrinsic radiative parameter of the road pavement surface. Then, (i) considering the surface horizontal, (ii) supposing to adopt the empirical formulation reported in Equation 2.32 to account the atmospheric (diffused) radiation, (iii) substituting α with $1 - \rho$ (on the basis of Equation 2.18), final formulation for $G_{in,pav}$ is (Equation 2.43):

$$G_{in,pav} = G_s \cdot \tau_a \cdot m \cdot \cos(\theta) \cdot (1 - \rho) + [0.77 - 0.28 \cdot 10^{-(0.074 \cdot \nu)}] \cdot \sigma \cdot T_{amb}^4 \quad (2.43)$$

Certainly, a further contribution should be given by the terrestrial radiation G_{Earth} (positive for a body on the soil) given by the Earth towards the body; otherwise, this could be ignored in the case of pavement since G_{Earth} term provide a negligible effect on general balance. $G_{out,pav}$ is constituted by three terms: $G_{cnv,pav}$ indicates the global energy on pavement related to convective heat flows, $G_{cnd,pav}$ represents that referred to conduction heat flows and $G_{em,pav}$ resumes the energy emitted from the pavement surface (infrared outgoing long-wave radiation). Convection energy $G_{cnv,pav}$ can be expressed by Equation 2.44:

$$G_{cnv} = h_e \cdot (T_{surf} - T_{air}) \quad (2.44)$$

where T_{air} and T_{surf} are the temperatures of the air and pavement surface respectively and h_e indicates the average convective heat transfer coefficient of the pavement. This parameter is not an intrinsic property of the surface because it depends on several factors, such as for example the surface geometry, the air characteristics and the wind speed; its experimental determination could be quite difficult since, in some cases, the difference of temperature between the air and the surface also matters. Literature-based mathematical procedure to calculate h_e proposed in Equation 2.45 has demonstrated appreciable precision [2.7]:

$$h_e = 6.98.24 \cdot [0.00144 \cdot T_m^{0.3} \cdot U^{0.7} + 0.00097 \cdot (T_{surf} - T_{air})^{0.3}] \quad (2.45)$$

where T_m is the average of the surface and the air temperatures (expressed in °K) and U is the average daily velocity of wind (in m/s). Similarly, the energy due to conductive heat flows $G_{cnd,pav}$ (from the surface to the inner part of the pavement) is a function of the thermal conductivity k , which denotes the aptitude to conduct heat, and is an intrinsic characteristic of the material which compose the whole pavement. For a given thickness d of a single pavement layer, G_{cnd} can be determined as (Equation 2.46):

$$G_{cnd,pav} = k \cdot \frac{T_{surf} - T_d}{d} \quad (2.46)$$

where T_d is the temperature of the material at the depth d . For instance, k values of bituminous mixtures are reported to range between 0.74 and 2.89 W/m·°K, mainly as a function of the thermal characteristics of the lithic skeleton of the mixture which composes the pavement layer [2.15]. Rigorously, different conduction processes should be taken into account within the pavement since it is generally composed of different layers characterized by different material, thus diverse thermal conductivities. Then, on the basis of Equation 2.10, $G_{em,pav}$ is function of the emissivity ε of the pavement surface, thus (Equation 2.47):

$$G_{em,pav} = \varepsilon \cdot \sigma \cdot T_{surf}^4 \quad (2.47)$$

Indeed, in the case of pavement materials, ε can be considered an intrinsic characteristic: namely, typical emissivity values for asphalt concretes ranges from 0.90 to 0.97, for cement concretes from 0.92 to 0.94 [2.16, 2.17]. As a summary, the general radiative balance (Equation 2.41) could be re-written as (Equation 2.48):

$$G_{net,pav} = (\pm G_{D,pav} \pm G_{d,pav}) - (\pm G_{cnd,pav} \pm G_{em,pav}) \quad (2.48)$$

Figure 2.19 schematizes the general balance on a surface exposed to solar radiations.

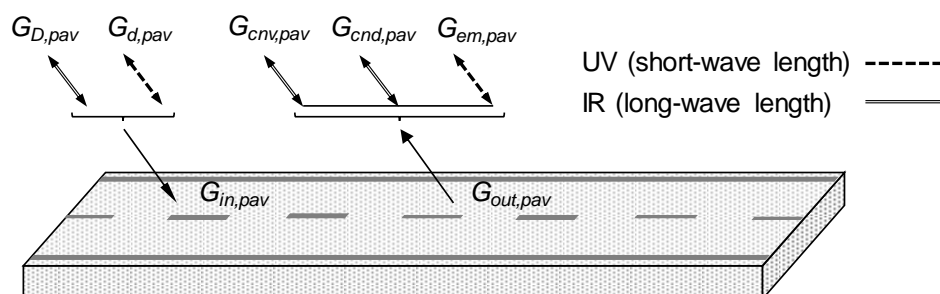


Figure 2.19. General radiative balance on a surface exposed to solar radiations.

Conventionally, incident energies $G_{D,pav}$ and $G_{d,pav}$ are assumed with positive signs because pavements are exposed to the solar radiations. Sign of convection energy $G_{cnv,pav}$ is generally negative since energy is transferred from the pavement (hotter) to the surrounding ambient (cooler). According to thermodynamic conventions, conduction energy sign is affected by the temperature pattern within the body considered. Thus, on summer time (during which pavement temperatures are supposed to be hotter at the surface) $G_{cnd,pav}$ is considered negative. Contrarily, $G_{cnd,pav}$ sign must be assumed positive during winter, when typically, higher temperatures are reached on deeper layers of pavements (cooler surface). Once again, since pavement is hotter with respect to the ambient, also $G_{em,pav}$ is considered with negative signs. In view of such conventions, the balance equation of a generic road pavement could be finally stated (Equation 2.49). Figure 2.20 reports a scheme useful to understand the effective heat transfers contributing to the UHI (more critical during the summer).

$$G_{net,pav} = G_{D,pav} + G_{d,pav} - G_{cnv,pav} - G_{cnd,pav} - G_{em,pav} \quad (2.49)$$

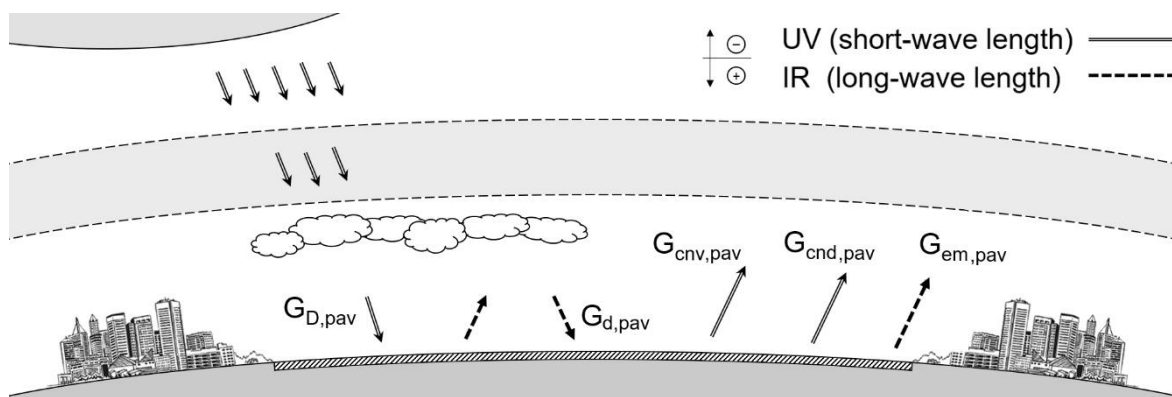


Figure 2.20. General radiative balance for road pavements (during summertime).

Given the above-explained theory, it is evident that the possible mitigation of urban heat island phenomena could be achieved acting on material properties of road pavements. According to formulations (see Equation 2.43), an increase of albedo ρ could support (with a proportional tone) the reduction of the energy absorbed by the pavement, contributing to the containing of reached temperatures. Also emissivity (ε) modification could represent an effective way to mitigate UHI (see Equation 2.47), thus the use of alternative materials (with respect to conventional paving concretes) could be an effective strategy. In general, materials owing higher thermal conductivity (k) tend to be more prone to diffuse heat towards deeper pavement layers, further reducing the perceived heat in the surface. In this regard, please note that, even the significant dimensions of the urban space and the complex and diffused heat flows, thermal comfort must be referred to an approximate height of 2 m (i.e. in the proximity of the spaces normally occupied by humans). Literature early dealt about radiative properties of road pavements and paving materials, principally in order to study cool solutions for UHI mitigation. An example is presented in Figure 2.21 [2.18].

Indeed, particular attention must be paid about materials properties reported in literature since they vary depending on several aspects, e.g. the surface condition (roughness, cleaning) and state of life (aging). Some experiences documented that flexible pavements emit about 150 W/m^2 more than soil in terms of IR radiation and absorb from the atmosphere 60 W/m^2 more than cement concrete surfaces. Other studies were able to demonstrate in what manner the energetic behavior of urban materials (in particular the superficial temperatures) is linked to the urban space's configuration and orientation with respect to the direction of solar radiation. For the sake of completeness, some data are reported on the basis of such researches: Table 2.5 presents some results (in terms of surface temperatures) obtained during summer on white pavements and asphalt concretes for different roads located within urban canyons; H/W parameter represents the ratio between the height of buildings (H) and their width (W). Results are differentiated for orientation (with respect to sun direction) and are expressed through the difference of maximum temperature between sunny and shaded zones (ΔT_{max}) and the overall maximum temperatures recorded for each road (T_{max}). Table 2.6 indicates temperatures reached by the surface of several construction materials for city paving (roads and marginal elements) of different color and in different state (texture: smoot: S ; rough: R). In this case it is interesting to note that, as expectable, color seems to influence the final response of pavements [2.19, 2.20].

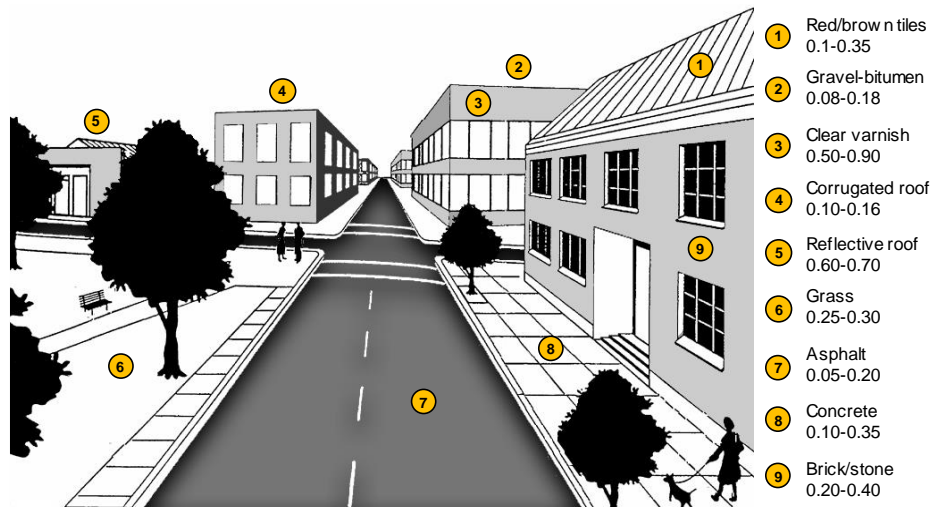


Figure 2.21. Examples of albedo for urban construction materials.

Table 2.5. Literature-based results about thermal responses of white pavements and asphalts.

Road	H/W	Orientation (to South)	White pavement		Asphalt concrete	
			ΔT_{max}	T_{max} [$^{\circ}\text{C}$]	ΔT_{max}	T_{max} [$^{\circ}\text{C}$]
1	0.725–1	40°	20	10	27	6
2	1	50°	18	14	20	6
3	1.75–2.62	35°	19	22	20	7
4	1–1.5	65°	10	7	8	3
5	2.47	60°	22	8	21	14
6	2.74	55°	15	10	-	-
7	2.47	30°	20	13	-	-

Table 2.6. Literature-based results about surface temperatures of different paving materials.

Material	Color	Texture	T_{max} [°C]	T_{min} °C]
Mosaic	Green	S	39.5	23.9
Mosaic	Black-white	S	40.6	23.7
Mosaic	Beige	S	40.7	23.6
Mosaic	Grey	S	43.3	24.7
Mosaic	White	S	37.7	22.2
Mosaic	Brown	S	42.5	23.7
Mosaic	Red	S	44.8	24.9

Material	Color	Texture	T_{max} [°C]	T_{min} °C]
Concrete	Grey	S	43	25.6
Concrete	Grey	S	44.6	25.7
Concrete	White	S	37.7	23.1
Concrete	White	S	39.3	23.5
Granite	White	S	36.8	22.8
Granite	Black-white	S	40.4	23.7
Granite	Green	S	41.4	24.6
Granite	White-green	S	44.3	25.1
Marble	White	S	38	23.4
Marble	Black-white-red	R	38.4	24.2
Marble	Black-white	S	36.1	22.5
Marble	Black-white	R	36.9	23.2
Marble	White	S	33.4	21
Marble	White	R	37.2	23
Marble	Black -white	S	39.9	23.7
Marble	White	S	34.2	21.1
Marble	White	S	36.6	22
Marble	Pink	S	44.5	26.1
Marble	Brown	S	37.5	22.1
Marble	Red	S	48.3	28.2
Marble	Black-white	S	43.2	25.6
Marble	Dark grey	S	50.7	29
Marble	Grey	S	45.7	26.4
Stone	Brown	R	46.7	27.4
Stone	Beige	R	46.7	26.7
Stone	Black-brown	R	45.8	26.7
Stone	Beige	R	44.7	26.1
Stone	Red	R	45.1	26.6
Stone	White-brown	R	41.1	24.7
Concrete	Grey	S	43.1	26
Concrete	Grey	R	44.2	25.9
Concrete	Grey	R	43.8	26.8
Concrete	Grey-white	S	43.5	25.1
Concrete	Black-white	S	48.1	27.2
Concrete	White-black	S	40.3	23.1
Concrete	Black	R	50.4	28.9
Concrete	Black	S	52	27.6
Concrete	Red	R	45.9	26.1
Concrete	Red	S	45.5	24.8
Concrete	Red-white	S	43.7	24.6

Material	Color	Texture	T_{max} [°C]	T_{min} °C]
Mosaic	Black	S	49.6	26.1
Concrete	Red	S	43.8	24.6
Concrete	Black	S	51.6	27.5
Granite	Red	S	46.6	26.7
Granite	Black	S	51.7	27.9
Concrete	Orange	S	42.7	25.2
Concrete	Brown	S	45.8	25.5

Material	Color	Texture	T_{max} [°C]	T_{min} °C]
Concrete	Red-black	S	48.2	25.5
Stone	Green	R	50.9	28.9
Stone	Dark grey	R	52.7	28.5
Stone	Grey	R	46.9	26.8
Stone	Light grey	R	46.3	26
Asphalt	Black	R	54	30.3
Concrete	White	R	38.1	23.7
Concrete	White	R	37.5	23.1
Concrete	White	S	39.2	24.1
Concrete	White-white	S	37.2	21.9
Concrete	Orange-white	S	42.9	24.4
Concrete	Orange	R	44.9	25.2
Concrete	Orange	R	44.8	25.3
Concrete	Orange-white	S	43.2	24.7
Concrete	Green	R	44.3	24.9
Concrete	Orange	R	42.9	24.3
Concrete	Dark-green	R	50	26.6
Concrete	Green	S	43.7	23.9
Stone	Green-white	R	43.6	25.1
Concrete	White-blue	S	43.3	24.5
Stone	White-green-red	R	42	24.6
Stone	White	R	38	23
Rock	Red	R	49.6	28.8
Rock	Grey	R	49.2	28.2
Rock	Brown	R	46.3	27.1
Rock	Black	R	50.4	28.5
Rock	Brown	R	46.9	26.3
Rock	Grey	R	49.3	28.3
Rock	Green	R	47.2	26
Rock	Black	R	48.2	26.7
Rock	Brown	R	43.8	24.4
Rock	Brown	R	45	25.1
Rock	Green	R	44.3	25.2
Rock	Brown	R	40.8	23.4
Rock	Brown	R	38.6	22.5
Rock	Brown	R	40.8	23.3
Rock	Brown	R	46.7	27.3
Rock	Red	R	48.8	27.9
Rock	Red	R	49.2	27.7

All the described factors exert concomitant effects on road pavements, which are traduced in specific T_{max} (maximum T reached during the solar irradiance). However, some literature

experiences tried to establish the influence of the single parameters in such T . For instance, solar absorptivity was linked to T_{max} , for different emissivity of the pavement (Figure 2.22): here, α seemed to be proportional to T_{max} ; an opposite situation was found for ε [2.7].

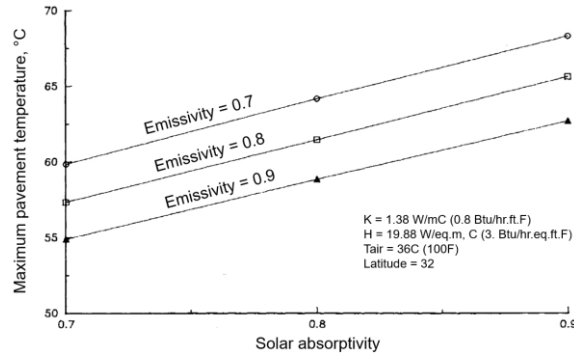


Figure 2.22. Maximum pavement temperature vs. absorptivity (for different emissivities).

The wind speed alters the convective coefficient (relatively to the pavement surface): thus, T_{max} and the related thermal conductivity (of the surface materials) were linked to such aspects (see Figure 2.23) [2.7]. In particular, lower convective coefficients increased T_{max} because of the lower dissipated heat through the convective exchange with the surrounding air; the increase of the thermal conductivity guaranteed lower T_{max} (a greater heat portion was transmitted to the pavement depth).

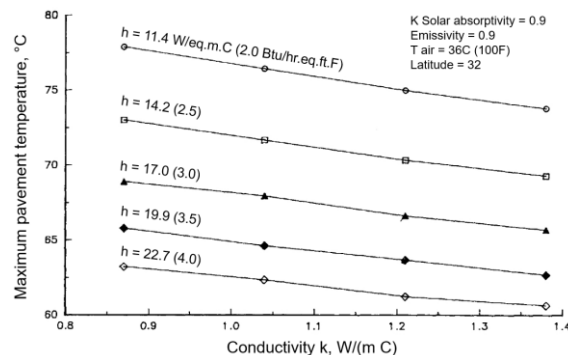


Figure 2.23. Maximum pavement temperature vs. conductivity (for different wind convections).

In turn, the cloudiness affects such T_{max} . This aspect can be simulated supposing to reduce the radiation incident on pavement. In this perspective, some relations were also defined to link the maximum hourly solar radiation to the latitude of the subject [2.7]. Figure 2.24 depicts such correlation for a surface normal to the sun rays and a generic horizontal surface (in the latter case, a sensible reduction of radiation was detected).

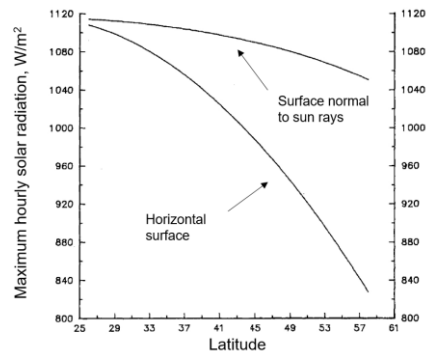


Figure 2.24. Maximum hourly solar radiation vs. latitude (normal and horizontal surface).

The latitude has a definite influence on the hourly solar radiation (Figure 2.25), resultant in the different temperature gradients between the pavement surface and the air (ΔT_{s-a}) that have been estimated based on the Equation 2.50. Figure 2.26 illustrates the relation for various maximum air temperatures [2.7].

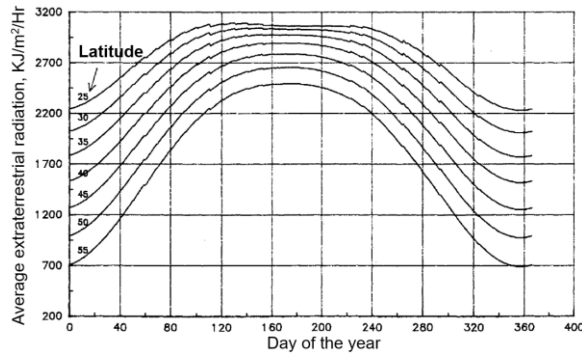


Figure 2.25. Yearly trends of hourly solar radiation for different latitudes.

$$\Delta T_{s-a} = -0.0062 \cdot \phi^2 + 0.2289 \cdot \phi + 24.38 \quad (2.50)$$

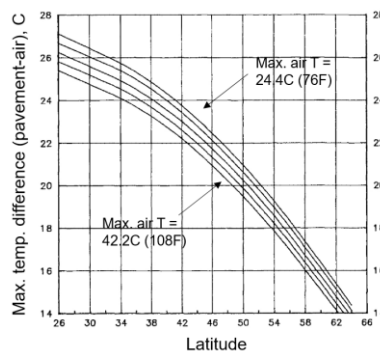


Figure 2.26. Gradients between maximum pavement and air temperatures vs. latitude.

Chapter 3

Literature Review

The present Chapter proposes a short review of some literature experiences made in the field of the road construction in order to design thermal-optimized structures and pavements useful to mitigate the UHI phenomena.

3.1. Heat mitigation

The first paragraph reports different literature experiences found in the literature concerning the investigation of thermal-optimized road pavements and applications for the heat mitigation.

3.1.1. Real-scale experiences

Some real-scale applications of systems and structures designed to mitigate the heat impacts within the city are following presented.

Going back to the '80s, Davies [3.1] started to study the thermal distribution on road pavement depth; through specific mathematical approaches [3.2], the heat transfer was computed among the various pavement layers (owing different characteristics from each other). Dealing with a flexible pavement (made of upper bituminous wearing courses and lower granular layers), system was analyzed through conductors subjecting it to an external heating. A schematic representation of the adopted structure is presented in Figure 3.1. In particular, the depth from the surface was identified as a key parameter in conditioning the temperature distribution, as well as the stiffness of the materials (computed with models and

assessed also with indirect tensile stiffness modulus tests). Interestingly, the maximum temperature within the pavement was reached at a certain depth rather than in the surface (depending on the external mitigation due to the wind). As an example, Figure 3.2 illustrates the temperature and stiffness distributions on the pavement depth obtained in the study.

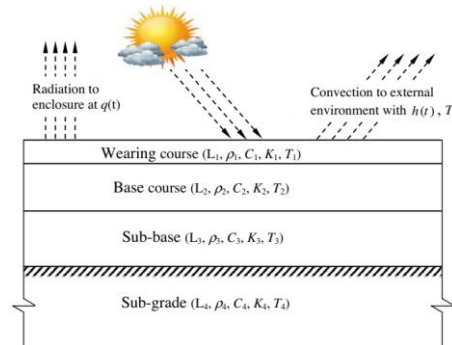


Figure 3.1. Schematic representation of the studied pavement [3.1].

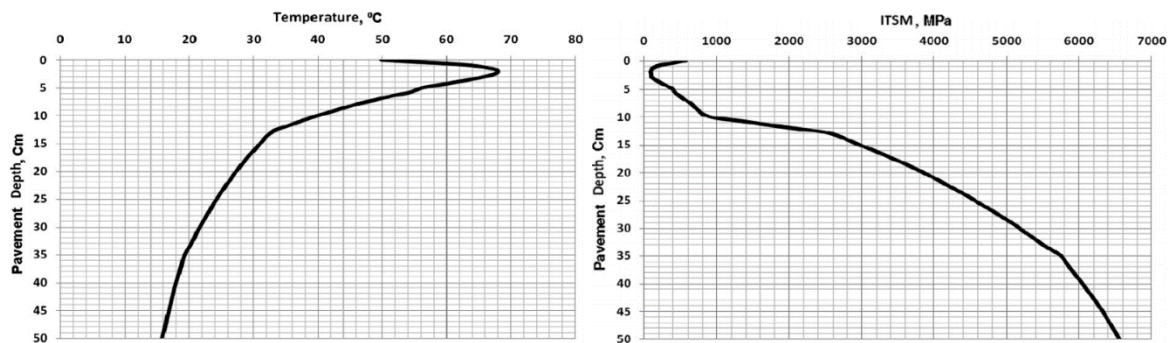


Figure 3.2. Heat (left) and stiffness (right) distribution through the depth of pavement layers [3.1].

As already presented in the previous Chapter, during the 90's, Solaimanian and Kennedy proposed a multi-parametric approach in order to compute the temperature on the road pavement based on the energetic balance referred to the short-wave and long-wave radiations and the convective and conductive heat transfers manifested under the wearing course surface [2.7].

In 2003, Pasetto et al. developed a theoretical model for the heat transmission able to evaluate in the transitional state the temperature of road and airport flexible and semi-rigid pavements [3.3]. Thermal-physical properties of the materials were studied supposing a mono-dimensional heat transfer in the vertical direction and neglecting the possible mass transfer within the structure. The temporal evolution of the air temperature, the wind intensity, the solar irradiation were considered, together with the convective and conductive coefficients, the emissivity and the conductivity, in order to determine the temperature distribution in the pavement depth and the heat transition across the layers of diverse materials. The model reliability was verified with a real application in some ad hoc-instrumented pavements located in an operating Italian airport. Some cores were taken in

order to define the pavement's structure (composed by 2 bituminous layers of 3 cm, a macadam base and a granular-stabilized sub-base); then, some thermocouples were applied at each pavement interface (between each layer). Good model accuracy was certified above all in presence of sunny weather conditions. For instance, the following Figure 3.3 shows an example of the model output.

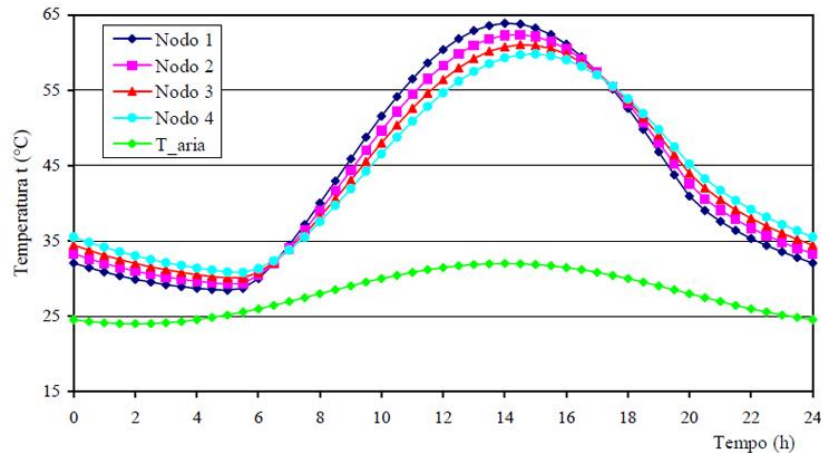


Figure 3.3. Model results about the temporal distribution of the pavement temperatures [3.3].

In the last decade, other authors set up real-scale trial sections with the objective to determine the thermal repercussion in the case of traditional and pervious concrete pavements. Pervious pavements are generally made by special type of concretes with a high porosity that allows water to pass directly through rather than to pass around [1.86]. Pervious concretes are manufactured using concrete paste or asphalt binder to coat large and single-graded aggregates [3.4–3.6]. These concretes have large interval cavity to drain water (the most percolating water is not stored inside the pervious pavers because the pavement systems drain readily) [3.7]. Otherwise, whether pervious pavements perform cooling is controversial in the reference literature. Pervious pavements have been found as hot as dark asphalt pavements in sunny summer days because they have higher solar absorptive and lower thermal inertia than conventional pavements [3.8, 3.9]. In some specific cases, pavements were instrumented to analyze the thermal characteristics of the materials, their thermal conductivities and their aptitudes to store the heat under various scenarios (under different atmospheric conditions) [3.10, 3.11]. In such cited studies, a wide parking area was divided in two areas, the first one paved with conventional concrete, the second one characterized by high permeability (ad-hoc granulometric distributions and voids' patterns allowed the water infiltration). Reflectivity concerns were adopted to compare the two rigid pavements. The thermal monitoring and sensing were organized also to account the daily heat (cumulated during the summer season) through parameters such as the temperatures of the pavements and the air, the stored energy for surface unit, the daily cooling rate and the temperature of the laying surface. Mainly, the experimental findings showed different

reactions for the two pavements: the conventional rigid pavement retained a greater heat quantity within the initial summer period and demonstrated a tendency inversion at the summer end; the pervious pavement exhibited similar behaviors to the traditional one, substantially demonstrating to be quite unuseful in preventing the UHI phenomenon. The following Figures 3.4 and 3.5 illustrate a picture and a schematic representation of the pavements tested in the studies.

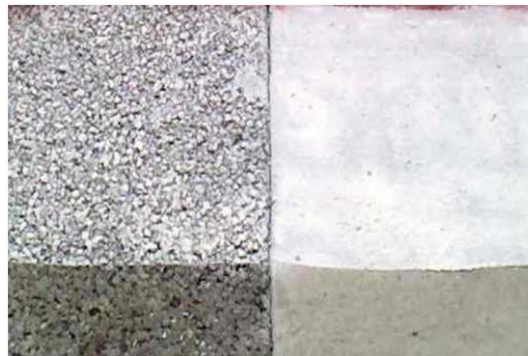


Figure 3.4. Picture of the pervious pavement (left) and the conventional rigid one (right) [3.10].

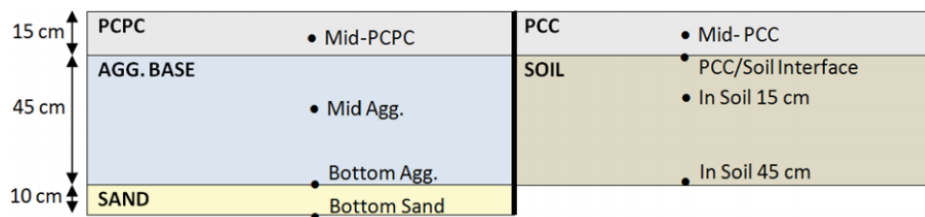


Figure 3.5. Schematic view of the pervious pavement (left) and the rigid one (right) [3.10].

Based on real-scale data acquisitions, in 2013, Gedafa et al. published a forward-looking model for the analysis of the temperatures interesting some permanent pavements [3.12]. These flexible structures were designed to guarantee a high durability, with an in-service life greater even than 50 years (with only ordinary maintenance on the surface layers). In situ tests carried out through a sensed falling weight deflectometer furnished the temperature of the wearing course (every 15 meters) to validate the proposed model. The statistical significance (see Figure 3.6) demonstrated the existence of a linear relation between the temperatures of the pavement layers and both the time of the day and the air temperature of the days before the tests.

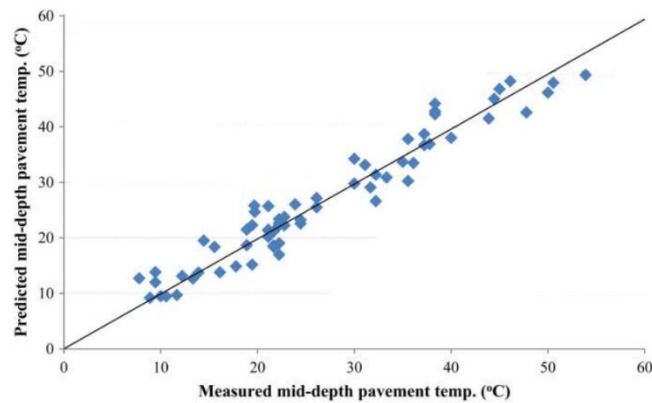


Figure 3.6. Comparison of measured and predicted mid-depth pavement temperatures [3.12].

Further, Wang et al. hypothesized the use of an empirical model for the study of the thermal variations regarding flexible pavements based on an existing approach which considered parameters as the solar radiation, the meteorology, the air humidity, the wind speed, the atmospheric and the soil temperatures [3.13, 3.14]. Trial sections were used to validate the temperature-distribution model also investigating the influence of the daily temperature variations and the seasonality. Under the experimental hypothesis, such a model showed an extreme reliability and allowed to state that: i) the surface temperature was not affected by the thermal conductivity of the pavement materials; ii) the nightly temperature gradients were quite meaningless despite the winter season and the existence of freezing-thawing cycles. For these reasons, authors suggested to design the pavement structure just considering the thermal variation to the seasonality.

A literature contribution published in 2015 developed a thermal analysis of road pavements in order to optimize an irrigation technique widely utilized to cool the urban surfaces and manage the UHI impacts [3.15]. Real-scale tests were performed in the city of Paris in the summer of 2013; a daily watering was calibrated upon the possible construction of an irrigation infrastructure using the non-drinking urban water. The studied pavement (whose scheme is presented in the following Figure 3.7) was equipped with thermocouples placed 5 cm under the surface; thermal recordings (mainly the thermal radiation characteristics and the surface thermal transfer) allowed to regulate the irrigation frequency and the requested water quantity. The more successful configurations resulted even in the halving of the heat and were obtained equalizing the watering, the evaporating mass and the water absorbed by the pavement. Therefore, it was concluded that a specific pavement design (i.e. the selection of precise materials) could optimize the system, attenuating the UHI effect contemporary preserving the water resources.

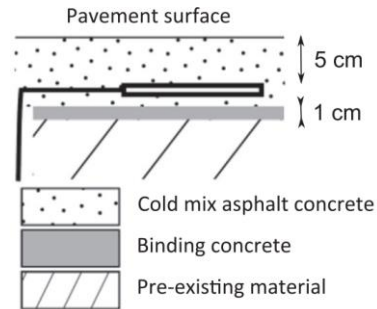


Figure 3.7. Cross-section detail of pavement sensor filling materials [3.15].

In analogy, another publication studied the same trial section to understand the effects of the irrigation on cool road pavements (realized with cold bituminous mixtures) at 5 cm under the wearing course surface. In this case, the daily thermal evolution was also reconstructed [3.16].

More recently (in 2016), a calculation model based on heat energetic balances has been also proposed in order to estimate the surface temperature of pavement for winter climates [3.17]. The validation has been done with long-period in situ monitoring considering also the albedo of the surfaces (responsible also of the degradation of the permafrost present in the ditches located in the road proximity). Figure 3.8 gives some photos of the site (a motorway stretch in Canada). Four different kinds of flexible structures (with various colors) were paved and were instrumented at a depth of 5 cm; the air temperature, the wind speed and solar radiation were also recorded by a local weather station to calibrate the validation.



Figure 3.8. Real-scale application of flexible pavements for winter climate [3.17].

Another recent study dealt with the design of a water-retaining pavement made with cementitious materials, ceramic powders, ashes and natural zeolite [1.18]. In this perspective, it is widely recognized that pavements made with cement materials can improve the surface reflectivity; the solar reflectance of the cement primarily dominates the albedo of the hydrated concrete while any other constituents act the secondary role [3.18]. The albedo grows when the Portland cement hydration produces calcium hydroxide and stabilizes after the hydration completes [3.19]. Adding fly ash to react with calcium hydroxide increases the concrete durability but can reduce the albedo [3.20]. Then, it must be also stressed that, at the aged stage, the albedo is determined mainly by the reflectance of the fine aggregates and paste of the mixture [3.19, 3.21]. The use of the above-mentioned water-retaining pavement was assessed through real-scale trial sections monitored during the summer season, recording the surface temperature of different pavement structures. Figure 3.9 gives some pictures of the in situ surveys. Main results indicated that cement and zeolite conferred a clear color to pavements, mitigating the heat concentration in such surfaces. Further details on the trial section arrangement can be found elsewhere [3.22].



Figure 3.9. Trial sections for the analysis of pavement thermal responses [1.18].

In general, it must be remembered that the thermal responses of the trial sections must be also analyzed in view of the location within the urban environment. In this perspective, Cuculic et al. published in 2014 a review of the main parameters influencing the heating phenomena typical of the Urban Heat Islands [3.23]; Figure 3.10 depicts the survey area.

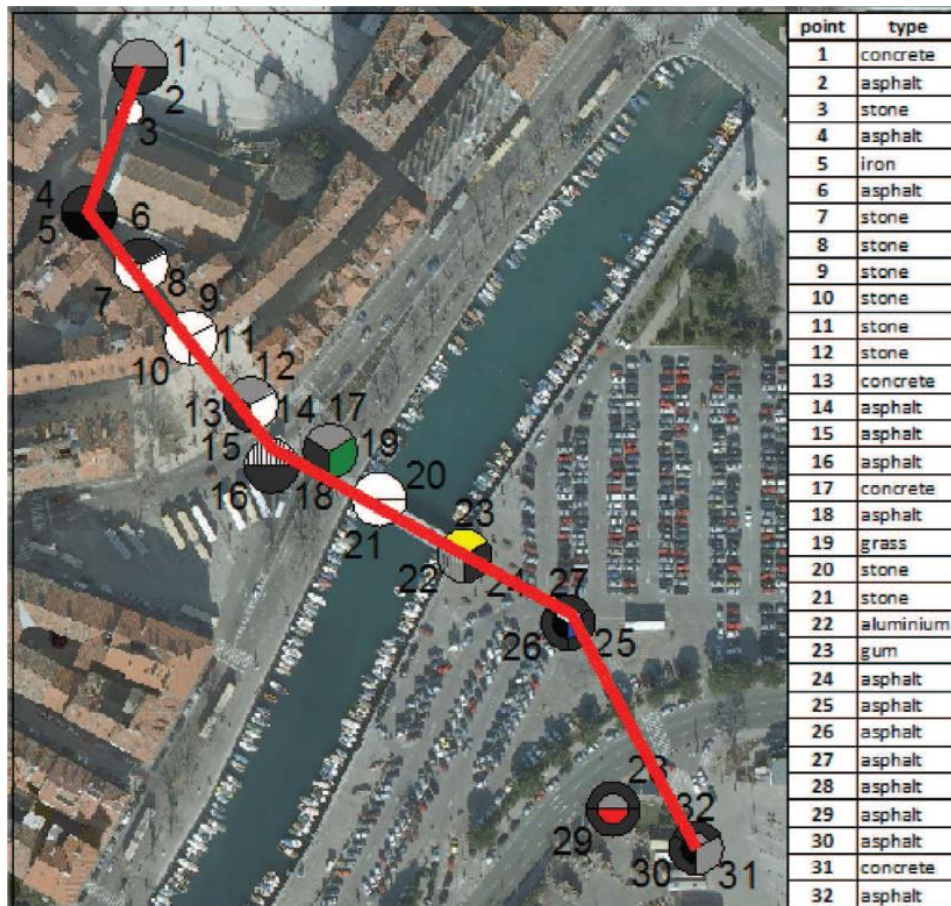


Figure 3.10. Survey area for the analysis of pavement thermal responses [3.23].

The core of the research dealt with an extended measuring campaign made in the city of Rijeka (Croatia) in order to detect the temperature of the various urban road surfaces. During the summers between the 2011 and 2013, data were collected on different pavements of low-trafficked road and parking lots: surface temperatures were related to the air temperature, the wind speed and the water presence. Principal findings evidenced that the residential areas (majorly non-always exposed to the direct sunlight), the sections located in the proximity of a water basin and those surrounded by vegetation were cooler than the other ones.

3.1.2. Small-scale experiences

The present paragraph illustrates some research contributions addressed to the study and the design of thermal-optimized pavements based on laboratory small-scale activities.

The use of the infrared technology for the laboratory simulation of the heat effects was proposed by Stroup-Gardiner et al. in 2000 as a synthesis of the NCHRP research project 9-11 [3.24]. In particular, such a radiation was employed to detect the segregation of asphalt mixture, i.e. to identify all that anomalies occurring during the mix's production which can cause densification problems.

The same year, Giuliani developed and validated an analytic model based on the thermal performance of flexible road pavements [3.25]. The heat transmission mechanisms on the bituminous mixes were analyzed testing in the laboratory several cylindrical samples (conditioning carried out also at low temperatures – up to $-30\text{ }^{\circ}\text{C}$). Thermal distribution inside the asphalt concrete was experimentally monitored also to comprehend internal cracking phenomena. Main results indicated that: i) integrating the general equation of the heat transfer in non-steady-state hypothesis (referring the computation to cylindrical shapes), a suitable prediction of the temperature distribution could be obtained in the case of bituminous mix; ii) the thermal diffusivity of asphalt concrete did not depend on the densification (equal temperature evolution on time were obtained regardless different void contents); iii) the thermal conductivity was directly proportional to the material density (at least up to 10% of voids); iv) the temperatures of samples approached that of the environment as a function of the cooling rate applied.

Similarly, another publication dealt with temperature modeling was verified with a laboratory validation applied to cylindrical specimens produced with the shear gyratory compactor [3.26]. Punctual measurements of temperature were carried while the samples were subjected to a controlled heating procedure given through air flows. Even with some constrains related to the small sample scale, good model reliability was obtained for what

concerning both the global temperature gradients suffered by the specimens and the localized thermal distributions. Figure 3.11 schematizes the experimental scenario.

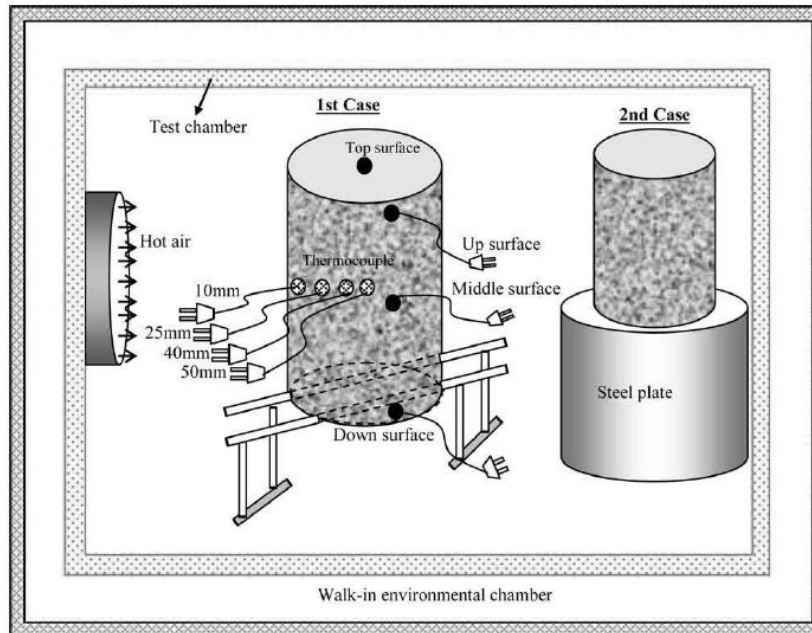


Figure 3.11. Experimental scenario set up to monitor the laboratory samples [3.26].

In 2012, Guangxi and Xiong described an innovative system to collect laboratory data on the long-period and applicable also to the in-service pavements to measure thermal gradients between the surfaces and the bearing sub-grade [3.27]. In this regard, Figure 3.12 illustrates some details of the utilized equipment.

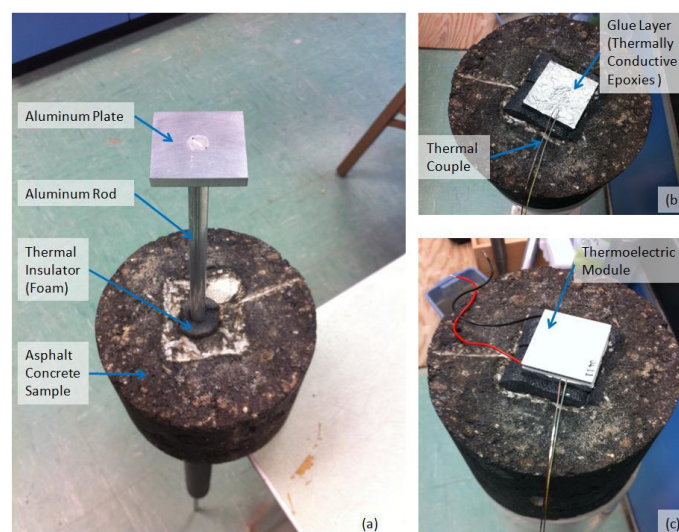


Figure 3.12. Details of the equipment used to monitor laboratory samples [3.27].

Later, Di Maria et al. dealt with flexible and rigid pavements ad hoc reproduced in the laboratory in form of slabs and exposed to the external environment [3.28]. A thermographic device and some thermal sensors recorded the surface temperatures; the reflectivity of surface was assumed as indicator of the aptitude to the thermal exchanges. Bituminous-based slabs were also tested in terms of aging and rutting resistance. Further, some slabs were also painted with a yellow varnish based on some literature statistic recordings which give promising indications for similar yellow surfaces [3.29]. All the colored slabs guaranteed cooler surfaces with respect to the original ones; indoor and external measurements indicated that bituminous specimens were always slightly hotter than the concrete ones (even if they were able to release the heat faster). The following Figure 3.13 presents some of the tested slabs.

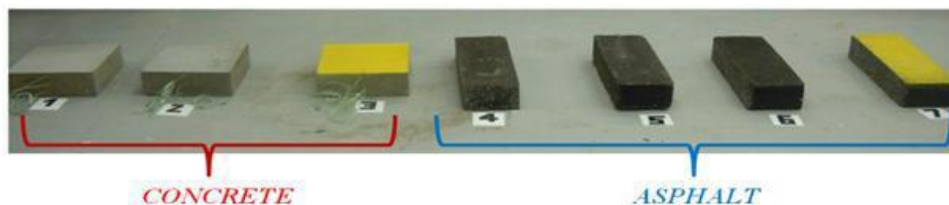


Figure 3.13. Slabs tested in the laboratory and in external environment [3.28].

In 2015, a thermal-oriented pavement structure composed by layers with different conductivity was proposed by Yinfei et al. [3.30]. This was particularly designed to reduce the temperature which affects the constituent materials (some polymer-modified bituminous mixtures – styrene-butadiene-styrene type – were added with low-conductive powders to lower the summerly and nightly heat releases). A reliable mathematical model was also proposed and validated through the laying of such asphalt concretes and the sensing of the constructed structure (thermocouples at depth of 4, 10 and 18 cm). Successful mix-designs were defined to obtain the research target. The following Figures 3.14 and 3.15 expose a schematic representation of the modeled structure and some concerns about the in-field measurements.

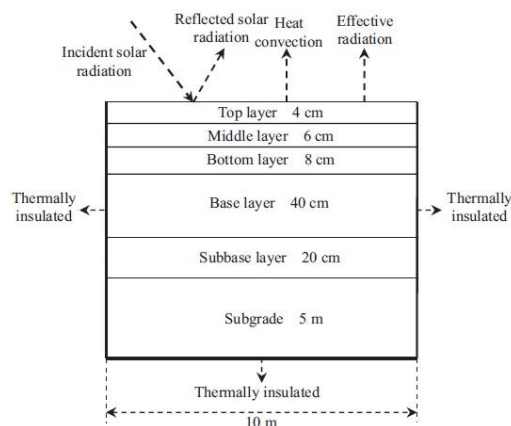


Figure 3.14. Scheme of the modeled structure [3.30].

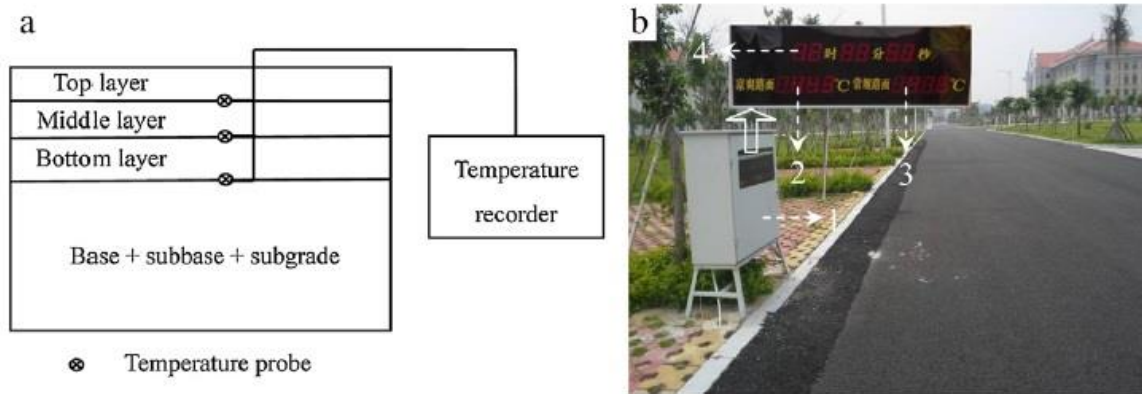


Figure 3.15. In-field measurement performed for the model validation [3.30].

The same year, an interesting publication was diffused by Yinfei et al. [3.31]. They presented a specific design addressed to the construction of a bi-directional inductive structure able to reduce the heat effects and impacts. Particular mix-designs with fine portions and ad hoc-chosen powders were utilized in the surface layers depending on the thermal performance of the deeper pavement layers. Figure 3.16 presents the width and some characteristics of the designed layers.

Punctual thermal characteristics were also modeled through the finite element theory (with a 2D model) and were also utilized as input information for more advanced models useful to estimate the possible rut depths on the pavement due to the rutting phenomena. The validation was again done within the laboratory; really, the successful reduction of the temperature interesting the samples produced also greater materials stiffness (symptom of better resistance to permanent deformations).

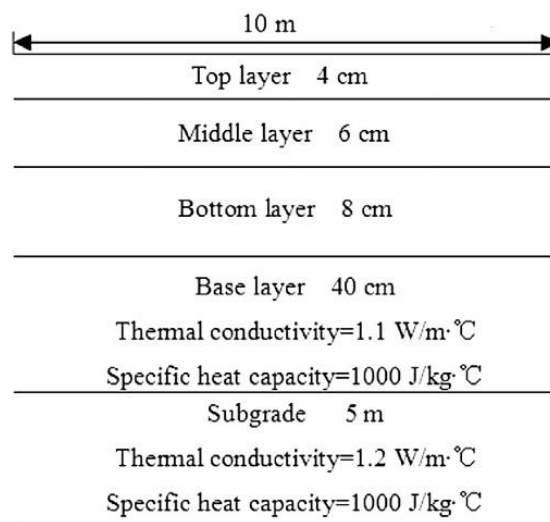


Figure 3.16. Scheme of the layers composing the studied pavement [3.31].

Recently, Hassn et al. have proposed an experimental protocol for the study of the effects of the voids' content on the temperature evolution regarding the bituminous mixtures (both in dry and wet conditions) [3.32]. More specifically, asphalt concrete dry slabs with different voids were exposed to artificial infrared lamps in the laboratory while monitored in terms of surface and sub-grade temperatures, heat fluxes and evaporation (weight loss). Figure 3.17 shows the test device, whereas Figures 3.18 and 3.19 illustrates some results about the surface and the bottom temperatures, respectively.

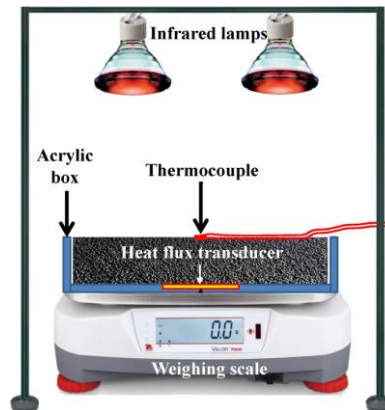


Figure 3.17. Laboratory heating of asphalt concrete slabs carried out with infrared lamps [3.32].

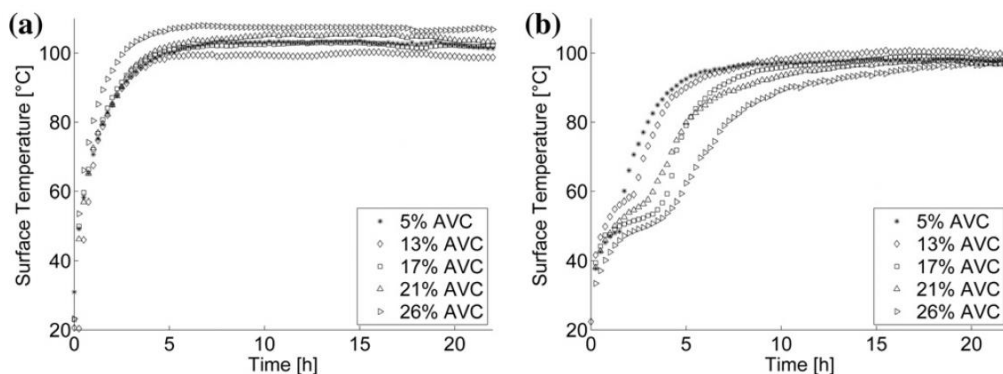


Figure 3.18. Surface temperature for different voids: dry (left) and wet (right) condition [3.32].

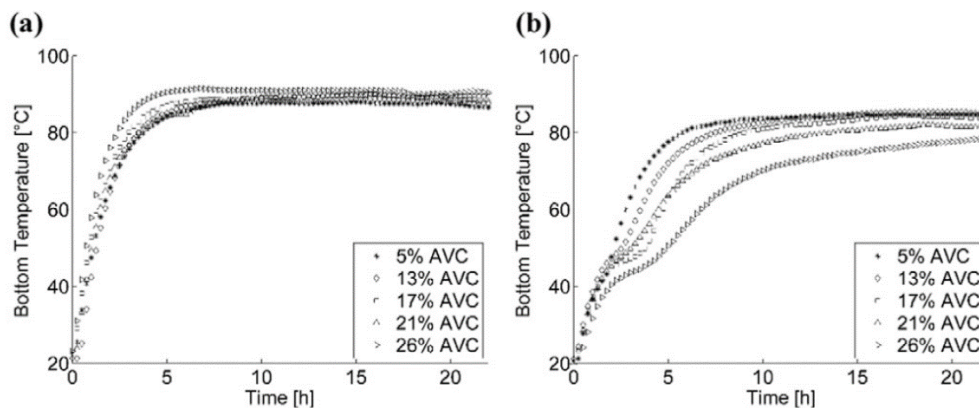


Figure 3.19. Bottom temperature for different voids: dry (left) and wet (right) condition [3.32].

The recorded parameters permitted the definitions of such trends: i) the maximum surface temperature reached at the equilibrium was greater in the case of higher void's percentage; ii) a greater susceptibility to the temperature increase was detected for the saturated samples (heat absorption by the water filling the voids); iii) the heat flux was inversely proportional to the void percentage and was influenced by the evaporation (in water presence, it reached the maximum and then decreased with an asymptotical tendency); iv) the thermal conductivity, greater with low voids, suddenly dropped once the evaporation was completed.

3.2. Heat management

The present paragraph reports some literature contributions regarding the study of thermal-oriented pavements with several targets connected to the management of the urban heat.

The growing consciousness about the topic of the sustainability is pushing towards the implementation of innovative technologies used for the harvesting of the energy interesting the pavements. Strong incentives in this direction are surely given by the progressive reduction of the available energy resources and the continuous increase in their demand; therefore, the production and use of renewable energies are going to be more and more promoted. Within this perspective, the recent scientific literature started to report some designs and applications of several harvesting systems for road pavements, with different targets and operating apparatuses. Depending on the final objectives set for such systems, various working mechanisms and practices applied to flexible and rigid pavements can be cited. Some of these harvesting technologies concern the collection of the thermal energy collected by the surfaces through pipe systems installed within the road wearing courses. As an example, Chiarelli et al. proposed a suitable pipe-based structure working with air flows [3.33]. Other applications considered the circulation of water in coils beneath pavements [3.34]. In general, these systems are reported to be versatile solutions, because they are able to extract or dissipate the heat of the pavement by managing the characteristics of the fluid circulating inside the pipes. In the typical case of harvesting, a flow of cool fluid (colder than the pavement surface) permits the collection of thermal energy derived from the solar irradiation, also decreasing the temperature in the pavement top. Thus, concurrently with the energy extraction, tangible benefits connected to the UHI problem can be achieved [1.145]; not least, intense abatements of surface heat could enhance the mechanical resistance of the pavements, as example for what interesting the permanent deformation resistance [3.35].

As an example of these applications, Guldentops et al. [3.36] exposed the study of an innovative pavement system for the heat collection able to store even small quantities of thermal energy due to the solar heating. In particular, a model was produced to evaluate the effects of a pavement equipped with pipe collectors embedded inside the flexible wearing course. Given the complexity of the structure, such a model was designed in three dimensions using the finite elements procedure to consider all the geometrical and environmental variable involved. Figure 3.20 presents the scheme of the modeled structure.

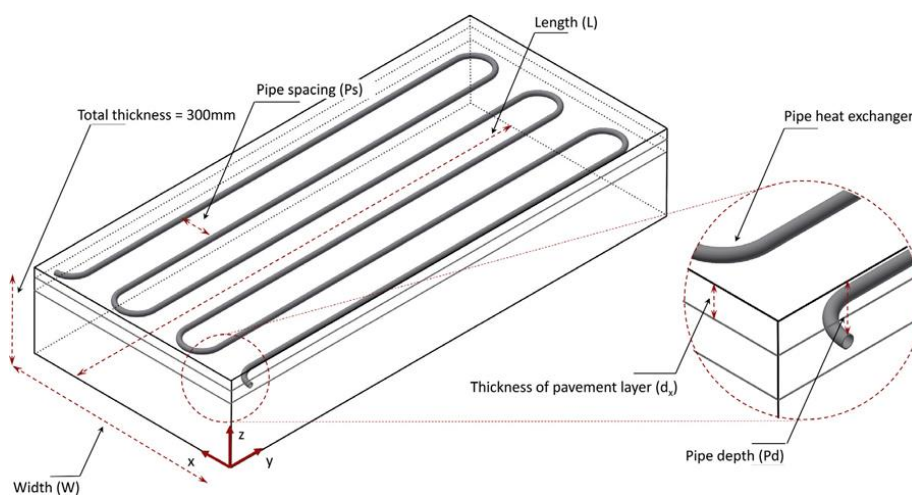


Figure 3.20. Scheme of the three-dimension modeled structure [3.36].

The model validation was performed in the laboratory: slabs of different types were manufactured with the hot technique (a pipe with a diameter of 15 mm was embedded in 119-mm-high slabs). Copper was used to construct the pipe in order to maximize the internal thermal exchanges. Some impermeable sensors collected information about the water circulating inside the system (temperature at the input and output sections). Further details of the experimentation are presented in the following Figures 3.21 and 3.22. Essentially, the computed results (in terms of pavement and fluid temperatures) complied with those evinced by the experimental findings: in particular, the most effective parameters in guaranteeing the system efficiency resulted the mixture thermal conductivity, the pavement absorption rate and the depth of the coil. Indeed, some concerns grew considering the possible clearing of the pavement surface due to the aging which could partially compromise the structure functioning.

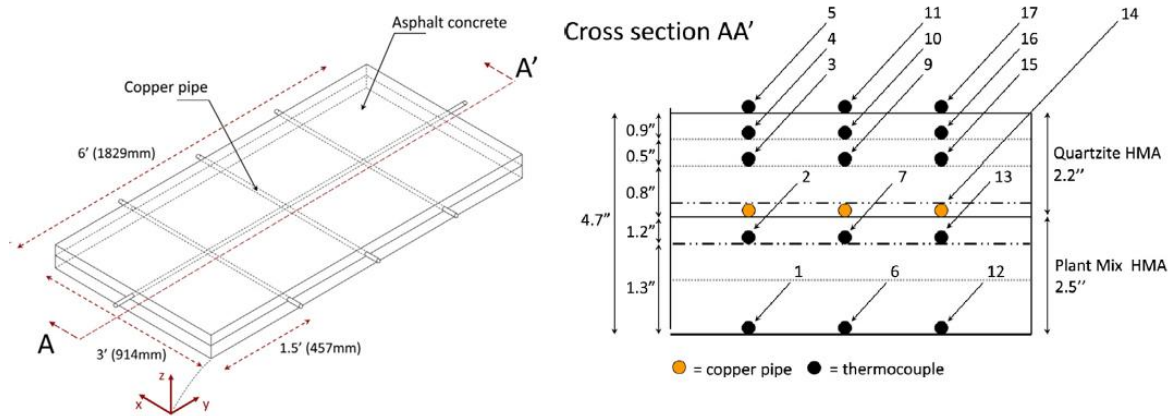


Figure 3.21. Scheme of the slabs prepared in the laboratory [3.36].



Figure 3.22. Slabs' construction details [3.36].

Another similar installation was proposed by Yinfei and Shengyue in 2015 [3.37]. In this case, steel bars were inserted in the intermediate and deep pavement layers to absorb the heat coming from the top and downward propagated. Different bars' dispositions were analyzed to compare the innovative structure to a traditional one from the thermal point of view. Some calculations were made to account the heat transmission: Figure 3.23 illustrates the theoretical scheme used for the simulations. The pavement structure was that already presented in the previous Figure 3.16. Figure 3.24 depicts an example of the heat flux distribution calculated for a given steel bar's configuration.

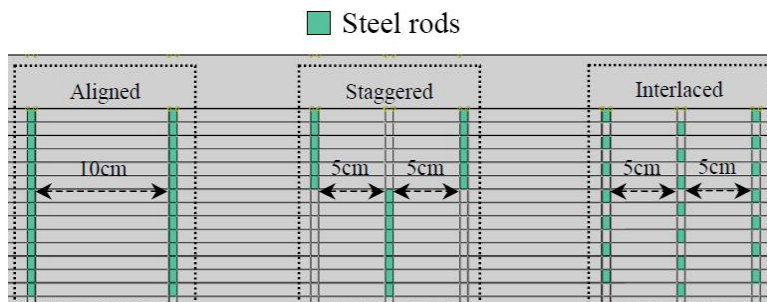


Figure 3.23. Scheme of the pavement equipped with the steel bars [3.37].

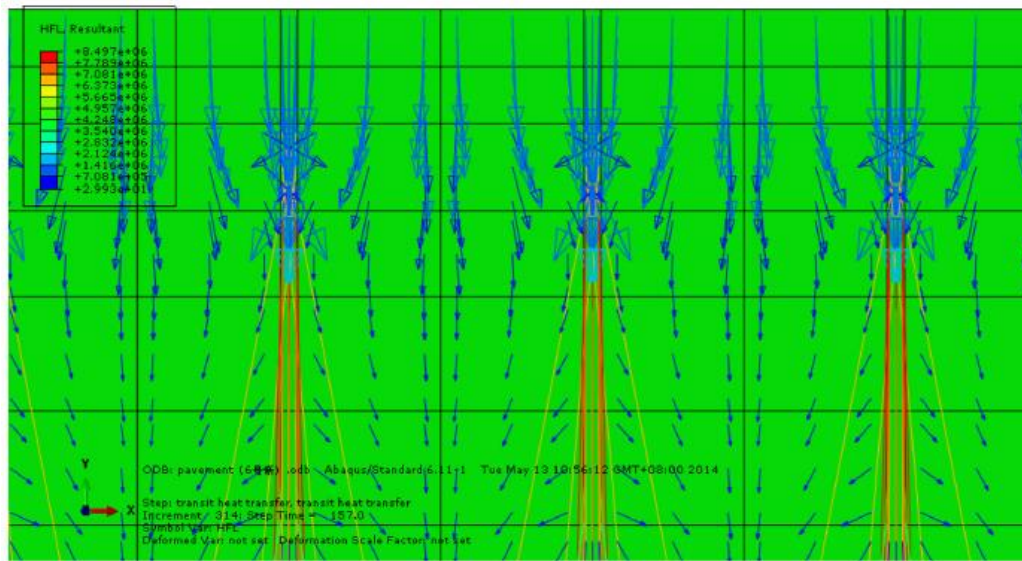


Figure 3.24. Simulation: heat flux distribution for a given steel bar's configuration [3.37].

The validation was conducted through thermal monitoring and rutting tests made in the laboratory on ad hoc realized samples (see Figure 3.25).

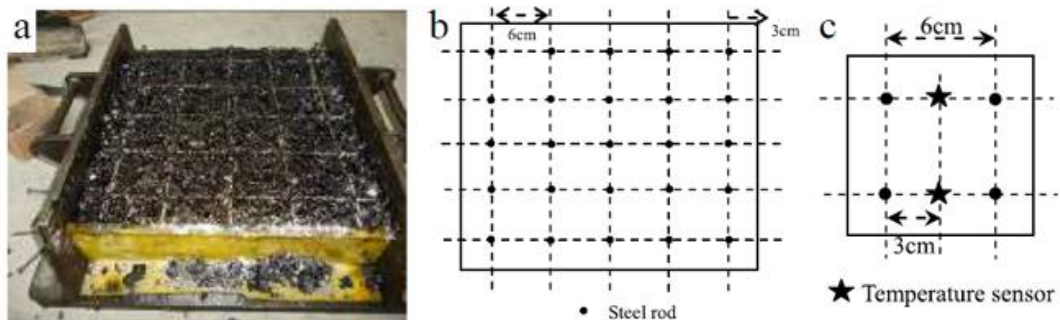


Figure 3.25. Laboratory samples produced to validate the numerical simulations [3.37].

Principal results demonstrate the ability of the structure to absorb the heat mainly during the day-time (a non-uniform distribution of the heat was detected). At a depth of 4 cm, horizontal and vertical heat fluxes interesting the steel bars resulted ten times greater than those affecting the asphalt concrete only. Therefore, the bar's presence seemed to ensure an appreciable reduction of the maximum temperature on pavement (at 4 cm from the surface, decreases up to 6.5 °C were found with respect to reference samples); in this sense they guaranteed a and noticeable prevention against such distresses realized in form of permanent strains (typical of the higher in-service temperatures). For instance, the following Figure 3.26 draws some rutting curves resulted from the experimental tests.

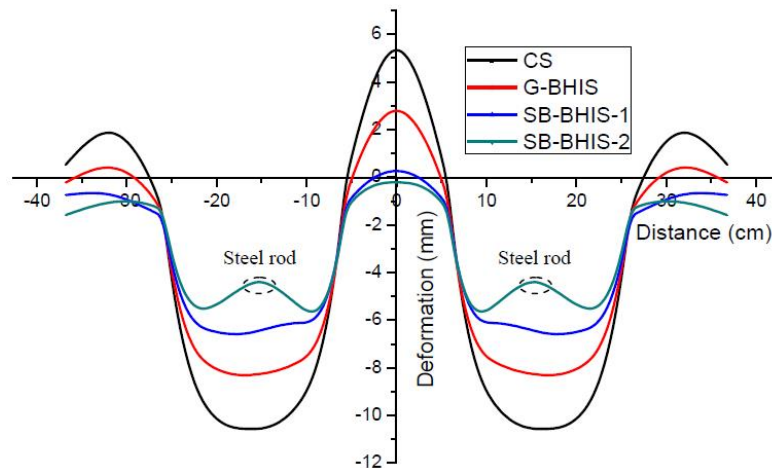


Figure 3.26. Rutting curves: conventional (CS), literature (G-BHIS) and designed (SB-BHIS-1,2) structures [3.37].

In general, further pavement applications could be designed in order to provide appreciable deicing or snow-melting effects to preserve a secure the driveway surfaces during the winter time. This could also avoid the conventional practices used for these purposes (spreading of chemical compounds or salts), relieving the pavements from the well-known distresses caused by such operations, with important gains in safety for pedestrians and vehicles [3.38].

As an example, pipe-based pavement structures could implement this principle though the circulation of a hot fluid under the surfaces [3.39].

More specifically, in 2001 Giuliani conducted an experimental investigation on the possible use of flexible pavements heated by the Joule effect to improve the winter road maintenance [3.40]. It considered that the avoiding of the conventional anti-icing operations could be even more beneficial in the case of high-performance asphalts (porous and sound absorbing surfaces) because of the high-void nature of such concretes. The physical principle which limited the constant formation of ice on the roads regarded the applications to the mixtures of heating resistive filaments. An experimental campaign was organized to measure the thermal gradients inside bituminous samples (dual-layer 50 x 50 cm specimens) equipped with this technology. Filaments were spaced with a pitch varying from 15 to 200 mm (installation depth of 30mm). Major results indicated that: i) filaments effectively heated the pavements, which resulted hooter with respect to a conventional case (without filaments); ii) thermal gradients were even programmable depending on the functioning of the filaments; iii) filaments could be powered with low (conservative) tensions; iv) the installation of filaments was as easy as that of a conventional pavement reinforcement; v) the structure was adapt to be remote controlled depending on the specific needs. The

following Figures 3.27 and 3.28 present a scheme of the instrumented sample and an example of the thermal distribution inside the asphalt concrete, respectively.

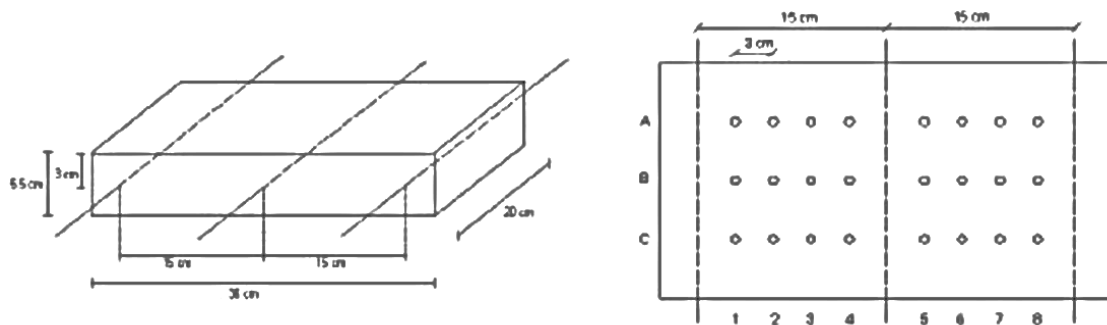


Figure 3.27. Schematic view of an instrumented laboratory sample [3.40].

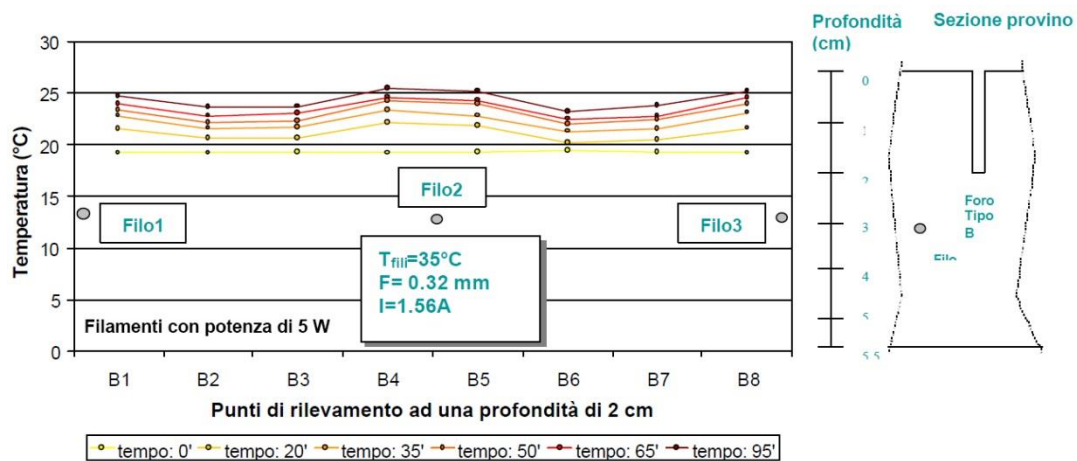


Figure 3.28. Example of thermal distribution inside a sample: filament's pitch of 150 mm [3.40].

Another interesting literature contribution concerning the effects of ice in road pavements was given by Khan et al. [3.41]. Thanks to the use of lightweight aggregates, they designed a road mixture able to limit the deterioration due to the winter freeze actions. The argillite was combined to traditional bitumen to produce hot mix asphalts; thermal properties of laboratory specimens such as the conductivity, the diffusivity and the specific heat were studied. A numerical model was also utilized to account the damage action of the ice. Depending on the mechanical properties of the mixtures and the vehicular loads, the lightweight aggregates effectively conferred to the mixtures a higher freezing resistance (they lowered their thermal conductivity, diffusivity and specific heat).

Chapter 4

Work Activity

4.1. Research objective

The present Chapter describes the core activity presented in the dissertation. As above-anticipated, the research aims at identifying the role of the road pavements with respect to the UHI phenomenon.

Throughout an extensive experimental plan (developed at various analysis scale in the laboratory and in the outside environment), a comprehensive review of different solutions for thermal-optimized road pavements was carried out to generate a wide database reporting the chromatic characteristics of the materials, their radiative properties and their thermal performance.

A further part of the study was aimed at verifying the solution's suitability from the mechanical point of view since, regardless the technology employed, adequate safety and functional standards must be always ensured. Also durability aspects was partially investigated.

Based on such concerns, a summary of the main objectives of the work is presented in the following list.

- Evaluation of the efficacy of the tested materials in mitigating the heat concentration.
- Assessment of mechanical performance of the selected materials.
- Identification of possible correlations between chromatic and radiative properties, as well as between materials characteristics and in-field thermal performance.
- Statement of possible guidelines useful to produce thermal-optimized pavements effectively able to limit the UHI phenomena.
- Definition of general mitigation strategies referred to roads and road networks.

4.2. Work approach

The work approach was divided into several steps. Firstly, the constituents of the selected materials for road pavements were characterized (mainly the binders). In this case, a chromatic evaluation was performed considering that the chromaticity of binders could early affect the final color of the mixture (i.e. the final material constituting the pavement surfaces). Then, a rheological characterization at binder-scale was done to predict the possible material's in-service performance, above all considering that some solutions supposed the replacement of the conventional bitumen for road pavements with synthetic transparent products (for the obtaining of clear wearing courses) or the coloring of the bitumen with particular pigments which directly acted on binder. Also mastic-scale (binders added with fillers < 0.063 mm) was rheologically investigated since such portion of the mixture is crucial for the adhesion phenomena, thus in developing the mechanical properties of mixtures. Furtherly, some tests were carried out on loose binder-aggregate blends in order to principally evaluate the affinity of the various constituents selected for the study. Once moved to mixture-scale, the principal activities were executed (the final materials composing pavements were tested). In this case, it was possible to produce samples to be tested in terms of color, radiative properties and thermal performance. Thermal findings were allowed thanks to an extended monitoring executed both on a controlled environment (within the laboratory) and in the outside environment (where the produced materials were subjected to the real environmental conditions due to sun and shadow, cloudiness, wind, humidity, etc.).

The post-elaboration of the collected results was functional to the identification of possible correlations between thermal properties and material's performance, as well as to evaluate their efficacy in mitigating the heat diffusion. The radiative balance was implemented under the environmental conditions recorded during the external monitoring and produced some

interesting finding about the thermal performance of the materials. Then, a numerical computation was organized in order to predict possible thermal responses of materials under different environmental condition. Various parameters of the general radiative balance were varied, including different cloudiness level (linked to the scattered radiations), wind and humidity perturbations, considering also several urban geometry in the proximity of the road pavements (this was computed through the sky portion free from obstacle). Final consideration were also done with respect to other aspects involved with the use of thermal-optimized road surfaces, mainly regarding the landscape-infrastructure integration, safety and illumination concerns and the human related-comfort involved by the various technologies.

All these findings were employed to pursue the final work objective, i.e. stating possible guidelines for thermal-optimized and environmentally-friendly road pavements.

In the following sections, all methods and assessment techniques utilized during the experimentation will be described. Specifically, the chromatic evaluation, the thermal assessment and the mechanical characterization will be presented giving indications about standards and tests performed on materials. Some details about laboratory and operational equipment will be also given for the sake of completeness.

4.3. Chromatic evaluation

The chromatic evaluation was aimed at the definition of the material colors through a scientific and objective system, repeatable on different samples (produced also through different techniques). Based on identical theoretical concepts, the proposed methods wanted to be suitable to characterize the color of both binders or mastics (binders and fillers) and mixture surfaces.

In the case of binders or mastics, assessment of color requested the production of specific round samples, poured in glass containers, with an adequate film thickness useful to prevent the transparency of the materials (requisite needed especially for clear binders). In the case of mixtures, surfaces did not request particular conditions (clean and regular faces were sufficient). In some instances, principally dealing with binders, chromatic evaluation procedure was performed also on materials preliminary subjected to standard aging procedure in the laboratory in order to determine the eventual effects of aging in the color of products.

Methods consisted in the acquisition of high-resolution photographs of samples and the elaboration of such images through a digital image processing approach. Specifically, specimens were placed in a confined chamber ad-hoc realized in order to achieve high quality images. This structure was composed by a rectangular box (100 cm long, 80 cm wide, 70 cm high) with white paper walls which allowed the transition of light generated by four sources (lamps) located near the box sides. The configuration prevented the acquisition of images affected by particular shades or reflections (eventually generated in the case of subjects illuminated by simple ambient lamps). Photographic acquisitions were made with a high-resolution camera from a circular hole on the upper “roof” of the box. Figure 4.1 presents the details of the chamber set up.

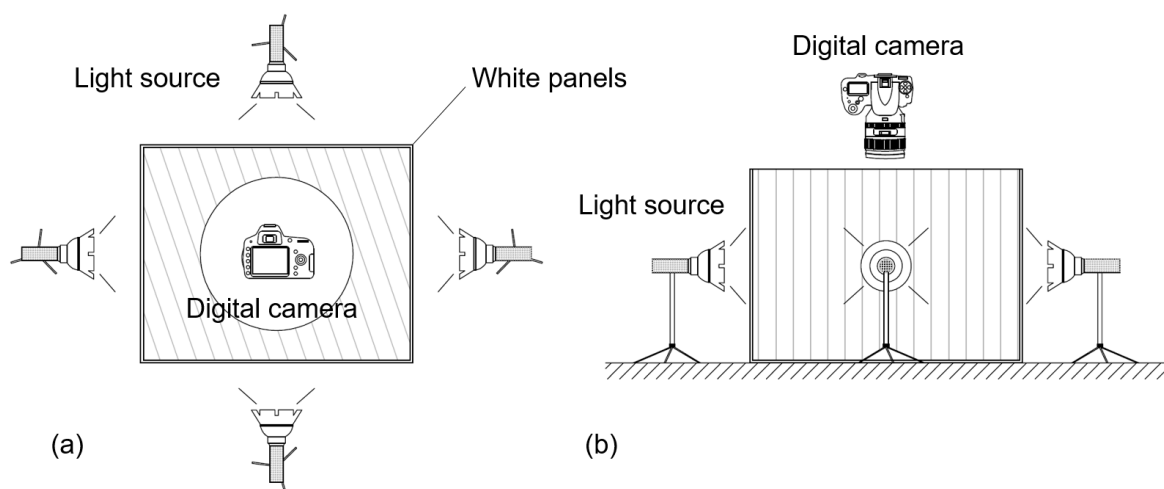


Figure 4.1. Acquisition chamber: top (a) and side (b) views.

In order to acquire images not affected by different exposures or light noises, some samples were photographed contemporary (in this way, comparison reliability was ensured).

Digital image processing was carried out with a back analysis of pictures through a commercial graphic software. The target was the definition of the RGB (Red-Green-Blue) code of the dominant color of samples. RGB color model (firstly introduced by the Commission Internationale de l'Éclairage in the 1931 [4.1]) is a common representation to display images in electronic/photographic systems that reproduces an array of colors from the three primary colors (red, green and blue). With the model, the single color could be represented by the numerical triad $R-G-B$ (digits range between 0–255 interval), where each number indicates the mean value of the Gauss distribution of each color. As a consequence, an image with limited chromatic variations could define localized Gauss curve distributions and provided a strict definition of the dominant RGB color (small standard deviations in Gauss curves indicated small variations of pixels' colors with respect to the dominant one). For this reason, the target of the picture acquisition was a high-resolution clean image, i.e. not influenced by reflections, shades or flaws in general. During the analysis of

binders/mastics, chamber environment avoided the insurance of light reflections (sources of noise and alteration of the real color), mostly detectable in the case of clear and colored samples. While assessing the dominant color of mixtures, supplementary attention was paid also in order to consider the natural roughness of surfaces (due to the nature of binder-aggregate systems) which could cause additional shadows or texturizing of the images. Here, further graphic filtering was adopted to effectively determine the dominant RGB. In this context, such operation, combined with the use of specific software able to account the filtered pixels, permitted the quantification of the covered/colored portions of the surfaces (significant parameter in the case of mixture colors given in forms of paints/varnishes). The following figures illustrates some operative steps performed during graphic back analysis: Figure 4.2 depicts an example of RGB dominant color determined on binder, whereas Figure 4.3 displays some passages for the calculation of the colored portion of the mix surface.

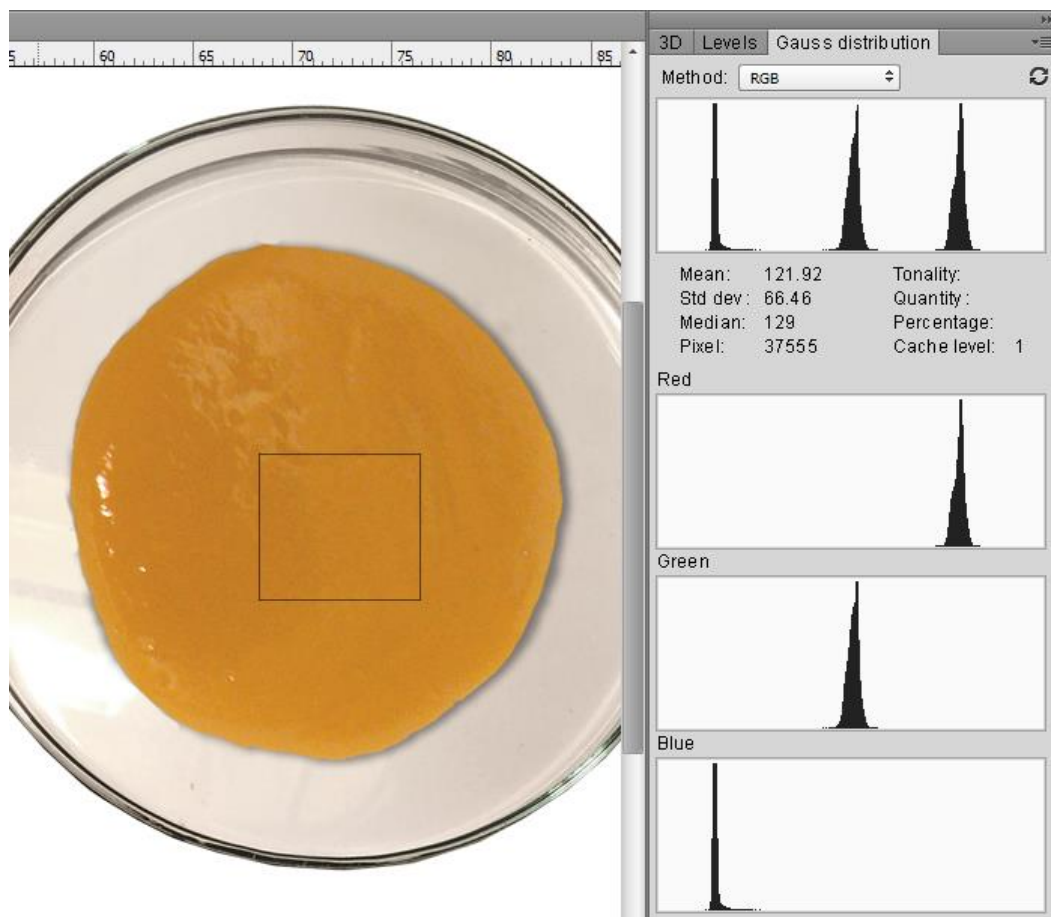


Figure 4.2. Color back analysis: determination of RGB dominant color of a binder sample.

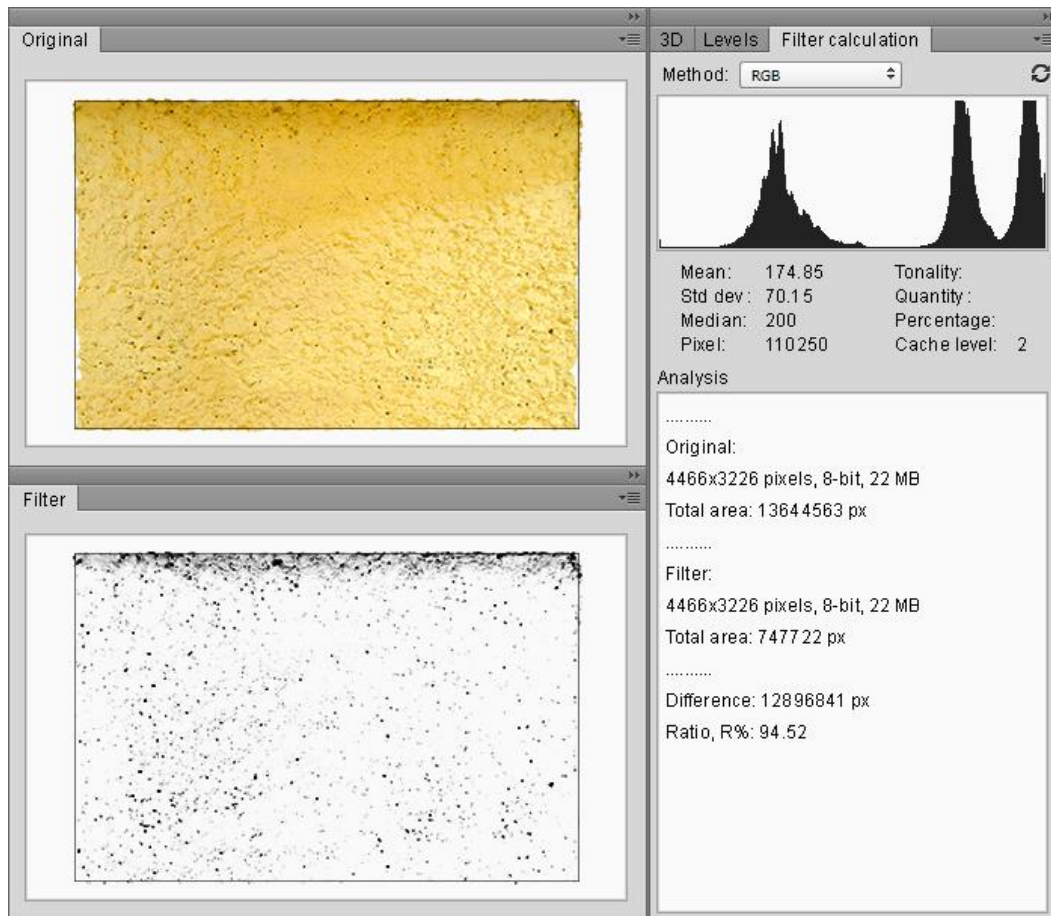


Figure 4.3. Color back analysis: calculation example of the colored portion (mix surfaces).

In a parallel way, since RGB defines a device-dependent color model (not strictly related to engineering quantities), further analysis that considered an objective psycho-physical representation (based on the human perception) was also proposed. In this perspective, it is known that color perception is related to the perceptive feedbacks of the optical system in relationship with electromagnetic light stimuli. Considering the eye composition with three retinal photoreceptor cones, three numerical functions are enough to the color definition with models. Figure 4.4 represents the physiological process happening inside the human eye which permits the conversion of light in brain stimuli.

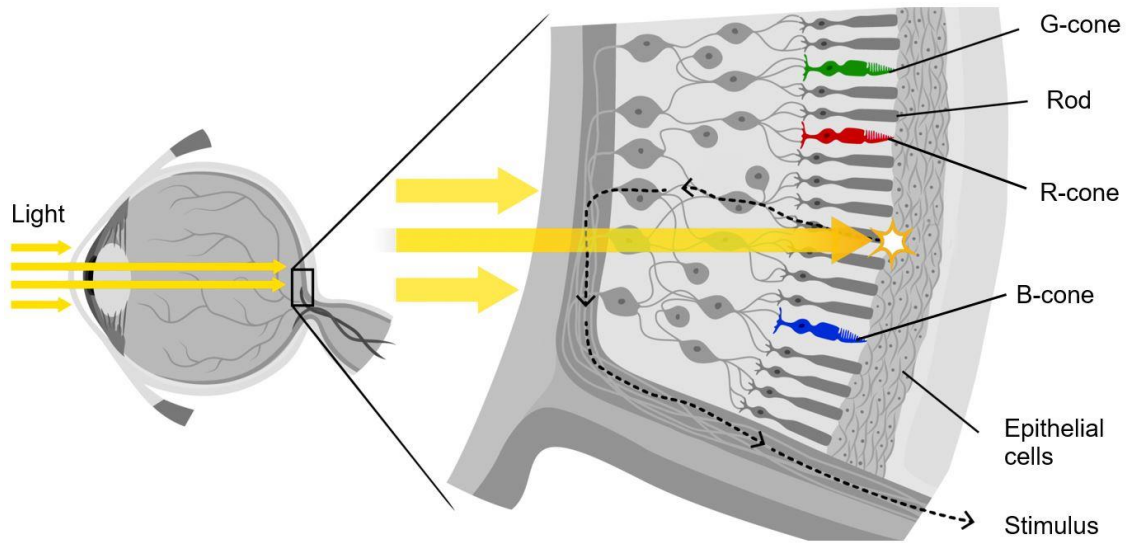


Figure 4.4. Human eye functioning: R-G-B receptor cones [4.2].

In this regard, one of the most spread models, the Hue-Saturation-Lightness (HSL) one, was employed [4.3, 4.4]. This representation uses the hue parameter (H), i.e. the color tonality (in the range of 0° – 360°), the saturation (S), which indicates the power of light emission (in percentage) and the lightness (L), which expresses the color brightness (in percentage). Thus, after the definition of samples' RGB codes, triads were converted in HSL coordinates. The procedure consisted in the following steps:

- i) calculation of non-dimensional red, green and blue values (in the range 0–1), dividing RGB digits by 255;
- ii) identification of maximum (max) and minimum (min) values among the normalized R - G - B triad;
- iii) conversion of obtained digits in H - S - L tern through the mathematical procedure hereafter reported (Equations 4.1–4.3.d).

$$L = 100 \cdot (max + min)/2 \quad (4.1)$$

$$S = 100 \cdot (max - min)/(max + min), \text{ if } L \leq 0.5 \quad (4.2.a)$$

$$S = 100 \cdot (max - min)/(2 - max - min), \text{ if } L > 0.5 \quad (4.2.b)$$

$$H = 0, \text{ if } S = 0 \quad (4.3.a)$$

$$H = 60 \cdot (G - B)/(max - min), \text{ if } max = R \quad (4.3.b)$$

$$H = 60 \cdot [2 + (B - R)/(max - min)], \text{ if } max = G \quad (4.3.c)$$

$$H = 60 \cdot [4 + (R - G)/(max - min)], \text{ if } max = B \quad (4.3.d)$$

For the sake of clearness, Figure 4.5 illustrates the RGB and HSL model's interpretation in a tridimensional space.

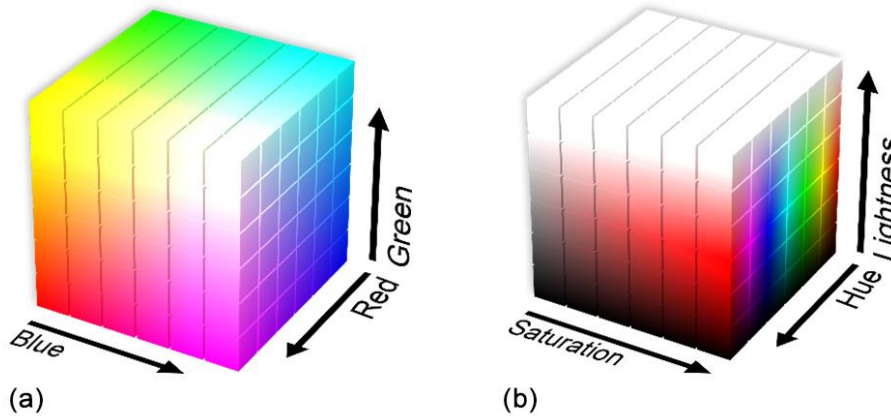


Figure 4.5. RGB and HSL models represented in a tridimensional space.

Once defined HSL codifications, comparison between different materials' colors were executed on the basis of such objective parameters (as an example, evolution of lightness L could be intended as an index of the possible darkening effect due to the aging processes interesting binders).

Overall, comparisons of chromatic findings collected on binders, mastics (binders and fillers) and mixtures allowed to investigate the existence of possible correlation at different scale.

4.4. Thermal assessment

The assessment of thermal performance mainly concerned the study of thermic responses of mixtures. In particular, basing on the theory explained in Chapter 2, radiative properties of mixes were firstly determined. Then, laboratory and outside experimentations were planned with the target to monitor the temperatures reached by the different materials exposed to radiations (artificial or sun light). The following paragraphs gives information also about the utilized equipment and methods.

4.4.1. Preliminary considerations

Before the description of laboratory and outside activities, some preliminary considerations are made.

The major part of the thermal analysis was performed with the use of a thermographic camera, i.e. a specific device which renders the infrared radiations as visible light and allows to record the heat distribution on objects. The heat is quantified as the sum of punctual temperatures among the subjects and is visualized through different colors after the digitalization of the collected images.

Examining the framing of real objects such as the mixtures, the local radiation emitted for a fixed incident rate of heat flow can be supposed function of the punctual temperature and the punctual emissivity ε of the body (see Equation 2.43). Indeed, it must be remembered that the mean emissivity of pavement materials could be considered as an intrinsic property of the same material [2.15]. Thus, a specific radiation recorded by the thermographic instrument could be transformed in a temperature reading only through the imposition of the emissivity values of the different subjects. For this reason, ε was assumed as a calibration parameter for the equipment. Therefore, a preliminary procedure was scheduled in order to measure the mixtures' emissivities that must be fixed as input setting before the thermal monitoring. This was accomplished using a portable infrared thermometer. Mixtures were equipped with a tape strip of known emissivity ($\varepsilon = 0.95$) and were subjected to a constant radiation source for a period of 5 hours (sufficient to suppose the reaching of the thermal equilibrium of the system). Then, the temperature of the strip was recorded and annotated through the portable infrared thermometer (set with the known emissivity). Subsequently, the target point of the thermometer was moved on the mixture surface and the emissivity setting was varied until the registered temperature coincided with those previously annotated (referred to the tape). In this way, the method furnished an indirect value of the material emissivity (some phases of procedure are depicted in Figure 4.6).

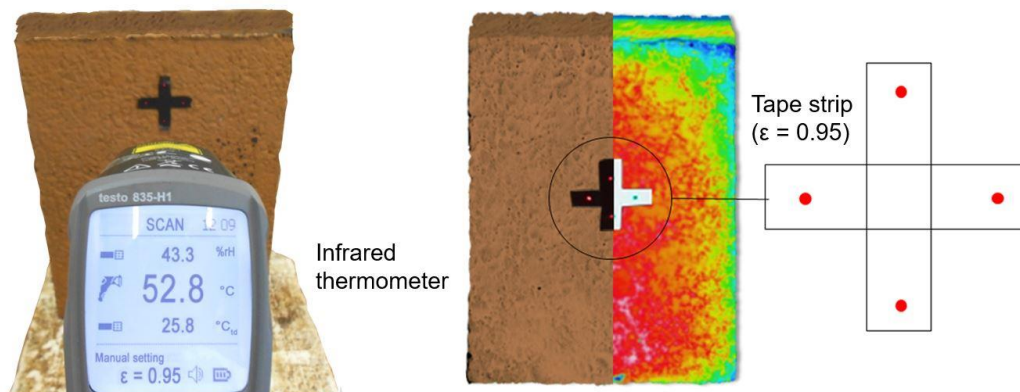


Figure 4.6. Determination of material emissivity: preliminary calibration phases.

Dealing with others radiative properties, also albedo ρ was calculated with an indirect procedure executed independently from the core of monitoring activity. In this case, mixtures were photographed with a high-resolution camera while a reference material with known albedo (a white rough paper sheet with ρ equal to 0.65) was laid on a part of the surface. A digital image processing was then performed in order to determine the lightness

(L) value of the mix surface. Once L was found, this was correlated with L of the paper (equal to 100, i.e. the white color) and, based on the following Equation 4.4, ρ of mixture was calculated.

$$\frac{\rho_x}{\rho_{ref}} = \frac{L_x}{L_{ref}} \quad (4.4)$$

where x -subscript indicates the unknown variables and ref -one those of the with paper sheet. The calculation of the albedo was based on the assumption that the albedos of the studied materials and the reference white sheet were proportional to the corresponding lightness, assuming a correlation between the reflected part of radiation and the visible wavelengths reflected by the bodies. Despite such assumption, method was verified to produce albedo results very close to those reported in literature for different materials [2.17, 4.5]. Figure 4.7 shows some steps of the image processing carried out to calculate the albedo values.

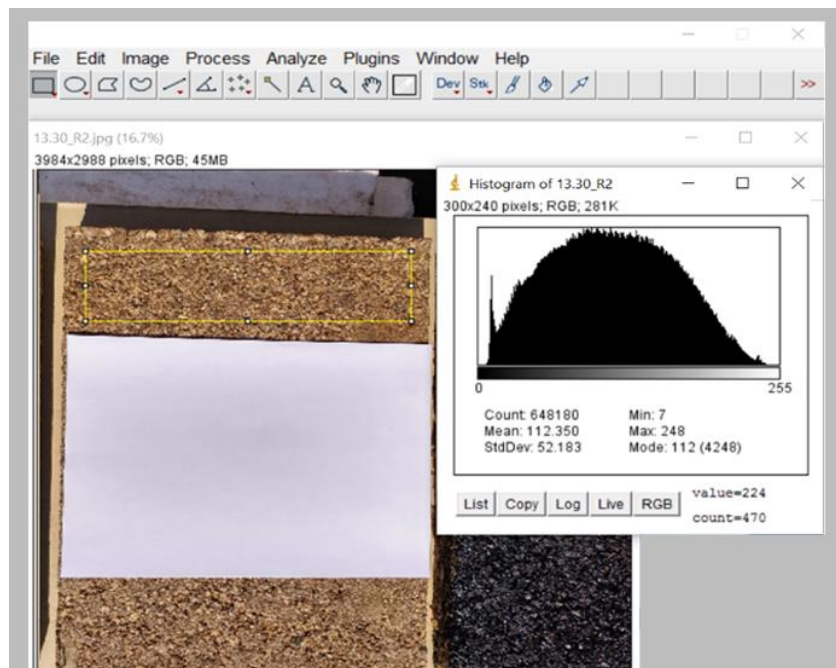


Figure 4.7. Determination of material albedo: image processing phases.

Other considerations about thermal conductivity k could be inserted to fully describe the thermic properties of the studied materials: otherwise, given the operational procedure involved (the use of thermography), such treatment is postponed to the next paragraphs, where all thermographic surveys are deeply explained.

4.4.2. Laboratory activity

The objective of the laboratory activity concerned the organization of an extended thermographic survey to monitor the heat transfer mechanisms on produced mixtures. Thus,

an isolated test environment was constructed to subject the studied materials to an artificial light able to simulate the outside exposure to the solar radiation. In this manner, testing operations could be performed also during winter when, because of the weather and the cold season, an outer experimentation should be less significant. Therefore, an artificial lamp was employed. Halogen light was chosen in view of the emission spectrum of such light typology (Figure 4.8 depicts spectrums of different light types in comparison to the typical emission shape of the natural sunlight [4.6]). Basing on such illustration, halogen source seemed to constitute the most suitable solution to obtain a round, high-intensity curve (even the lack of intensity at certain wavelengths near the UV region). Technical specifications of utilized light source are following presented (see Table 4.1).

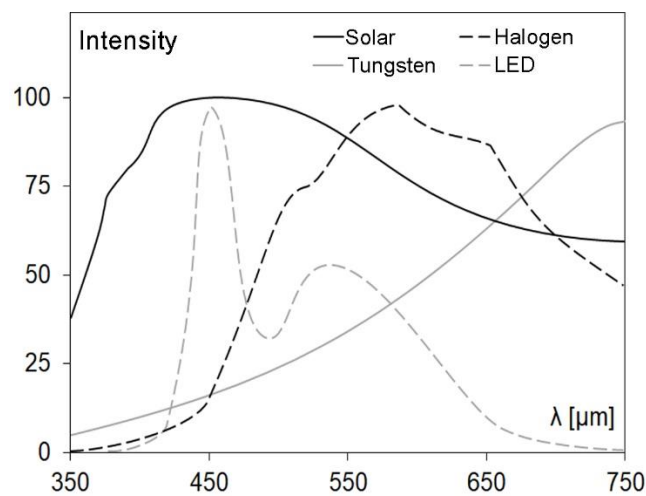


Figure 4.8. Typical emission spectra of artificial lamps.

Table 4.1. Technical specifications of utilized halogen lamp.

Property	Unit	Quantity
Nominal power	Watt	400
Luminance	Lumen	35 000
Diffusion angle	°	180
Color type	-	Graphite
Color temperature	° K	4 500

The test environment consisted in a huge box (200 cm long, 150 cm wide, 150 cm high) equipped with the above-mentioned lamp in the rear panel. Mixtures were laid on specific polystyrene supports placed on the box floor which owned insulation functions (they avoided the heat exchange by convection with the substructure). The top and the front sides of the box were left free of obstacles to permit the operational movements and the thermographic monitoring, respectively. Geometry of test configuration was set fixing a distance between the acquisition and the subject equal about to 1.5 m and a lamp-subject separation of 50 cm. Figure 4.9 summarizes the test environment.

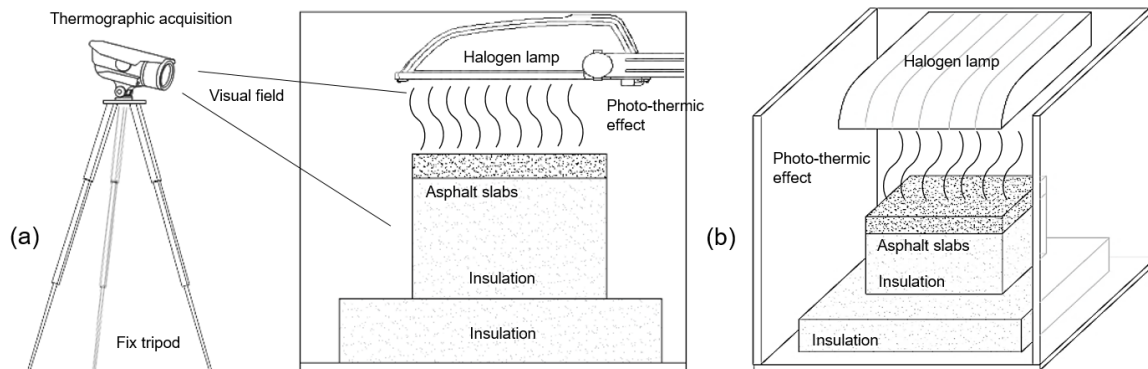


Figure 4.9. Experimental equipment and set up: side (a) and front (b) views.

Thermography activities were organized in different stages: first, a monitoring was planned to record the temperature distribution on mixtures (within the exposed surface and along the thickness) and its evolution on time. In particular, measurements were carried out for a fixed duration of 8.5 hours: at time 0, lamp was turned on and light exposure lasted for 5.5 hours; after that, light was switched off and temperature was still recorded for 3 hours to construct the cooling trend (simulation of the effects on pavement occurring when solar exposure stops, e.g. at the sunset). Acquisition apparatus was calibrated setting the emissivity of mixtures (determined according to the above-described procedure) and inserting some environmental parameters to enhance the accuracy (local ambient temperature, relative humidity of the laboratory, distance of the subject and of the frame background). Elaboration of collected data was made every 15 minutes through a specific software, applying the following analysis tools: a rectangular box (hereafter coded *Box.A*) positioned on the central part of the mixture surface (area was distanced from edges in order to limit the border effect); a straight line (hereafter named *Line.A*) along the thickness of the mix (in the center portion) to measure the distribution of temperature on depth. Each tool returned the punctual values of temperature (T) (pixel by pixel) and information such as the average, the minimum and the maximum T on the tool pertinence. Described configuration is illustrated in Figure 4.10, whereas Figure 4.11 presents some images of the activities.

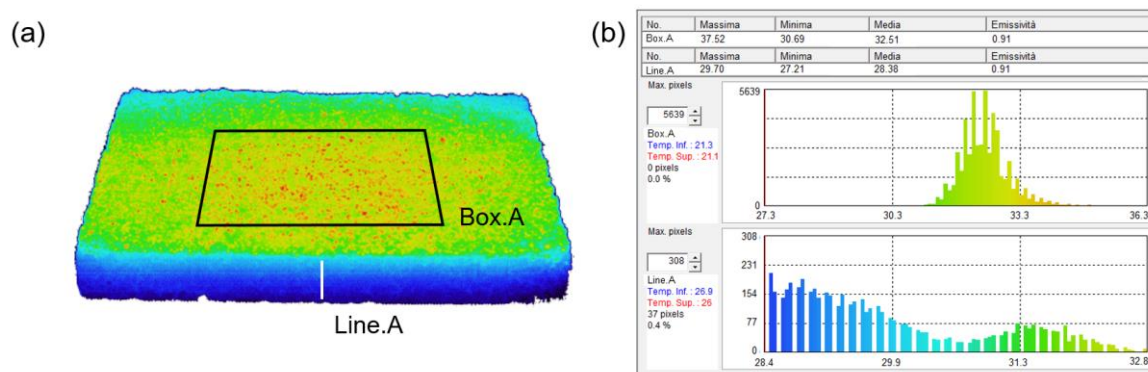


Figure 4.10. Analysis tools implemented in elaboration software (a); example of recordings (b).

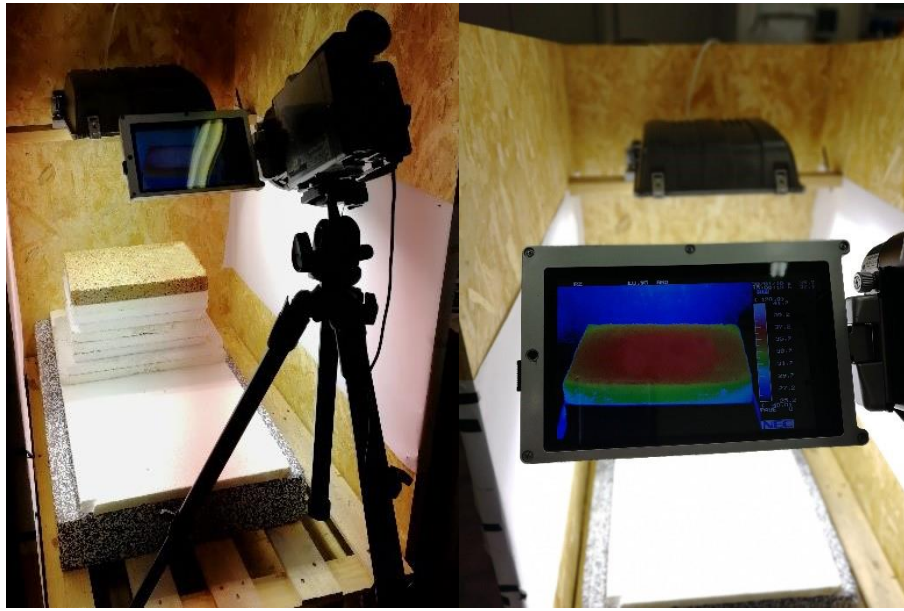


Figure 4.11. Images of monitoring activities performed in the laboratory.

Basing on the acquired results, different elaborations could be proposed. Evidently, evolution of punctual temperatures could be plotted as a function of the time to construct the heating and the cooling processes of mixes. Indeed, comparison between distinct materials could suppose an initial transposition, referring all readings to those recorded for reference mixture (i.e. black conventional asphalt concrete) to obtain effective differences in materials' responses (temperature gradients, heating and cooling speed, etc.). Additional mathematical operations could be carried out to average the data of different monitoring days get on the same mixtures (measurement reproducibility), even if the controlled environment of the laboratory minimized such fluctuations. Then, using data achieved from *Line.A*, further information could be collected in terms of material thermal conductivity (k). This was calculated, based on Equation 2.42, utilizing an indirect method; a reference material with known conductivity (a white marble slab) monitored with the same procedure allowed the calculation of different k values starting from the Equation 4.5:

$$k^i \cdot \frac{T_{surf}^i - T_d^i}{d^i} = k^{ref} \cdot \frac{T_{surf}^{ref} - T_d^{ref}}{d^{ref}} \quad (4.5)$$

where, T_{surf} and T_d were the temperatures at the surface (upper extremity of *Line.A*) and at depth d , respectively, *ref*-superscript indicated the reference material and *i*-superscript expressed the investigated one (k^{ref} was set equal to 2.35 W/(m·K) [4.7]). For the reverse formula, k^i was finally found with Equation 4.6.

$$k^i = k^{ref} \cdot \frac{T_{surf}^{ref} - T_d^{ref}}{T_{surf}^i - T_d^i} \cdot \frac{d^i}{d^{ref}} \quad (4.6)$$

The second stage of the laboratory activity aimed at the deeper evaluation of the heat release mechanisms from the mixture's surface after the suspension of the exposure to radiation. An ad-hoc experimental set up was used; a wide vertical panel (of white color) was installed to provide a clear high-contrast background for the thermal camera measurements, making appreciable the isotherms released from the materials (temperature observations concerning heat holes generated against the background). Thus, the spatial distribution of the air temperature above the mix surface was measured over time, from 0 to 30 minutes after the lamp switch off (sampled every 30 seconds). Assuming limited edge effects in the central alignment of the surface, such measurements of temperature were specifically referred to a centered vertical line (hereafter named *Line.B*) extended from 0 (the mix surface) up to 40 cm. Figure 4.12 and 4.13 give some details of experimental set up and results obtained, respectively.

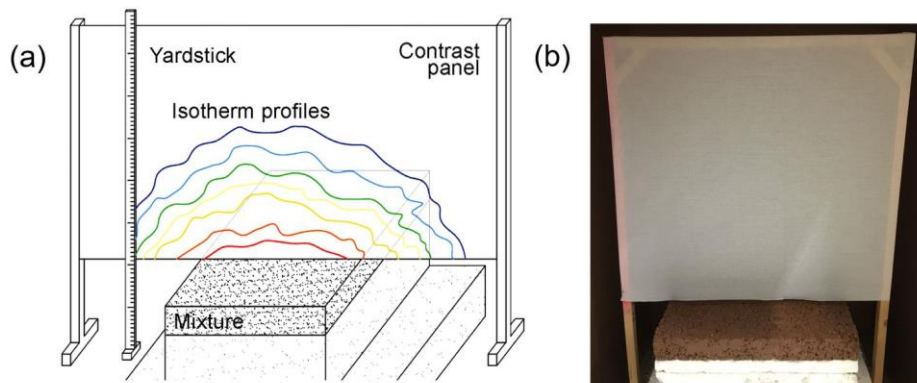


Figure 4.12. Set up for heat release study: schematic representation (a) and image (b).

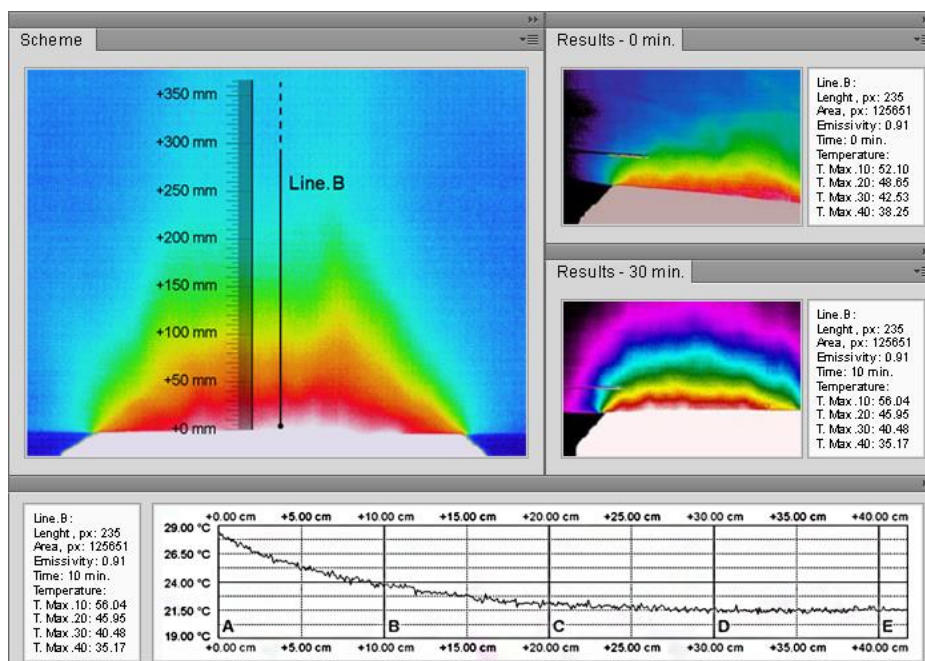


Figure 4.13. Example of output images and data.

4.4.3. In-field experimentation

In-field experimentation was planned to replicate a part of the protocol performed in the laboratory. It was organized during spring and summer good-wheatear days in order to directly expose the mixtures to the solar radiation. Prepared mixes were placed in a wide free area and were monitored with the thermographic camera. Once again, surveys took 8.5 hours, 5.5 of which with direct sunlight and 3 with mixtures moved to a shaded area (the construction of temperature evolution on space and time was carried out with a sampling rate of 15 minutes). Thus, experimental set up was very similar to that previously described (Figure 4.14), even if some precautions were adopted (at least during the hottest days) in order to protect the acquisition device from excessive heat and glares and acquire accurate data (a protective structure was used – see Figure 4.14.a). Otherwise, given the complexity of the working environment, additional efforts with respect to the in-side activity were spent to account all variables which affected heat readings. In particular, meteorological data such as evolution of air temperature, ambient humidity, wind direction and speed were recorded for each monitoring day. It was impossible to numerically quantify the condition of the sky; therefore, the OKTA scale [4.8] (i.e. a descriptive index of the cloud cover) was used to categorized the sky status which significantly influences the scattered part of the solar radiation, thus the rate of heat flow effectively incident on mixtures. Figure 4.15 illustrates all the scale categories and gives some examples of sky cloudiness. In this regard, it must be specified that the conformation of the testing area (a free space) avoided the possible influence of surrounding buildings or structures (the SVF was considered equal to 1).

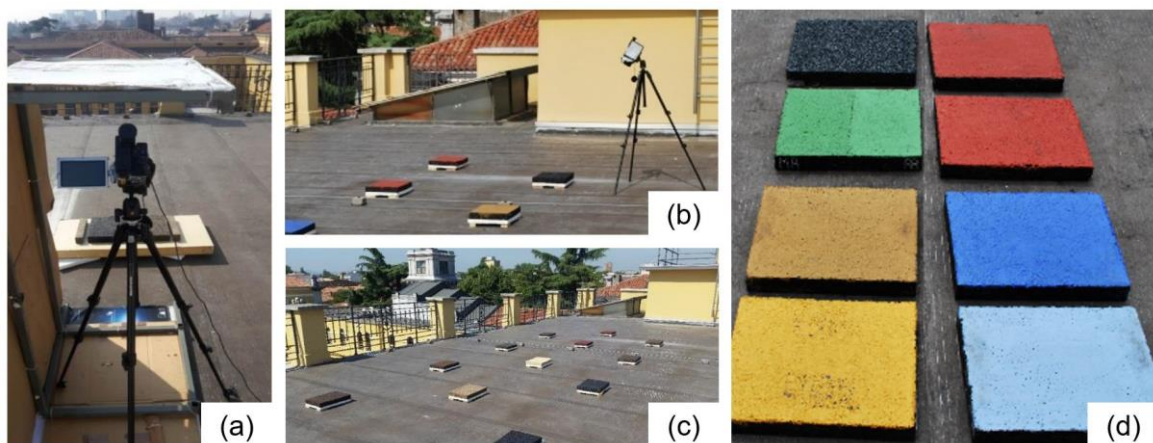


Figure 4.14. Outside set up: acquisition phases (a, b); images of materials tested (c, d).

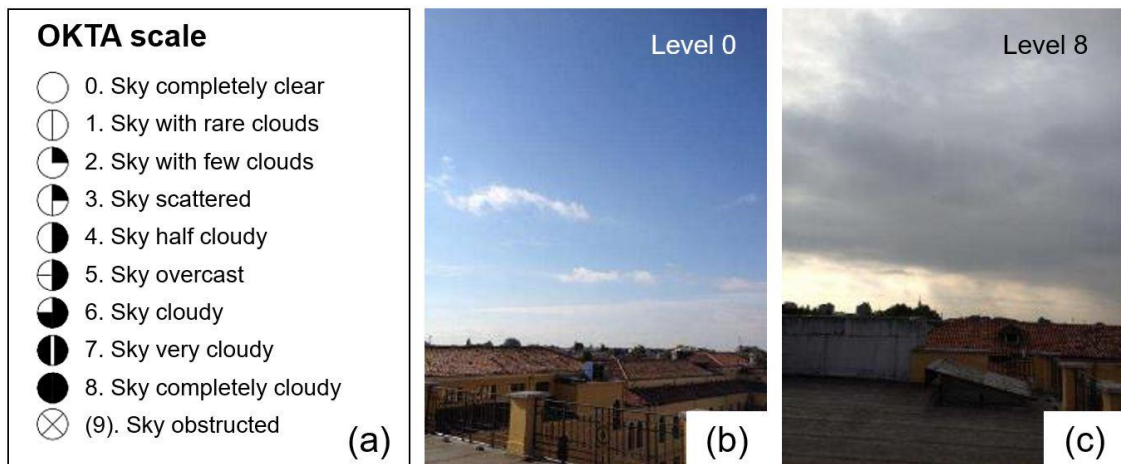


Figure 4.15. OKTA scale: levels and standard symbols (a); example of cloud cover levels (b, c).

Please, note that such environmental parameters were taken into account during the comparison of thermal responses of different materials. Moreover, with the objective to standardize the thermal data, various mixtures were monitored contemporary in the same day (in this way, environmental condition were supposed to affect all materials in the same manner): repeated monitoring on following days gave different thermic readings on the same materials and furnished several test replicates (averaging was performed considering also external/ambient conditions). Also fluctuations of such conditions along the recording periods were taken into account. In general, these parameters were also useful to the further modeling of the mechanisms of heat transfers within the mixtures (based on the theory previously explained in paragraph 2.2.2). In analogy with that executed in the laboratory, elaborations of temperature results were executed considering outputs of *Box.A* and *Line.A* (see Figure 4.10). Oppositely, heat release dynamic was not analyzed because readings of air isotherms released from surfaces resulted scarcely visible and jammed in view of the high outside temperatures.

4.5. Mechanical Characterization

The paragraph describes all methods utilized to assess the mechanical performance of studied materials. Using a multi-scale approach, procedures used to analyze the characteristics and the rheological properties of binders and mastics are firstly presented. Then, some tests on bitumen-aggregate blends are detailed. Finally, tests adopted to determine the performance of mixtures are illustrated.

4.5.1. Multi-scale approach

The principal distresses that interest road pavements contemporary concern low-temperature and fatigue cracking and rutting in the light of the wide temperature range which in-service materials are subjected to. In general, asphalt concretes could be

schematized as granular materials stabilized by the binders, whose behavior is affected by the structures and the working mechanisms of each component. Then, overall characteristics of final products are also function of the whole systems' properties due the interactions developed between such components. Moreover, distress phenomena are governed by bitumen properties (consistency, content, etc.) and aggregate characteristics (size, shape, gradation, etc.), as long as by the properties of the binder-aggregate interface and the final density and void content which regulate the propagation of cracks. For this reason, a multi-scale approach is generally needed to exhaustively describe the global performance of studied materials [4.9, 4.10]. Thus, work plan consisted in the study of material behaviors as consequence of mechanisms developed at different length scales: therefore, a rheological assessment of binder or mastic properties, responses of binder-aggregate blends and performance of final mixtures were subsequently analyzed. Table 4.2 schematizes the multi-scale approach adopted.

Table 4.2. Scheme of adopted multi-scale approach.

Scale dimension	Analysis scale	Composition
Small	Binder	Binder
	Mastic	Binder + filler
Medium	Blend	Binder + aggregate (loose)
Large	Mixture	Binder + filler + aggregate (compacted)

4.5.2. Rheological characterization

Rheological performance of studied binders/mastics were assessed through the use of the Dynamic Shear Rheometer (DSR). Indeed, when fillers were added to binders, no significant difference in experimental protocol had to be supposed (procedures following described should be considered valid both for binders and mastics).

Preliminary empirical tests were executed to firstly identify the basic characteristics of materials. For the sake of brevity, such tests are only listed: density (EN 15326), penetration (EN 1426), softening point (EN 1427), ductility (ASTM D-113), elastic recovery (EN 13398), Fraass breaking point (EN 12593).

On the basis of reference standards, DSR tests were carried out on unaged, short-term aged, or long-term aged samples in order to replicate in the laboratory the worst conditions for the specific trials (e.g. fatigue, a phenomenon typical of end-of-life materials, was investigated on long-term aged specimens representative of materials after several years of exercise; rutting potential was investigated on short-term aged samples, representative of fresh-paved materials, since permanent deformation are common on new-laid pavements). Standardized laboratory procedures for ageing were adopted: Rolling-Thin-Film-Oven (RTFO) tests (EN 12607-1) were used to obtain short-term aged binders, Pressure-Ageing-Vessel (PAV) tests (EN 14769) to prepare the long-term aged ones. In the case of mastics, binders were

previously aged and then blended with fillers. Filler were also characterized in terms of basic properties: particle density (EN 1097-7), plasticity index (CEN ISO/TS 17892-12), rigden voids (EN1097-4) and delta ring&ball temperature (EN 13179-1) were determined along with their morphological compositions.

Sampling and DSR set up were done according to standard EN 14770. Cylindrical samples of 8 or 25-mm diameter were poured in special silicon moulds and were tested utilizing parallel-plate geometries with corresponding diameter dimensions (8.00 mm or 25.00 mm) depending on the test temperature. Measurement gaps were set equal to 2.00 mm when using 8-mm plate or 1.00 mm when adopting the 25-mm one. Some tests also needed the use of a cone-plate geometry (diameter of 50.00 mm – inclination angle of 1° – used with a gap of 0.101 mm). Temperature of samples was managed pre-heating the chosen geometry according to specifications; then, it was set equal to the test temperature (assuring at least 15 minutes of conditioning period for each temperature setting in order to guarantee homogeneous thermal distribution within materials during tests).

4.5.2.1. Viscosity

Dynamic viscosity η was evaluated only on binders through the DSR. Dynamic viscosity (DV) tests were executed on unaged samples since viscosity is important during the mixing phases of mixtures, when virgin (unaged) materials are used. According to EN 13702, the cone-plate geometry was utilized; viscosity η was calculated based on the applied rotational shear rate $\dot{\gamma}$ and the shear stress τ according to Equations 4.7 and 4.8. Based on standard prescriptions, constant $\dot{\gamma}$ were fixed at different temperatures T ; in particular, $\dot{\gamma} = 0.05 \text{ s}^{-1}$ at $T = 60 \text{ }^\circ\text{C}$, $\dot{\gamma} = 50 \text{ s}^{-1}$ at $T = 100 \text{ }^\circ\text{C}$ and $\dot{\gamma} = 500 \text{ s}^{-1}$ at $T = 150 \text{ }^\circ\text{C}$. Binder's viscosity was plotted as a function of time (test duration was set equal to 300 seconds to check eventual η changes). In some cases, further combinations of $\dot{\gamma}$ and temperature were assessed with the objective to construct the flow curves (τ vs. $\dot{\gamma}$) which estimate the rheological behavior of materials. Following Figure 4.16 exemplifies possible flow curve trends.

$$\eta = \tau / \dot{\gamma} \quad (4.7)$$

$$\tau = A \cdot M_d \quad (4.8)$$

where, A is a factor function of the test geometry (expressed in m^{-3}) and M_d is the recorded torque (in $\text{N}\cdot\text{m}$).

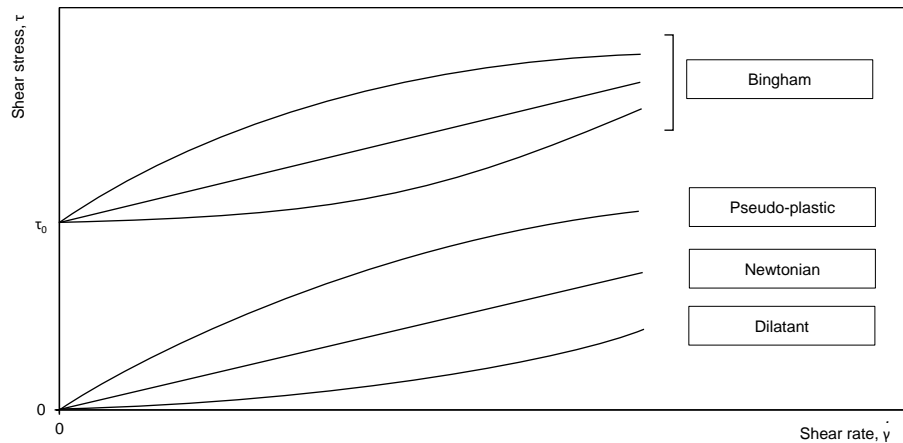


Figure 4.16. Flow curves (τ vs. $\dot{\gamma}$): examples of possible rheological behaviors.

4.5.2.2. Stiffness characteristics

Stiffness characteristics were investigated testing samples subjected to different ageing procedures (generally, suitable information are achieved mainly in the case long-term aging, thus the worst conditions for mid-temperature resistance to cracking). The evaluation of stiffness was carried out on successive steps, both on binders and mastics. Preliminary trials aimed at determining the Linear Visco-Elastic (LVE) limits of materials that must be taken into account to test samples and perform data elaborations further proposed [4.11]. These were investigated through Amplitude Sweep (AS) tests, i.e. oscillatory loads applied at constant frequency while strain was progressively increased. Specifically, an angular frequency ω of 10 rad/s (equal to 1.59 Hz) was fixed; deformation γ was given with a logarithmic increase, from 0.01 to 100% (see Figure 4.17.a). Temperature was chosen case-by-case within the desired range of study, mainly recording the evolution of G^* on time t (i.e. the shear stiffness modulus indicating the overall resistance to deformations, expressed as the ratio of the shear stress τ to the strain γ). Alternatively, evolution of γ vs. τ could be evaluated to construct isochronal plots useful to depicts the effectively liner part of the strain domain, i.e. the LVE region. Indeed, the general method used to identify the limit value of LVE domain suggests the verification of a 95% reduction of the initial complex modulus G^* (LVE limit equal to the deformation at such value of stiffness) [4.12, 4.13]. Further considerations about stiffness could be early proposed also investigating the temperature dependency of binders/mastics. This was accomplished performing oscillatory temperature sweep (TS) tests which furnished plots of storage modulus G' (elastic part) and loss modulus G'' (viscous part) as functions of the temperature. The latter was linearly increased among the entire range of investigation (with a rate of 2 °C every 2 minutes). Once again, a constant frequency was requested (ω was chosen equal to 10 rad/s for the sake of coherence). Strains

were maintained constant, within the LVE limits previously identified. Figure 4.17.b depicts the thermal load evolution applied during TS tests.

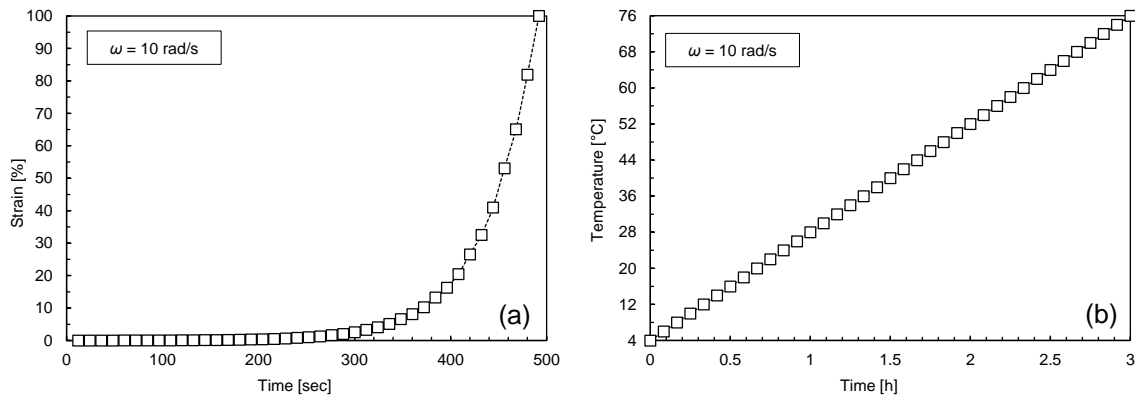


Figure 4.17. Stiffness investigation: applied loads for AS (γ vs. t) (a) and TS (T vs. t) (b) tests.

Frequency sweep (FS) tests were then carried out in strain-controlled mode, applying oscillatory loads within LVE regions between 100 and 0.1 rad/s (ramp log decrease with 10 points/decade slope). The same sample (binder or mastic) was tested repeating the described loadings at different temperature (properly in the range between 4 and 76 °C, at intervals of 6 °C). 8 and 25-mm diameter parallel-plates were utilized for tests between 4 °C and 34 °C and between 34 and 76 °C, respectively. FS tests were used for the generation of the master curves of the materials: arranging the modest temperatures and frequencies effectively tested, the general rheological behavior was predicted in wider domains (facing the operative laboratory constrains about the duration of the low-frequency analysis and the impossibility to supply too high frequencies). This elaboration is generally possible thanks to the Time-Temperature Superposition Principle (TTSP), valid for thermos-rheological simple materials as traditional bituminous binders. TTSP is reported to be valid when relaxation mechanisms and stress magnitudes at all time own the same temperature dependences [4.14]. In this case, a single smooth master curve can be obtained by shifting the experimental data series with horizontal shift factors a_T related to frequency (or time) and vertical shift factors b_T proportional to the material density [4.15]. The final purpose concerned the presentation of the master curves both for complex modulus G^* and phase angle δ (i.e. the visco-elastic balance of material behavior). Indeed, a prediction of TTSP validity was done firstly analyzing the experimental results themselves. In this perspective, Black spaces of materials (i.e. δ vs. G^*) were constructed and the presence of a single aligned curve shape (composed by the data series referred to different T) was verified. When possible (i.e. when TTSP was verified), shifting of different temperature series (T_i) was executed towards a unique reference temperature T_0 (generally fixed at 34 °C) using the reduced angular frequency ω_r according to Equation 4.9.

$$\omega_r(T_0) = a_T \cdot \omega_i(T_i) \quad (4.9)$$

When bitumens are studied, horizontal a_T could be sufficient to describe the material properties. These shift factors could be generally fitted through the Williams-Landel-Ferry (WLF) formulation [4.16] (Equation 4.10):

$$\log a_T = -\frac{C_1 \cdot (T_i - T_0)}{C_2 + (T_i - T_0)} \quad (4.10)$$

where C_1 and C_2 represent empirical constants related to the free volume and its thermal expansion coefficient. Despite the specific elaboration used for bituminous materials, vertical shifting is also possible. It could be realized with b_T vertical factors, implying the following Equation 4.11:

$$T_0 \cdot \rho_0 = b_T \cdot T_i \cdot \rho_i \quad (4.11)$$

whit ρ_i expressing the punctual material density and ρ_0 the density at the reference temperature T_0 . Regardless the shifting procedures, other information could be also collected only basing of experimental data: thus Cole-Cole representations (i.e. linear-scale evolution of the shear loss modulus G'' with the shear storage modulus G') were used to check the ideal Maxwell behavior of the materials (a Maxwell fluid should exhibit a Cole-Cole plot showing a semicircular shape [4.17.]). Finally, whit the objective to extend stiffness concerns, an overall prediction of general response of materials (in all the temperature and frequency ranges) was tried through the modeling of G^* and δ parameters. Literature-based models were used: specific formulations are reported in following Equations 4.12–4.15.

$$G^* = G_e^* + \frac{G_g^* - G_e^*}{[1 + (f_c - f')^k]^{m_e/k}} \quad (4.12)$$

where G_e^* represents the equilibrium complex modulus (equal to 0 in the case binders), G_g^* is the glassy complex modulus (generally equal to 10^9 Pa for conventional bitumens), f' is the generic experimental frequency, f_c is the crossover frequency, k and m_e are dimensionless shape parameters. Figure 4.18 gives a representation of the typical s-shaped curve of G^* obtained through such model; in particular G_g^* and G_e^* represent the upper and lower asymptotes respectively, to which the master curve approaches. m_e indicates the slope of the s-shaped G^* master curve in the middle linear part, whereas f_c is located in the x-axis in correspondence with the intersection of G_g^* asymptote and the straight line passing through such middle part.

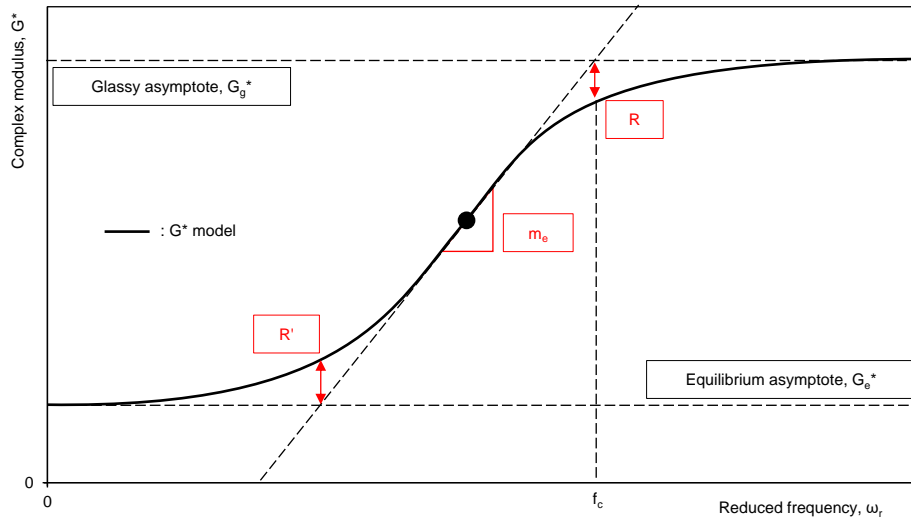


Figure 4.18. Model of stiffness master curve (G^* vs. ω_r).

Further, rheological index R was calculated according the following Equation 4.13. Such an index should give indications about the width of the relaxation spectrum: as illustrated in Figure 4.18, it identifies the rate of the transition from the elastic to the viscous behavior (the higher the R , the lower the sensitivity to frequency).

$$R = \log \left[\frac{2^{me/k}}{(1+2^{me/k}-1) \frac{G_g^*}{G_e^*}} \right] \quad (4.13)$$

In analogy, R' represents the distance between G^* model and G_e^* asymptote and is given by Equation 4.14 (in the case of binders, $G_e^* = 0$ determines a R' equal to $\log 2$).

$$R' = \log \left\{ 1 + \left(\frac{G_g^*}{G_e^*} - 1 \right) \cdot \left[1 + \left(\frac{G_g^*}{G_e^*} \right)^{k/me} \right]^{-k/me} \right\} \quad (4.14)$$

On the other hands, phase angle models of the master curves were constructed on the basis of shifted data of δ according to the Equation 4.15:

$$\delta = 90 I - (90 I - \delta_m) \{ 1 + [\log (f_d / f') / (f R_d)]^2 \}^{-md/2} \quad (4.15)$$

where δ_m is the constant phase angle at the inflexion point of G^* master curve model, f' is the generic experimental frequency, f_d is the constant location frequency at which δ_m occurs, R_d and m_d are shape parameters and I assumes the value of 0 or 1 when $f' > f_d$ or $f' < f_d$, respectively. Figure 4.19 gives a representation of the typical shape of modeled δ curve. Further details about the utilized models can be found elsewhere [4.18].

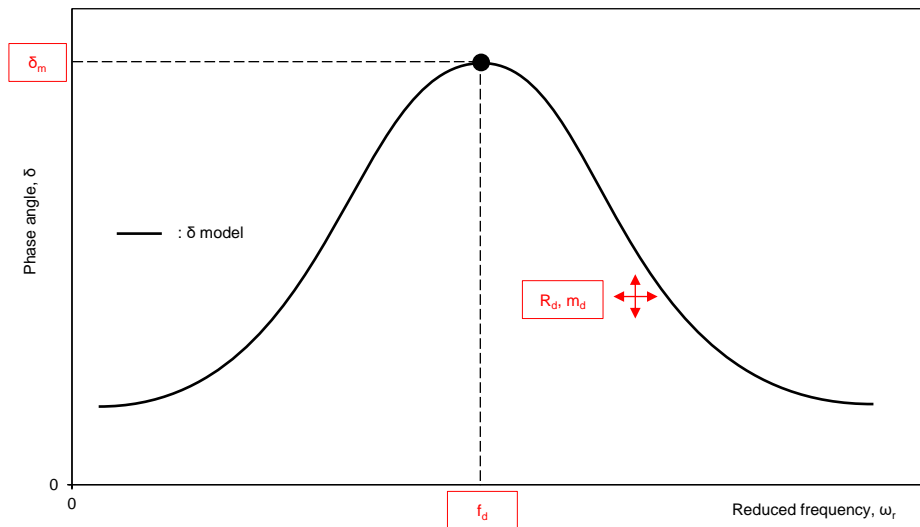


Figure 4.19. Model of phase angle master curve (δ vs. ω_r).

4.5.2.3. Fatigue resistance

Fatigue resistance of binders was investigated through DSR developing Linear Amplitude Sweep (LAS) test according to AASHTO TP 101-14 standard. The choice derived from operational considerations, since such method is reported to predict the fatigue performance of binders/mastics with a simple and time-saving procedure [4.19, 4.20]. LAS involves laboratory trials quicker than the traditional time sweep analysis which consist in repeated oscillatory loads (applied at constant strain and frequency) and implicates at least the damage of samples with the reduction of initial stiffness to the 50% (typical failure criterion utilized [4.21]). Moreover, time savings due to LAS use could be even more evident if advanced fatigue law predictions (requiring further time sweep progression) are planned [4.22]. Therefore, long-term aged samples (simulating end-of-life binders, i.e. the worst condition for fatigue) were tested with the 8-mm diameter geometry at the temperature of 20 °C (fatigue cracking is commonly associated to mid-service temperatures [4.23]). According to standard, LAS was divided in two parts: the first one aimed at analyzing the material properties in undamaged conditions. This was accomplished subjecting specimens to an oscillatory FS test, applying the constant strain of 0.1% over a frequency interval ranging from 0.2 to 30 Hz (linear continuous ramp). Figure 4.20.a depicts the loads applied during the first LAS part. Basing on FS results, performance of undamaged materials were summarized by the α parameter, calculated as a function of m , i.e. the slope of the best-fit straight line obtained plotting in a bi-logarithmic space the FS results, in particular G' on the y-axis vs. ω on the x-axis (Equation 4.16). Regardless some literature ambiguity concerning the α calculation (some authors reported an adapted formula to determine it [4.24]), this was calculated according to standard specifications using the Equation 4.17.

$$\log G' = m \cdot (\log \omega) + b \quad (4.16)$$

where b indicates the straight line intercept.

$$\alpha = 1/m \quad (4.17)$$

The second part of LAS consisted in an AS developed at the constant frequency of 10 Hz, while the strain was linearly increased from 0 to 30% (over 3 100 loading cycle n). This was supposed to produce an accelerated damage on materials comparable to fatigue loads. Figure 4.20.b illustrates the loads applied during the second LAS part. Here, τ , G^* and δ values were recorded to perform further elaborations.

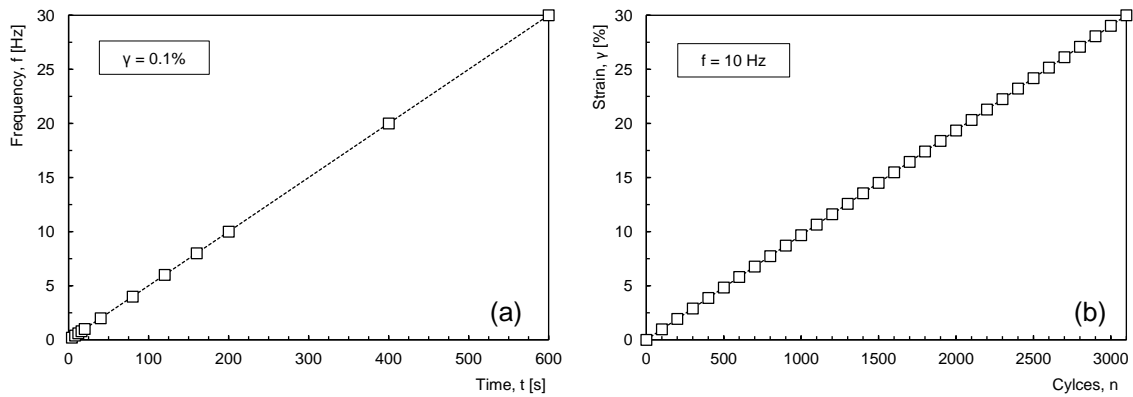


Figure 4.20. Loads applied on LAS phases – 1st: FS (f vs. t) (a); 2nd: AS (γ vs. n) (b).

In particular, Visco-Elastic Continuum Damage (VECD) theory [4.25] was utilized to estimate the damage accumulated by DSR samples during the second LAS phase on the basis of the approach originally developed for the study of the evolution of microcracks due to fatigue on asphalt mixtures [4.26]. Schematizing the body as the sum of infinitesimal elements which own the properties of the bulk material, the concept of strain is substituted by the pseudo-strain ε_R in order to determine the constitutive equations for visco-elastic materials (as binders) in analogy to those valid for elastic bodies [4.27]. Then, the damage accumulation in the material is summarized with the fictitious parameter D representing the amount of the material micro-damage and calculated according to Equation 4.18 [4.25].

$$D(t) = \sum_{i=1}^N [\pi \cdot \gamma^2 \cdot (C_{i-1} - C_i)]^{\frac{\alpha}{1+\alpha}} \cdot (t_i - t_{i-1})^{\frac{1}{1+\alpha}} \quad (4.18)$$

where N is the total number of cycles applied, i indicates the generic loading step, γ is the instantaneous strain applied (in percentage), t is the considered instant and α is that previously defined. As evident, D depends also on the pseudo-stiffness parameter C , i.e. the ratio between the stiffness modulus at a certain time (G_i^*) and the initial (undamaged/linear visco-elastic) modulus (G_0^*), being at the same time the ratio between the stress σ and the pseudo-strain ε_R in the uniaxial formulation (Equation 4.19).

$$C_{t=i} = \frac{G_i^*}{G_0^*} \quad (4.19)$$

Namely, $D(t)$ (the damage accumulated during second phase of test) could be considered function of the material integrity $C(t)$ and the punctual applied strain γ . By convention, $C(t)$ corresponding to $D(0)$ is assumed equal to 1, whereas $D(0)$ (at $t = 0$) is considered null. Graphically constructing the $D(t)$ vs. $C(t)$ relationship (Figure 4.21.a), damage characteristic curves can be modeled to govern the damage evolution under all possible conditions (stress and strain levels, frequencies and temperatures). Then, the relationship between $C(t)$ and $D(t)$ could be fit to the power law presented in Equation 4.20:

$$C(t) = C_0 - C_1 \cdot (D(t))^{C_2} \quad (4.20)$$

where C_0 is the initial value of C and is assumed equal to 1 and C_1 , C_2 parameters are curve-fit coefficients derived from the mathematical linearization of the power law (Equation 4.21).

$$\log(C_0 - C(t)) = \log(C_1) + C_2 \cdot \log(D(t)) \quad (4.21)$$

Logarithmic plot of $C_0 - C(t)$ (which can be considered the integrity loss) vs. damage ($D(t)$) allows the determination of C_1 and C_2 (Figure 4.21.b).

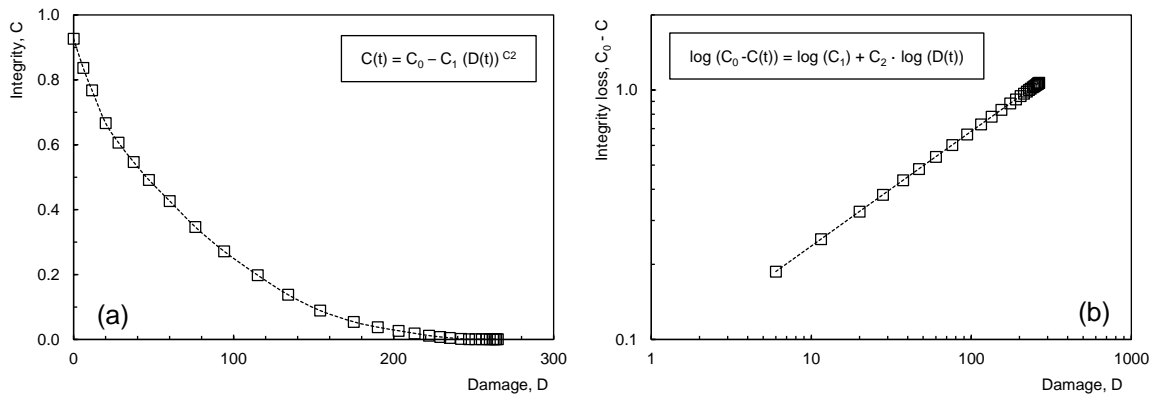


Figure 4.21. Damage evolution: integrity (C vs. D) (a) and integrity loss ($C_0 - C$ vs. D) (b).

Furtherly, the damage value at sample failure (D_f) was identified basing on the shear stress τ (the D corresponding to the reduction in initial complex modulus at the peak shear stress) according to Equation 4.22:

$$D_f = \left[\frac{C_0 - C_{at \tau peak}}{C_1} \right]^{1/C_2} \quad (4.22)$$

Finally, A and B parameters of the fatigue curves (curve location and slope, respectively) were determined according to Equations 4.23 and 4.24 to construct the fatigue law of the tested binders/mastics (Equation 4.25).

$$A = \frac{f \cdot (D_f)^{1+(1-C_2) \cdot \alpha}}{(1+(1-C_2) \cdot \alpha)(\pi \cdot C_1 \cdot C_2)^\alpha} \quad (4.23)$$

where f is the test frequency, equal to 10 Hz.

$$B = 2 \cdot \alpha \quad (4.24)$$

$$N_f = A \cdot \gamma^{-B} \quad (4.25)$$

where the number of cycles to failure N_f is related to the shear strain level γ through the regression coefficient A and B . In general, several replicates of each material were tested for the sake of prediction repeatability.

4.5.2.4. Permanent deformation resistance

Permanent deformation resistance of binders was assessed with DSR, developing Multiple Stress Creep Recovery (MSCR) tests (EN 16659) executed at high-service temperatures (typical scenario of rutting potential). Considering that softer materials should be more prone to accumulate permanent deformations, the worst condition was reproduced testing RTFO-aged binder (short-term aging simulation) representative of new-paved material (not yet subjected to stiffening due to long-term aging). Test consisted in a repeated sequence of 10 creep-recovery cycles (1 sec. of creep and 9 sec. of no-loading recovery) successively executed at two different stress levels (0.1 and 3.2 kPa). In the case of mastics, additional τ of 10 kPa was investigated. 25-mm diameter samples were tested in the temperature range between 50 and 80 °C; sampling was set according to reference standard to collect suitable results. For the sake of clarity, Figure 4.22 illustrates a generic creep-recovery cycle. In particular, considering the n -cycle, ε_0^n represents the deformation at its initial instant, ε_{10}^n indicates the strain after 1 second (when load is removed) and ε_{10}^n stands for the final deformation (within the n -cycle).

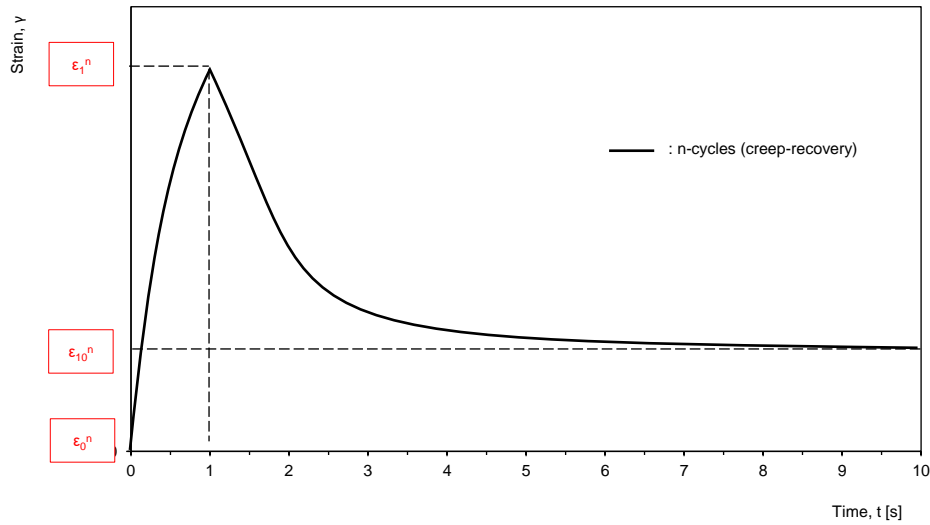


Figure 4.22. Example of n -cycle (creep-recovery): γ vs. t .

Rutting potential was then accounted representing the strain evolution on time and calculating for each stress the percent recovery $R\%$ as the average of the 10 cycles according to Equation 4.26:

$$R\% = \frac{\varepsilon_1^n - \varepsilon_{10}^n}{\varepsilon_1^n} \cdot 100 \quad (4.26)$$

In analogy, non-recoverable creep compliance J_{nr} (i.e. the plastic strains at the cycle ends) were evaluated for each τ according to Equation 4.27; $J_{nr-diff}$ (Equation 4.28) was intended as the average difference between J_{nr} at 0.1 and 3.2 kPa. In the case of mastics, $J_{nr-diff}$ could be intended as the average difference between J_{nr} at 3.2 and 10 kPa (Equation 4.29) because of the scarcely significant deformations suffered at $\tau = 0.1$ kPa.

$$J_{nr}^n = \frac{\varepsilon_{10}^n}{\tau^n} \quad (4.27)$$

$$J_{nr-diff} = \left(\frac{J_{nr,3.2} - J_{nr,0.1}}{J_{nr,0.1}} \right) \cdot 100 \quad (4.28)$$

$$J_{nr-diff} = \left(\frac{J_{nr,10} - J_{nr,3.2}}{J_{nr,3.2}} \right) \cdot 100 \quad (4.29)$$

J_{nr}/J_{TOT} ratios (i.e. the ratios between non-recoverable compliances and the compliances at load removals) were finally assessed to refer the non-recoverable parameter to the total strain accumulated by samples (Equation 4.30)

$$J_{nr}/J_{TOT} = \frac{\frac{\varepsilon_r^n - \varepsilon_0^n}{t^n}}{\frac{\varepsilon_c^n - \varepsilon_0^n}{\tau^n}} = \frac{\varepsilon_r^n - \varepsilon_0^n}{\varepsilon_c^n - \varepsilon_0^n} \quad (4.30)$$

where ε_r^n wants to indicates the absolute strain value at the end of the specific recovery portion ($\varepsilon_r^n = \varepsilon_0^n + \varepsilon_{I0}^n$) and ε_c^n for the absolute strain value at the end of the creep portion ($\varepsilon_c^n = \varepsilon_0^n + \varepsilon_{I1}^n$).

4.5.3. Characteristics of blends

Following paragraph describes the method utilized to test the produced bitumen-aggregate blends, in particular assessing the adhesion of different materials' combinations.

4.5.3.1. Adhesion properties

Adhesion of blends was investigated evaluating the tendency to stripping, which represents the aptitude to lose the bond between the aggregate surfaces and the binder films and is the main cause of the pavement raveling. In general, adhesion of blends is influenced by the charges that aggregate surfaces tend to assume when are in contact with water, thus is also related to moisture susceptibility of mixtures. Although such debonding is a complex and not yet fully understood phenomenon, it is generally recognized that mineralogy and chemical composition of the aggregates, as long as binder characteristics, cover a crucial role [4.28]. This occurs because of different chemical affinities of aggregate for water over asphalt. When aggregates do not own a specific chemical affinity with water (hydrophobic), they tend to be basic and do not suffer stripping problems; in the opposite way, when hydrophilic aggregates (affine to water) are used, an acidic nature prevails and stripping is suffered after exposure to water.

In order to assess such aspects, specific tests were conducted on loose mixtures (non-compacted bitumen and aggregate blends) through the Ancona Stripping Test (AST) method (EN 12697-11). This standardized boiling procedure was based on the original protocol [4.29], otherwise, some improvements in determining the stripped portion of blends was proposed using a DIP. In particular, high-resolution photos of samples were acquired and analyzed to separate pixels' colors and determine the residual binder coverage after the tests. Figure 4.23 reports an example of results obtained as output of the DIP.

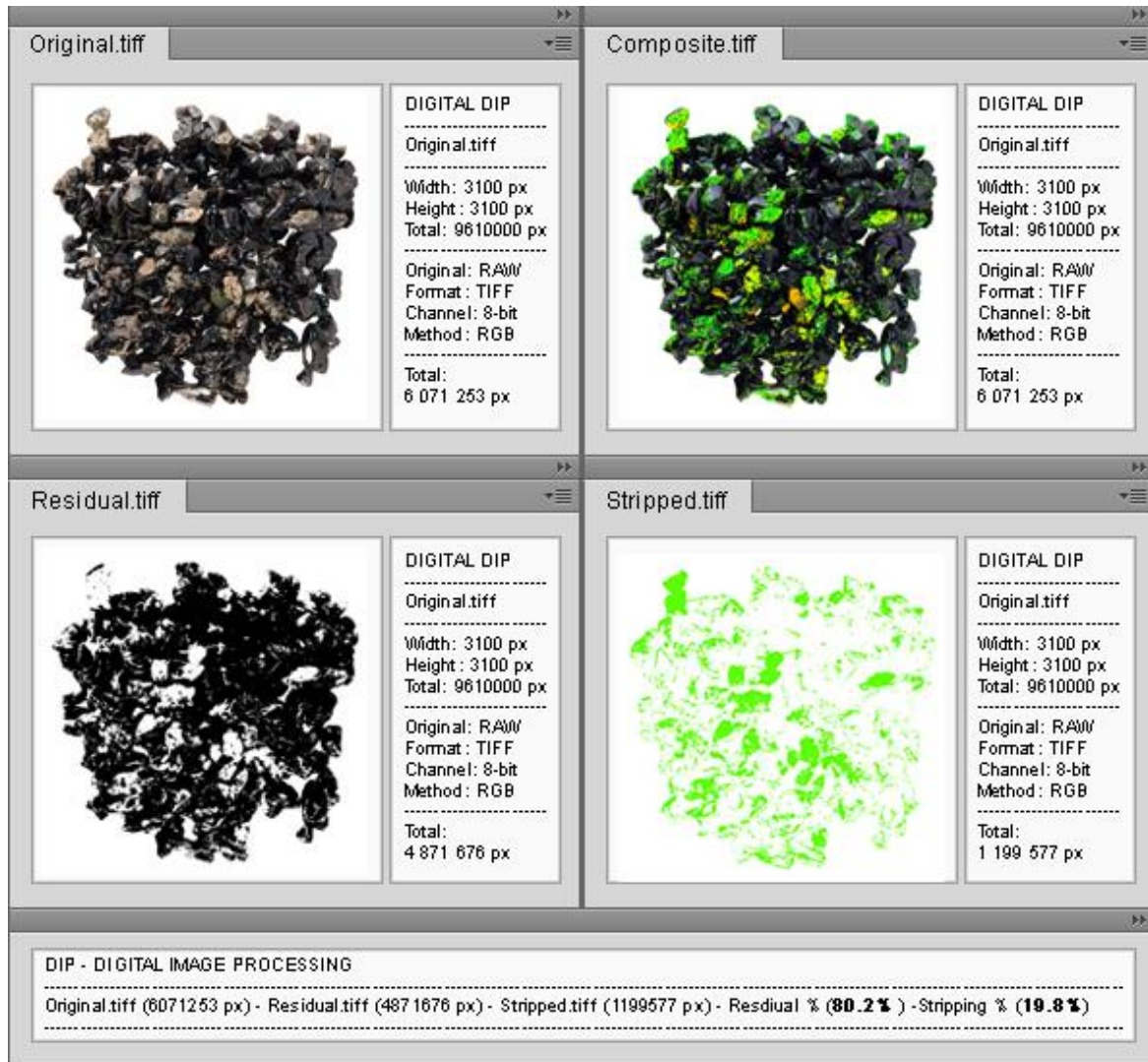


Figure 4.23. Stripping results: example of DIP output.

4.5.4. Performance of mixtures

Performance of studied mixtures were assessed performing several laboratory tests on the basis of the reference standards. Preliminary, information about mixture components were given. Once, defined the basic properties of binders, basic characteristics of the utilized aggregates were investigated. For the sake of brevity, such tests are only listed: particle density (EN 1097-6), flakiness index (EN 933-3), shape index (EN 933-4), Los Angeles coefficient (EN 1097-2), sand equivalent (EN 933-8), Atterberg limit (ASTM D-4318-10).

4.5.4.1. Mechanical strength

Preliminary tests were conducted on cylindrical specimens to assess their mechanical strength. First, traditional Marshall tests (EN 12697-34) were carried out on 100-mm diameter samples to determine stability and flows at the standard temperature of 60 °C.

Indeed, Marshall trials were also employed in the preliminary optimizations of binders' contents (following details will be provided within mix-design paragraphs). Then, Indirect Tensile Strength (ITS) tests were performed at 25 °C both on 100-mm and 150-mm diameter cylindrical samples according to EN 12697-23 standard. ITS values of 150-mm diameter specimens were also utilized to further evaluate the moisture susceptibility as an index of the mixture's durability (see the following paragraph 5.3.4.6).

4.5.4.2. Stiffness

Stiffness responses at mixture scale were firstly assessed through non-destructive Indirect Tensile Stiffness Modulus (ITSM) tests in accordance with EN 12697-26/Annex C. After a conditioning period of at least four hours at the test temperature, cylindrical specimens with 150-mm diameter were analyzed in strain-controlled mode, applying five load pulses along the vertical diameter. The corresponding horizontal deformation was measured by two linear variable displacement transducers (LVDT) mounted opposite one another in a rigid frame clamped to the specimen. A rise time (time for applying the load from zero to peak load) of 124 ms and a target peak horizontal deformation of 7 µm were selected according to the standard specifications. The Poisson's ratio ν was assumed equal to 0.35 and the indirect tensile stiffness modulus was calculated according to Equation 4.31. Different replicates for each mix were tested also varying the temperature (10, 20 and 30 °C).

$$ITSM = \frac{F \cdot (\nu + 0.27)}{z \cdot h} \quad (4.31)$$

where F represents the peak value of the applied vertical load, z is the amplitude of the horizontal strain obtained during the load cycle and h stands for the mean thickness of the cylindrical specimen.

Further, stiffness was assessed also on prismatic specimens through non-destructive 4-Point-Bending (4PB) tests according to EN 12697-26/Annex B standard. Cyclic loadings-displacements were applied on a beam through inner movable clamps positioned at the middle of the sample, that was held at its extremities by outer fixed clamps. In particular, frequency sweeps were conducted in strain-controlled mode: time-dependent stiffness was evaluated ranging f from 0.1 to 30 Hz (0.1, 0.3, 1, 3, 10 and 30 Hz) and imposing a strain amplitudes ε_0 of 50 µstrain. Mechanical properties measured at the 100th loading cycle were assumed as starting point, i.e. as representative of the intrinsic (undamaged) condition of the tested specimens. The applied loads and the corresponding controlled displacements at the mid span of the beam were measured; the norm of complex modulus E^* (based on the linear elastic beam theory) and the corresponding phase angle δ (time lag between the applied displacement and the corresponding load response due to visco-elasticity) were recorded. In analogy with previous ITSM tests, several replicates were analyzed varying the temperature (once again 10, 20 and 30 °C): in this case, this was useful also to construct the

stiffness mater curves (E^* and δ) similarly to that executed for the investigation of binder/mastic stiffness. Theory used was the same above-described (see paragraph 5.3.2.2). Also modeling was proposed (using the above-explained approach) to extend the experimental data and obtain indications on stiffness in a wider range of frequency (or temperature).

4.5.4.3. Fatigue life

The 4PB equipment was also used to analyze the fatigue resistance of mixtures. According to EN 12697-24/Annex D standard, a continuous sinusoidal waveform characterized by a frequency of 10 Hz was applied on prismatic samples under stress-controlled mode; stress levels ranged from 350 to 700 kPa. Stress and strain data, as long as E^* and δ were continuously recorded; the conventional fatigue curves were constructed basing on the number of loading cycles N_f at which a 50% reduction of the initial stiffness was achieved, according to the empirical approach. Fatigue lines were obtained arranging the experimental data in a bi-logarithmic plot (reporting the stress as a function of the number of cycles to failure) by regression analysis of data, using a power law according to that already presented in Equation 4.25.

4.5.4.4. Rutting resistance

Rutting resistance of mixtures was assessed through confined Repeated Load Axial (RLA) tests (EN 12697-25/Method A). Several replicates for each mix were tested at 40 °C (after a conditioning period of at least four hours) according to reference standard. Confinement was reproduced loading 150-mm diameter cylindrical specimens with an upper plate having a diameter of 100 mm (the “ring” of the material not directly loaded simulated the confining action replicating field conditions). Cyclic axial stop-pulse pressures, with a frequency of 0.5 Hz (1 s loading time and 1 s rest period) were applied for a total duration of 3600 pulses. A stress level σ equal to 100 kPa was selected according to the standard procedure. Rutting behavior was finally described by the evolution of cumulative axial strain ε_n as a function of the number of loading cycles n (Equation 4.32).

$$E_n = \frac{u_n}{t_i} \cdot 100 \quad (4.32)$$

where ε_n is expressed in percent, u_n is the cumulative permanent deformation after n loading cycles and t_i is the initial thickness of the specimen. Commonly, also creep rate f_c , which represents the slope of the ε_n vs. n curve in the central quasi-linear part, defined the material attitude to resist to rutting. Such steady state was located over the final 2400 loading cycles and was referred to permanent deformation resistance assuming that a steeper tendency

indicated a material more susceptible to rutting. f_c was calculated according to Equation 4.33.

$$f_c = \frac{\varepsilon_{n1} - \varepsilon_{n2}}{n_1 - n_2} \quad (4.33)$$

where ε_{n1} and ε_{n2} are the cumulative axial strains after n_1 and n_2 loading cycles respectively. Creep modulus E_n was finally determined according to Equation 4.34.

$$E_n = \frac{\sigma}{\varepsilon_n} \quad (4.34)$$

4.5.4.5. Surface characteristics

Surface characteristics of mixtures were analyzed on the basis of different tests. Particularly, these properties were evaluated considering that some solutions studied supposed the use of paints/varnishes applied on the mix surface; thus, the acceptability of such characteristics was investigated in order to ensure adequate safety standard with respect to main technical specifications for wearing courses (possible problems of adherence, permeability, etc.). Therefore, mean texture depth values (*MTD*) were determined to define the superficial macro-textures of materials in accordance with EN 13036-1 standard. Pavement surface horizontal drainabilities (*P*) were assessed on the produced mixes according to EN 13036-3 specifications. The skid-resistance tester was finally used to calculate the pendulum test values *PTV* (reference standard EN 13036-4).

4.5.4.6. Durability

Initially, moisture susceptibility was intended as an index of mixture's durability [4.30]. This was estimated with the calculation of the Indirect Tensile Strength Ratio *ITSR* (EN 12697-23 standard) which represented the *ITS* decrease of wet conditioned samples (*ITS_{wet}*) with respect to unconditioned dry ones (*ITS_{dry}*). Thus, following the above-described procedure (see paragraph 5.3.4.1), additional 150-mm diameter cylindrical samples were subjected to *ITS* tests (at 25 °C) after being exposed to a wet conditioning procedure. In particular, this was performed according to ASTM D4867/D standard, exposing specimens to a single freeze-thawing cycle constituted by a first phase of cooling (-18.0 ± 2.0 °C for at least 15 hours) and a second phase of soaking in water bath at the temperature of 60.0 ± 1.0 °C for 24 hours. Finally, *ITSR* ratios were calculated basing on the Equation 4.35.

$$ITSR = \frac{ITS_{wet}}{ITS_{dry}} \cdot 100 \quad (4.35)$$

Further, durability was also analyzed in terms of time-endurance of the mixture colors. Indeed, this was realized only for the solutions which supposed the application of products on the mix surfaces in order to evaluate their durability on time. An ad-hoc procedure was organized using the skid-resistance apparatus; repeated skid tests were executed to produce superficial abrasion (100 replicates on the same mix) and accelerate the surface color deterioration. Before and after such procedure, a digital image processing similar to those described on paragraph 5.1 was carried out and permitted the evaluation of the de-colored surface portions (in percentage) because of the abrasion.

In conclusion, durability was also evaluated in terms of mixture resistance to fuel spillages. Recalling the approach of EN 12697-43 procedure, a modified method was applied to painted/varnished mixes: surfaces were exposed to fuel (for 24 hours) and were then brushed with a metallic tool (according to standard specifications). A qualitative visual evaluation of paints was then done to establish the resistance to fuel of such color surface treatments. On the basis of the recorded masses during the operational phases, resistance category was estimated following the reference standard.

Chapter 5

Experimental Results

The present Chapter deals with the core activity of the research project. The previous-mentioned multi-scale approach is applied to characterize different material for thermally optimized road pavements likely able to mitigate the UHI and the heat-related phenomena. Based on protocols described at Chapter 4, chromatic, thermal and mechanical results are following presented and discussed with respect to binders, mastics, loose blends and mixtures.

5.1. Binders and mastics

The current paragraph defines the activities performed on binders and mastics. The utilized materials are firstly introduced and described; then, results about chromatic characteristics and rheological performance are detailed.

5.1.1. *Materials and plan*

Experimental activity supposed the use of three different kinds of binder: a conventional unmodified bitumen, a synthetic resin and some binders obtained combining the conventional bitumen with coloring pigments.

The conventional unmodified binder (hereafter coded B), was a 50/70 penetration grade bitumen derived from an Italian refinery. Being a wide-diffused product employed for common road works, it was used as control material for the whole experimentation. The synthetic binder (hereafter coded S) was a proprietary product composed by thermoplastic

bi-component resins (solid granular elements and liquid catalyst) with binding properties similar to those of a traditional bitumen. In particular, it was considered a clear product able to compose cool road pavements: in fact, in the original state, it appeared with a color varying from the amber-orange to the straw-yellow. S could allow the realization of clear or colored pavements totally substituting the traditional use of bitumen (owing similar volumetric binder contents) by bringing out the color of the aggregates composing the final mixture (after paving operations, a yellow-clear – almost tending to transparency – mortar matrix was obtained). Similar operational ways and analog equipment utilized during paving of conventional roads could be employed treating such product. Traditional (unmodified) bitumen (B) was then added with coloring oxide-pigments to obtain a colored binder. Such pigments (hereafter coded OX) had to be joined with other components during the mixing operations and had the objective to confer a specific color to the entire matrix of the final mixture. Supposing that oxides acted only at the binder scale (without modifying the aggregate color), these were dosed according to the produced specifications, based on the contents suggested with respect to the mixture weight: resulting weight ratio between B and OX was of 1:1 (OX dosages by aggregate weight ranged around the 5%, i.e. next to the typical optimum content of bitumen by the aggregate weight). Therefore, final binders were obtained blending B and OX through a mechanical stirring equipment (blending temperature equal about to 160 °C). Colorants were available in different tonalities; in order to evaluate the effect of such oxides, red and green pigments (hereafter coded R and G, respectively) were alternatively utilized. Thus, according to the introduced codification, final oxide-colored bitumen were coded B-OX-R and B-OX-G for the red and the green declination, respectively. The basic properties of the described binders are presented in Table 5.1.

Table 5.1. Basic properties of studied binders.

Property	Standard	Unit	B	S	B-OX-R	B-OX-G
Nature	-	-	Pol. ^b	Synt. ^c	Misc. ^d	Misc. ^e
Color	-	-	Black	Yellow	Red	Green
Density	EN 15326	Kg/m ³	1020	700	1120	1130
Penetration	EN 1426	0.1·mm	56	69	22	20
Penetration ^a	EN 1426	0.1·mm	38	54	12	10
Softening point	EN 1427	°C	61.6	61.3	84.2	80.9
Softening point ^a	EN 1427	°C	71.1	64.6	90.0	94.5
Penetration index	EN 12591	-	1.6	2.2	2.9	2.3
Ductility	ASTM D-113	cm	100+	21	99	100+
Elastic recovery	EN 13398	%	7	91	4.0	4.5
Breaking point	EN 12593	°C	-6.9	-7.5	n.a. ^f	n.a. ^f

^a after RTFO ageing;

^b Pol.: polymeric; ^c Synt.: synthetic; ^d Misc.: miscellaneous (iron); ^e Misc.: miscellaneous (chromium)

^f n.a.: not-available data

In order to prepare the mastics, different typologies of fillers (aggregates passing the 0.063 mm sieve) were used. Mastics were prepared in the laboratory by heating fillers and binders at about 160 °C for 1 hour. Then, fillers were slowly added with accurate blending in order to achieve homogeneous mixes without segregation. Mainly, limestone (coded Lf), steel slag (coded Sf), cement (coded Cf) and basalt (coded Bf) fillers were included in the experimentation: their basic properties, as long as morphological compositions (where available), are presented in Table 5.2 and 5.3, respectively.

Table 5.2. Basic properties of utilized fillers.

Property	Standard	Unit	Lf	Sf	Cf	Bf
Particle density	EN 1097-7	Mg/m ³	2.74	3.86	3.15	2.77
Plasticity index	CEN ISO/TS 17892-12	-	NP ^a	NP ^a	NP ^a	NP ^a
Rigden voids	EN 1097-4	%	32.7	60.4	40.3	33.8
Delta R&B temperature	EN 13179-1	°C	5.8	22.1	n.a. ^b	n.a. ^b

^a NP: non plastic;

^b n.a.: not-available data;

Table 5.3. Morphological compositions of fillers.

Material	Oxide content [%]							
	MgO	Al ₂ O ₃	SiO ₂	CaO	TiO ₂	Cr ₂ O ₃	MnO	FeO
Lf	2.50	1.00	3.34	52.71	-	-	-	0.39
Sf	3.65	9.30	13.02	29.60	0.35	4.03	5.09	32.84
Cf	n.a. ^a	n.a. ^a	n.a. ^a	n.a. ^a	n.a. ^a	n.a. ^a	n.a. ^a	n.a. ^a
Bf	n.a. ^a	n.a. ^a	n.a. ^a	n.a. ^a	n.a. ^a	n.a. ^a	n.a. ^a	n.a. ^a

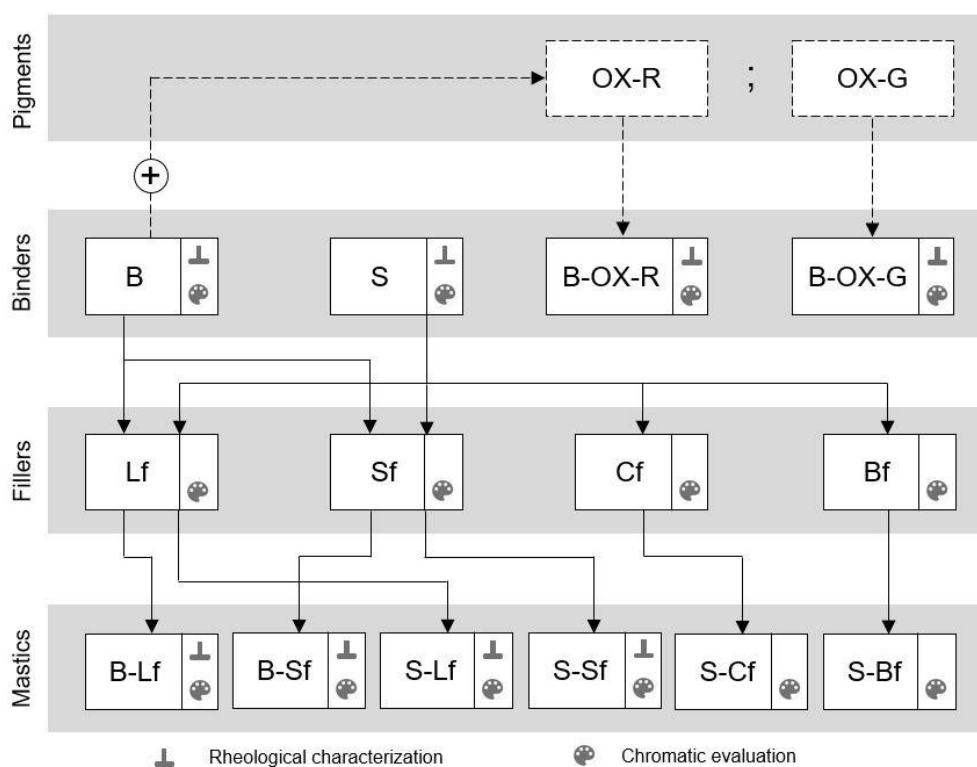
^a n.a.: not-available data

Indeed, some mastics were manufactured with the intention to performing the rheological characterization, other ones were created to carry out specific chromatic evaluations at mastic-scale. Dosages were maintained constant in volumetric terms; in order to early reproduce what happening at mixture scale, traditional bitumen and limestone (aggregate commonly employed for road pavement materials) were dosed with a 1:1 weight ratio (analog bitumen content and percentage of fillers by weight – with respect to the aggregate weight). This corresponded to a 73-27% binder-filler proportion and was then reproduced (in volumetric terms) for the other filler types to ensure analog coating mechanisms at the mastic-scale. In the case of aging, binders were previously subjected to short or long-term simulations and then blended with fillers. The following Table 5.4 indicates all the combination of binders and fillers selected to compose the mastics, giving also indications about the specific scope for which they were prepared.

Table 5.4. Mastic's composition and test program.





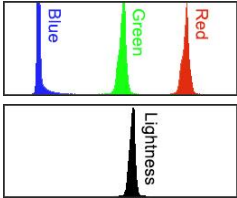


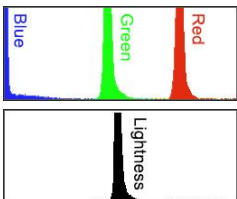


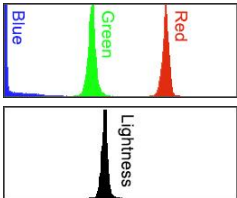


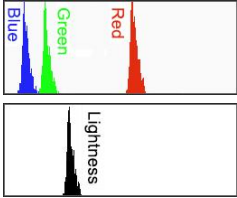


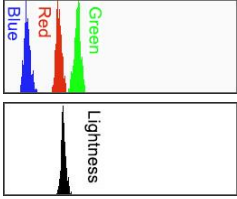

Mastic code	Binder	Filler	Test
B-Lf	Bitumen (B)	Limestone (Lf)	Chromatic / Rheological
B-Sf	Bitumen (B)	Steel slag (Sf)	Chromatic / Rheological
S-Lf	Synthetic resin (S)	Limestone (Lf)	Chromatic / Rheological
S-Sf	Synthetic resin (S)	Steel slag (Sf)	Chromatic / Rheological
S-Cf	Synthetic resin (S)	Cement (Cf)	Chromatic
S-Bf	Synthetic resin (S)	Basalt (Bf)	Chromatic

As a summary, Figure 5.1 presents a concise scheme of the experimental protocol planned to characterize the produced binders and mastics. Based on the protocol described at Chapter 4, the following Table 5.5 details the rheological protocol developed on all the utilized materials.

**Figure 5.1.** Scheme of the planned experimental protocol.


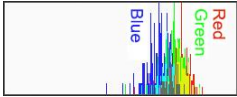

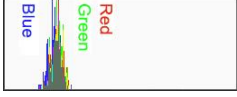

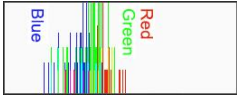

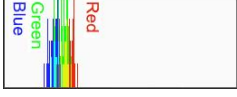
that of S was equal to 47 at the same ageing state). In general, it must be stressed that B-OX bitumens are employed to directly produce colored mixtures, whereas synthetic resin owns definite opacity which tend to furnish it transparent properties; thus, color of aggregates is supposed to be dominant with S use, whereas is considered negligible employing B-OXs.

Table 5.6. Chromatic results of binders.

Material	DIP sample	Color histogram	Chromatic characteristics		
B			R	G	B
			2	3	1
			H	S	L
			90	50	1
			Dominant color 		
S (U) (unaged)			R	G	B
			200	130	38
			H	S	L
			34	68	47
			Dominant color 		
S (S) (RTFO)			R	G	B
			193	114	2
			H	S	L
			35	98	38
			Dominant color 		
S (L) (PAV aged)			R	G	B
			177	76	1
			H	S	L
			26	99	35
			Dominant color 		
B-OX-R			R	G	B
			141	45	21
			H	S	L
			12	74	32
			Dominant color 		
B-OX-G			R	G	B
			52	77	22
			H	S	L
			87	56	19
			Dominant color 		

Further focuses about such thematic were planned at the mixture-scale; indeed, some preliminary information could be collected early analyzing the chromatic responses at the mastic-scale. To this purpose, Table 5.7 depicts analog chromatic results about the employed fillers: in this case, an accurate filtering procedure was used in the DIP to neglect the shading effects due to the texturized-nature of the acquired images. According to the visual characteristics, darkness of fillers (basing on the L parameter) progressively increased passing from Lf (limestone) to Cf (cement), to Bf (basalt) and Sf (steel slag).


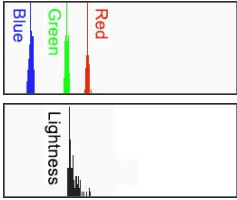


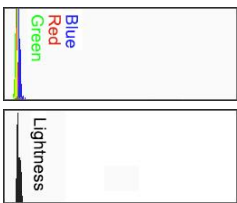


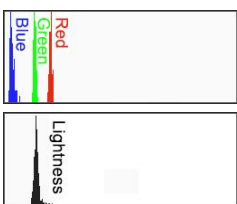


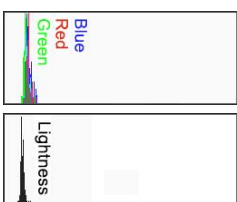

Table 5.7. Chromatic results of fillers.

Material	DIP sample	Color histogram	Chromatic characteristics		
			R	G	B
Lf (filler)			R	G	B
			195	189	175
			H	S	L
			42	14	73
Sf (filler)			R	G	B
			60	61	58
			H	S	L
			80	3	23
Cf (filler)			R	G	B
			133	120	106
			H	S	L
			31	11	47
Bf (filler)			R	G	B
			71	64	56
			H	S	L
			32	12	25

Finally, Table 5.8 presents the chromatic results at the mastic-scale concerning the combination of S with fillers. As evident, the final colors obtained deeply differ from that of the original S. Hue H (i.e. tonality) of 47° in the case of S (located in the family of the yellow/ochre) changed towards 29° and 35° for S-Lf and S-Cf, respectively (family of browns); in the same way, it turned to 252° and 280° for S-Sf and S-Bf, respectively (family of dark-greys/blacks). According to filler findings, L parameter indicated increasing darkness moving from the use of limestone (S-Lf) to cement (S-Cf), basalt (S-Bf) and steel slag (S-Sf). Despite the proposed considerations, the collected data did not permit to identify consistent mathematical relations between HSL values of bitumens, fillers and mastics. This was ascribed to the limited number of available data but also to a certain compliance proper of the DIP method utilized (even slight variability derived from image acquisition and elaboration procedures could produce appreciable scattering in the HSL numerical results). Nevertheless, such findings could be considered suitable in comparative terms and clearly indicated that, as initially supposed, the final color of the mixture should be strongly affected

by the color of the utilized aggregate (already at mastic-scale, the filler color fully modify the amber-orange/straw-yellow S color).

Table 5.8. Chromatic results of mastics.

Material	DIP sample	Color histogram	Chromatic characteristics		
S-Lf (U) (unaged)			R	G	B
			102	69	38
			H	S	L
			29	47	27
			Dominant color		
S-Sf (U) (unaged)			R	G	B
			16	15	20
			H	S	L
			252	14	7
			Dominant color		
S-Cf (U) (unaged)			R	G	B
			52	34	9
			H	S	L
			35	70	12
			Dominant color		
S-Bf (U) (unaged)			R	G	B
			25	23	26
			H	S	L
			280	6	10
			Dominant color		

5.1.3. Rheological characterization

The following paragraphs illustrate and discuss the main rheological results obtained.

5.1.3.1. Viscosity

Viscosity results are presented in Figure 5.2, where η is plotted for each binder at the standard reference shear rates and temperatures. As evident, B owned the lower viscosity; η progressively increased, passing from B to S and then towards B-OX-R and B-OX-G. At temperature equal to 60 °C and shear rate of 0.05 s⁻¹, the determination of B-OX-R and B-OX-G viscosities resulted impossible (probably because of their expectable huge η under

such conditions – not compatible with the instrument tolerance). Where available, η of B-OX-R and B-OX-G were each other quite similar.

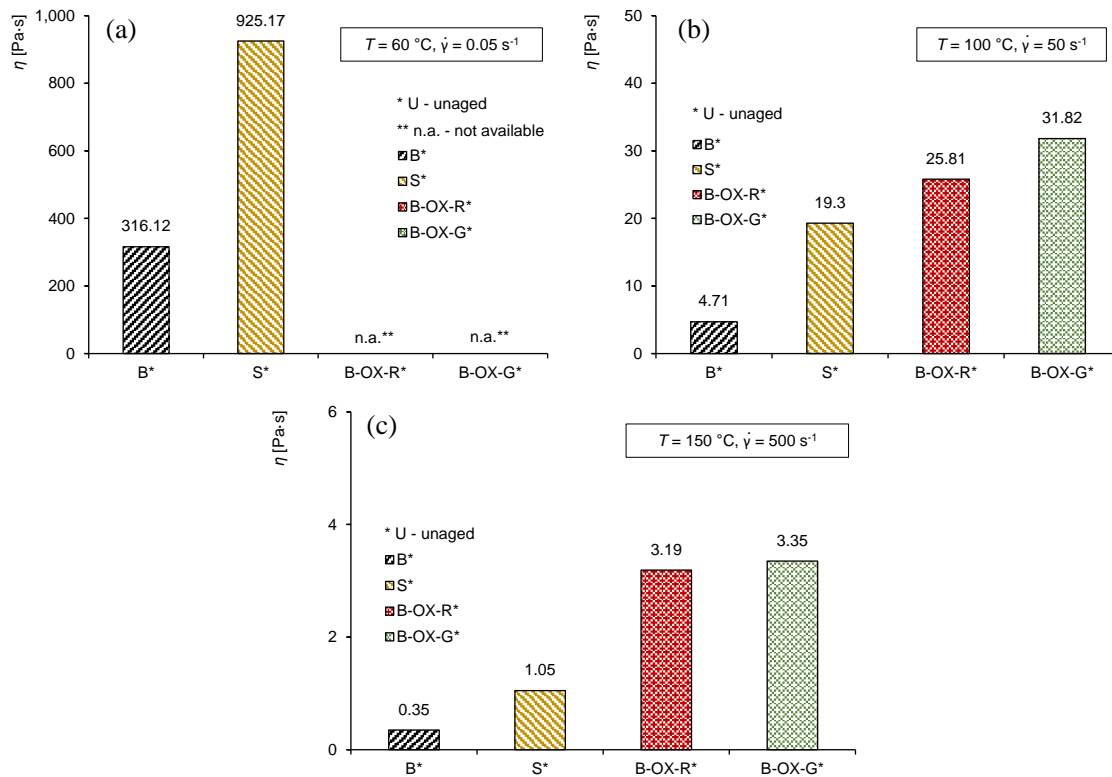


Figure 5.2. Viscosity: η of binders in unaged (a) RTFO-aged (b) and PAV-aged (c) condition.

Further analysis were proposed basing on the following Figure 5.3, where the flow curves (shear stress vs. shear rate) of the binders are illustrated considering different trials performed at selected strains (temperature is fixed equal to 100 °C). As evident, the curve shapes seemed to indicate a linear relation between the applied shear rate and the corresponding measured shear stress in the case of B and S (dynamic viscosity η is the curve slope); this represents the typical Newtonian behavior exhibited by conventional bitumens. Accordingly to previous findings, S flow curve was steeper than that of B and was characterized by greater shear stresses. B-OX-R and B-OX-G lines demonstrated τ greater of one order of magnitude with respect to B: otherwise, they also tent both them to show curved trends indicating the well-known behavior of pseudo-plastic materials. In this case, binder viscosity decreases under the shear strain and such shear thinning non-Newtonian behavior inhibits the time-dependent effects. In witness of the fact, some operational advisories were noticed in the bitumens-pigments mixing phases, in which the efficacy of the oxide's dispersion depended on the blending intensity applied to the compounds. In general, comparing B-OX-R and B-OX-G, the green solution resulted slightly more viscous with respect to the red one (see also η on Figure 5.2).

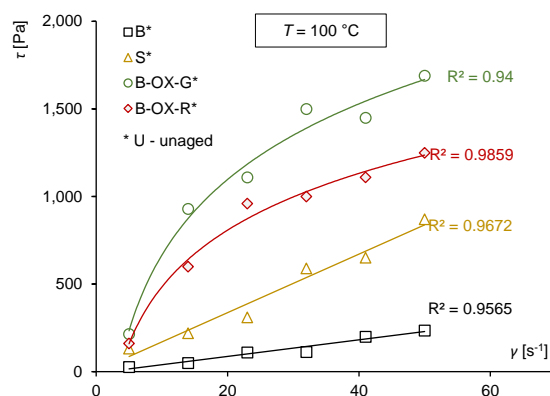


Figure 5.3. Flow curves of binders (τ vs. $\dot{\gamma}$).

Finally, other interesting information were collected also plotting the material viscosities against the temperature (Figure 5.4) in order to identify the suggested mixing and compaction temperatures on the basis of literature specific prescriptions [5.1]. Indeed, the elaboration was applied only with B and S because of the flow curve shapes identified for B-OX-R and B-OX-G (the proposed interpolation was suitable only in the case of Newtonian fluids, for which the time-temperature dependency allows to superpose the effects of strain and temperature). The obtained results indicated that B could be mixed and compacted at about $160\div 155$ °C and $150\div 155$ °C respectively, whereas S at about $165\div 170$ °C and $170\div 175$ °C respectively. The greater temperatures identified for S were compatible with those employed in the laboratory procedures and were also in line with the specs given by the S producer. As anticipated, no tests were planned at mastic-scale (because of operational constrains due to equipment limit connected to the difficulty of performing DV tests on harder materials).

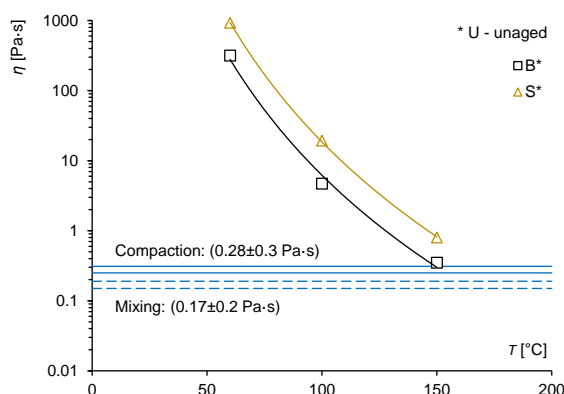


Figure 5.4. Projections of η with respect to mixing and compaction temperature ranges.

5.1.3.2. Stiffness characteristics

As anticipated, AS tests were preliminary carried out in order to investigate the strain-dependency of the studied materials and to identify their LVE limits. The obtained experimental data are firstly depicted in Figure 5.5. In particular, Figure 5.5a illustrates the

evolution of G^* with strain at T equal to 34 °C, whereas Figure 5.5b presents the isochronal plots of the binders (γ vs. τ) at the same temperature. At first sight, the greater stiffness of oxide-pigmented bitumens (B-OX-R and B-OX-G) is well recognized; S seemed to be less stiff than the reference B. All binders exhibited the typical behavior with a complex modulus independent on the strain level until the corresponding LVE limit: after it, rapid decreases of G^* occurred and the non-linear visco-elastic domains were highlighted. According to the conventional rule, such LVE limits corresponded to the 5% decrement of the initial stiffness: Table 5.9 indicates the found LVE limits with respect to the case presented in Figure 5.5: proportionally to the absolute values of stiffnesses, such strains resulted gradually lower passing from the softer S to B, and then to the stiffer B-OX-R and B-OX-G. Comparing the latter pigmented-bitumens, no significant strain-dependency differences seemed to be detectable depending on the utilized color.

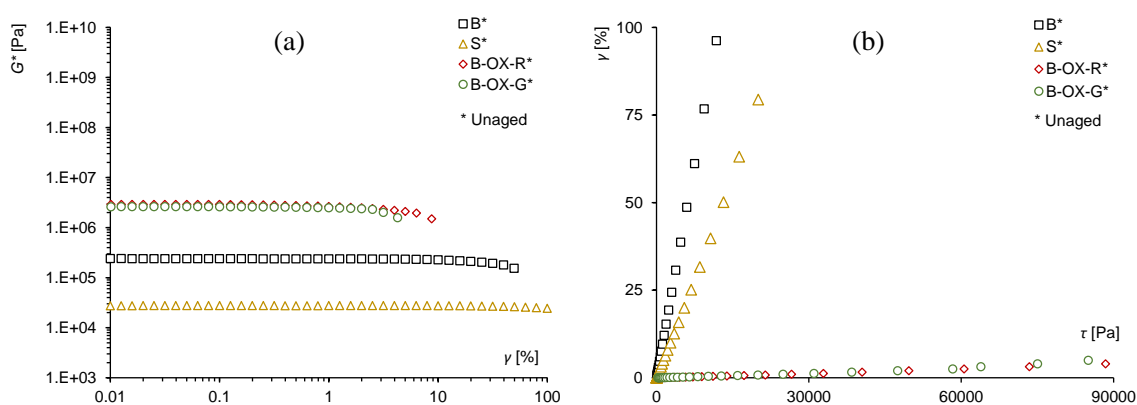


Figure 5.5. AS binders' results: G^* vs. γ (a) and isochronal plots, γ vs. τ (b).

Table 5.9. AS binders' results: LVE limits at 34 °C (unaged samples).

Material	G^* initial	G^* at LVE limit	Strain at LVE limit
B	241327 Pa	229260 Pa	8.05 %
S	27593 Pa	26213 Pa	63.08 %
B-OX-R	2909967 Pa	2764468 Pa	1.99 %
B-OX-G	2601820 Pa	2471729 Pa	1.78 %

A deeper understanding of binders' behaviors could be also evinced plotting the storage (elastic) and loss (viscous) moduli with the strain evolution. Comparing B and S (Figure 5.6), synthetic resin seemed to demonstrate a more balanced response (similar G' and G'') with respect to B when unaged condition is considered (Figure 5.6a); in the long-term aged one (Figure 5.6b), such behavior tent to disappear ($G'-G''$ distance of S is comparable or even greater than that of B). No definite causes of the trend could be early hypothesized, otherwise more detailed explanations of the phenomenon will be deepened on the further sections. In general, the conceivable higher stiffness for the long-term aged samples was found in all case (oxidization and hardening of the binder with aging).

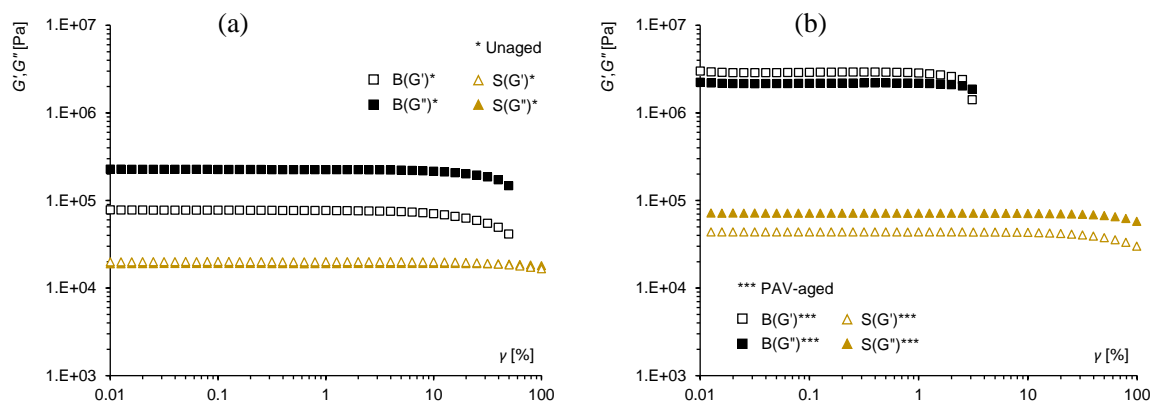


Figure 5.6. AS binders' results: G' , G'' vs. γ for B and S: unaged (a) and PAV-aged (b) condition.

The following Figure 5.7 compares the AS results of B, B-OX-R and BOX-G at different temperatures within the 4÷64 °C range. LVE limit trends are also plotted interpolating the 95% values of initial sample's stiffness. Notwithstanding the already-mentioned higher stiffness of B-OXs, they also presented clearly visible steeper LVE lines, anticipating a sort of lower temperature dependency with respect to the reference B (more evident for red OX).

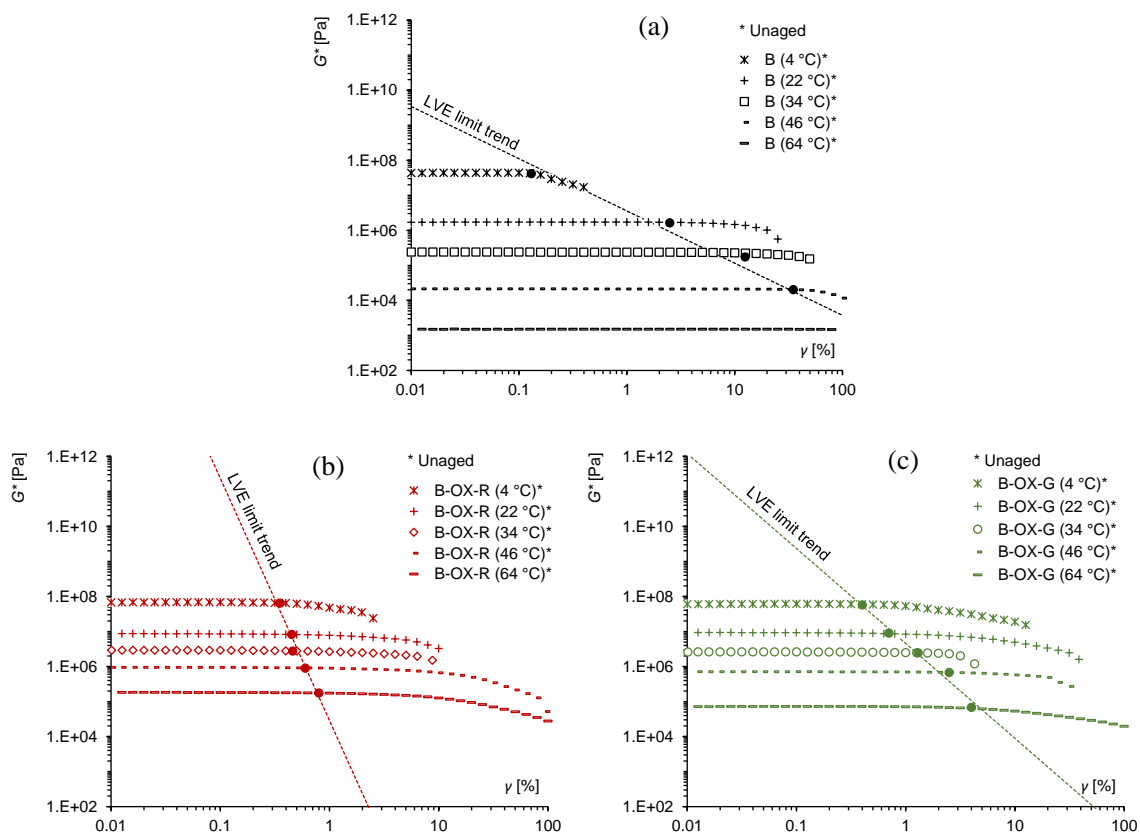


Figure 5.7. AS: G^* vs. γ and LVE trends at different T for B (a), B-OX-R (b) and B-OX-G (c).

Analog elaborations were proposed also at mastic-scale for B and S (B-OX-R and B-OX-G were avoided in view of their high stiffness). Figure 5.8a depicts G^* evolutions with strain and Figure 5.8b presents the isochronal plots at 34 °C. Once again, S resulted softer than B;

however, a different contribution of the fillers was highlighted. In general, the steel slag filler (Sf) stiffened the mastic more than the limestone one (Lf), regardless the ageing condition. In the case of bitumen, such Sf contribution seemed more marked at unaged condition (B-Lf* and B-Sf* curves are closer than B-Lf** and B-Sf* ones); analyzing the synthetic resin, S-Sf curves were equally far from the corresponding S-Lf. In absolute terms, the clearly stiffening effects due to the filler presence was evinced with respect to the corresponding binders, but it is also interesting to note that the stiffness of the oxide-pigmented bitumens was comparable to that of a bitumen-based mastics in the unaged condition (G^* at 34 °C of B-OX-R or B-OX-G was comparable to that of B-Sf*, or even greater than that of B-Lf*). This seemed also to agree with the deeply greater viscosities found for B-OX-R and B-OX-G (see Figure 5.2).

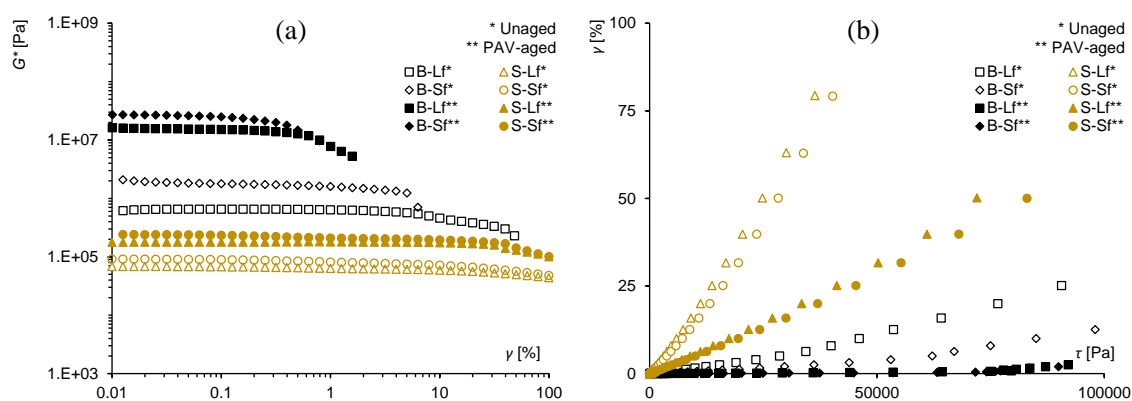


Figure 5.8. B and S mastics at unaged and PAV-aged condition: : G^* vs. γ (a) and γ vs. τ (b).

Temperature dependency was finally analyzed through the specific test: Figure 5.9 displays the evolution of complex stiffness moduli of binders with the temperature (samples in unaged conditions). As already anticipated, B-OX-R and B-OX-G owned a lower temperature dependency with respect to the reference B (flatter curves), without sensible variations depending on the used color; such aptitude was more pronounced at the higher temperatures (at 4°C, G^* of B, B-OX-R and B-OX-G were quite similar). At the lower temperatures, the synthetic resin curve seemed comparable to that of bitumen (S and B curve were parallel), whereas a lower temperature dependency could be supposed at the higher T . Thus, the inversion of trends (the crossing of S and B lines), located in the proximity of 45÷50 °C, could suppose different behavior of S depending on the temperature. In this perspective, further information will be given later, also considering the effect of the load frequency, since TS was performed at the unique ω of 10 rad/s (i.e. f of 1.59 Hz) (the visco-elastic time-dependent nature of the studied binders must consider all these aspects).

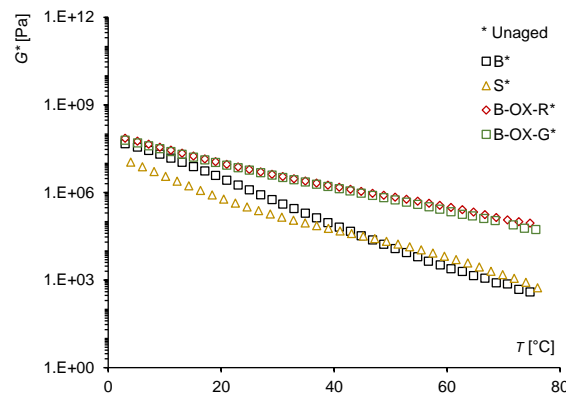


Figure 5.9. TS results: temperature dependency (G^* vs. T) of the studied binders.

Further, managing the FS results, the validity of the time-temperature superposition principle was preliminary checked for the tested binders by analyzing the experimental complex moduli and phase angles in the Black space presented in Figure 5.10 (δ vs. G^* plot). In fact, it is widely ascertained that smoothed curves in this diagram (composed by aligned data series representing the different test temperatures) indicate the validity of the TTSP [5.2, 5.3]. This is a symptom useful to avoid inconsistent and meaningless data fitting with arbitrary horizontal or vertical shifting. In this perspective, binder B exhibited a perfect-smoothed line, thus a consistent construction of the G^* master curve and δ master curve at a fixed reference temperature could be proposed. Differently, in the case of synthetic binder S, the experimental data did not provide a smooth curve, indicating the partial inconsistency of the TTSP, at least for the analyzed temperatures and frequencies; Therefore, the construction master curves for S was considered impossible. In any case, different behaviors seemed to be recognized depending on the test temperatures (in accordance to the above-described concerns). This finding could be rationally explained considering the bi-component nature of the tested resin and the fact that the melting processes could cause the discontinuity and the transition (different compounds reasonably conferred distinct properties to the synthetic binder). Moreover, it is interesting to note the unconventional “bell-shape” of the S data series measured at temperatures up to 58 °C; δ initially increased with G^* (opposite trend with respect to that of the reference B) and then started to decrease. In this sense, the overall distribution of the measured LVE characteristics seemed to indicate the existence of distinct regions, as discussed in detail below. Evaluating the B-OX-R and B-OX-G responses, very close trends, with no evident global-aligned curves, were detected regardless the pigment color. Then, once again the TTSP failure was verified and the master curves were considered not significant. However, prevalent elastic natures of such compounds were clearly visible since the recorded overall range of the phase angles varied in the restricted region between 15 and 50°. In general, B-OXs curves’ shapes tent to indicate opposite behaviors with respect to the reference B, with a direct proportionality between G^* and δ (phase angles increasing with stiffness modulus, at least up to 64÷70 °C).

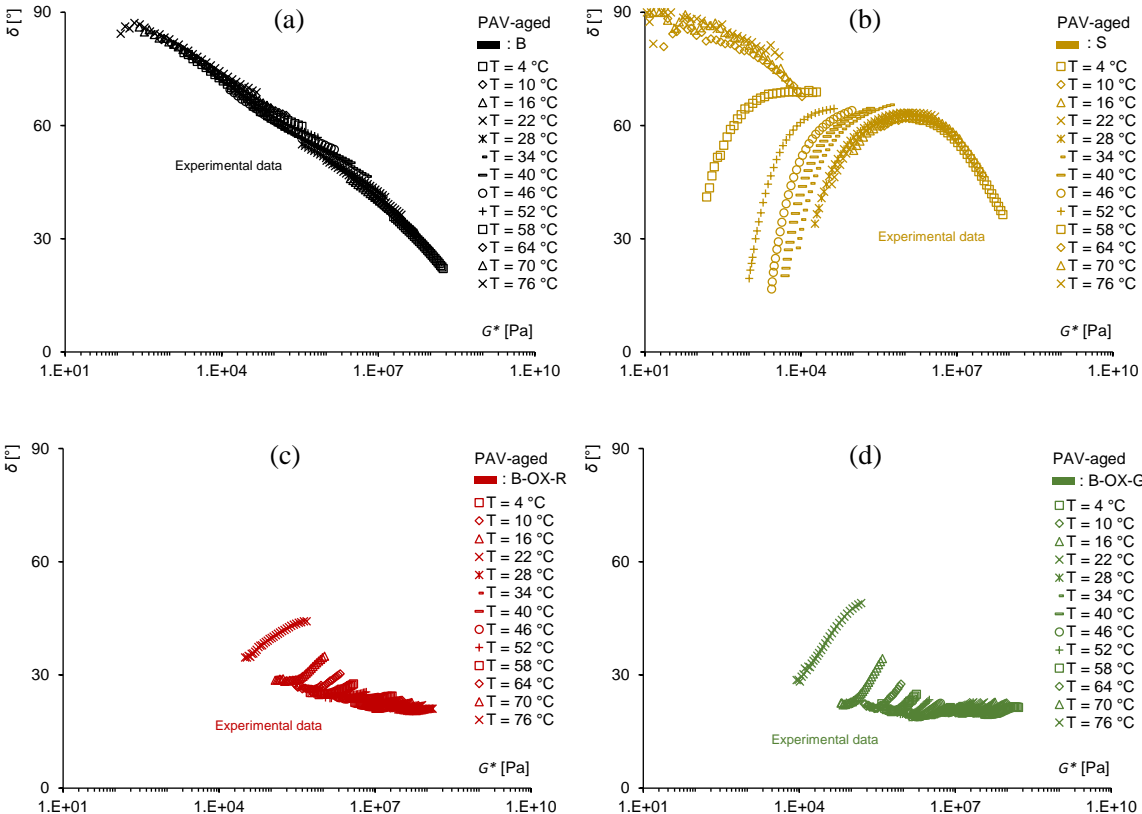


Figure 5.10. Black diagrams (δ vs. G^*) of binders B (a), S (b), B-OX-R (c) and B-OX-G (d).

Stricter indications about the visco-elastic nature and the prevalent behavior of binders can be evinced also through the Cole-Cole plots (i.e. the loss modulus against the storage one) reported in Figure 5.11. Within the tested temperature range, bitumen B demonstrated a prevalent elastic behavior ($\delta < 45^\circ$, or $G'' < G'$) only up to $34\div 40^\circ\text{C}$, depending on the test frequency; other data series (T between $34\div 40^\circ\text{C}$ and 76°C) were characterized by a prevalent viscous behavior (experimental points above the black-dashed equality line in the graph). Also S binder curve indicated an overall viscous tendency; only few T series resulted under the equality line with respect to isolated frequency values. This could be likely considered a crucial characteristic of such binder in view of a significant resistance to rutting phenomena, which are traditionally involved in the case of higher service-temperatures. Then, as anticipated, oxide-colored bitumens (B-OX-R and B-OX-G) were clearly located in the elastic regions (only 76°C series approached the equality line). This was reasonably ascribed to the higher stiffness recorded with respect to other binders (B and S).

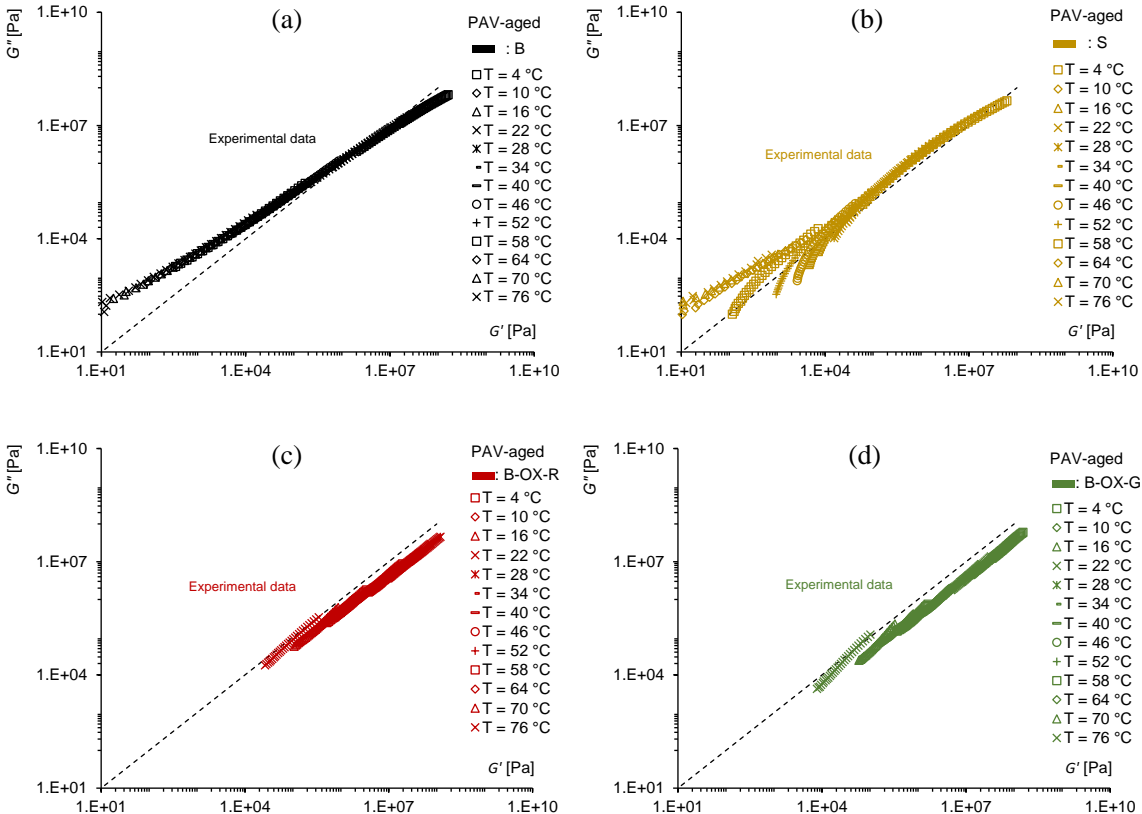


Figure 5.11. Cole-Cole plots (G'' vs. G') of binders B (a), S (b), B-OX-R (c) and B-OX-G (d).

Final concerns about FS results were drawn linking the collected stiffnesses and phase angles with the experimental frequencies (or the reduced ones where master curve’s constructions were available). Thus, Figures 5.12–5.15 plot the G^* and δ against ω for B, S, B-OX-R and B-OX-G; master curves were obtained only for reference B, whose mathematical elaboration details are reported in the following Table 5.10. Basing on Figure 5.12 (reference B), it can be noticed that the complex shear modulus smoothly increased with the test frequency and seemed to approach the typical glassy asymptote $G^* = 10^9$ Pa at the lower tested temperature and at the highest frequency; the measured phase angle increased with the test temperature (thus decreasing the reduced frequency) approaching values of about 80° . Proposed model seemed to properly fit the experimental data, giving the possibility to extend the curves in a wider domain. Concerning S resin (Figure 5.13), G^* experimental data progressively increased with the test frequency and decrease with the test temperatures, according to a typical viscous thermo-plastic behavior of bituminous binders. However, at the lowest and the highest investigated temperatures, it exhibited conventional quasi-linear trends (similar to those of B), whereas at intermediate temperatures (approximately between 22 and 58 °C) G^* revealed unusual s-shaped curves, flattened in the proximity of the lowest experimental ω . As far as the phase angle δ concerns, a non-conventional behavior (i.e. different from that of bitumen) was observed in the tested domain, distinguishing the above-mentioned different regions dependent on the temperature

(three main tendencies were clearly distinguished). These one can be broadly schematized as following: i) from 4 to 16 °C, the phase angles decreased as the frequency increased; ii) from 16 to 58 °C, a transition towards the opposite tendency can be detected (δ increasing with ω); iii) from 58 to 76 °C, a further recognizable change of behavior occurred towards a trend similar to that observed for the lowest temperatures (δ decreasing as the ω increases). Furthermore, comparing the B and S visco-elastic properties, the synthetic resin showed the above-mentioned lower stiffness (than B) at any given temperature (within the investigated frequency domain). Moreover, S owned noticeably higher δ at both low (4÷22 °C) and high (64÷76 °C) test temperatures (even approaching 90°, i.e. a pure-viscous behavior). As already observed, B-OX-R and B-OX-G manifested very close trends regardless the type of pigment (red or green). In terms of stiffness, G^* - ω relations indicated similar trends to that of B, with G^* progressively increasing with the angular frequency. Otherwise, flatter B-OX-R and B-OX-G series (than B) tent to indicate a lower susceptibility to the frequency in the case of oxide-pigmented bitumens. In turn, the small dispersion of the series certify the lower thermal dependency already detected with the specific TS tests (see Figure 5.9). B-OX-R and B-OX-G phase angles increased with the frequency (i.e. an opposite trend with respect to B). In other terms, the increase of frequency tent to enhance the viscous nature of such products. As conceivable, this aspect resulted more evident at the highest temperature (this seemed to agree also with the already-cited operational evidences faced during the mixing phase, during which, at high temperatures, only significant stirring frequencies were able to provide the adequate viscosity for blending).

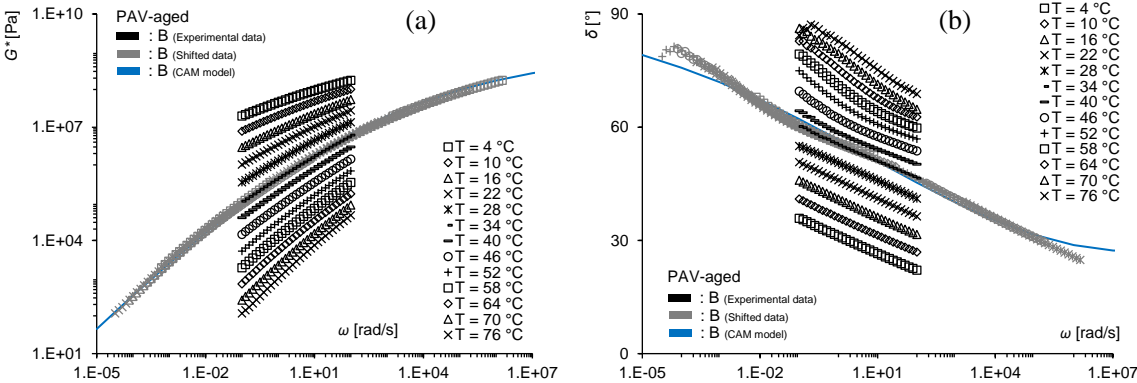


Figure 5.12. G^* (a) and δ (b) vs. ω for binder B: experimental data and master curves.

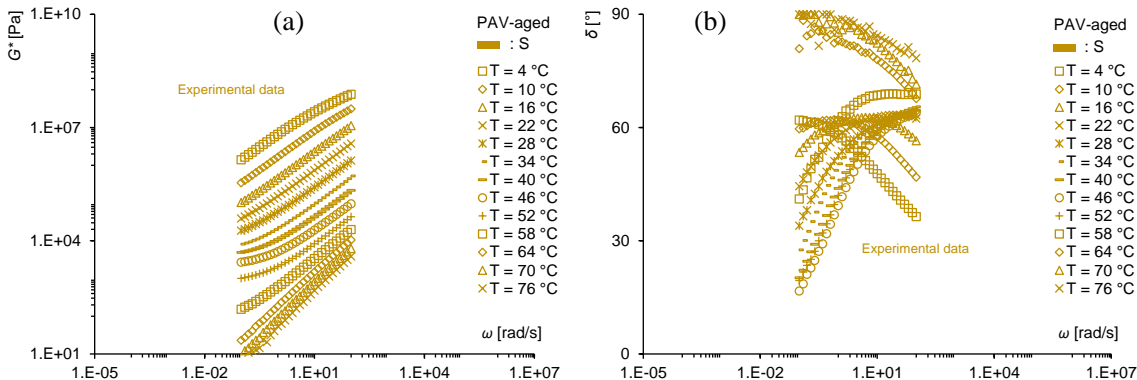


Figure 5.13. G^* (a) and δ (b) vs. ω for binder S: experimental data.

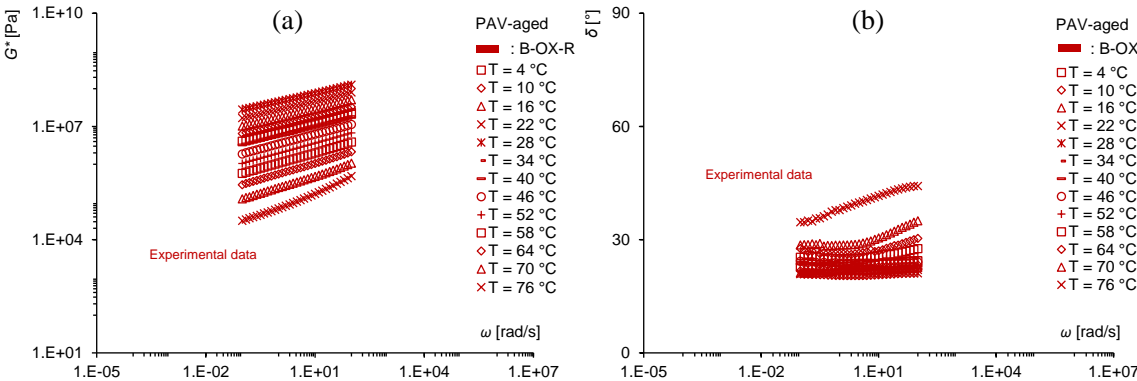


Figure 5.14. G^* (a) and δ (b) vs. ω for binder B-OX-R: experimental data.

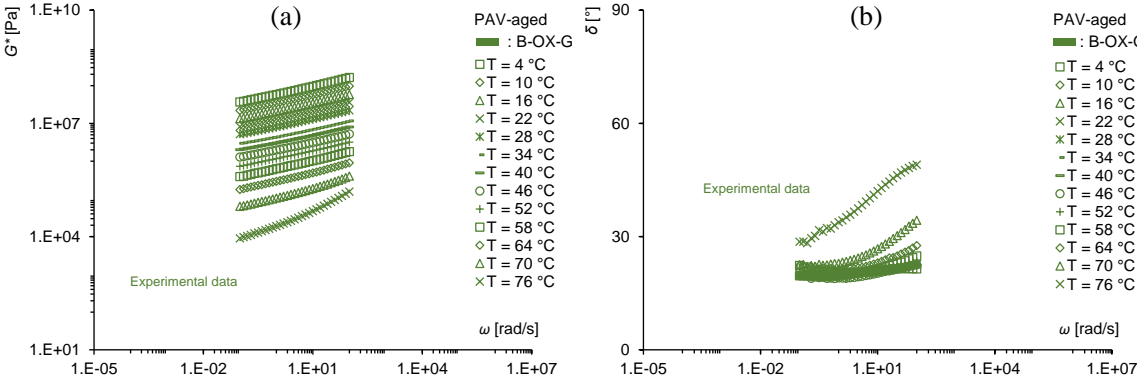


Figure 5.15. G^* (a) and δ (b) vs. ω for binder B-OX-G: experimental data.

Table 5.10. Elaboration details for the construction of B master curves.

T [°C]	4	10	16	22	34	40	46	52	58	64	70	76
$a(T)$ [-]	4.17	3.24	2.36	1.54	0.76	0	-0.54	-1.10	-1.70	-2.21	-2.61	-3.11
CAM model of G^*						CAM model of δ						
f_c [-]	130.125					R_d [-]	247.701					
k [-]	0.141					δ_m [-]	27.153					
m_e [-]	0.992					f_d [-]	32961248					
R [-]	2.118					m_d [-]	1376					
R' [-]	0.301											

In analogy, basing on FS results, the above-proposed evaluations were also carried out to compare the different responses of the prepared mastics (combining B or S binder with Lf limestone filler or Sf steel slag one). For the sake of conciseness, the following discussions are based on the representations of G^* and δ experimental data proposed in Figures 5.16–5.19. As expected, the filler addition was traduced in an upward shifting of the single curves; therefore, the global shapes of the data series closely followed those of the corresponding binder. In fact, bitumen-based mastics (B-Lf and B-Sf) exhibited increasing G^* and decreasing δ with the frequency progression, whereas resin-based ones (S-Lf and S-Sf) presented increasing G^* with the frequency progression and unconventional phase angle trends (bell-shaped curve up to 46 °C and discontinuity above that T). Indeed, considering the same binder, it is worth noting that steel slag filler Sf caused slightly higher stiffness (moreover at the lower temperature) and slightly lower phase angles which indicated a quite higher elasticity (at least up to 52 °C). This was in accordance with previous results about the AS tests and seemed to match with many literature experiences that indicate higher G^* and lower δ with the use of steel slag (with respect to limestone) mainly due to the high hardness, roughness and angularity of this kind of marginal aggregate [5.4]. In this perspective, please remind that also small discrepancies in the $G^*-\omega$ or $\delta-\omega$ plots could represent appreciable different materials, given the logarithmic scale of representations.

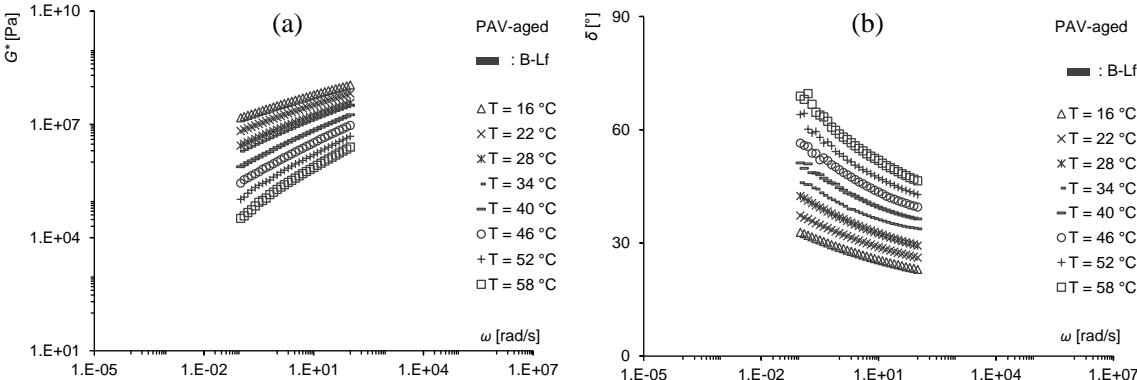


Figure 5.16. G^* (a) and δ (b) vs. ω for mastic B-Lf: experimental data.

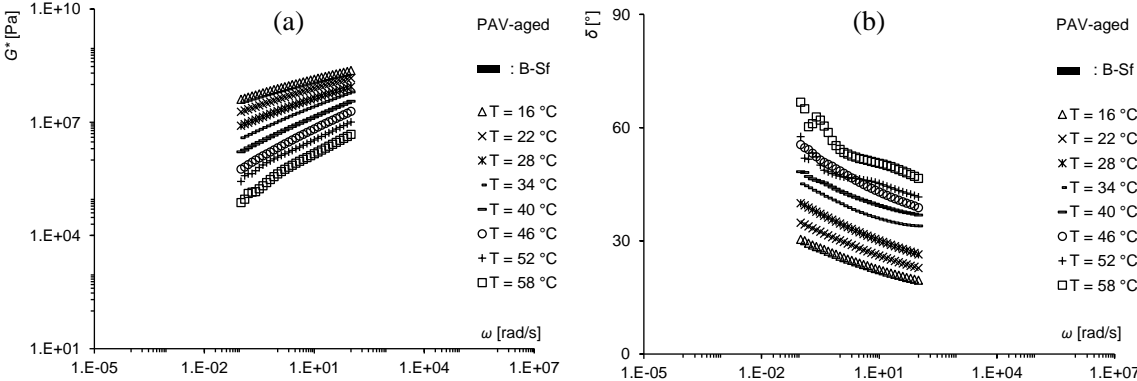


Figure 5.17. G^* (a) and δ (b) vs. ω for mastic B-Sf: experimental data.

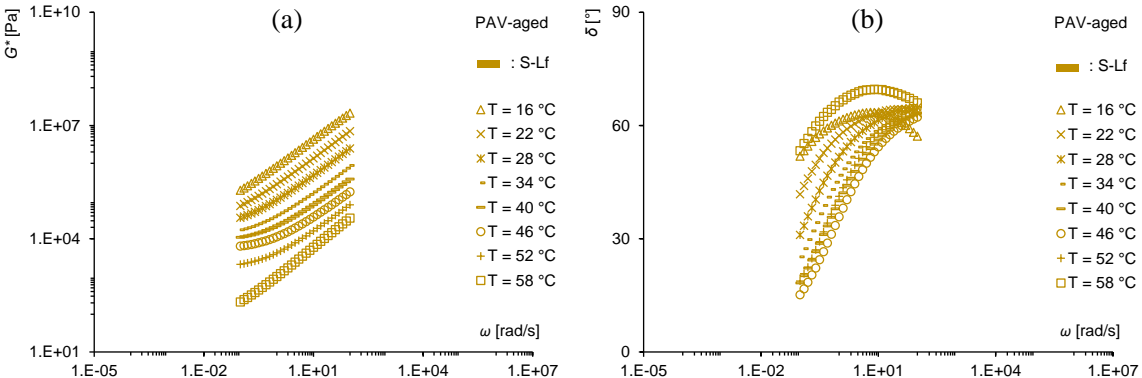


Figure 5.18. G^* (a) and δ (b) vs. ω for mastic S-Lf: experimental data.

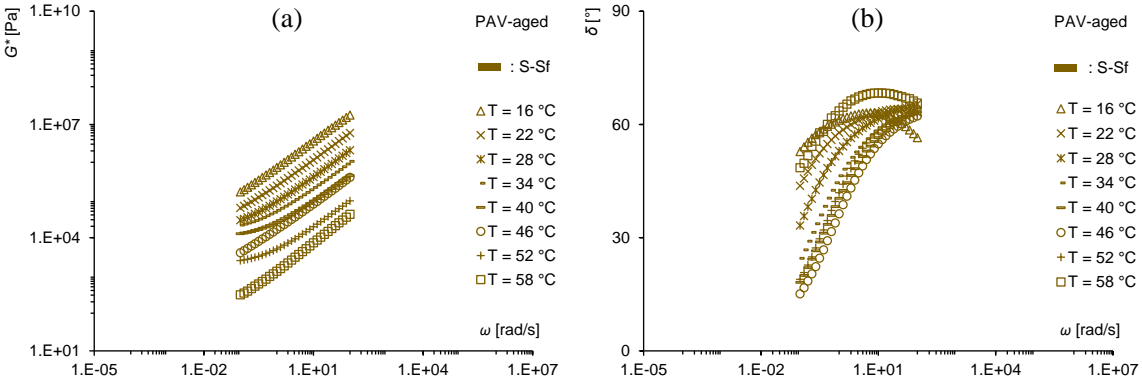


Figure 5.19. G^* (a) and δ (b) vs. ω for mastic S-Sf: experimental data.

5.1.3.3. Fatigue resistance

The fatigue resistance of binders, assessed by LAS tests, is summarized in Table 5.11 and Figure 5.20 that report the main LAS outcomes and the corresponding predicted fatigue lines, respectively. Data for B-OX-R and B-OX-G are not presented because of the impossibility of applying the linear amplitude sweep to the pigmented-bitumens (some constrains were faced during the operational test phases). Likely, the high stiffnesses of B-OXs caused the failure of the procedure since the shear stress developed during the accelerated-damage (second) phase reached the maximum values within the first test instants and made impossible the above-detailed mathematical elaboration of the experimental readings. First, the soundness of the obtained results seems to be confirmed by the fact that they were in accordance with those of previous studies on traditional bitumens [5.5]. Studying B and S, the derived fatigue curves (Figure 5.20a) indicated a significant improvement of the fatigue resistance in the case S (with a substantial increase of the number of cycles to failure at any fixed strain level). These findings seemed to agree with the main linear visco-elastic rheological properties discussed in the previous sections, where a reduced stiffness for S was highlighted at the intermediate temperatures (LAS tests were carried out at 20 °C); this should lead to a higher ductility of the synthetic binder, thus to the reduction of the cracking phenomena. Fatigue *B* parameters seemed also to indicate

slightly higher strain dependency for S (quite steeper S fatigue line). Figure 5.20b illustrates also the produced shear stress (during LAS damage): the lower stiffness of S (at 20 °C) led to lower τ , at fixed strain levels, up to the peak value (failure) of B, as well as to a noticeably higher damage at failure D_f (see Table 5.11). Thus, slower G^* reduction and more gradual damage accumulation for S were reasonably possible.

Table 5.11. LAS calculated parameters.

Material	m [-]	α [-]	C_1 [-]	C_2 [-]	D_f [-]	A [-]	B [-]
B	0.6749	1.4817	0.0872	0.5624	14.517	7970	2.963
S	0.7681	1.3019	0.0365	0.6264	45.484	60419	2.604
B-OX-R	n.a.*	n.a.*	n.a.*	n.a.*	n.a.*	n.a.*	n.a.*
B-OX-G	n.a.*	n.a.*	n.a.*	n.a.*	n.a.*	n.a.*	n.a.*

* n.a.: not-available data

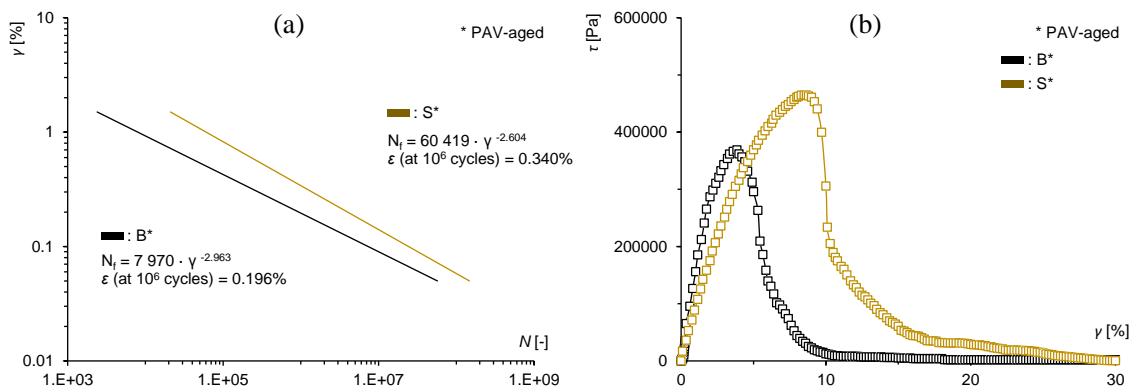


Figure 5.20. Binder's LAS results: fatigue law – γ vs. N (a) and shear stress evolution – τ vs. γ (b).

An additional discussion on binders' behaviors can be also proposed considering the performance-based standard specifications proposed by AASHTO T-315, which is used to identify acceptable in-service temperatures (in particular concerning the mid-range temperature performance used for the conventional Performance Grade – PG – classification). In this sense, the $G^* \cdot \sin \delta$ parameter, i.e. the combination of complex modulus and phase angle, is reported as a function of the temperature with comparison purposes (see Table 5.12). Depending on the selected traffic class (“S” or “H”, “V” and “E”), it must be by up to $5 \cdot 10^6$ or $6 \cdot 10^6$ Pa, respectively, in order to ensure adequate responses against the fatigue failure. Analyzing the results, temperatures of 28, 16, 40 and 34 °C were identified for B, S, B-OX-R and B-OX-G, respectively, regardless the chosen traffic class. Thus, according to the above-presented LAS readings, resin S seemed able to guarantee better fatigue resistances with respect to B; this agreed also with the softer behavior of S, since the stiffness is widely considered a possible threat for the fatigue resistance because of the possible embrittlement suffered by binders with higher moduli [5.6]. Then, despite the inefficacy of the LAS tests for B-OX binders, greater classification temperatures (40 and 34 °C) were supposed reasonable in view of the higher stiffness of

such bitumens. However, this kind of products were not early considered unsatisfactory in terms of fatigue resistance also because of the high elasticities identified for B-OX-R and B-OX-G – see Figure 5.11 (a prevalent elastic response is thought crucial against the brittleness and the subsequent fatigue phenomenon [5.6]). Thus, more accurate fatigue resistance evaluations will be rationally obtained further, analyzing such aspect at the mixture-scale.

Table 5.12. Binder's $G^* \cdot \sin \delta$ as a function of T (AASHTO PG classification).

Material	B			S		
Aging	PAV			PAV		
T	G^* [Pa]	δ [°]	$G^* \cdot \sin \delta$ [Pa]	G^* [Pa]	δ [°]	$G^* \cdot \sin \delta$ [Pa]
4 °C	94268982	26.53	42112228	26337911	47.78	19505068
10 °C	48008401	31.35	24973707	8052498	57.71	6807220
16 °C	22828247	36.19	13478215	2333599	62.48	2069551
22 °C	10313115	41.09	6778379	734843	62.83	653757
28 °C	4420499	45.90	3174439	262098	61.11	229480
34 °C	1780557	50.81	1379972	101000	61.20	88507
40 °C	790486	54.16	640821	43200	59.00	37030
46 °C	346042	57.51	291878	19300	57.70	16314
52 °C	155430	60.76	135628	8330	59.90	7207
58 °C	70764	64.13	63670	3410	68.60	3175
64 °C	32957	67.71	30494	1490	78.00	1457
70 °C	15182	71.40	14389	822	82.40	815
76 °C	7466	75.19	7218	480	84.30	478

Material	B-OX-R			B-OX-G		
Aging	PAV			PAV		
T	G^* [Pa]	δ [°]	$G^* \cdot \sin \delta$ [Pa]	G^* [Pa]	δ [°]	$G^* \cdot \sin \delta$ [Pa]
4 °C	11549241	23.42	4590105	95565147	21.01	34266482
10 °C	18510504	22.88	7195588	56543326	20.87	20144875
16 °C	29215216	22.13	11007109	34425585	20.80	12227236
22 °C	46591500	21.35	16965021	21240739	21.11	7651164
28 °C	75573036	20.64	26641220	17229127	21.28	6252338
34 °C	16647671	21.87	6201855	7015794	20.63	2471944
40 °C	10435270	22.80	4043276	4812128	20.47	1682922
46 °C	6244236	23.79	2518775	3108114	20.31	1078682
52 °C	3617936	24.72	1513073	1870654	20.56	656875
58 °C	1987428	25.79	864763	1021480	21.42	373126
64 °C	1048135	27.04	476461	485822	23.05	190242
70 °C	476185	30.47	241494	187796	26.78	84600
76 °C	163587	41.63	108665	47242	42.03	31631

5.1.3.4. Permanent deformation resistance

As far as permanent deformation resistance is concerned, MSCR test results about binders are presented in the following Figure 5.21, where the experimental data collected are reported in terms of strain evolution over time. Firstly, it has to be noticed that the strain scale was ad-hoc set depending on the binder type in order to appreciate the curves' evolutions. Thus, it is definitely evident that B-OX-R and B-OX-G (Figure 5.21c and 5.21d, respectively) were characterized by sensibly lower accumulated strains (about one extra order of magnitude). Moreover, they seemed to present a greater recovery aptitude after the creep phases; this was reasonable attributed to the higher stiffness and elasticity of these products with respect to B and S. In addition, only at 76 °C the deformation started to evidently increase (B-OX-R and B-OX-G series at 58, 64 and 70 °C presented very similar strain accumulations). Oppositely, B and S curves were homogeneously-spaced, depending on the test temperature, indicating a greater *T* susceptibility. In accordance with all previous findings, the softer S tent to accumulate greater deformations at the imposed loads since it is recognized that a reduced stiffness can favor the rutting potential [5.7, 5.8]. In particular, S and B showed a comparable behavior at 58 °C, whereas higher strains were measured for S samples at the higher analyzed temperatures (64, 70 and 76 °C).

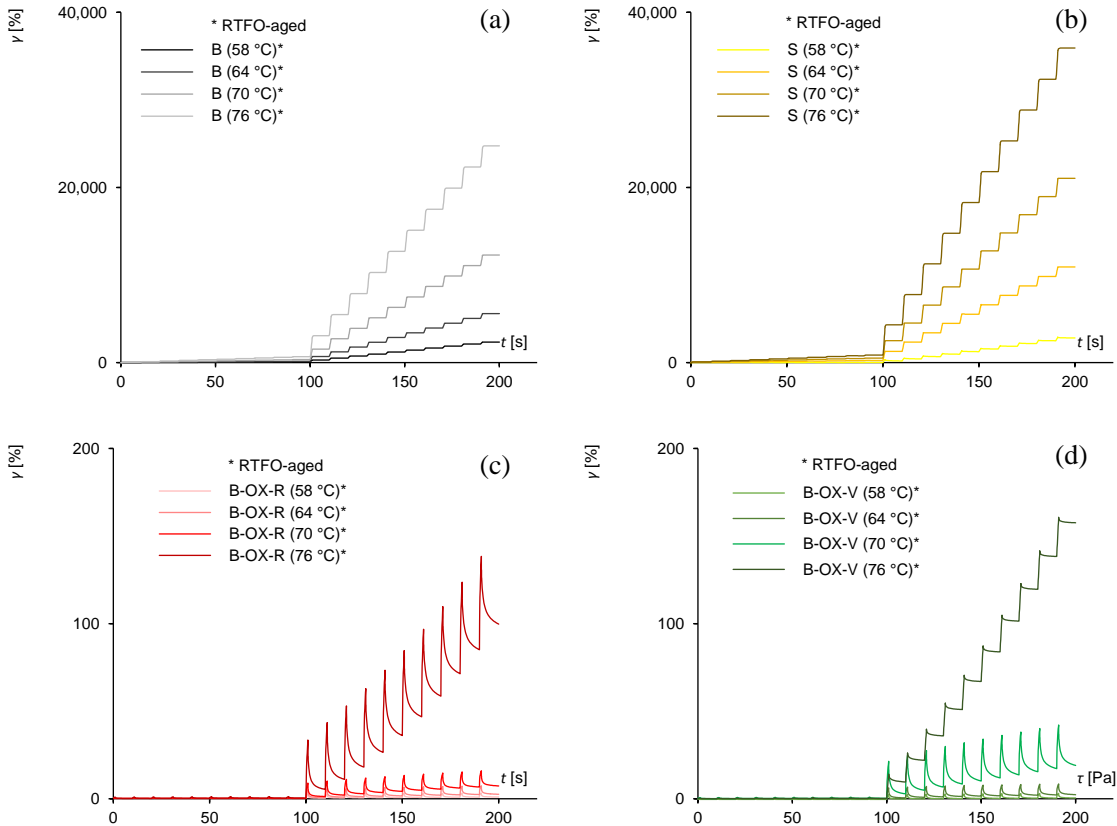


Figure 5.21. γ evolution on time: binder B (a), S (b), B-OX-R (c) and B-OX-G (d).

Further information are then given in Figures 5.22 and 5.23, where $R\%$ and J_{nr}/J_{TOT} are depicted, respectively. The percent recovery $R\%$ highlighted the different stress and temperature dependencies of the studied binders; in particular, a marked aptitude to the recovery was demonstrated by B-OX binders, regardless the applied stress or temperature. Only at 3.2 kPa and 76 °C, B-OX-R and B-OX-B owned $R\%$ lower than 90÷95%. A notable tendency to the elastic recovery was also found for S resin for temperature up to 58 °C; here, $R\%$ of S was equal at 88% (at 0.1 kPa) and 23% (at 3.2 kPa), thus sensibly different from that of the reference B (equal to 3 and 1%, respectively). Such discrepancies were progressively attenuated increasing the temperature (after 70 °C, S and B were completely comparable). However, considering the different stiffness and visco-elastic properties of the binders, additional information should be drawn analyzing J_{nr}/J_{TOT} , i.e. the non-recoverable creep compliance referred to the total compliance accumulated during the loading cycles. In this sense, S seemed effectively able to prevent the permanent deformations only at 58 °C (J_{nr}/J_{TOT} equal to 12% – at 0.1 kPa – and 77% – at 3.2 kPa, i.e. significantly lower than of B, equal to 95% – at 0.1 kPa – and 98% – at 3.2 kPa). Then, from 64 °C, S behavior start to approach that of the bitumen. As already identified, completely different responses were again visible for B-OX-R and B-OX-G, that were substantially able to avoid the strain accumulations (except for the last loading combination with τ of 3.2 kPa and T of 76 °C). All this readings accorded with the above-described properties of binders: between 58 and 64 °C, S was characterized by a behavioral transition (see Figure 5.13b); in turn, the higher elasticity of oxide-pigmented bitumens (see Cole-Cole diagram on Figure 5.11c or Figure 5.11d) prevented the permanent deformations. As proposed in the case of mid-range service temperatures, rutting potentials were evaluated also determining the PG temperature concerning the highest T ; in this case, Table 5.13 reports the J_{nr} (at 3.2 kPa) and the $J_{nr-diff}$ (between 0.1 and 3.2 kPa) parameters proposed by the AASHTO TP-70 standard to classify the short-term aged binders. Depending on the traffic classes (“S”, “H”, “V” or “E”), the following requirements must be respectively matched to select the upper temperature: maximum J_{nr} of 4 Pa⁻¹ and $J_{nr-diff}$ of 75%, maximum J_{nr} of 2 Pa⁻¹ and $J_{nr-diff}$ of 75%, maximum J_{nr} of 1 Pa⁻¹ and $J_{nr-diff}$ of 75%, or maximum J_{nr} of 0.5 Pa⁻¹ and $J_{nr-diff}$ of 75%. The obtained results agreed with $R\%$ and J_{nr}/J_{TOT} indications; fixing the traffic class, S generally presented a lower PG upper temperatures with respect to B (except for the case of “V” class), thus could be supposed to present lower rutting resistance. Surprisingly, B-OX-R and B-OX-G did not show significantly higher PG temperatures with respect to B, even their marked elastic properties. However, please note that such results are strictly correlated to the $J_{nr-diff}$ parameter, i.e. the relation of the compliances at different shear stresses; considering the small values of J_{nr} (at 3.2 kPa), it could be hypothesized that the proposed requirements should not properly exemplify the rutting behavior of this kind of products (reference standard was calibrated basing on traditional, non-modified bitumens). For this reasons, B-OX-R and B-OX-G were thought to still represent the best promising binders to prevent the rutting potential, even the identified PG temperatures.

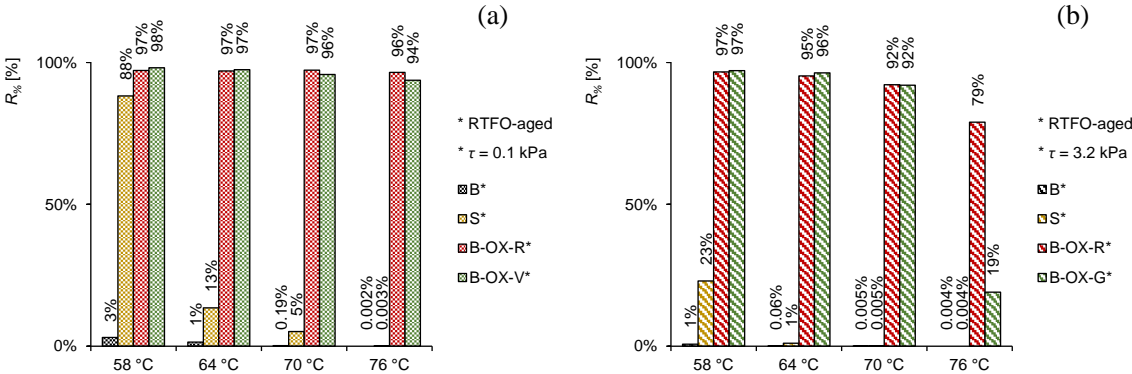


Figure 5.22. $R\%$ for binders at T of 58, 64, 70, 76 °C and τ of 0.1 (a) and 3.2 kPa (b).

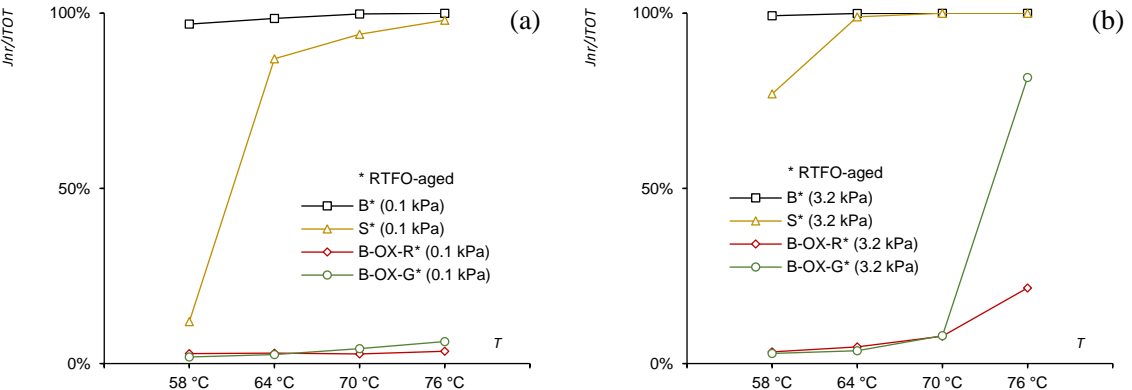


Figure 5.23. J_{nr}/J_{TOT} for binders at T of 58, 64, 70, 76 °C and τ of 0.1 (a) and 3.2 kPa (b).

Table 5.13. Binder’s J_{nr} and $J_{nr-diff}$ as a function of T (AASHTO PG classification).

Material		PG parameters				PG upper temperatures			
		58 °C	64 °C	70 °C	76 °C	“S”	“H”	“V”	“E”
B	J_{nr} [Pa ⁻¹]	0.712	1.702	3.730	7.522	76°C	64°C	56 °C	< 56°C
	$J_{nr-diff}$ [%]	7.72	8.68	7.56	7.64				
S	J_{nr} [Pa ⁻¹]	0.877	3.336	6.414	10.955	64°C	56 °C	56 °C	< 56°C
	$J_{nr-diff}$ [%]	47.13	37.83	28.55	24.04				
B-OX-R	J_{nr} [Pa ⁻¹]	0.0002	0.0007	0.0022	0.0310	64°C	64°C	64°C	64°C
	$J_{nr-diff}$ [%]	23.77	72.43	233.14	953.05				
B-OX-G	J_{nr} [Pa ⁻¹]	0.0002	0.0007	0.0022	0.0310	64°C	64°C	64°C	64°C
	$J_{nr-diff}$ [%]	56.70	47.33	119.89	2652.8				

In the case of mastics, $R\%$ and J_{nr}/J_{TOT} are illustrated in Figures 5.24 and 5.25, respectively (in order to consider significant data, results were referred only to shear stresses of 3.2 and 10 kPa). First, the stiffening contribution provided by the fillers seemed deeply important to lower the strain accumulations. In fact, since the higher the stiffness the lower the permanent deformations, the tested mastics (harder than the corresponding binders) demonstrated higher recovery percentages. The influence of fillers types seemed to indicate that, adopting the steel slag Sf, $R\%$ was enhanced regardless the binder used (with respect to the corresponding mastic prepared with limestone). This behavior was considered in

agreement with the higher stiffness always provided by Sf (harder, rougher and more angular aggregate). Overall, S-based mastics (S-Lf and S-Sf) had greater recovery values than B-based one (as for binders, such discrepancies were progressively attenuated increasing the testing temperatures). Basing on Figure 5.25, the described tendencies were followed by the J_{nr}/J_{TOT} terms (the use of Sf lowered the non-recoverable creep compliance referred to the total one in the case of both B and S). Differently from the binder case, at 58 °C, S-based materials did not show very different behaviors from B-based one: temperature and stress dependencies of mastics seemed strictly influenced by the filler typologies (at mastic-scale, stiffening contribution provided by filler became predominant against permanent deformation with respect to the visco-elastic properties of the binder).

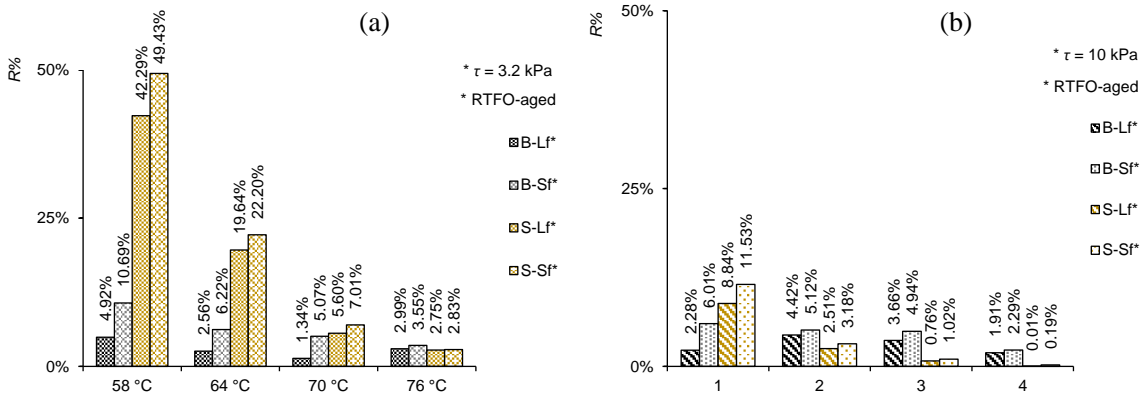


Figure 5.24. $R\%$ for mastics at T of 58, 64, 70, 76 °C and τ of 3.2 (a) and 10 kPa (b).

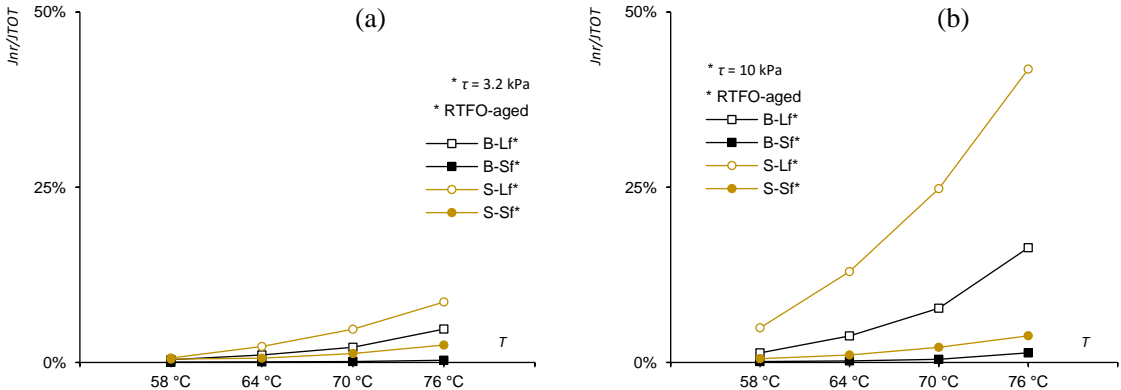


Figure 5.25. J_{nr}/J_{TOT} for mastics at T of 58, 64, 70, 76 °C and τ of 0.1 (a) and 3.2 kPa (b).

Overall, the identified permanent deformation resistances must be also considered in view of the final product applications. Referring such mechanical results to the mixture manufacturing and in-field functioning, it is worth highlighting that, at given environmental conditions (air temperature, solar radiation, humidity, wind, etc.), pavements realized using clear or colored binders should achieve distinctly lower in-service temperatures than traditional “black” one, mainly thanks to their chromatic and thermal properties [5.9]. Thus, a proper comparison regarding the rutting resistances at high-temperatures should be carried out taking into account the different temperatures to which cool and traditional materials

will be subjected. For these reasons, further focuses about such aspects are postponed to the following parts of the study, where the mechanical properties will be analyzed at the mixture-scale also considering the thermal properties of the materials and the results of the planned thermal monitoring.

5.2. Loose blends

The paragraph briefly describes the testing activity performed at the blend-scale in order to investigate the affinity between some of the studied binders and aggregates.

5.2.1. Materials

Six different types of bitumen-aggregate loose blends were produced combining the bitumen B, the synthetic resin S and a B-OX binder (using the red one as example) with different aggregate typologies (some of them were further used to produce the mixtures). Sieving suitable gradations of the different aggregate types, adequate quantities passing the 10 mm sieve and retained on the 6 mm one were selected according to EN 12697-11 standard. Firstly, 60.0 g of limestone and 3.0 g of the bitumen B were used to comply the dosage suggested by the standard (for the conventional reference blend). Then, basing on such proportion (binder of 13.4% by aggregate volume), other blends were produced maintaining constant the binder-aggregate volumetric ratio in order to obtain always the same aggregate coverage. Thus, the different specific gravities of aggregates and binders were considered to produce analog film thicknesses in the blends. Table 5.14 presents the different blends tested and the final quantities of components utilized. Mixing operations were performed by hands heating the materials according to the protocol already employed in the case of the mastic preparations.

Table 5.14. Composition (by weight) of binder-aggregate loose blends.

Blend code	Binder		Aggregate	
	Type	Quantity	Type	Quantity
B-La	Bitumen (B)	3.0 g	Limestone (La)	60.0 g
S-La	Resin (S)	3.0 g	Limestone (La)	88.0 g
S-Wa	Resin (S)	3.0 g	White marble (Wa)	89.0 g
S-Ya	Resin (S)	3.0 g	Yellow marble (Ya)	81.0 g
S-Pa	Resin (S)	3.0 g	Pink stone (Pa)	85.0 g
B-OX-La	Bitumen + oxide (B-OX)	3.0 g	Limestone (La)	58.0 g

5.2.2. Adhesion properties

As anticipated, AST was used to evaluate the percentages of binder stripping after a boiling procedure in order to establish the different bitumen-aggregate affinities, which can be considered a strict indication of the susceptibility to moisture damages. The results of the DIP approach are illustrated in the following Figures 5.26 and 5.27.



Figure 5.26. Example of stripping results: DIP output (original samples before AST).

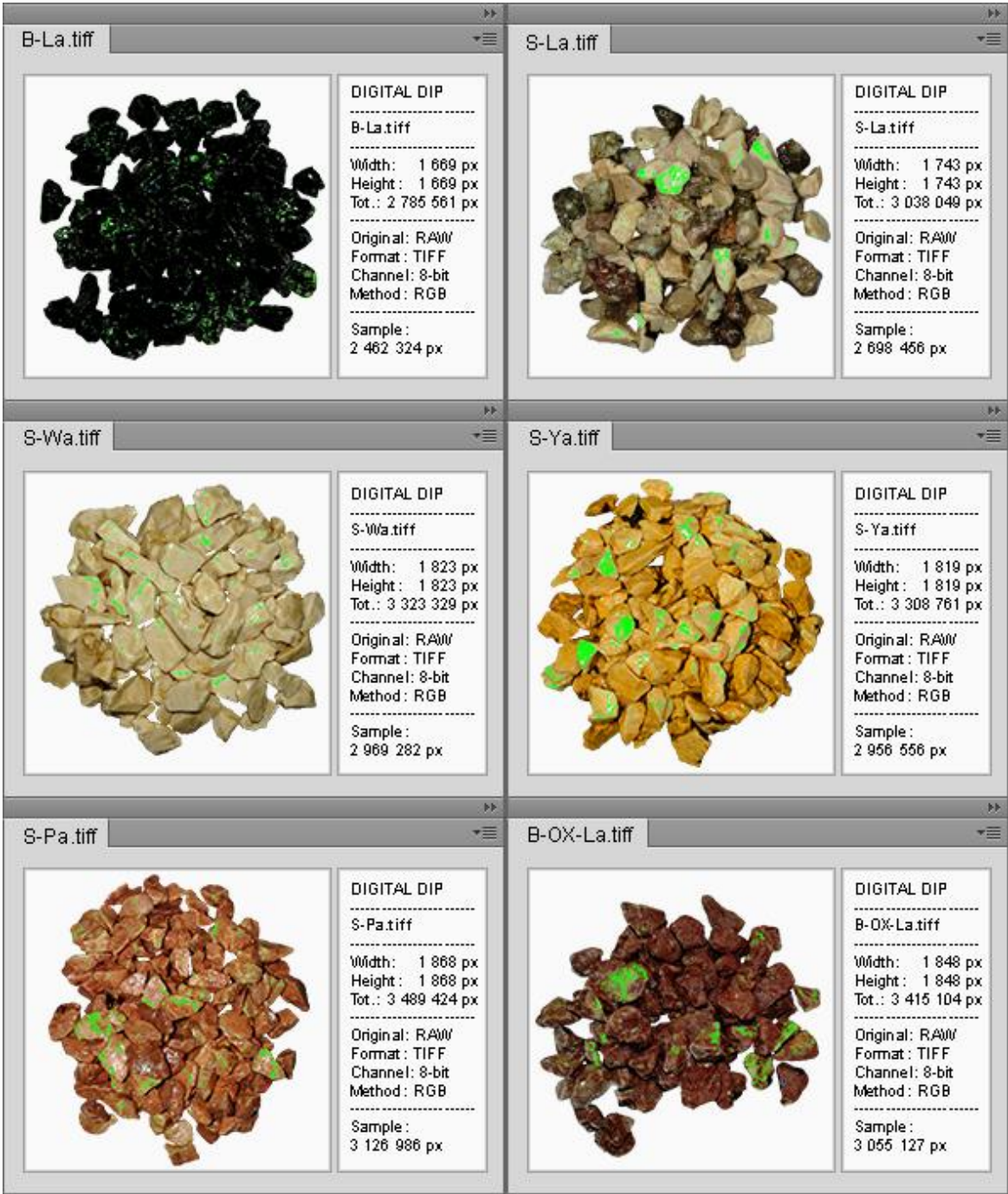


Figure 5.27. Example of stripping results: DIP output (composite samples after AST).

Table 5.15 reports the results of stripping susceptibility in terms of binder coverage percentage after the AST. As it can be observed, no significant stripping phenomena were detected analyzing the various binder-aggregate combinations. Blends containing resin furnished residual binder coverages slightly variable with respect to the reference blend (B-La), thus comparable moisture susceptibilities were supposed regardless the nature of the utilized aggregate. When oxide-pigments were added to the bitumen (B-OX-La) a certain

increase of the stripping aptitude was observed; otherwise, such a result was considered satisfactory (residual binder coverage near 90%).

Table 5.15. AST results about binder-aggregate loose blend's adhesion.

Blend code	Pixels			Binder residual coverage
	Analyzed (total)	Coated	Stripped	
B-La	2462324	2377620	84704	96.56%
S-La	2698456	2492024	206432	92.35%
S-Wa	2969282	2930978	38304	98.71%
S-Ya	2956556	2822920	133636	95.48%
B-Pa	3126986	2906221	220765	92.94%
B-OX-La	3055127	2677819	377308	87.65%

5.3. Mixtures

The following paragraphs present the main results collected during the experimentation carried out at the mixture-scale. First, produced mixtures, along with their main properties, will be presented. Then, chromatic, thermal and mechanical characteristics will be detailed and discussed.

5.3.1. Materials

5.3.1.1. Conventional asphalt mixtures

The conventional asphalt mixture (coded BL) was constituted using the reference binder B and natural limestone aggregates La (whose properties are following presented in Table 5.16); hereafter, BL will be intended as the reference mixture for the entire experimentation. The selected aggregate gradation is presented in Figure 5.28: it was composed based on a typical envelop for wearing courses proposed by Italian technical prescriptions, also taking into account the different granulometric distributions of the available stockpiles.

Table 5.16. Basic properties of La aggregate (referred to different stockpiles).

Property	Standard	Unit	La
Particle density	EN 1097-6	Mg/m ³	2.74
Flakiness index	EN 933-3	%	10.3
Shape index	EN 933-4	%	13.5
Los Angele coefficient	EN 1097-2	%	16.0
Sand equivalent	EN 933-8	%	78.0
Liquid limit (Atterberg)	ASTM D 4318-10	%	26.0
Plastic limit (Atterberg)	ASTM D 4318-10	%	0.0
Plasticity index (Atterberg)	ASTM D 4318-10	%	26.0

The optimum binder content was established performing the Marshall optimization method; the details of the procedure are presented in Table 5.17 and Figure 5.29; final B dosage was set equal to 5.5% by the aggregate weight. Figure 5.30 illustrate the utilized aggregate and one of the BL slab produced (compaction at about 160 °C according to EN 12697-33 standard); the typical black color was obtained using the bitumen. Several slabs were obtained (height of 50 mm); some of them were used for the chromatic and thermal evaluations, other ones were employed to produce cylindrical or prismatic samples (by sawing) for the mechanical testing.

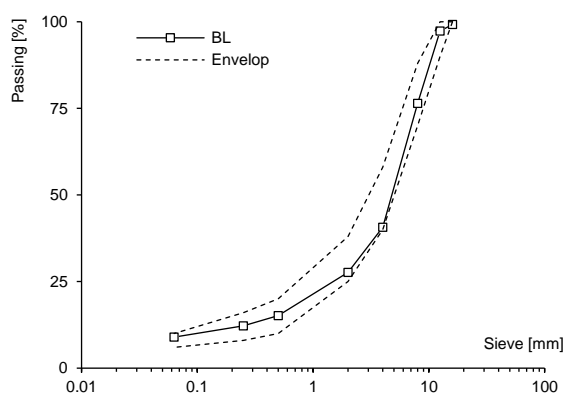


Figure 5.28. Selected gradation for BL mixture.

Table 5.17. Marshall tests and optimization details.

B content [%]	Stability [KN]	Flow [mm]	Quotient [KN/mm]	Voids [%]	Density [g/cm ³]
4.5	6.858	3.733	1.837	7.430	2.463
5.0	7.921	4.301	1.842	6.905	2.470
5.5	9.853	5.023	1.961	5.657	2.495
6.0	8.126	6.655	1.221	4.701	2.514

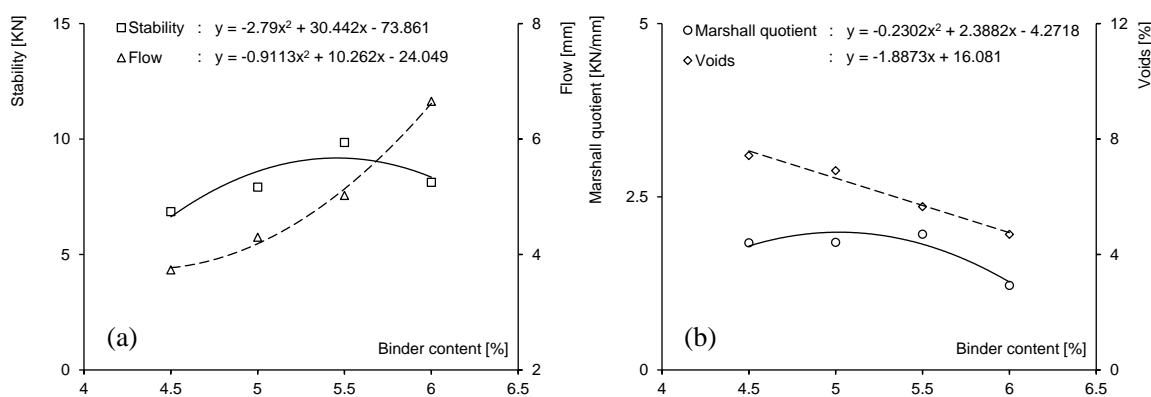


Figure 5.29. Optimization of BL mixture: stability, flow (a), Marshall quotient and voids (b).



Figure 5.30. Limestone aggregate (left) and example of produced slab (BL mixture – right).

5.3.1.2. Resin-based mixtures

Four different types of resin-based mixtures were produced utilizing the S binder. In this case, various aggregates (of different colors) were alternatively used considering that the transparency of the resin could exalt the aggregate chromaticity and led to mixture of different clearness and tonality. Such aggregates were a limestone (La), a white marble (Wa), a yellow-Siena marble (Ya) and a coral-pink stone (Pa); their basic properties are presented in Table 5.18.

Table 5.18. Basic properties of La, Wa, Ya and Pa aggregates (referred to different stockpiles).

Property	Standard	Unit	La	Wa	Ya	Pa
Particle density	EN 1097-6	Mg/m ³	2.74	2.76	2.52	2.65
Flakiness index	EN 933-3	%	10.3	19.0	17.9	17.2
Shape index	EN 933-4	%	13.5	19.9	18.0	9.9
Los Angele coefficient	EN 1097-2	%	16.0	23.0	21.0	20.0
Sand equivalent	EN 933-8	%	78.0	85.0	89.0	73.0
Liquid limit (Atterberg)	ASTM D 4318-10	%	26.0	24.0	17.0	20.0
Plastic limit (Atterberg)	ASTM D 4318-10	%	0.0	0.0	16.0	15.0
Plasticity index (Atterberg)	ASTM D 4318-10	%	26.0	24.0	1.0	5.0

Mixing La, Wa, Ya and Pa aggregates with binder S (at about 160 °C), the SL, SW, SY and SP mixtures were prepared, respectively. The gradations selected to compose them are presented in Figure 5.31: these were ad-hoc calibrated based on a typical envelop for wearing courses proposed by Italian technical prescriptions, also depending on the available aggregate stockpiles.

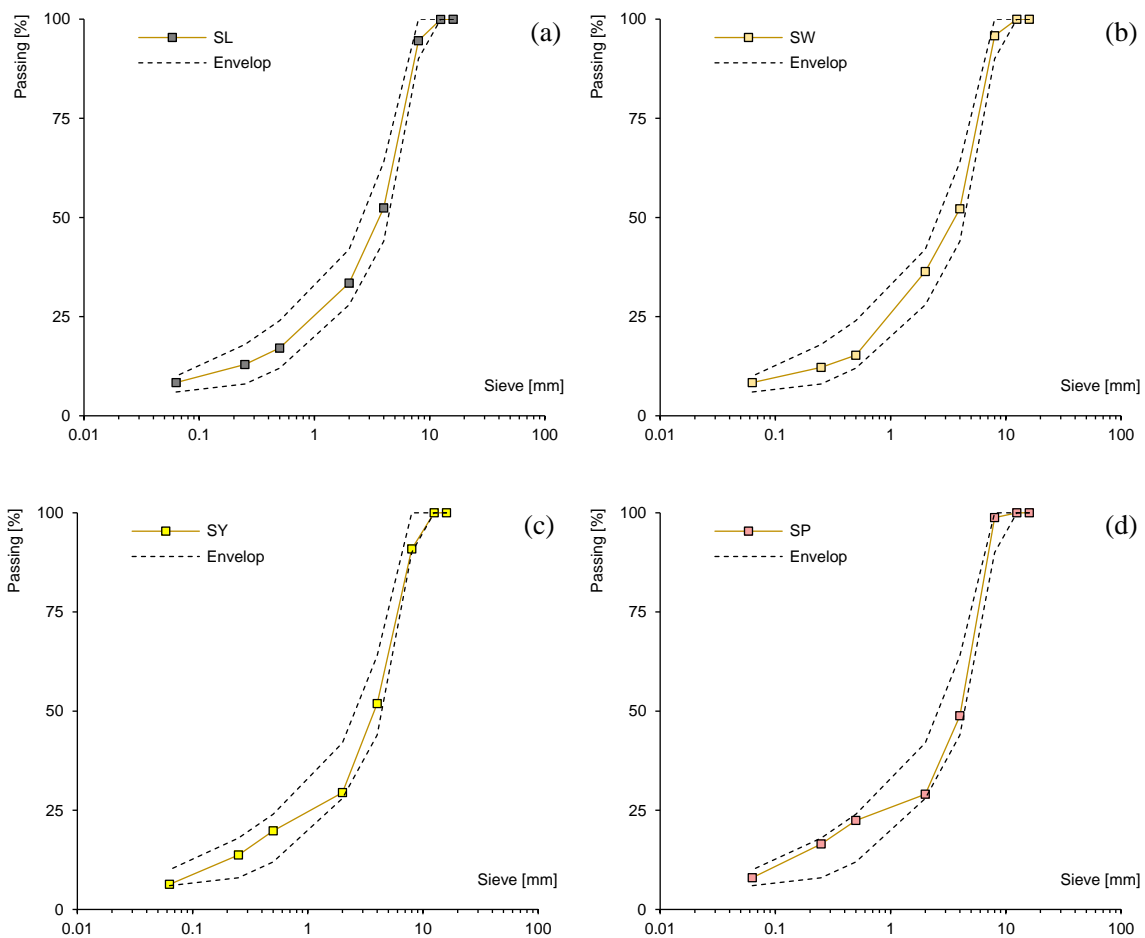


Figure 5.31. Selected gradation for SL (a), SW (b), SY (c) and SP (d) mixtures.

In this case, the optimum binder content was determined for SL mixture: the procedure details are given in Table 5.19 and Figure 5.32. Final S dosage was selected equal to 7.0% by the limestone aggregate weight. Based on such percentage, the same S content was reproduced (in volumetric terms) for SW, SY and SP mixes (considering the different aggregate specific gravities). Again, slabs (50 mm high), cylindrical specimens and prismatic samples were produced in the laboratory. Figures 5.33–5.36 illustrates the utilized aggregates and the corresponding S-based slabs obtained.

Table 5.19. Marshall tests and optimization details.

S content [%]	Stability [KN]	Flow [mm]	Quotient [KN/mm]	Voids [%]	Density [g/cm ³]
6.0	4.351	4.610	0.944	8.261	2.420
6.5	6.654	4.717	1.411	7.219	2.439
7.0	6.816	5.230	1.303	6.545	2.451
7.5	6.326	5.955	1.062	5.236	2.478

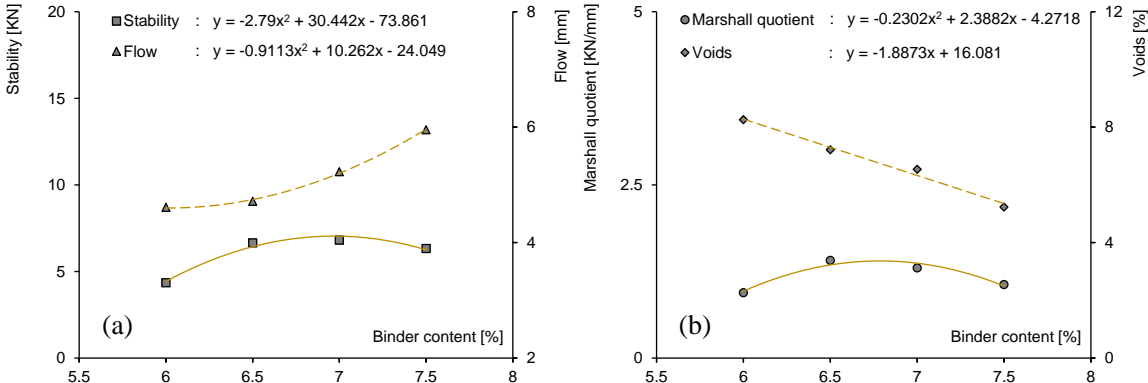


Figure 5.32. Optimization of SL mixture: stability, flow (a), Marshall quotient and voids (b).



Figure 5.33. Limestone aggregate (left) and SL slab (right).



Figure 5.34. White marble aggregate (left) and SW slab (right).



Figure 5.35. Yellow-Siena marble aggregate (left) and SY slab (right).



Figure 5.36. Coral-pink stone aggregate (left) and SP slab (right).

5.3.1.3. Oxide-colored mixtures

Fully-colored mixtures were produced using the B-OX binders, i.e. the reference B blended with oxide-pigments. Given the peculiarity of such technology, they were classified as “fully-colored” since the pigments were dispersed in all the mixture and colored all the concrete (also the inside matrix). Four different tonalities were used to assess eventual differences in terms of thermal and mechanical performance. Red and green oxide pellets were those previously studied at the binder-scale and were based on iron and chromium compounds, respectively; then, white and yellow oxides were joined to the experimentation (they were based on titanium dioxide and iron compounds, respectively). For the sake of clarity, all oxides will be hereafter coded as (oxR), (oxG), (oxW), (oxY), respectively. Accordingly, the obtained mixtures (prepared using B, one oxide and limestone aggregate) will be named as: BL(oxR), BL(oxG), BL(oxW), BL(oxY). Since BL constituted the base for the mixture’s preparation, the aggregate gradations was omitted (it was the same already reported in Figure 5.28). At the mixture-scale, the oxide pellets were directly added to the binder and the aggregate during the mixing operations (performed at about 160 °C). OX dosage was set equal to 5.0 % by the aggregate weight, according to producer indications. Since no specific alteration in the mix design was reported by the manufacturer, B dosage was maintained equal to 5.5%, based on the previous-identified optimum content for BL mixture (this allowed also to avoid the introduction of a further variable to the study). However, some Marshall tests were also carried out for each mixture (using the described contents) for comparison purposes: results presented within Figure 5.37 clearly indicated analog working mechanisms of the oxides, regardless the employed tonality. Slabs (50 mm high), cylindrical and prismatic samples were again produced in the laboratory. The following Figures 5.38–5.41 depicts the utilized oxide-pigments and the corresponding BL-based slabs obtained.

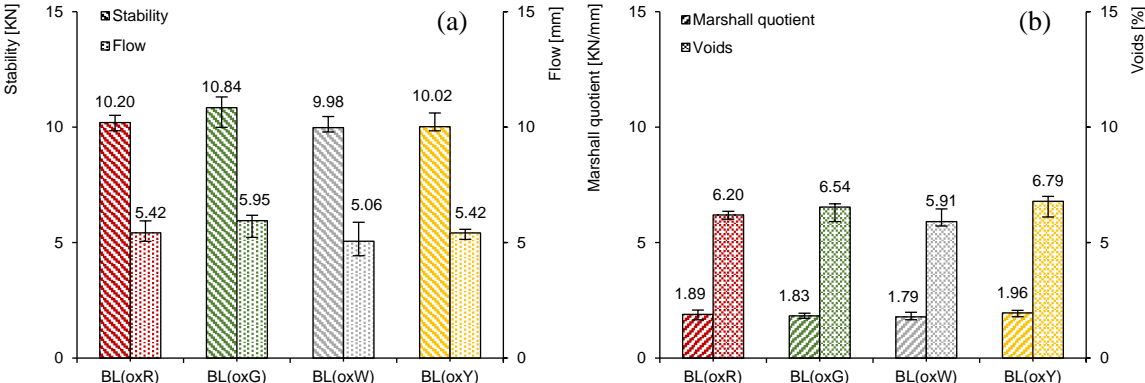


Figure 5.37. Marshall results for oxide fully-colored BL-based mixtures: stability (a) and flow (b).



Figure 5.38. Red oxide-pigment (left) and BL(oxR) slab (right).

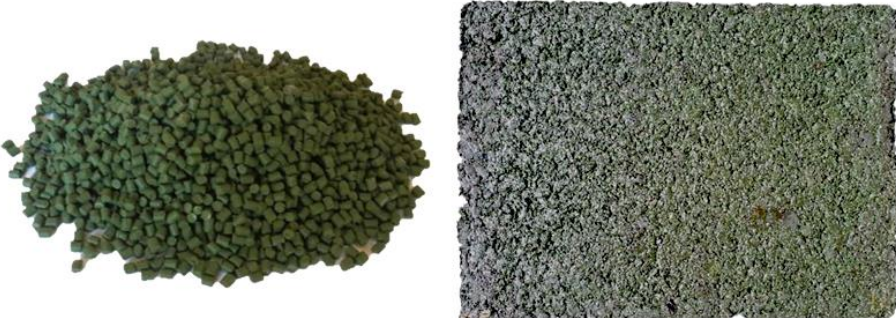


Figure 5.39. Green oxide-pigment (left) and BL(oxG) slab (right).



Figure 5.40. White oxide-pigment (left) and BL(oxW) slab (right).



Figure 5.41. Yellow oxide-pigment (left) and BL(oxY) slab (right).

5.3.1.4. Surface-treated mixtures

The last typology of slabs was produced painting with different products and colors some conventional BL mixtures. Therefore, the mixes' components were the reference bitumen B and the limestone aggregates La: gradation and binder content were those above-presented (see paragraph 5.3.1.1). The surface treatments were applied above the slab surfaces once compacted and cooled; resins (hereafter coded r) or mortars (hereafter named m) were dosed at 2 kg/m^2 according to the producer instructions (dosage and surface application were the same for both products, for the sake of comparison). The two products mainly differed for their composition: r consisted in a polymeric-based resin and additives, whereas m was a compound of vinyl constituents, inorganic colorants and quartz powders (different products owned very similar densities, ranging around 1.50 g/cm^3). Red, green, yellow and blue colors were applied in the case of both resins and mortars. The codes hereafter adopted for the produced mixtures are: BL(rR), BL(rG), BL(rY), BL(rB) and BL(mR), BL(mG), BL(mY), BL(mB) for red, green, yellow or blue resin or mortar, respectively. Supposing that the surface painting did not affect the mechanical strengths, no specific evaluations about the Marshall parameters were provided. As a summary, the following Figures 5.42–5.45 present the produced slabs.



Figure 5.42. Red slabs painted with resin (left) or mortar (right).



Figure 5.43. Green slabs painted with resin (left) or mortar (right).



Figure 5.44. Yellow slabs painted with resin (left) or mortar (right).

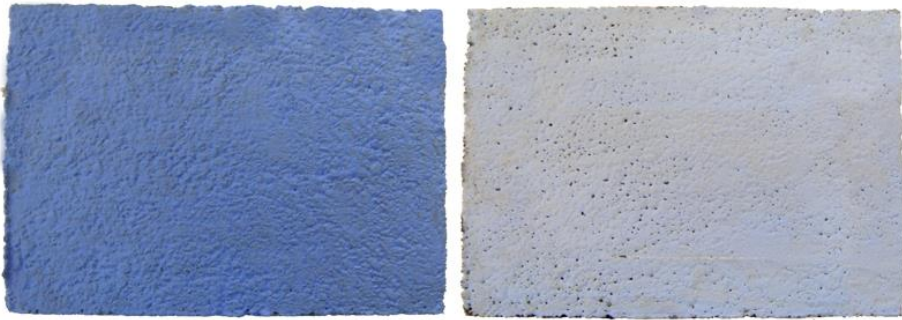


Figure 5.45. Blue slabs painted with resin (left) or mortar (right).

As a conclusion, Table 5.20 summarizes the characteristics of all the produced mixture and gives the codifications hereafter adopted to identify the mixtures/slabs.

Table 5.20. Summary of mixtures' compositions.

Mixture	Binder		Pigment	Aggregate				Painting	
	B	S	ox	La	Wa	Ya	Pa	r	m
BL	✓ (5.5%)	✗	✗	✓	✗	✗	✗	✗	✗
SL	✗	✓ (7.0%)	✗	✓	✗	✗	✗	✗	✗
SW	✗	✓ (7.0%)	✗	✗	✓	✗	✗	✗	✗
SY	✗	✓ (7.0%)	✗	✗	✗	✓	✗	✗	✗
SP	✗	✓ (7.0%)	✗	✗	✗	✗	✓	✗	✗
BL(oxR)	✓ (5.5%)	✗	✓ (R: 5%)	✓	✗	✗	✗	✗	✗
BL(oxG)	✓ (5.5%)	✗	✓ (G: 5%)	✓	✗	✗	✗	✗	✗
BL(oxW)	✓ (5.5%)	✗	✓ (W: 5%)	✓	✗	✗	✗	✗	✗
BL(oxY)	✓ (5.5%)	✗	✓ (Y: 5%)	✓	✗	✗	✗	✗	✗
BL(rR)	✓ (5.5%)	✗	✗	✓	✗	✗	✗	✓ (R)	✗
BL(rG)	✓ (5.5%)	✗	✗	✓	✗	✗	✗	✓ (G)	✗
BL(rY)	✓ (5.5%)	✗	✗	✓	✗	✗	✗	✓ (Y)	✗
BL(rB)	✓ (5.5%)	✗	✗	✓	✗	✗	✗	✓ (B)	✗
BL(mR)	✓ (5.5%)	✗	✗	✓	✗	✗	✗	✗	✓ (R)
BL(mG)	✓ (5.5%)	✗	✗	✓	✗	✗	✗	✗	✓ (G)
BL(mY)	✓ (5.5%)	✗	✗	✓	✗	✗	✗	✗	✓ (Y)
BL(mB)	✓ (5.5%)	✗	✗	✓	✗	✗	✗	✗	✓ (B)

Legend:

- (B) conventional reference bitumen (binder)
- (S) clear synthetic resin (binder)
- (ox) oxide pigment (pellet)
- (La) limestone aggregate
- (Wa) with marble aggregate
- (Ya) yellow-Siena marble aggregate
- (Pa) coral-pink stone aggregate
- (r) resin surface treatment (painting)
- (m) mortar surface treatment (painting)
- (R) color (red)
- (G) color (green)
- (W) color (white)
- (Y) color (yellow)
- (B) color (blue)

5.3.2. Mixture’s testing plan

The paragraph is aimed at defining the experimental activity performed at the mixture-scale: once described the produced mixtures, the operations and tests performed on mixes’ slabs and samples are following listed: in this perspective, Figure 5.46 summarizes the experimental plan.

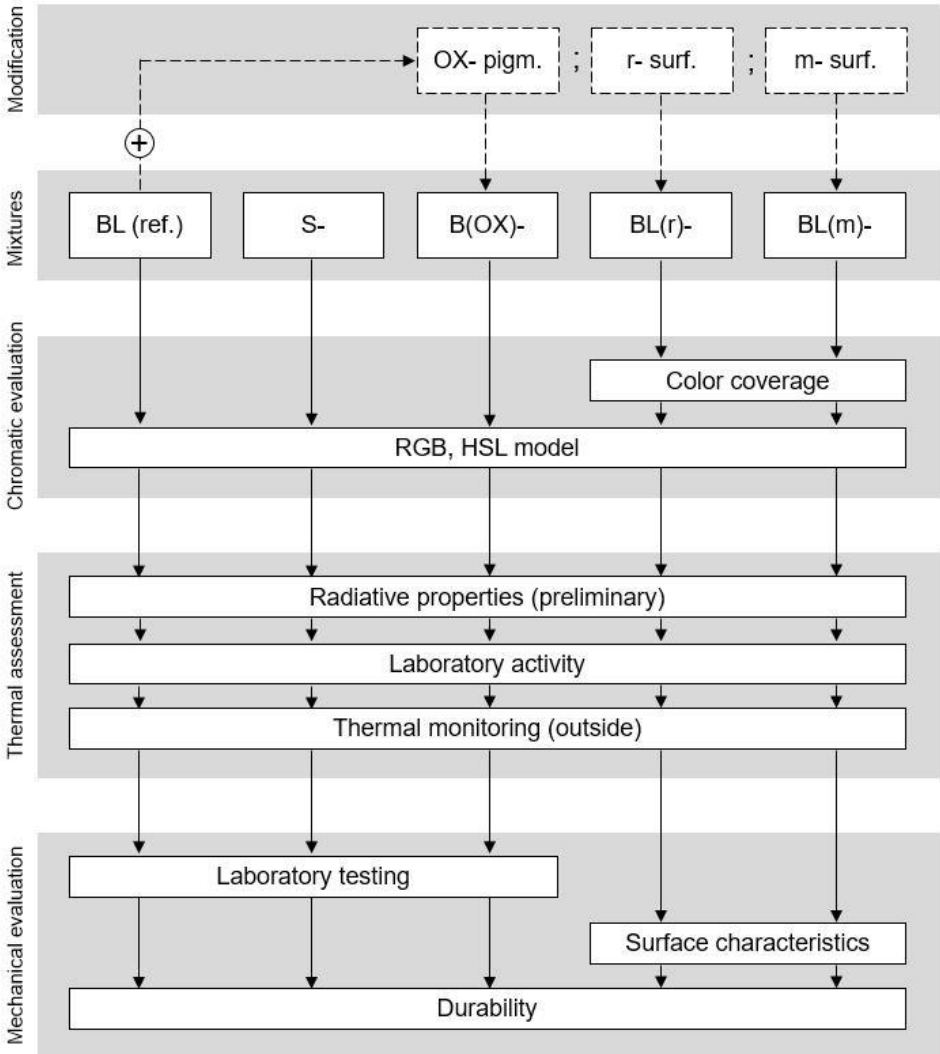


Figure 5.46. Scheme of experimental plan (mixture-scale).

Concerning the mechanical characterization, main tests were executed only on reference, S-based and oxide-pigmented mixtures since the surface-treatments were supposed to be not influent on strengths and performance, whereas surface characteristics were assessed only on r- and m-treated concretes (more crucial in the case of painted surfaces). As a summary, the following Table 5.21 sums up the mechanical test plan.

Table 5.21. Mechanical testing (mixture-scale).

Mixture	Strength	Stiffness		Fatigue	Rutting	Surface characteristics			Durability	
	ITS ^a	ITSM ^a	4PB ^b	4PB ^b	RLA ^a	MTB ^c	P ^c	PTV ^c	ITSR ^a	Fuel ^b
BL	✓	✓	✓	✓	✓	✗	✗	✗	✓	✗
SL	✓	✓	✓	✓	✓	✗	✗	✗	✓	✗
SW	✓	✓	✓	✓	✓	✗	✗	✗	✓	✗
SY	✓	✓	✓	✓	✓	✗	✗	✗	✓	✗
SP	✓	✓	✓	✓	✓	✗	✗	✗	✓	✗
BL(oxR)	✓	✓	✓	✓	✓	✗	✗	✗	✓	✗
BL(oxG)	✓	✓	✓	✓	✓	✗	✗	✗	✓	✗
BL(oxW)	✓	✓	✓	✓	✓	✗	✗	✗	✓	✗
BL(oxY)	✓	✓	✓	✓	✓	✗	✗	✗	✓	✗
BL(rR)	✗	✗	✗	✗	✗	✓	✓	✓	✗	✓
BL(rG)	✗	✗	✗	✗	✗	✓	✓	✓	✗	✓
BL(rY)	✗	✗	✗	✗	✗	✓	✓	✓	✗	✓
BL(rB)	✗	✗	✗	✗	✗	✓	✓	✓	✗	✓
BL(mR)	✗	✗	✗	✗	✗	✓	✓	✓	✗	✓
BL(mG)	✗	✗	✗	✗	✗	✓	✓	✓	✗	✓
BL(mY)	✗	✗	✗	✗	✗	✓	✓	✓	✗	✓
BL(mB)	✗	✗	✗	✗	✗	✓	✓	✓	✗	✓

^a cylindrical samples^b prismatic samples^c slabs


















5.3.3. Chromatic evaluation

The chromatic evaluation at mixture-scale was performed analyzing the slab surface of the different mixture produced. Table 5.22 reports the main results expressed in terms of RGB (red, green, blue) terns and HSL (hue, saturation, lightness) parameters (psycho-physical representation based on the human perception). It contains also an estimation (in percentage on the total area) of the covered/colored portions of the surfaces (significant aspect to quantify the effective color coverage case of painted slabs).

According to the results, the clearer slab was the SW (resin-based mixture with marble), with L of 64%; very close lightness was recorded for BL(mB), i.e. BL painted with blue mortar (62%) and BL(rY), i.e. BL painted with yellow resin (60%). However, not significant correlations could be early drawn analyzing H (hue) and S (saturation) parameters. Painted slabs (with resins or mortars) exhibited quite similar coverage percentages demonstrating that, at equal painting concentration, tint or product typology did not influence such aspect (results variability could be easily attributed to the intrinsic uncertainty of the graphical elaboration procedure).

The existence of possible correlations of such chromatic properties will be given in the next sections considering the colors of the materials at different scale and also the mixture's thermal performance.

Table 5.22. Results of chromatic evaluation at mixture-scale.

Mixture	RGB model			HSL model			Tint	Coverage [%]
	R [-]	G [-]	B [-]	H [°]	S [%]	L[%]		
BL	3	5	6	200	33	2		n.s.*
SL	148	124	84	37	28	46		n.s.*
SW	184	168	144	36	22	64		n.s.*
SY	149	107	32	38	65	36		n.s.*
SP	126	82	53	24	41	35		n.s.*
BL(oxR)	143	67	38	11	48	38		n.s.*
BL(oxG)	104	134	80	94	25	42		n.s.*
BL(oxW)	130	125	120	30	4	49		n.s.*
BL(oxY)	149	119	70	37	36	42		n.s.*
BL(rR)	213	103	69	14	63	55		98.94
BL(rG)	113	133	110	112	9	48		99.00
BL(rY)	227	187	78	44	73	60		99.46
BL(rB)	102	126	177	221	32	55		97.32
BL(mR)	186	80	51	13	57	46		95.48
BL(mG)	104	127	93	101	15	43		94.62
BL(mY)	175	134	42	42	61	43		98.20
BL(mB)	169	177	196	222	19	62		93.42

* n.s.: not significant

5.3.4. Thermal assessment

The paragraph illustrates all the results collected during the thermal assessment.

In particular, the radiative properties measured for each mixture are firstly presented: the emissivity ε and the albedo ρ of the slabs, determined according to the above-described procedures, are indicated in Table 5.23.

Table 5.23. Radiative properties (emissivity and albedo) determine for each mixture.

Mixture	Emissivity ε [-]	Albedo ρ [-]
BL	0.90	0.107
SL	0.92	0.271
SW	0.92	0.497
SY	0.91	0.217
SP	0.91	0.169
BL(oxR)	0.94	0.151
BL(oxG)	0.91	0.127
BL(oxW)	0.92	0.135
BL(oxY)	0.94	0.163
BL(rR)	0.93	0.235
BL(rG)	0.92	0.296
BL(rY)	0.94	0.323
BL(rB)	0.92	0.241
BL(mR)	0.93	0.215
BL(mG)	0.92	0.289
BL(mY)	0.92	0.251
BL(mB)	0.93	0.442

As it can be seen, the albedo was characterized by a significant variation among the different materials. It varied from 0.107 in the case of the reference “black” surface (BL slab) to 0.497 in the case of the clear mix prepared with white marble aggregates and synthetic resin (SW): in general, it seemed that the higher the lightening, the higher the albedo. On the other hand, emissivity barely vary around 0.92, typical value for paving materials [5.10]. This agreed also with the above-cited concept for which it is possible to consider the emissivity as intrinsic property of the material [2.16].

5.3.4.1. Laboratory activity

The results of the thermal laboratory activity are following presented. Figure 5.47 can suggest some early considerations about the reliability obtained in the lab; it depicts the

trends of the maximum temperatures recorded inside the *Box.A* (central part of slab surfaces) during different days and on various slabs of the same typology. As it can be noticed, slightly variations were obtained among the replicates (probably, the controlled – inside – test environment limited the T fluctuations). Practically, the humidity (equal about to 30%) and the room temperature (of about 20 °C) were considered constant for the different recording days since the activity was developed in a consecutive period. Therefore, further results are directly presented using the mean trends detected. For similar reasons, only T_{max} on *Box.A* will be discussed (average and minimum temperature trends were very close to those of T_{max}).

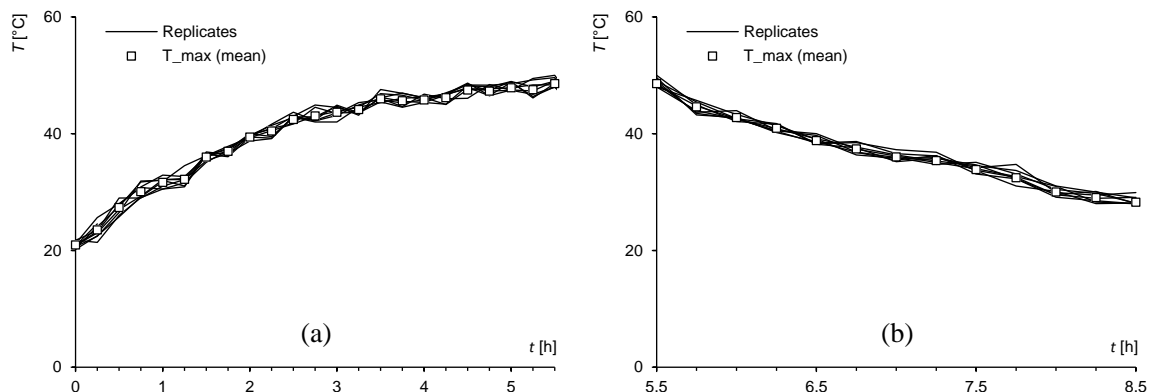


Figure 5.47. Inside thermal monitoring (BL): reliability of T_{max} for lighting (a) and darkening (b) periods.

Comparisons between different slab types are shown in Figure 5.48 (BL vs. S-based mixtures), Figure 5.49 (BL vs. oxide-pigmented mixes), Figure 5.50 (BL vs. r surface-treated mixes) and Figure 5.51 (BL vs. m surface-treated mixes). Overall, SW and BL(oxY) (Figures 5.48 and 5.49, respectively) seemed to provide the greater temperature abatements, whereas surface-treated slabs tend to approach the reference temperature trend (BL). Concerning S-based mixes, white marble guaranteed colder surface with respect to yellow-Siena one, pink coral stone and limestone. Green and white oxides were less effective than the red and yellow ones. r or s paints did not demonstrated significant differences (at least, comparing the correspondent colors). Regardless the mixture considered, the lower temperatures reached using clear or colored surfaces were always maintained during the whole analysis periods (i.e. also during the second phase, after the lamp switch off).

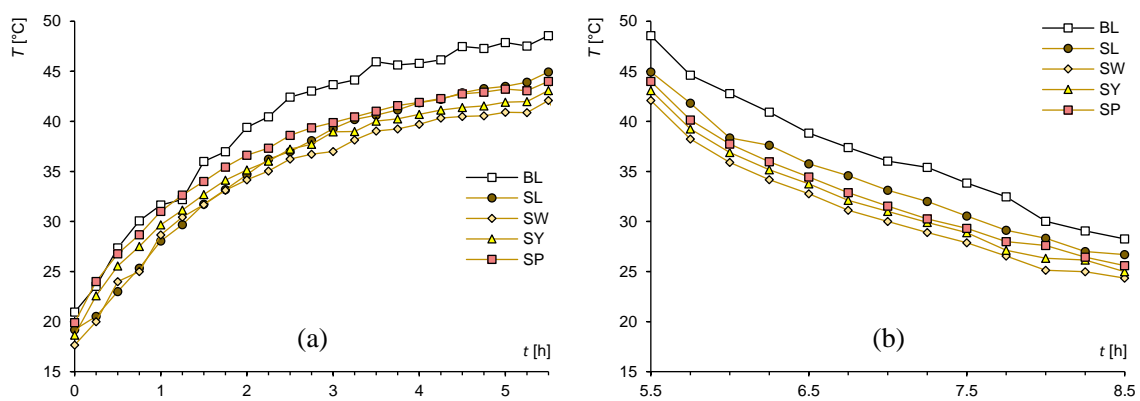


Figure 5.48. Lighting (a) and darkening (b) periods (inside BL vs. S-based mixes).

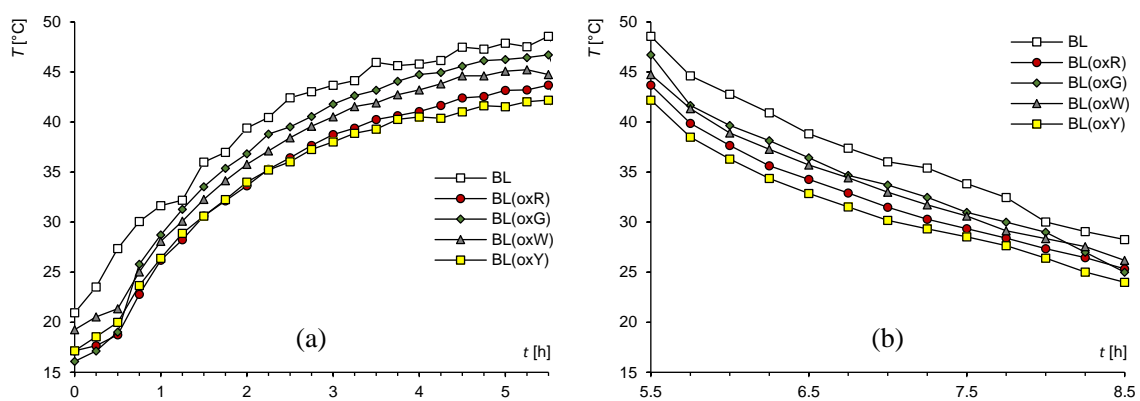


Figure 5.49. Lighting (a) and darkening (b) periods (inside BL vs. oxide-pigmented mixes).

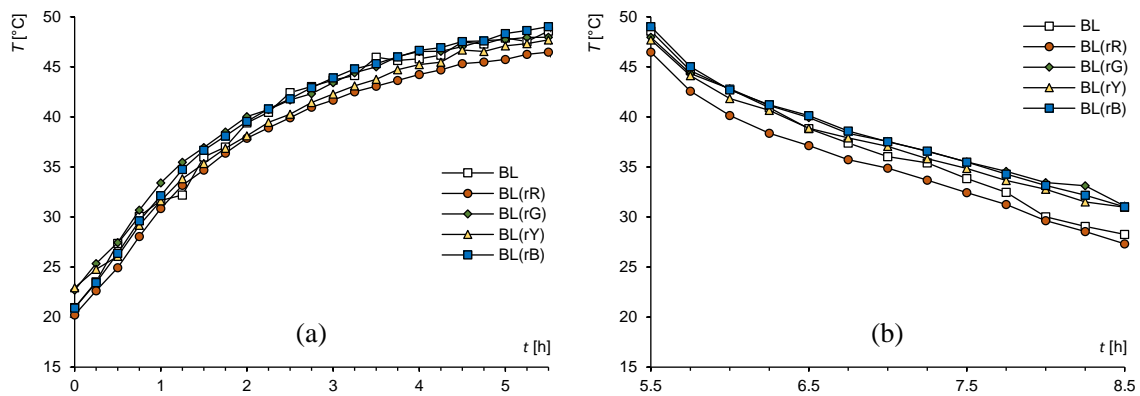


Figure 5.50. Lighting (a) and darkening (b) periods (inside BL vs. r-surface-treated mixes).

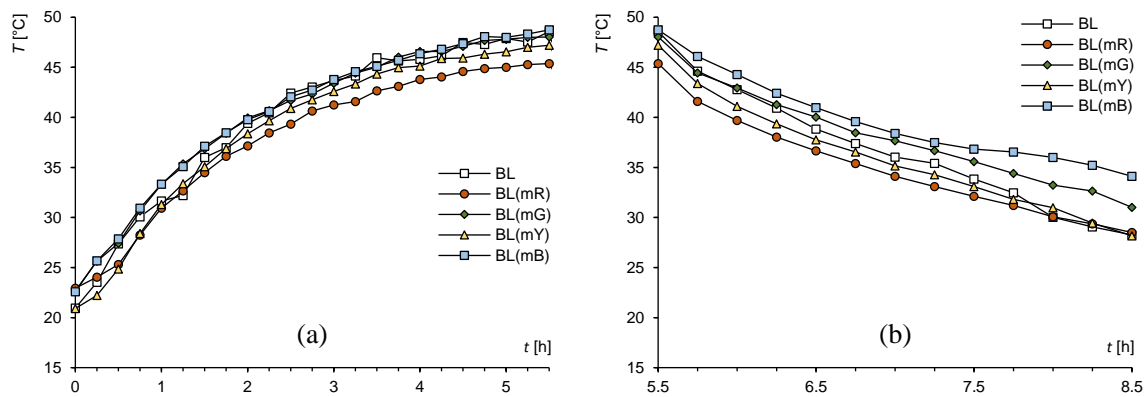


Figure 5.51. Lighting (a) and darkening (b) periods (inside BL vs. m- surface-treated mixes).

In order to strictly compare temperature mitigations given by the various products, further plots of the experimental readings are illustrated in Figure 5.52, where the ΔT gradients between the single mix and the reference one (BL) are presented. Effectively, such elaboration was performed shifting the starting temperatures to that of BL; this expedient could give only an estimations of the solution's efficacy in mitigating the maximum T because each single line is representative of average data, moreover collected during different days (for these reason, fluctuations of mean data caused even negative ΔT in certain points). Therefore, the curves' translations could be only indicative. Despite the fact, it is worth noting that general curve trends seem to reasonably reproduce the indications owned by the previous graphs (curve orders of different plots accord with those of the corresponding above-reported graphs).

Focusing further attention on the temperature evolutions on time, the maximum temperature peaks are reported in Figure 5.53 (the normalization towards BL was carried out also in this case). Indicatively, once again the SW mixture (synthetic resin with white marble) was the most promising one (T_{peak} equal to 44.91 °C). But, in some instances – see BL(oxG) or BL(rB) – T_{peak} resulted greater than that of BL (improbable for non-black surface), still suggesting some slight criticalities of the proposed normalization.

In general, such results must be critically interpreted since the artificial irradiation (with laboratory lamp) cannot exactly reproduce the sunlight because of some lacks in the emission spectrum and the intensity. Considering the proposed results only as a preliminary index of mixture efficacy, a more faithful analysis will be performed treating the outside monitoring, also in view of the real temperatures reached in-service (reasonably, during summer-time, the presented peaks could be supposed quite underestimated).

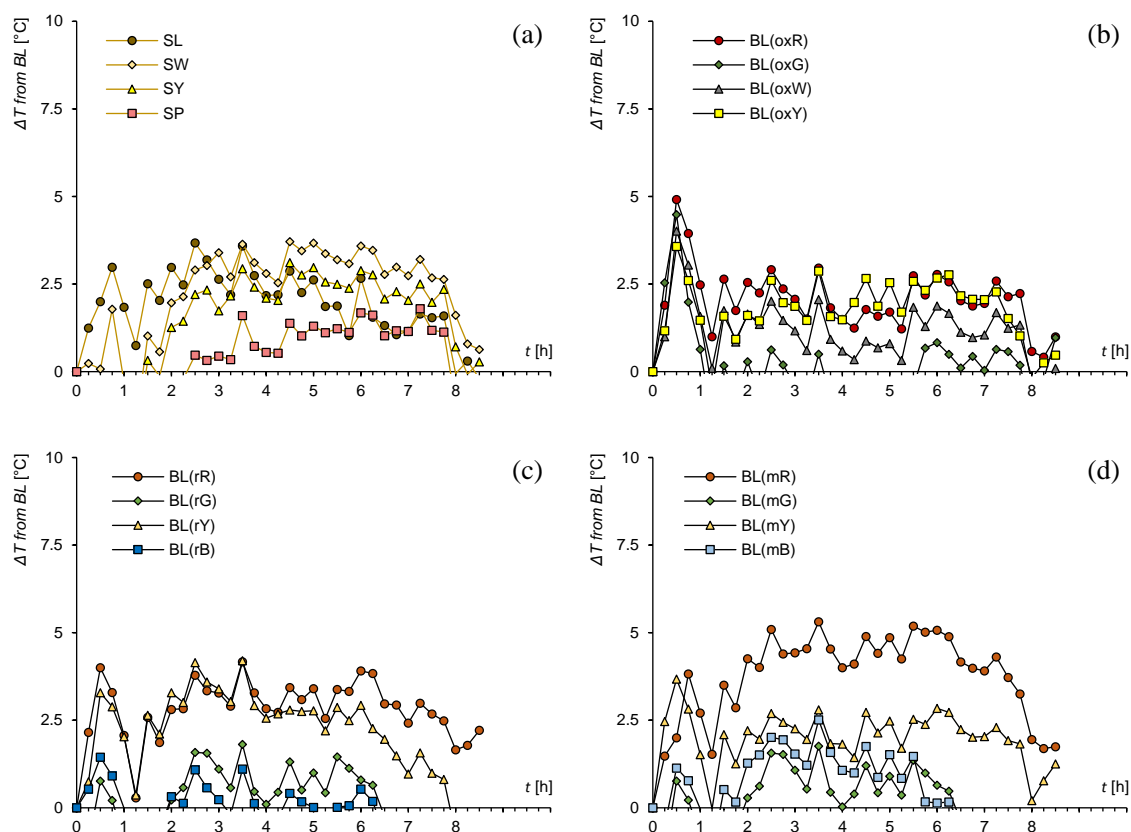


Figure 5.52. Temperature gradient from reference BL: S-based (a), oxide-pigmented (b), r-surface-treated (c) and m-surface-treated (d) mixes.

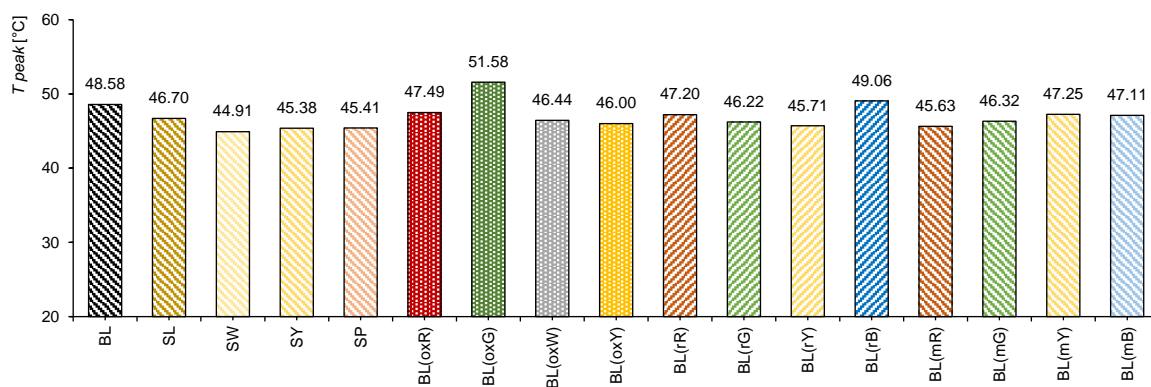


Figure 5.53. Maximum temperature peaks (at 5.5 h) normalized on reference BL.

Dealing with the thermal results recorded on slab thicknesses (the above-mentioned *Line.A*), conductivity was then estimated using the mean temperature distributions along the slab sides. Figures 5.54–5.57 presents such temperature distributions and some punctual T data positioned every 10 mm of depth (various mixtures were grouped in two plots for spacing concerns). The temperatures on the top-edge were proportional to the maximum T recorded on the central *Box.A* (they were slightly lower because of the dissipation effects located in the edge proximity). However, a different heat transmission along the depth was detected,

mainly as a function of the mixture typology. Broadly, S-based ones seemed to be more prone to limit the heat penetration (in the most pronounced case, SW exhibited a top-bottom gradient of only 2.27 °C – in the reference BL this was of 4.34 °C). It was also interesting to note that color did not seem so effective as the mixture typology; as example, surface-treated slabs was characterized by analog heat penetrations regardless the color used (only r or s painting was relevant). This fact is in accordance with quite consolidated literature, which indicate that the heat transmission mechanisms are mainly related to the lithic matrix, thus are influenced by the aggregate type and its mineralogical composition [2.15].

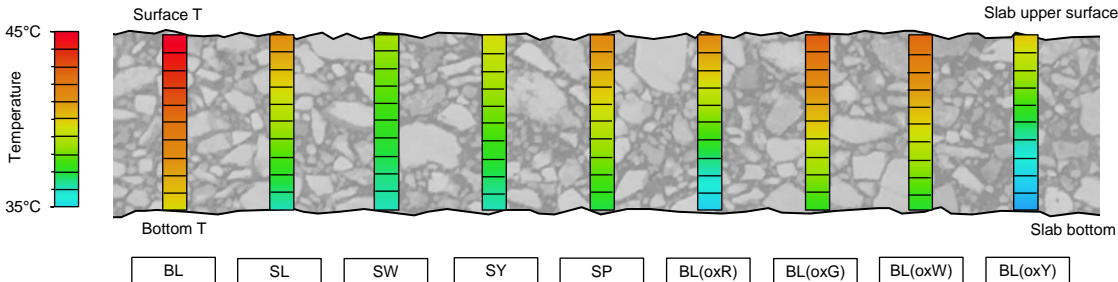


Figure 5.54. Temperature distribution on slab depth (BL vs. S-based vs. oxide-pigmented mixes).

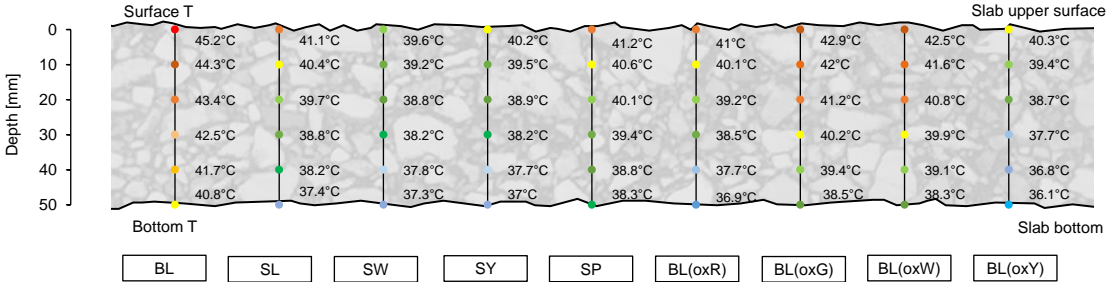


Figure 5.55. Temperature recordings on slab depth (BL vs. S-based vs. oxide-pigmented mixes).

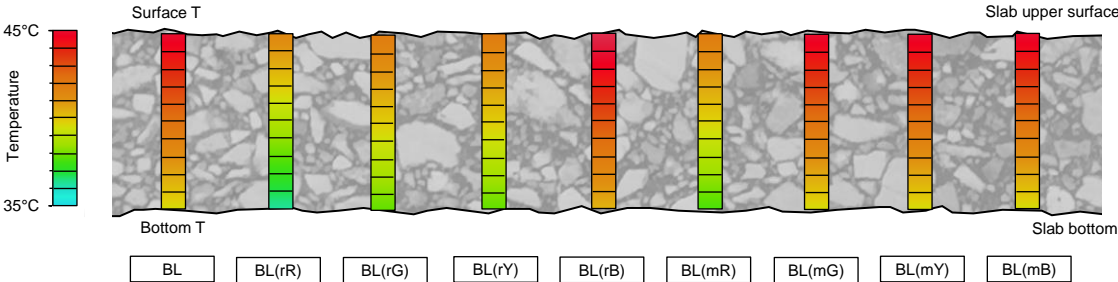


Figure 5.56. Temperature distribution on slab depth (BL vs. m- and r- surfaced-treated mixes).

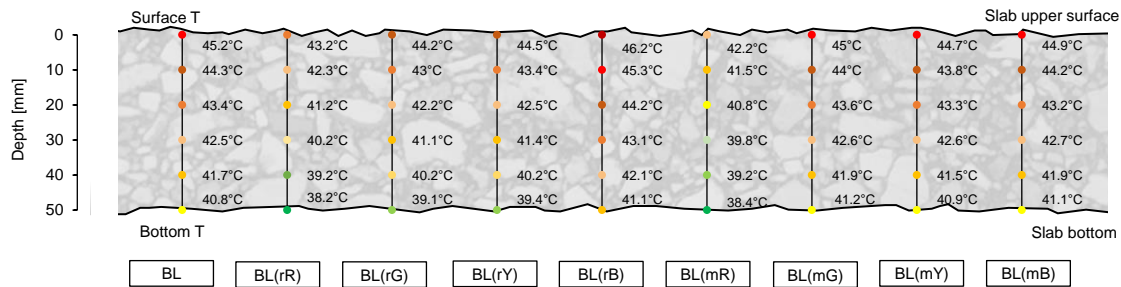


Figure 5.57. Temperature recordings on slab depth (BL vs. S-based vs. oxide-pigmented mixes).

Based on the collected results, Table 5.24 summarizes some details recorded and finally exposes the mean conductivity k calculated for each mix. In general, the identified values seemed to conform to literature findings, which indicate typical k values for conventional paving materials ranging around $1.2 \text{ W/m}\cdot\text{°C}$, mainly depending on composition and gradation [5.11; 5.12]. In the case of surface-painted materials, slightly k variations were evinced (the same bitumen and limestone were utilized for all such mixtures). Surface resins inhibited the heat transfer more than mortars; considering the equal paintings' dosages used, this was ascribed to intrinsic compositions of the surface treatments (the lower density of r-seemed not correlated to this aspect).

Table 5.24. Mixture conductivity determined along slab thickness.

Mixture	T_{surf}^* [°C]	T_{bottom}^* [°C]	ΔT^{**} [°C]	k [W/(m·°C)]
BL	45.16	40.82	4.34	1.211
SL	41.11	37.42	3.69	1.423
SW	39.64	37.37	2.27	2.269
SY	40.16	36.99	3.17	1.659
SP	41.23	38.30	2.93	1.789
BL(oxR)	40.95	36.88	4.07	1.291
BL(oxG)	42.94	38.46	4.48	1.171
BL(oxW)	42.49	38.25	4.24	1.237
BL(oxY)	40.29	36.07	4.22	1.243
BL(rR)	44.16	39.09	5.07	1.041
BL(rG)	44.52	39.46	5.06	1.043
BL(rY)	46.18	41.09	5.09	1.037
BL(rB)	42.19	37.13	5.06	1.042
BL(mR)	44.97	41.18	3.79	1.392
BL(mG)	44.73	40.95	3.78	1.395
BL(mY)	44.91	41.10	3.81	1.385
BL(mB)	40.29	36.52	3.77	1.399

* Along slag thickness

** Surface-bottom gradient

Conductivities of BL(ox) mixtures were similar to that of BL: considering that limestone was equally used as aggregate, the found variations can be ascribed at the role of binder, i.e. the oxide-modified bitumen, which governs the mastic-scale functioning an the mortar that surrounds the aggregate matrix. In general, the value scattering could be also attributed to the natural data variability included in the elaborations; no evident relations between the oxide compositions and colors was highlighted with respect to the k values. Analyzing the S-based mixes, the further effects provided by the aggregate substitutions must be taken into account. Therefore, white marble aggregate induced the higher value of k (2.269 W/m·°C) and the lower top-bottom T gradient (2.27 °C); yellow-Siena or coral-pink aggregate behaved in analog ways, furnishing greater conductivities with respect the reference BL. Overall, this could also agree with some literature findings which report higher k for marbles than certain types of limestone stones [4.7].

Finally, for what concerns the indoor (laboratory) experimental activities aimed at measuring the heat effectively released by the slabs after the exposure to the artificial light source, Figure 5.58 depicts, as representative examples, the mean isothermal curves at 25 °C above the S-based and oxide-pigmented slabs (i.e. the air temperature measured through the thermal camera in the surface proximity). In particular, the situations immediately after the light source was switched off ($t = 0$ min.) and the condition after 30 minutes ($t = 30$ min.) are represented. As it can be observed, different spatial distributions of the air temperatures were observed immediately after the removal of the heat source. However, the hierarchic response of the different materials was confirmed (BL black isotherm is always the upper one and implies a higher surface temperature on the slab). In the case of S-based mixes (Figure 5.58a), SW presented the lowest isotherm; this accorded with the previous findings since SW reached the lowest T_{surf} . Dealing with the oxide-colored mixes (Figure 5.58b), mean isothermal curves were always lower than the BL one, even if it was not possible to strictly identify the influence of the specific color. As expected, after 30 minutes, the cooling phenomenon determined 25 °C isothermal curves each other closer, located in the proximity of the slab surface. However, the cooling rates in the different analyzed situations appeared almost the same, thus suggesting that the thermal benefits achievable during the heating period by using clear/colored mixes should be maintained (or enhanced) also during the cooling.

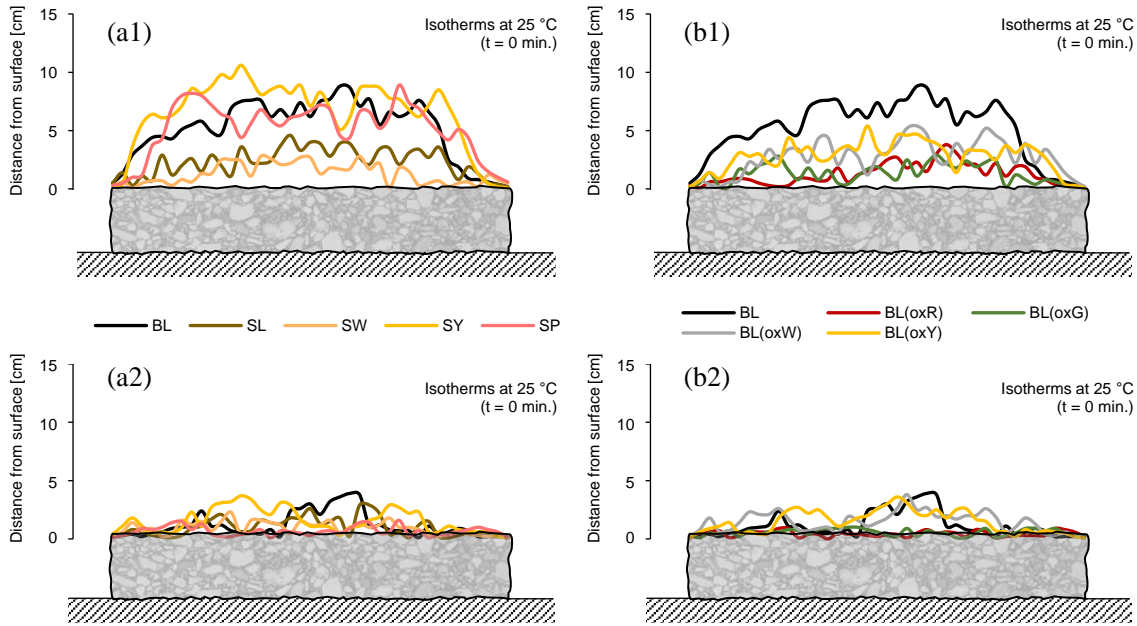


Figure 5.58. Isotherms (25 °C) at t = 0 and 30 min.: BL vs. S-based (a) and oxide-pigmented (b).

The same representations were also proposed for r- and m- surface treated mixtures (see the following Figure 5.59). In this case, very small differences between resin and mortar could be evinced (color seemed scarcely influent). Once again, cooling process caused the above-described effects.

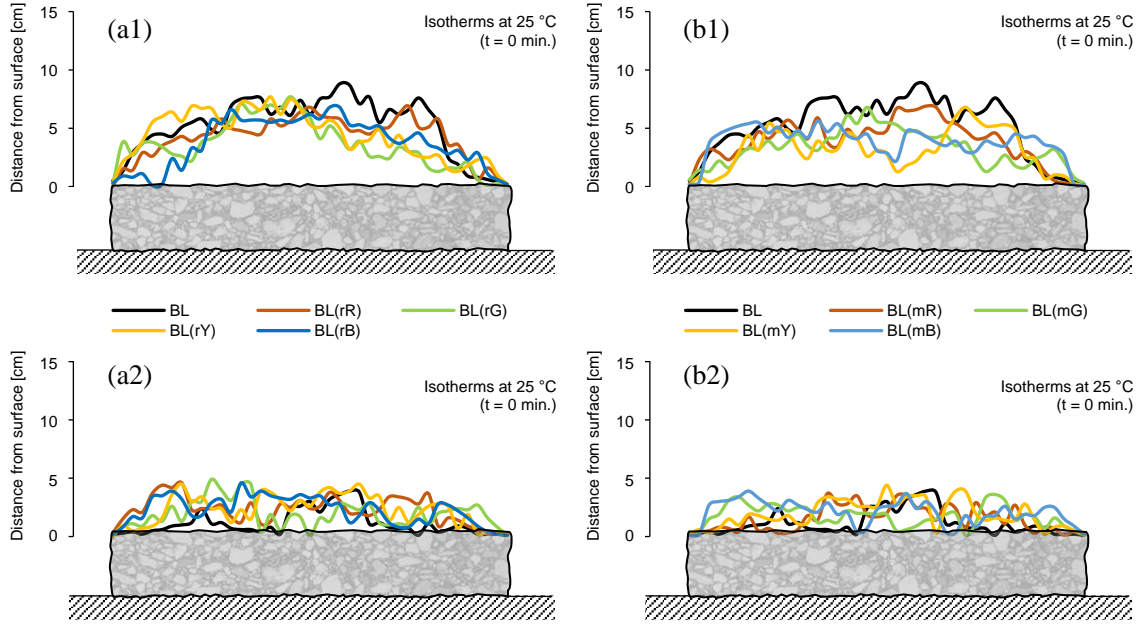


Figure 5.59. Isotherms (25 °C) at t = 0 and 30 min.: BL vs. r- (a) and m- (b) treated mixes.

Specific considerations can be also drawn by observing the data reported in Figure 5.60, where the temperature distributions along the *Line.B* (vertical centered line) are reported.

Considering the tendency to reach the thermal equilibrium after the cooling, plots were referred only to t of 0 minutes (immediately after the lamp switch off). In particular, such a representation allows confirming the enhanced thermal properties of the clear/colored materials during the heating period; again, the above-mentioned similar cooling rates were highlighted.

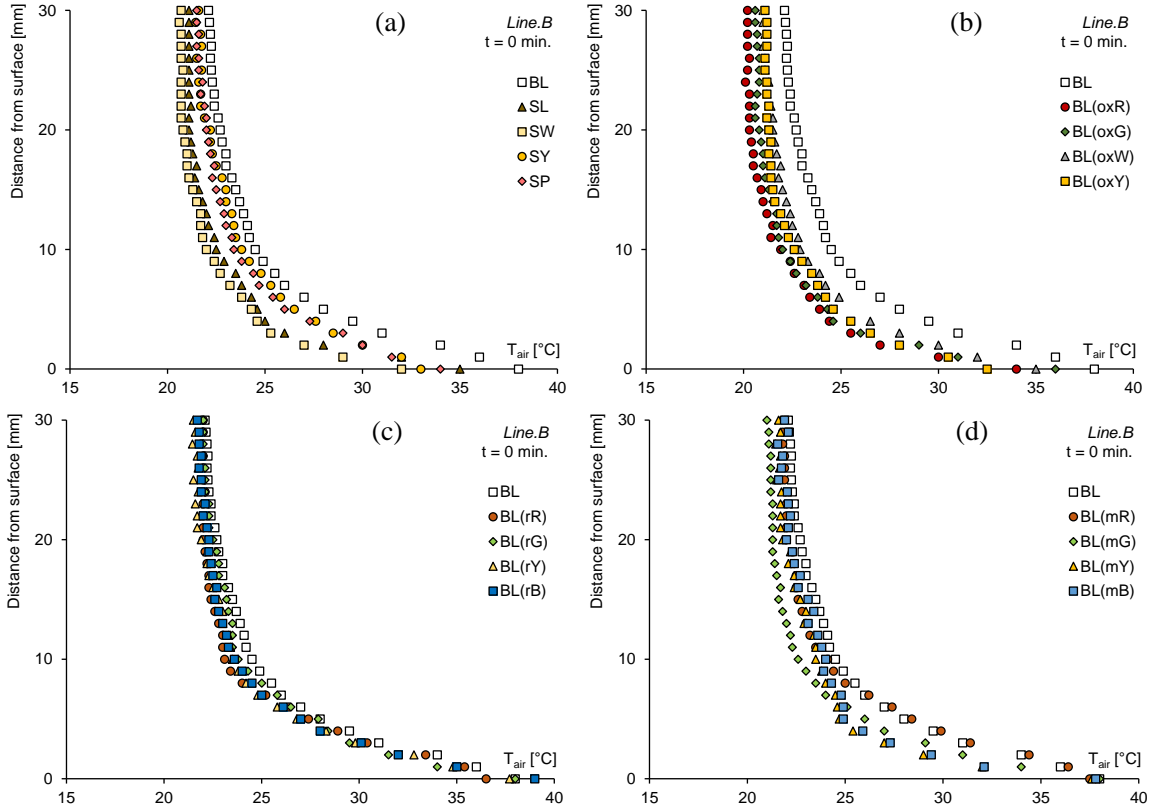


Figure 5.60. Air temperature distribution vs. distance from slab (at 0 min): BL vs. S-based (a), oxide-pigmented (b), r- (c) and m- (d) surface-treated mixtures.

Based on the proposed results, the most promising mixture for the heat mitigation was effectively the SW one (clear synthetic binder with white marble aggregate). As a conclusion, Figure 5.61, finally illustrates the mean heat distribution above SW the slab (in comparison with the reference BL) at the critical time (5.5 h), i.e. at the peak of irradiation.

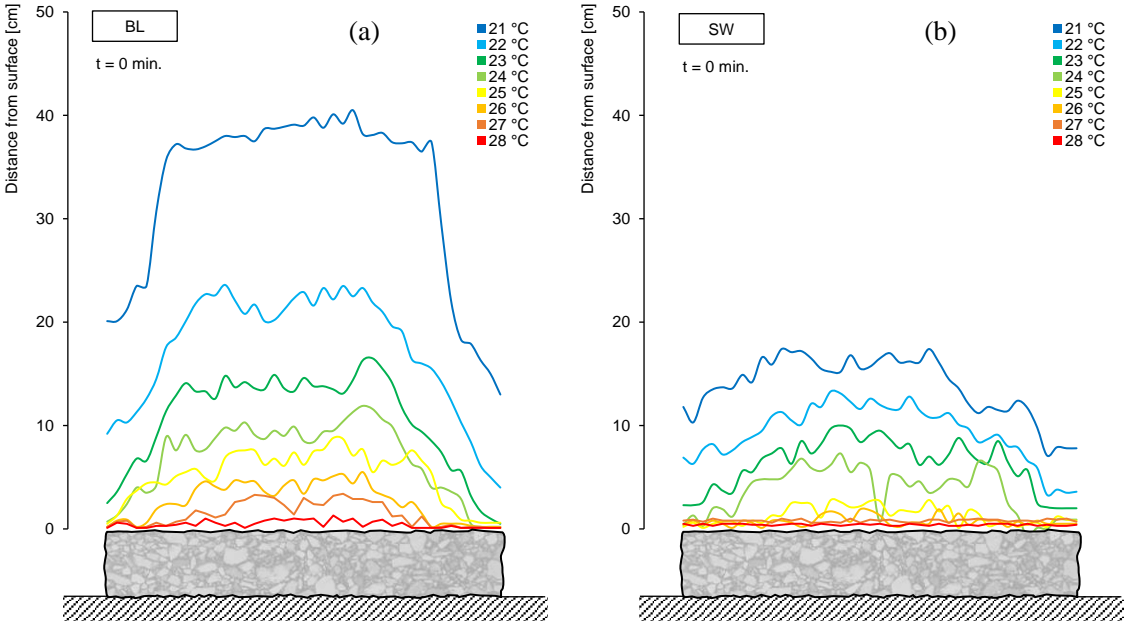


Figure 5.61. Air temperature distribution above BL (a) and SW (b) slabs (at 0 min).

5.3.4.2. In-field experimentation

The results of the thermal activity performed outside are following presented. Indeed, the test environment was firstly analyzed in order to understand the mixture’s functioning considering all the main aspects which influence final thermal performance of the materials. Thus, the main environmental parameters recorded during the monitoring days (sampled each 15 minutes, i.e. the fixed measurement interval for the temperature) are indicated below. In particular, Tables 5.25–5.28 report the air temperature evolution, the cloud coverage (evaluated through the OKTA scale), the relative humidity and the wind characteristics, respectively. Then, each quantity was averaged on the total of the monitoring days; this was considered acceptable since the outside activity was carried out during consecutive good-weather days of summer, for which no significant atmospheric events was detected – local climate was considered stable (in this sense, the values proposed within Tables 5.25–5.28 certified the fact).

Table 5.25. Environmental characteristics: air temperature recorded outside.

Time [h]	Air temperature [°C]										Mean
	Day 1	Day 2	Day 3	Day 4	Day 5	Day 6	Day 7	Day 8	Day 9	Day 10	
0	29.6	29.8	32.5	32.6	30.3	29.4	31.8	31.5	32.2	32.8	31.25
0.25	29.9	30.3	31.1	33.1	31.5	29.8	30.1	32.3	33.8	31.7	31.36
0.50	30.8	32.8	31.5	33.8	33.9	30.2	30.2	32.7	33.7	31.1	32.07
0.75	30.1	31.4	32.2	34.5	32.9	30.7	31.4	33.3	34.2	32.7	32.34
1.00	31.5	31.5	32.8	35.1	32.7	31.4	31.6	34.4	35.6	32.9	32.95
1.25	30.4	32.8	32.7	34.5	33.3	30.5	31.9	33.3	34.5	32.2	32.61
1.50	30.5	33.3	32.9	33.3	34.9	30.9	31.1	32.7	33.4	32.3	32.53
1.75	30.7	32.3	32.1	34.2	33.1	30.2	31.3	33.6	34.5	32.3	32.43
2.00	30.1	32.2	33.9	34.7	33.5	30.9	32.1	33.9	34.9	33.6	32.98
2.25	30.8	32.9	32.5	34.9	33.6	30.9	31.3	33.9	34.5	32.9	32.82
2.50	30.5	32.6	33.7	35.6	33.5	30.8	32.7	34.4	35.3	33.8	33.29
2.75	31.6	32.2	33.8	35.8	33.1	31.4	32.6	34.7	35.7	33.3	33.42
3.00	31.8	32.2	33.7	35.6	33.9	31.5	32.7	34.3	35.7	33.8	33.52
3.25	31.7	32.8	33.2	35.2	33.6	31.1	32.5	34.6	35.3	33.5	33.35
3.50	31.1	33.5	33.6	35.2	34.3	31.6	32.8	34.3	35.1	33.9	33.54
3.75	31.9	33.4	33.6	35.9	34.6	31.1	32.3	34.2	35.7	33.9	33.66
4.00	32.3	33.6	34.3	36.7	34.5	32.3	33.8	35.2	36.5	34.8	34.40
4.25	32.2	34.9	34.7	35.8	35.4	32.8	33.2	34.1	35.2	34.2	34.25
4.50	32.5	35.5	35.9	36.4	36.8	32.5	34.5	35.2	36.6	35.7	35.16
4.75	32.4	35.1	35.5	36.6	36.7	32.4	34.2	35.5	36.6	35.7	35.07
5.00	32.7	35.8	35.7	36.3	36.5	32.6	34.3	35.2	36.3	35.2	35.06
5.25	33.2	34.2	35.7	36.8	35.8	33.2	34.9	35.8	36.2	35.8	35.16
5.50	33.2	34.6	35.1	36.1	35.6	33.7	34.4	35.8	36.1	35.2	34.98
5.75	33.4	34.8	35.4	36.5	35.1	33.6	34.3	35.2	36.6	35.1	35.00
6.00	33.1	34.1	35.8	37.3	35.3	33.8	34.3	36.5	37.8	35.5	35.35
6.25	33.9	35.1	35.3	37.6	36.4	33.3	34.4	36.7	37.6	35.1	35.54
6.50	34.1	35.6	35.9	37.4	36.1	34.4	34.6	36.4	37.6	35.6	35.77
6.75	33.4	34.8	35.4	37.3	35.8	33.4	34.9	36.9	37.2	35.9	35.50
7.00	32.3	33.6	35.7	37.6	34.2	32.6	34.9	36.7	37.4	35.9	35.09
7.25	32.5	33.3	34.9	38.2	34.2	32.2	33.6	37.8	38.3	34.3	34.93
7.50	32.3	33.6	34.6	38.9	34.9	32.4	33.8	37.7	38.2	34.2	35.06
7.75	32.6	33.6	34.8	38.2	34.2	32.8	33.7	37.4	38.6	34.7	35.06
8.00	32.5	33.7	35.9	39.8	34.8	32.1	34.2	38.1	39.6	35.7	35.64
8.25	32.4	33.3	34.3	38.3	34.4	32.9	33.4	37.5	38.4	34.2	34.91
8.50	32.9	33.6	34.1	38.5	34.4	32.3	33.2	37.3	38.6	34.7	34.96

Table 5.26. Environmental characteristics: OKTA cloud coverage recorded outside.

Time [h]	OKTA level [-]										Mean
	Day 1	Day 2	Day 3	Day 4	Day 5	Day 6	Day 7	Day 8	Day 9	Day 10	
0	1	1	0	0	1	1	0	2	2	0	0.8
0.25	1	1	0	0	1	1	0	2	2	0	0.8
0.50	1	1	0	0	1	1	0	2	2	0	0.8
0.75	1	1	0	0	1	1	0	2	2	0	0.8
1.00	1	0	0	0	1	1	0	2	2	0	0.7
1.25	1	0	0	0	1	2	0	2	2	0	0.8
1.50	1	0	0	0	1	2	0	2	2	0	0.8
1.75	1	0	0	0	1	2	0	2	2	0	0.8
2.00	1	0	0	0	1	2	0	2	2	0	0.8
2.25	1	0	0	0	1	2	0	2	2	0	0.8
2.50	1	0	0	1	1	2	0	2	2	0	0.9
2.75	1	0	0	1	1	1	0	2	3	0	0.9
3.00	1	0	0	1	1	1	0	2	3	0	0.9
3.25	1	0	0	1	1	1	0	1	3	1	0.9
3.50	1	0	0	1	1	1	0	1	3	1	0.9
3.75	1	1	0	1	1	1	0	1	3	1	1.0
4.00	2	1	0	1	0	1	0	1	3	1	1.0
4.25	2	1	0	1	0	1	0	1	3	1	1.0
4.50	2	1	1	2	0	0	0	1	3	1	1.1
4.75	2	1	1	2	0	0	0	1	3	1	1.1
5.00	2	1	1	2	0	0	0	1	3	1	1.1
5.25	2	1	1	2	0	0	0	1	3	1	1.1
5.50	2	1	1	2	0	0	0	1	3	1	1.1
5.75	2	1	1	2	0	0	1	0	3	1	1.1
6.00	2	1	1	2	0	0	1	0	2	1	1.0
6.25	2	1	1	1	0	0	1	0	2	1	0.9
6.50	2	1	1	1	0	0	1	0	2	1	0.9
6.75	2	1	1	1	0	0	1	0	2	1	0.9
7.00	2	1	1	1	0	1	1	0	2	1	1.0
7.25	2	1	1	1	0	1	1	0	2	1	1.0
7.50	3	1	1	1	1	1	1	0	2	2	1.3
7.75	3	1	1	0	1	1	1	0	1	2	1.1
8.00	3	1	1	0	1	1	1	0	1	2	1.1
8.25	3	1	1	0	1	1	1	0	1	2	1.1
8.50	3	1	1	0	1	1	1	0	1	2	1.1

Table 5.27. Environmental characteristics: relative humidity recorded outside.

Time [h]	Relative humidity [%]										Mean
	Day 1	Day 2	Day 3	Day 4	Day 5	Day 6	Day 7	Day 8	Day 9	Day 10	
0	45.7	50.8	51.6	49.8	53.9	32.5	46.4	48.4	42.2	48.4	47.0
0.25	44.5	48.5	45.1	47.6	52.5	32.1	48.2	48.2	40.1	42.7	45.0
0.50	43.3	46.1	41.6	45.2	53.1	33.7	46.2	45.8	42.5	36.7	43.4
0.75	40.6	49.8	41.8	43.2	52.2	33.6	47.9	46.3	45.7	39.1	44.0
1.00	36.4	46.1	41.4	42.5	52.9	32.5	45.6	48.7	50.7	41.9	43.9
1.25	36.3	48.7	36.3	43.1	50.6	34.1	45.4	45.7	51.3	35.4	42.7
1.50	36.6	49.4	33.9	43.3	49.7	35.6	41.1	44.3	52.9	35.2	42.2
1.75	35.7	47.7	34.4	39.3	46.8	36.5	43.1	42.3	53.5	31.4	41.1
2.00	34.7	45.9	35.9	37.5	45.9	35.8	40.9	42.3	50.8	33.4	40.3
2.25	34.3	46.6	35.7	38.6	44.3	34.7	39.5	43.9	48.5	32.6	39.9
2.50	34.4	46.9	36.3	38.3	44.3	32.5	39.7	41.7	50.8	34.2	39.9
2.75	34.8	46.1	36.8	38.3	43.2	33.9	37.2	44.8	52.6	31.1	39.9
3.00	34.8	45.6	36.4	38.6	43.1	30.3	36.8	44.4	47.7	34.7	39.2
3.25	34.8	45.1	35.8	38.2	42.6	30.7	35.7	38.3	49.8	35.7	38.7
3.50	34.4	44.3	34.5	38.5	42.1	30.9	36.9	40.2	44.5	31.1	37.7
3.75	33.6	43.9	33.5	39.5	41.1	32.7	38.9	37.3	46.5	31.1	37.8
4.00	33.5	42.2	33.3	40.5	40.9	32.9	35.7	36.3	45.7	28.1	36.9
4.25	33.7	42.1	32.9	38.2	39.7	33.5	34.9	33.5	44.1	30.8	36.3
4.50	34.6	41.5	31.2	37.9	37.5	34.5	32.4	31.3	42.2	31.9	35.5
4.75	32.7	41.3	31.7	36.4	36.9	35.3	30.4	36.8	45.2	31.8	35.9
5.00	32.2	41.5	31.6	35.3	36.7	36.3	32.8	33.6	50.4	27.4	35.8
5.25	32.7	40.3	32.1	36.6	38.8	36.2	36.9	38.9	48.2	29.6	37.0
5.50	32.6	41.9	33.4	37.1	43.1	35.8	35.6	38.6	44.4	33.7	37.6
5.75	31.1	42.1	33.3	39.4	41.3	35.6	34.6	32.6	52.2	31.4	37.4
6.00	30.1	44.4	34.6	43.2	40.8	34.5	32.5	35.1	47.8	31.5	37.5
6.25	30.9	43.2	34.2	42.6	38.9	31.3	33.8	34.8	46.9	28.2	36.5
6.50	32.9	43.5	36.2	41.6	37.3	32.3	37.1	36.1	43.2	31.1	37.1
6.75	31.9	42.1	38.1	43.2	38.1	31.3	32.4	32.8	53.5	36.7	38.0
7.00	31.5	42.7	41.1	44.9	40.8	33.7	36.9	33.8	48.8	37.2	39.1
7.25	31.2	41.2	41.1	45.5	35.6	33.3	32.5	35.8	47.7	38.9	38.3
7.50	33.6	41.7	41.5	48.2	34.2	32.9	38.8	34.6	47.6	38.4	39.2
7.75	34.8	41.9	40.9	45.6	36.2	34.3	36.6	33.6	47.7	35.1	38.7
8.00	35.5	41.8	40.9	44.2	40.6	35.7	32.2	33.6	43.6	34.1	38.2
8.25	35.7	41.9	40.5	45.7	40.6	36.1	35.6	34.4	45.2	39.8	39.6
8.50	35.4	41.3	39.7	46.7	41.8	35.9	32.1	36.2	43.1	33.9	38.6

Table 5.28. Environmental characteristics: wind speed recorded outside (from North-East).

Time [h]	Wind speed [km/h]										
	Day 1	Day 2	Day 3	Day 4	Day 5	Day 6	Day 7	Day 8	Day 9	Day 10	Mean
0	2.9	4.6	5.2	5.4	3.9	4.4	6.0	7.6	3.7	4.9	4.86
0.25	6.5	6.2	5.9	8.4	4.4	5.7	7.5	6.9	6.3	5.9	6.37
0.50	3.5	5.6	4.5	6.8	6.3	4.9	7.4	6.8	3.5	7.0	5.63
0.75	2.8	7.1	5.1	6.0	4.4	3.6	7.9	5.3	5.0	4.7	5.19
1.00	5.0	6.2	7.6	6.1	5.8	6.4	7.3	6.9	6.4	4.2	6.19
1.25	6.7	4.5	5.9	7.0	6.9	5.0	6.6	6.9	5.3	7.3	6.21
1.50	3.9	4.8	8.3	8.3	4.2	4.7	8.5	8.0	6.0	5.0	6.17
1.75	6.4	5.9	7.8	5.8	4.7	5.6	7.3	5.4	6.1	4.4	5.94
2.00	5.6	5.8	4.6	5.5	3.9	4.2	7.6	8.2	4.1	7.0	5.65
2.25	3.3	6.7	8.3	8.8	3.4	6.0	6.3	5.1	5.5	7.8	6.12
2.50	5.7	4.6	8.2	6.0	4.7	4.0	5.9	7.9	6.2	7.7	6.09
2.75	5.5	7.3	4.2	8.2	4.9	6.6	8.4	6.3	5.8	6.3	6.35
3.00	3.0	6.6	5.3	7.1	3.7	3.5	8.6	6.3	5.1	7.9	5.71
3.25	6.4	4.8	6.2	7.8	4.1	5.7	6.6	5.5	7.3	6.5	6.09
3.50	6.5	4.5	4.5	7.6	6.5	5.2	8.7	6.2	4.9	8.0	6.26
3.75	3.9	7.0	7.1	5.9	4.0	6.6	6.9	7.7	6.4	5.1	6.06
4.00	2.8	6.3	5.8	9.2	6.6	5.3	8.2	7.0	5.8	6.8	6.38
4.25	3.9	4.7	8.2	6.7	5.4	4.0	6.3	6.1	4.6	5.4	5.53
4.50	4.5	5.9	4.1	5.5	4.7	3.5	8.3	7.1	3.6	8.0	5.52
4.75	4.7	6.7	7.7	7.8	4.7	3.8	7.1	7.2	6.9	6.8	6.34
5.00	5.1	4.3	6.1	8.7	4.2	3.4	8.1	8.3	3.9	5.9	5.80
5.25	5.3	6.2	8.2	5.5	6.8	4.7	8.1	7.8	6.6	6.8	6.60
5.50	6.0	6.0	4.3	5.4	3.5	5.7	6.6	6.5	6.2	8.1	5.83
5.75	5.8	4.7	4.6	8.4	5.7	5.8	8.2	7.8	7.3	6.4	6.47
6.00	4.3	5.4	5.1	7.2	3.3	4.7	6.5	8.3	4.4	7.8	5.70
6.25	6.7	6.1	6.3	8.5	6.1	4.7	7.2	7.9	4.0	4.4	6.19
6.50	5.4	6.7	4.4	8.3	4.4	5.5	5.5	7.7	4.9	6.2	5.90
6.75	4.1	6.0	4.8	5.4	6.5	6.6	6.6	5.8	3.7	7.7	5.72
7.00	2.7	6.6	6.2	8.0	4.7	5.8	8.6	7.3	5.4	5.6	6.09
7.25	2.7	5.9	4.8	8.9	5.2	6.2	5.6	5.2	7.2	5.3	5.70
7.50	4.4	4.7	4.1	9.2	5.0	3.8	5.5	7.6	4.3	6.9	5.55
7.75	5.4	4.7	5.4	8.2	6.4	4.8	7.3	5.5	7.2	5.3	6.02
8.00	6.4	4.5	7.3	7.3	6.7	6.1	6.5	8.1	3.8	6.6	6.33
8.25	3.5	4.4	6.4	6.0	3.9	6.5	6.6	5.9	4.2	6.5	5.39
8.50	3.6	5.0	4.9	6.4	6.5	4.2	5.6	6.0	4.9	5.4	5.25

As anticipated, monitoring was performed in a wide-open space, therefore no interferences due to building or vegetation presence were accounted (the fact could influence the solar radiation reaching the mixtures' wearing courses). As hypothesized, the derived SVF was equal to 1 during the exposure of the slab (5.5 hours); in this perspective, Figure 5.62 illustrates the elaboration made with a specific software to effectively calculate the SVF

value. Concerning the second part of the monitoring (3 hours), SVF was set equal to 0 since the slabs were placed in a shaded area (direct radiations completely avoided).

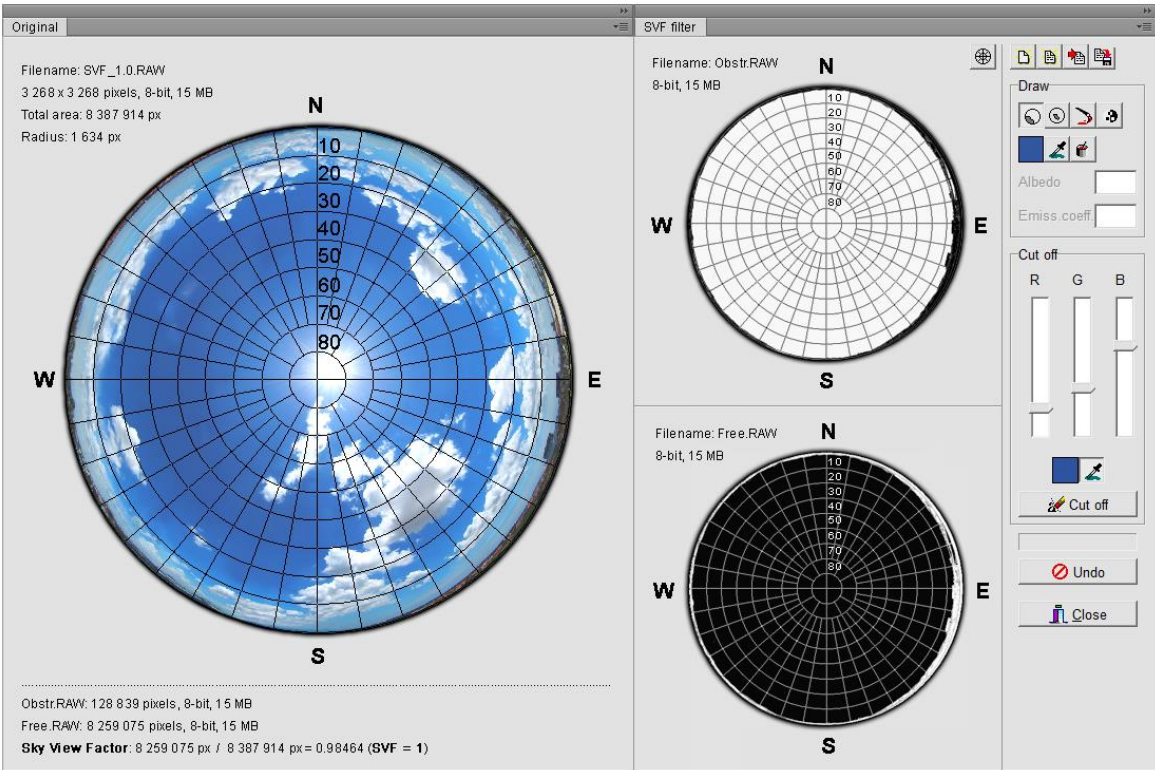


Figure 5.62. SVF calculation (direct irradiation periods – 5.5 h).

Thermal results in terms of surface temperature evolution are presented in Figure 5.63–5.66 (they are referred to the maximum temperatures recorded on *Box.A* and averaged on the different monitoring days). As it can be observed, SW mix again reached the lower temperatures (among the S-based slabs but also the other ones). Oxide-pigmented mixes showed slight reduction of T with respect to BL; surfaced-treated one (r or m) had an intermediate behavior between S-based and ox-based solutions. In general, acceptable T fluctuations were identified on the different recordings (see error bars on the graphs): this confirmed again the stability of the environmental conditions among the different recording days. An overall sight of such results is appreciable also in the following Figure 5.67, where the average temperature evolutions are depicted for all the tested materials.

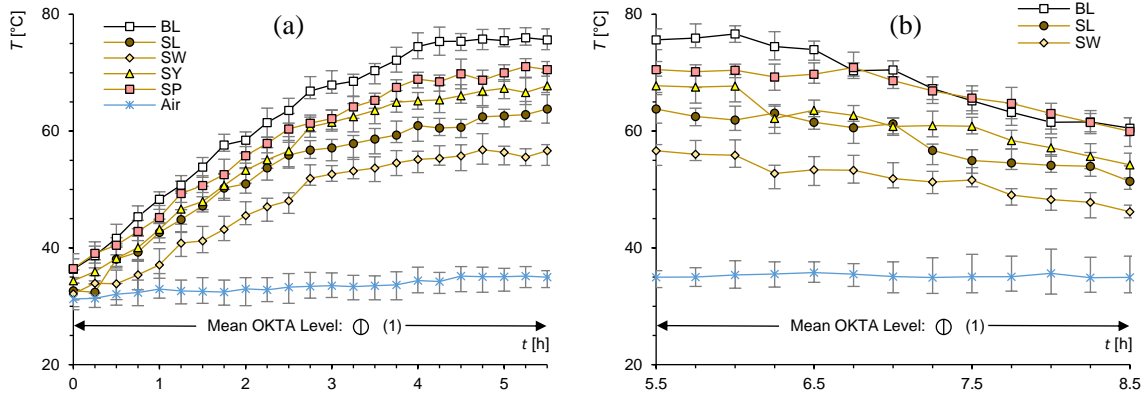


Figure 5.63. Irradiation (a) and shading (b) periods (outside BL vs. S-based mixes).

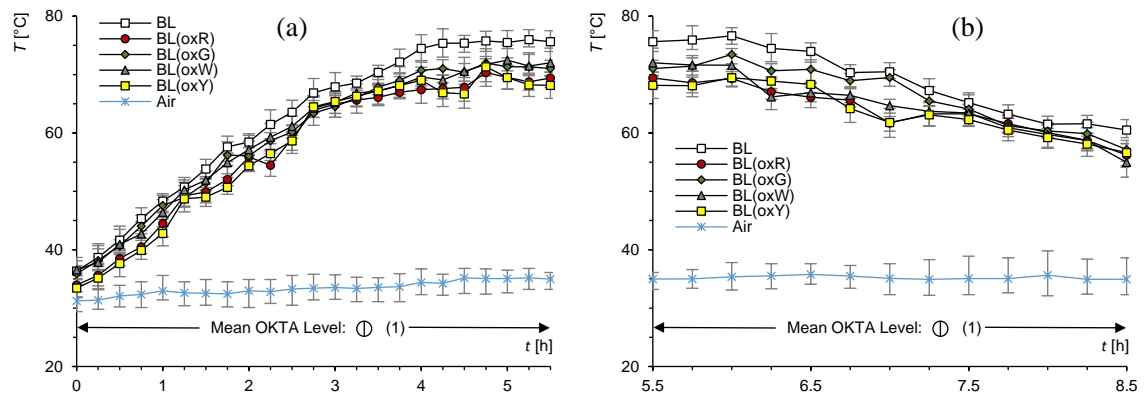


Figure 5.64. Irradiation (a) and shading (b) periods (outside BL vs. oxide-pigmented mixes).

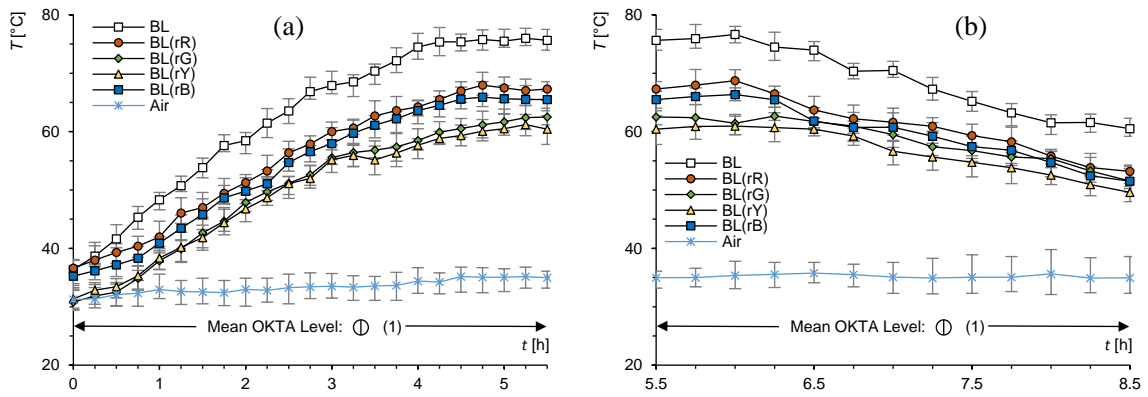


Figure 5.65. Irradiation (a) and shading (b) periods (outside BL vs. r- surface-treated mixes).

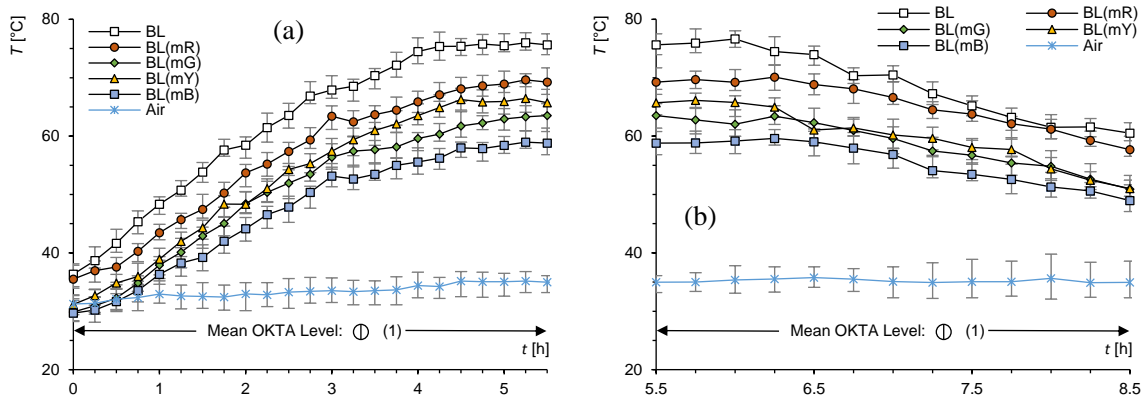


Figure 5.66. Irradiation (a) and shading (b) periods (outside BL vs. m- surface-treated mixes).

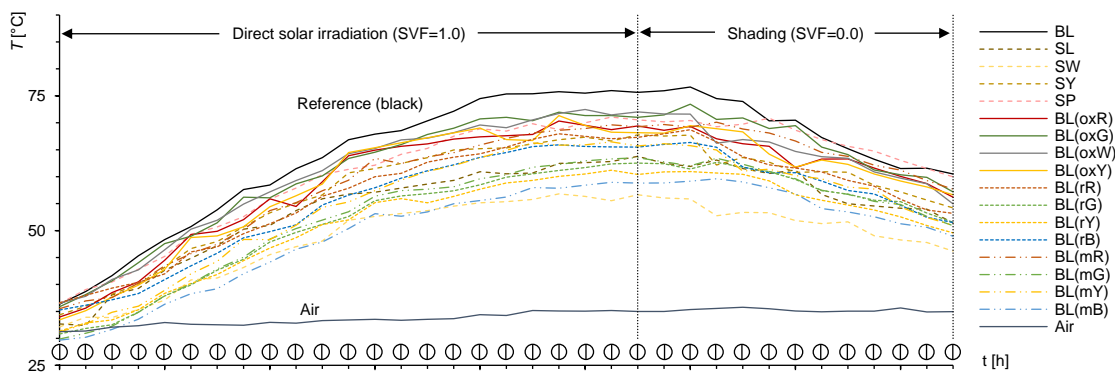


Figure 5.67. Summary of outside thermal results: temperature evolution of mixtures' surfaces.

Further elaborations were also proposed trying to normalize the obtained results with respect to the air temperature; Figure 5.68 plots the evolution of slab-air temperature gradients of all the prepared mixtures. Mainly, the above-described results were confirmed (please note that the air temperature was substantially constant all along the recording period); a hierarchic response dependent on the color and the mixture type could be supposed and will be evaluated in the following Chapter 6, trying to link the effective thermal responses with the radiative properties of the concretes.

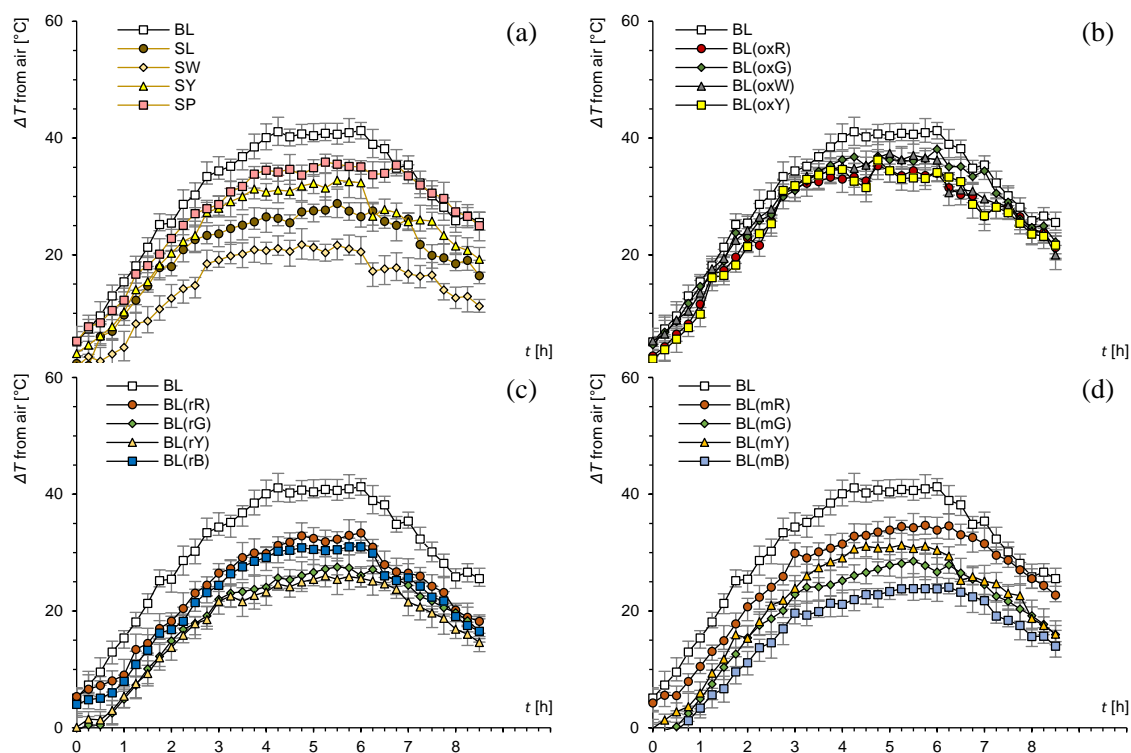


Figure 5.68. Temperature gradient from air: BL vs. S-based (a), oxide-pigmented (b), r- surface-treated (c) and m- surface-treated (d) mixes.

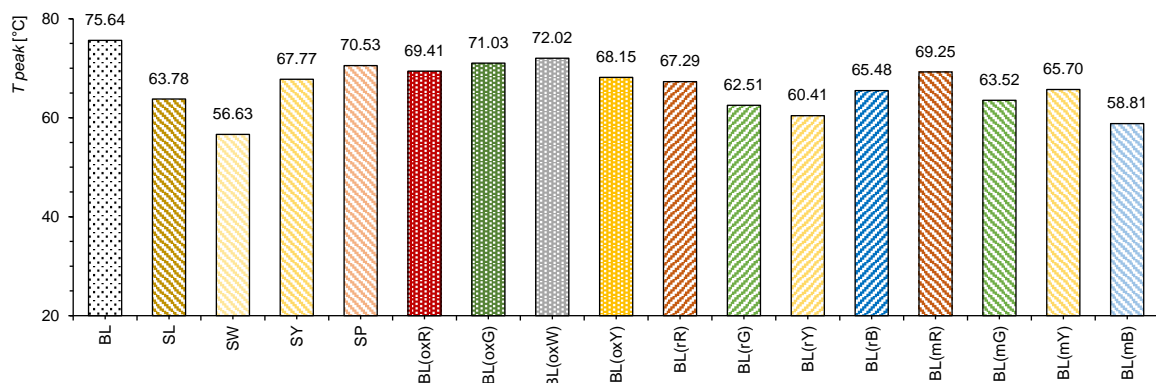
Figure 5.68 was also used to describe the heating and cooling mechanisms furnished by the different products. In this perspective, it was interesting to note that all the plotted curves tend to present three-region shaped trends. The first region, with a rapid increasing of T , a central portion with stable T , and a third one with decreasing T (properly caused by the slab shading). Based on such consideration, Table 5.29 reports some data about the slopes of the first and the third part of the curves, representing the heat collection and heat releasing speeds furnished by the different materials. In particular, the heating process was considered between 0 and 4 hours, the cooling one between the slab's shadings' (5.5 hours) and the end of the recordings (8.5 hours).

As evident, different heating and cooling rate were evinced, demonstrating that, depending on the types and tonality, clear/colored mixtures not only reached lower maximum temperature, but were also able to slow the heat collection (in the heating phase) and its release (during cooling). A slower heat absorption could have a strategic importance in mitigating the heat concentration in the urban spaces. Instead, a slower heat release could intensify the UHI phenomenon during the night-time; otherwise, it was considered a minor aspect since the lower slope must be linked to the maximum temperature reached (starting the decreasing from a lower T , a more gradual cooling towards a fixed ambient temperature is expectable).

Table 5.29. Heating and cooling speeds provided by the different mixtures.

Mixture	Heating slope [$^{\circ}\text{C}/10 \text{ min.}$]	Cooling slope [$^{\circ}\text{C}/10 \text{ min.}$]
BL	1.59	-0.84
SL	1.18	-0.69
SW	0.96	-0.58
SY	1.28	-0.75
SP	1.35	-0.59
BL(oxR)	1.39	-0.73
BL(oxG)	1.45	-0.77
BL(oxW)	1.38	-0.95
BL(oxY)	1.48	-0.64
BL(rR)	1.15	-0.78
BL(rG)	1.15	-0.61
BL(rY)	1.10	-0.60
BL(rB)	1.18	-0.78
BL(mR)	1.27	-0.64
BL(mG)	1.24	-0.70
BL(mY)	1.35	-0.82
BL(mB)	1.08	-0.55

Finally, the following representations were proposed to discuss about the maximum T reached by the surfaces (concerning the second stable regions of the above curves). Figure 5.69 presents the T peaks (recorded at 5.5 h), whereas Figure 5.70 indicates the maximum temperature mitigation guaranteed with respect to reference BL. Based on the results, it is worth noting that the SW mixture, being the most promising product, was able to decrease the T of about 20°C (absolute T of 56.63°C). Since encouraging results were also obtained in the cases of BL(mb) (-17.03°C , 58.81°C) or BL(rG) (-13.98°C , 62.41°C), it was supposed that results were strongly linked to the color of the surface rather than only to the mixture typology. In general, such findings must be surely considered also dealing with the mechanical characterization of the proposed materials (the visco-elastic thermal-dependent behavior of the concretes should be strongly influenced by so evident T gradients).

**Figure 5.69.** Temperature peaks (at 5.5 h) recorded outside.

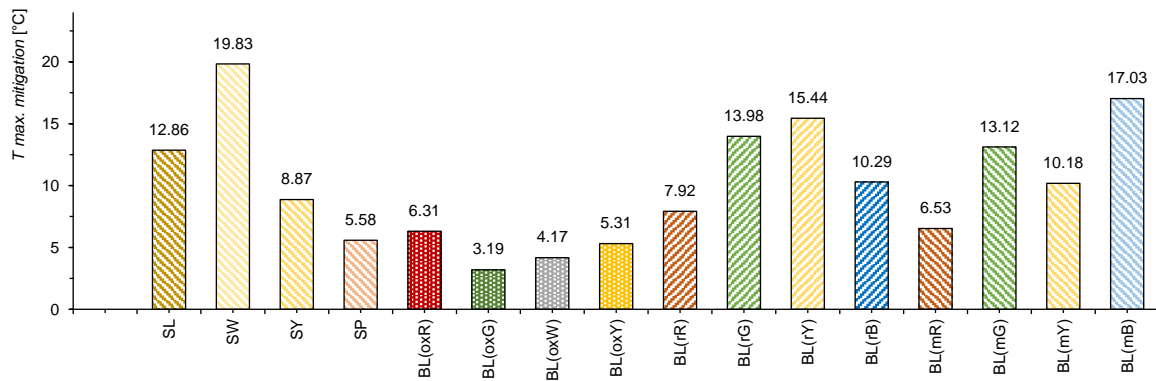


Figure 5.70. Maximum temperature mitigation with respect to reference BL.

5.3.5. Mechanical characterization

Results derived from the mechanical characterization at mixture-scale are following presented and discussed.

5.3.5.1. Mechanical strength

Mechanical strengths of the tested mixtures are presented in Table 5.30, where results of each mix are given as the mean of three test replicates. As expectable, the S-based samples tend to achieve definitely lower tensile strengths with respect to the reference BL (almost one third), whereas oxide-pigmented ones presented better ITS in all the case (almost twice with respect to BL mix). Within the same category (S-based or oxide-pigmented mixes), no appreciable ITS differences were recorded, thus nor the aggregate typology neither the oxide morphology seemed to be relevant in determining the tensile resistance. The first sentence definitely accords with the most part of literature statements for such kind of test, which principally attributes to the binders the most significative role to develop the tensile strength. In fact, ITS values are reported to be generally influenced by several factors regarding the binder, such as, for example, its properties and the consequent film thicknesses, the adhesive forces developed with the aggregate surface textures and its particles interlocking abilities [5.13–5.15]. Overall, it must be remembered that ITS represents a largely utilized parameter in the pavement mixture characterizations, since huge experience exists correlating such parameter with the in-field behavior [5.16]. Moreover, considering that ITS tensile properties are commonly utilized to predict the aptitude to the cracking of pavements (the ability to tolerate higher strains prior to the failure), some hypothetical restrains should be early taken into consideration in the case of S-based mixes, i.e. when quite poor ITS results are obtained [5.17]. Such fact must be keep in mind also accounting that the ITS values recorded for S-based mixes resulted quite smaller than the typical ITS limits prescribed for the most diffused technical specifications given for the acceptance of traditional open-traffic wearing courses.

Table 5.30. ITS results (25 °C): BL vs. S-based and oxide-pigmented mixtures.

Mixture	D [mm]	h [mm]	P [kN]	P _{mean} [kN]	s [mm]	S _{mean} [mm]	ITS [MPa]	ITS _{mean} [MPa]
BL	100.16	50.16	5.293	5.326	2.894	2.969	0.671	0.670
	100.49	50.98	5.764		2.999		0.716	
	101.23	49.75	4.921		3.014		0.622	
SL	100.88	51.78	2.191	2.293	3.354	3.245	0.267	0.286
	100.98	50.32	2.371		3.115		0.297	
	99.98	50.07	2.317		3.267		0.295	
SW	100.48	50.58	2.005	1.754	3.102	3.307	0.251	0.220
	100.92	50.15	1.565		3.451		0.197	
	100.34	50.67	1.691		3.367		0.212	
SY	101.54	50.77	2.157	1.972	3.0155	3.245	0.266	0.244
	100.35	51.61	1.723		3.456		0.212	
	100.53	50.66	2.036		3.264		0.255	
SP	100.47	51.33	1.956	1.940	3.451	3.477	0.241	0.240
	100.32	50.57	2.059		3.334		0.258	
	100.14	51.90	1.804		3.647		0.221	
BL(oxR)	100.71	51.73	8.644	8.714	1.416	1.448	1.056	1.063
	101.69	51.40	8.233		1.601		1.003	
	100.26	51.99	9.264		1.326		1.131	
BL(oxG)	100.94	51.37	9.125	9.144	1.013	1.224	1.120	1.136
	100.73	49.94	9.945		1.126		1.259	
	100.10	51.64	8.363		1.532		1.030	
BL(oxW)	100.58	50.40	6.947	7.363	1.741	1.526	0.872	0.934
	100.27	49.06	7.991		1.325		1.034	
	100.18	50.73	7.152		1.513		0.896	
BL(oxY)	100.35	51.46	8.768	8.732	1.236	1.433	1.081	1.089
	100.80	49.70	8.326		1.6124		1.058	
	100.85	50.95	9.101		1.452		1.128	

5.3.5.2. Stiffness

Stiffness is considered a suitable indicator to analyze the performance of mixes for bounded-layers [5.18]. Firstly, ITSM results are presented in Figure 5.71 (error bars indicate the variability among the different replicates executed). According to that expected considering the early indications collected at binder-scale, resin-based mixtures owned lower stiffness at each temperature with respect to BL. The most critical situation was recorded in the case of SW (mixture manufactured with white marble); limestone, yellow-Siena marble and coral-pink stone gave slightly higher stiffness to the mixes (under the same binder type). This was probably linked to the slightly worse characteristics of such aggregates with respect to limestone (as example, higher flakiness and shape index could weaken the interlocking with binder and partially limit the stiffness). Conversely, the oxide-pigmented

solutions exhibited stiffness comparable (or even slightly higher) than that of the black BL, regardless the oxide color. Only at 10 °C, BL(oxY) seemed to have lower ITSM than the other pigmented solutions and the reference BL (the fact could be even ascribed to some operational imprecisions and the results uncertainty since, at greater temperatures, this did not occur).

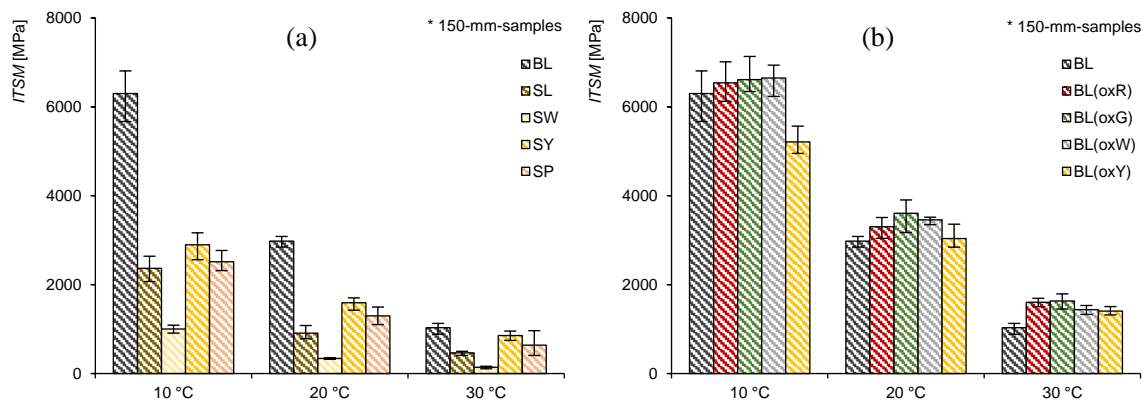


Figure 5.71. ITSM results: results: BL vs. S-based (a) and oxide-pigmented (b) mixtures.

More accurate evaluations about stiffness could be collected analyzing the results furnished by 4PB tests. In this perspective, the following Figures 5.72-5.80 depict for each mixture the Black diagram, the Cole-Cole plot, the E^* and δ master curves (identified with a, b, c and d marks, respectively). Within Cole-Cole plots, the dotted segment indicates the equal-slope line (plane bisector) corresponding to the visco-elastic balanced behavior (conservative modulus equal to dissipative one and phase angle equal to 45°). In the case of master curves (E^* and δ), continuous curves depict the construction attempts of the master curve models according to the theory already-introduced at Chapter 4 and used also at binder-scale.

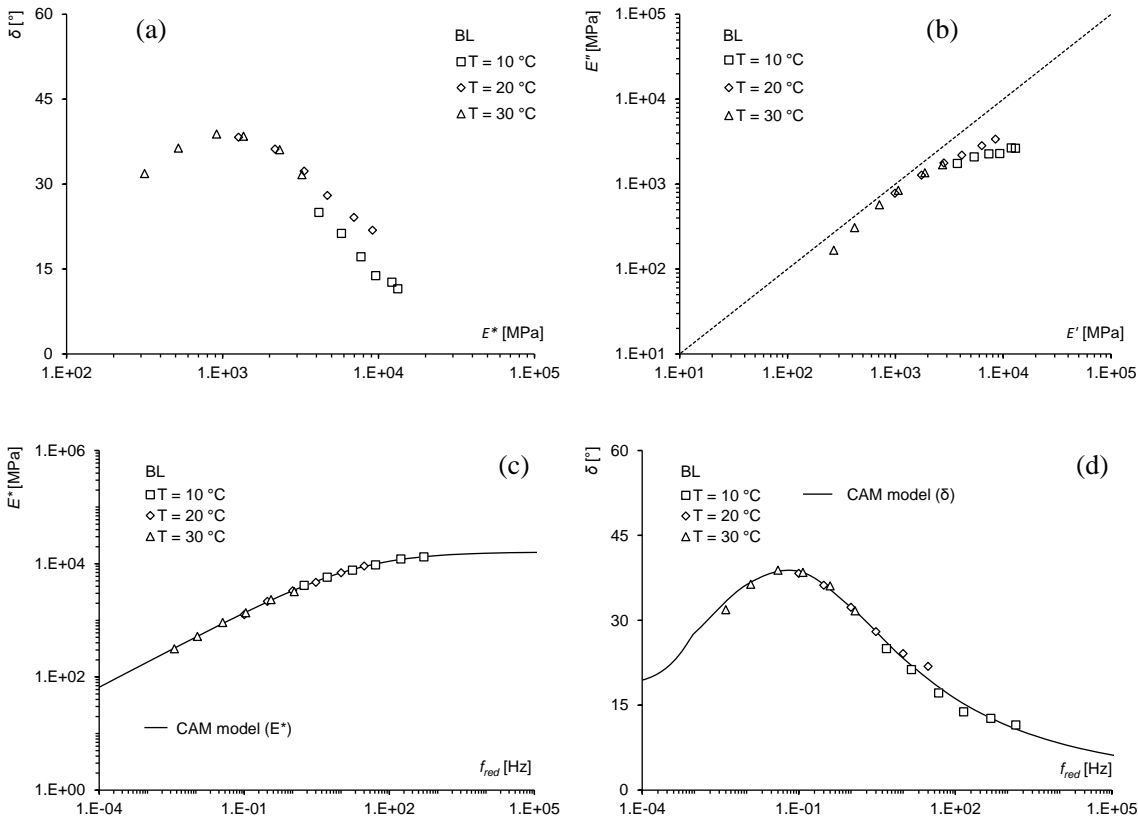


Figure 5.72. Black diagram (a), Cole-Cole plot (b), master curves of E^* (c) and δ (d) of BL.

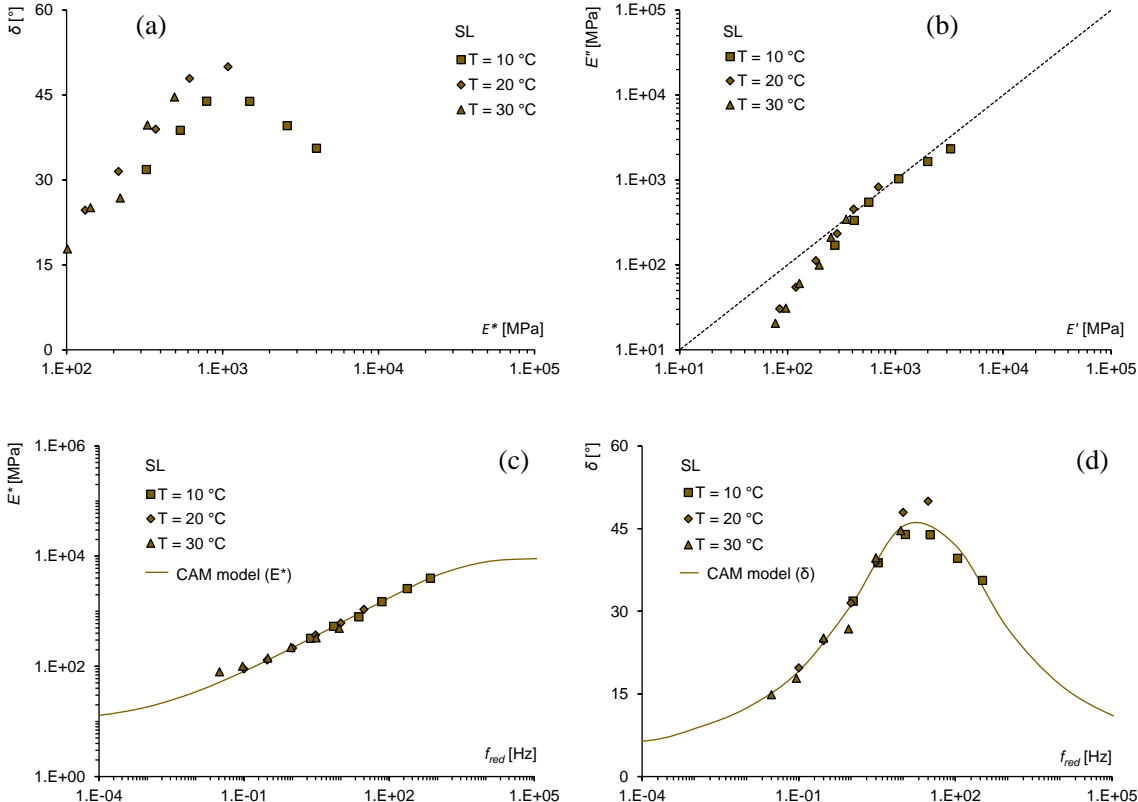


Figure 5.73. Black diagram (a), Cole-Cole plot (b), master curves of E^* (c) and δ (d) of SL.

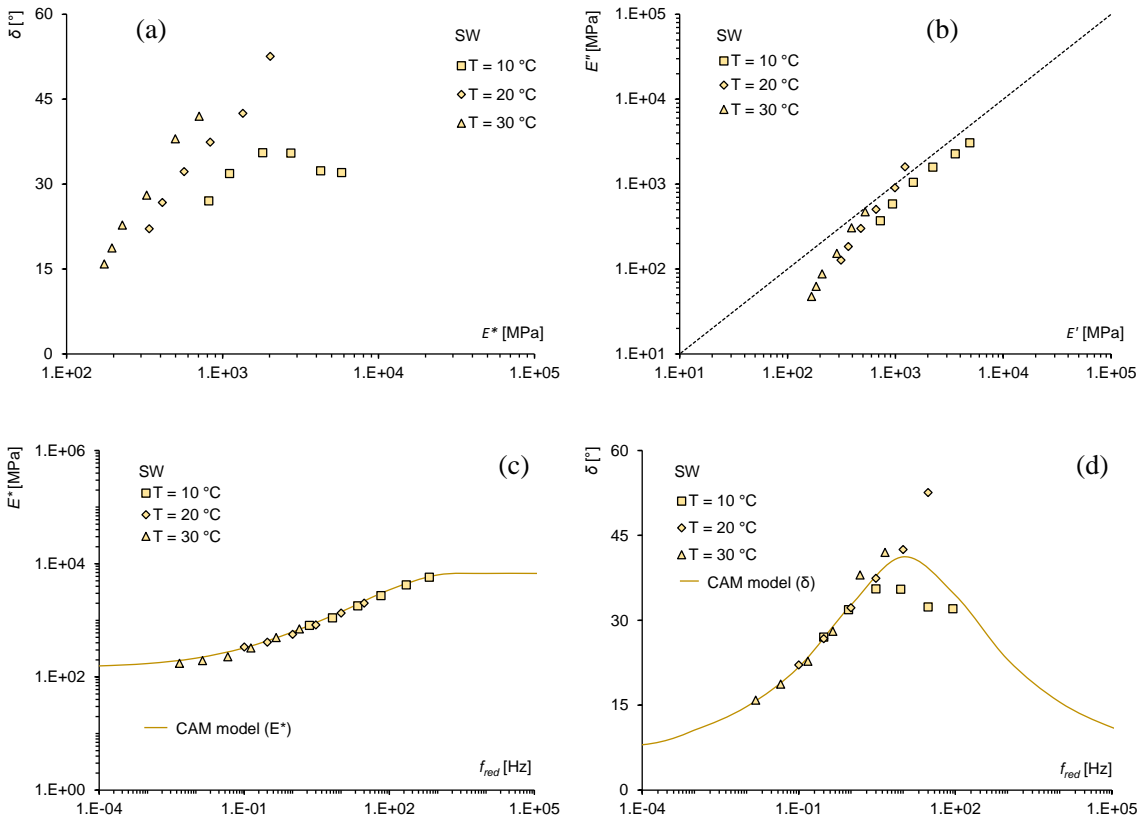


Figure 5.74. Black diagram (a), Cole-Cole plot (b), master curves of E^* (c) and δ (d) of SW.

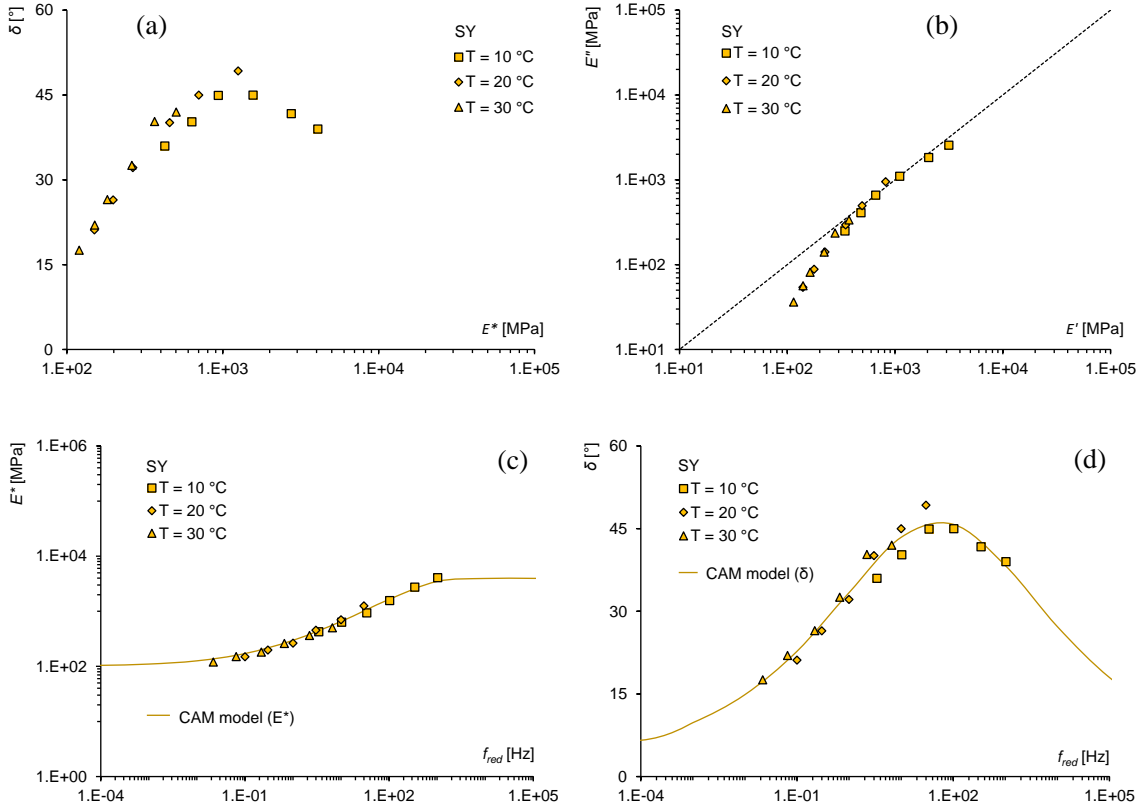


Figure 5.75. Black diagram (a), Cole-Cole plot (b), master curves of E^* (c) and δ (d) of SY.

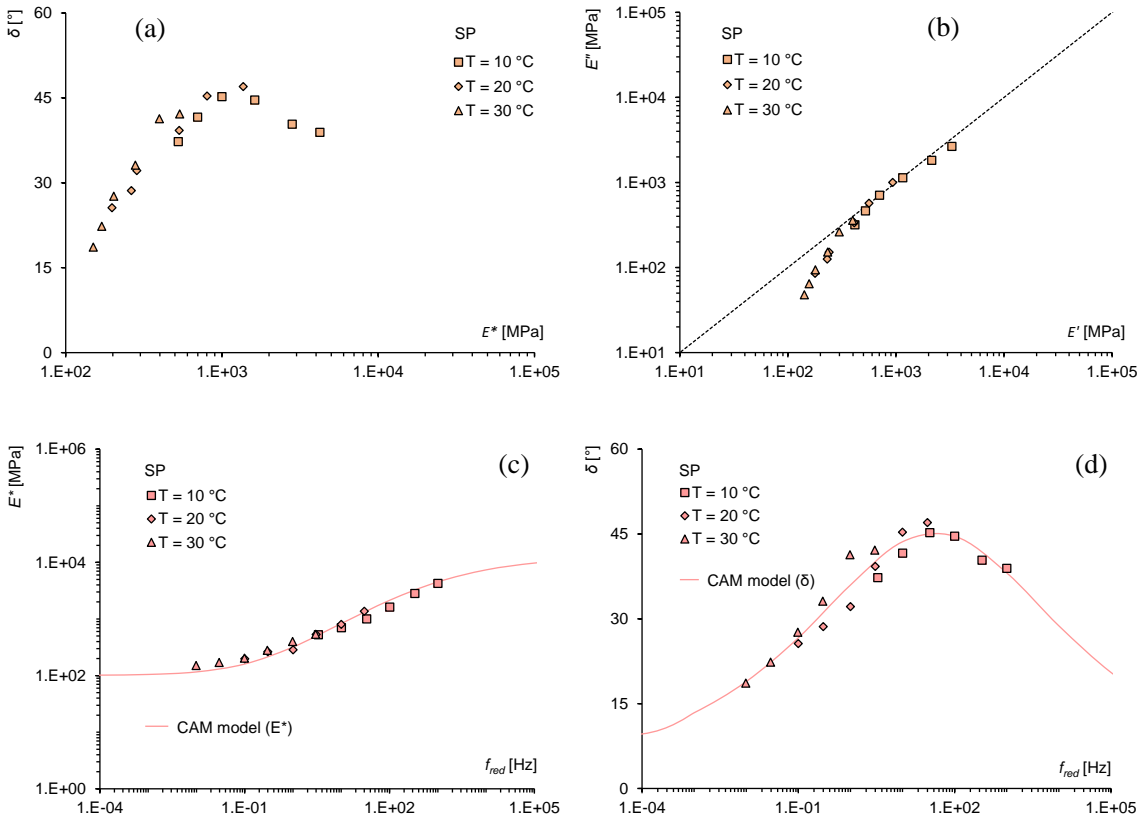


Figure 5.76. Black diagram (a), Cole-Cole plot (b), master curves of E^* (c) and δ (d) of SP.

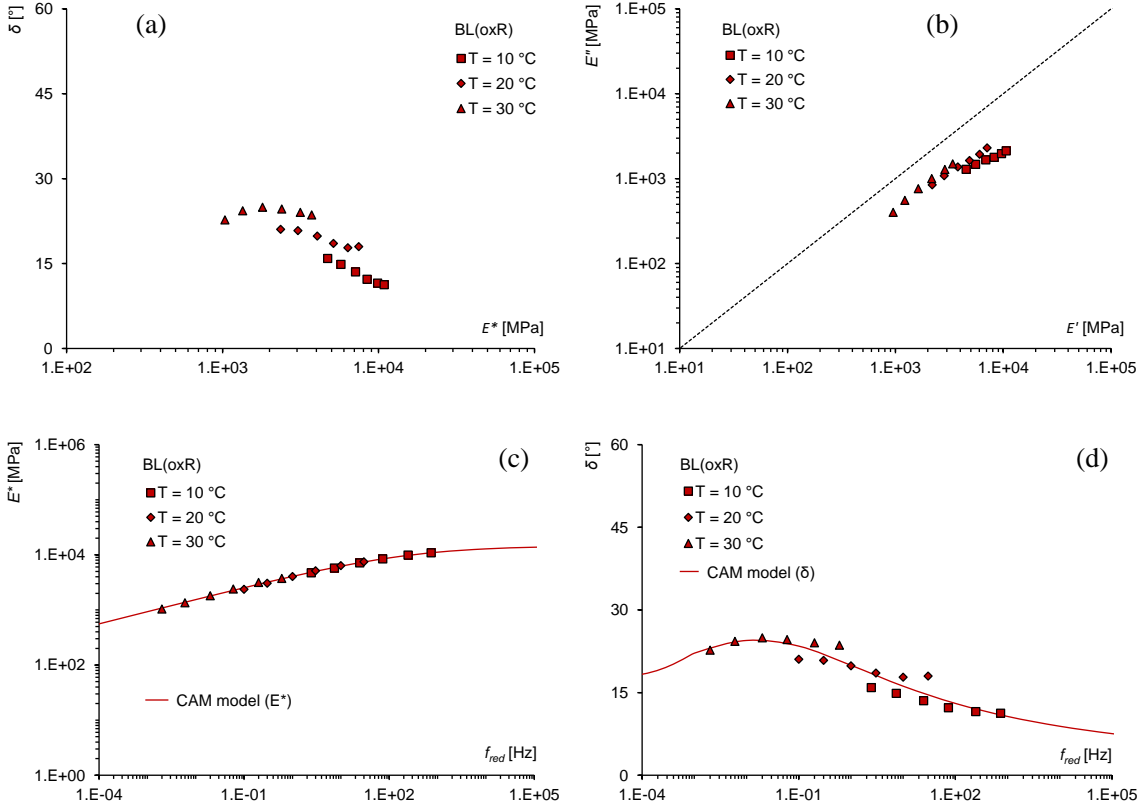


Figure 5.77. Black diagram (a), Cole-Cole plot (b), master curves of E^* (c) and δ (d) of BL(oxR).

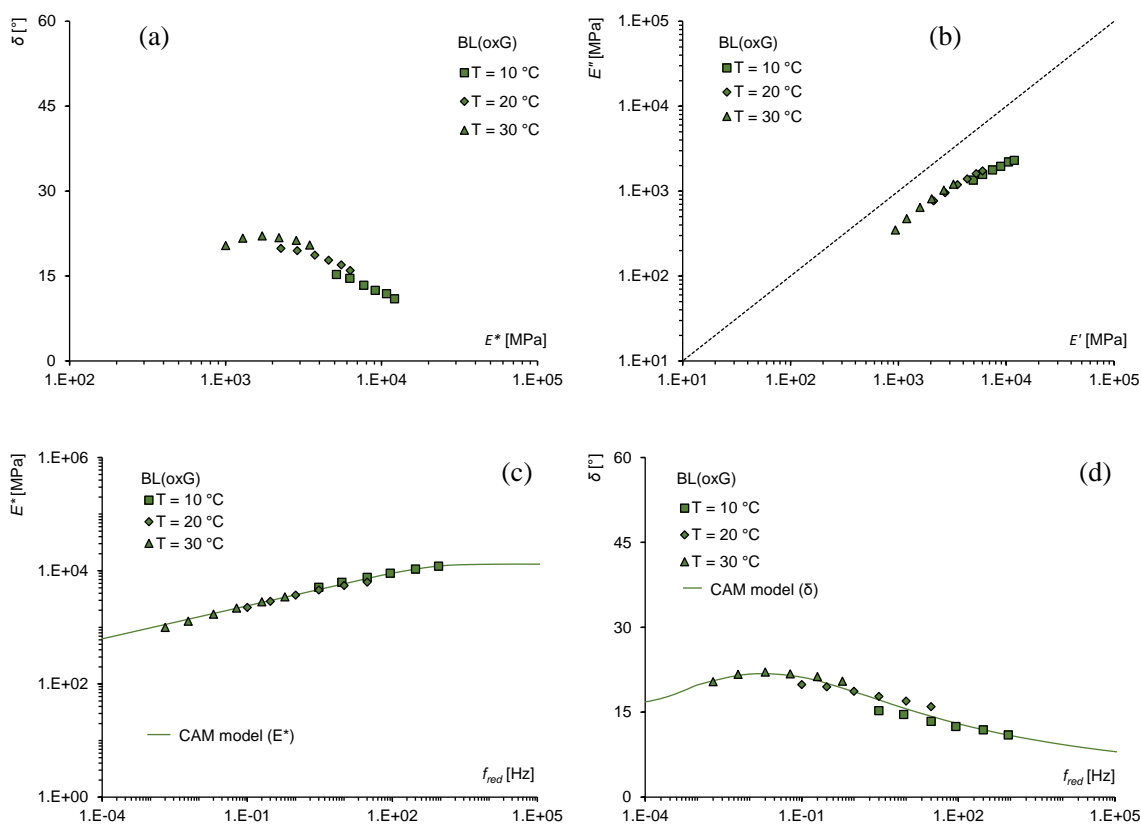


Figure 5.78. Black diagram (a), Cole-Cole plot (b), master curves of E^* (c) and δ (d) of BL(oxG).

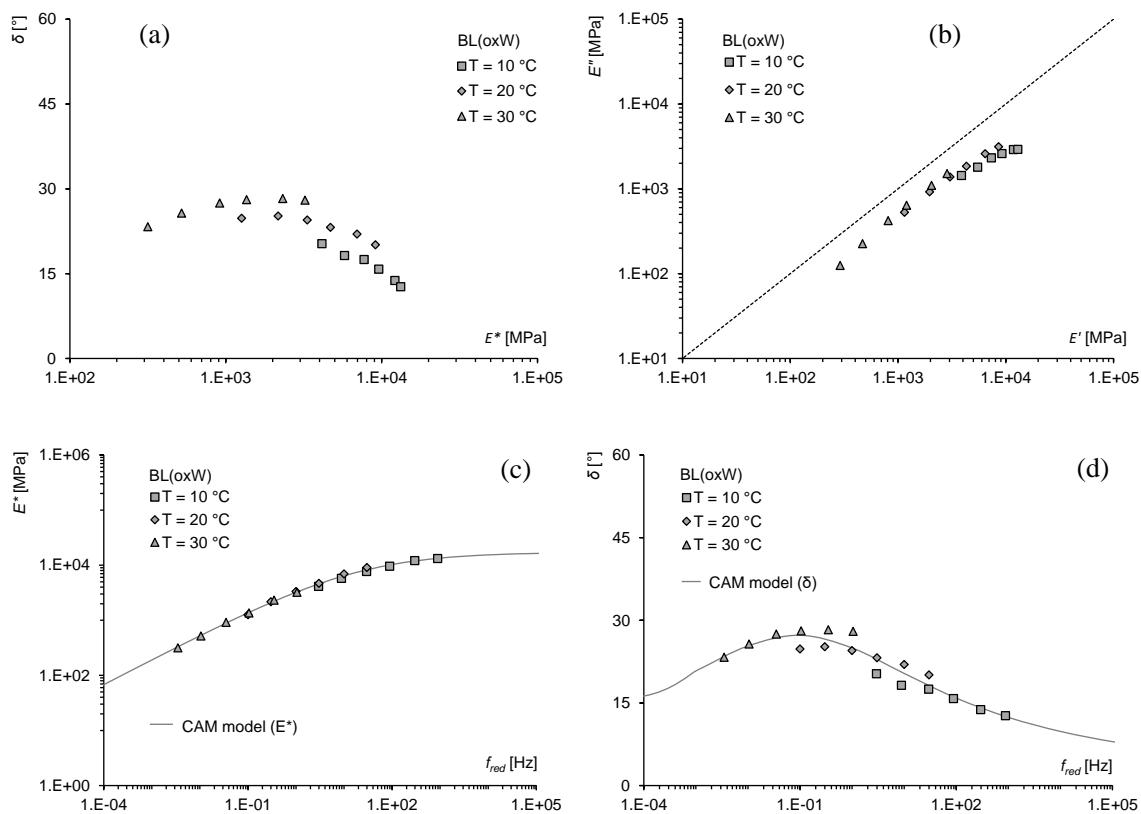


Figure 5.79. Black diagram (a), Cole-Cole plot (b), master curves of E^* (c) and δ (d) of BL(oxW).

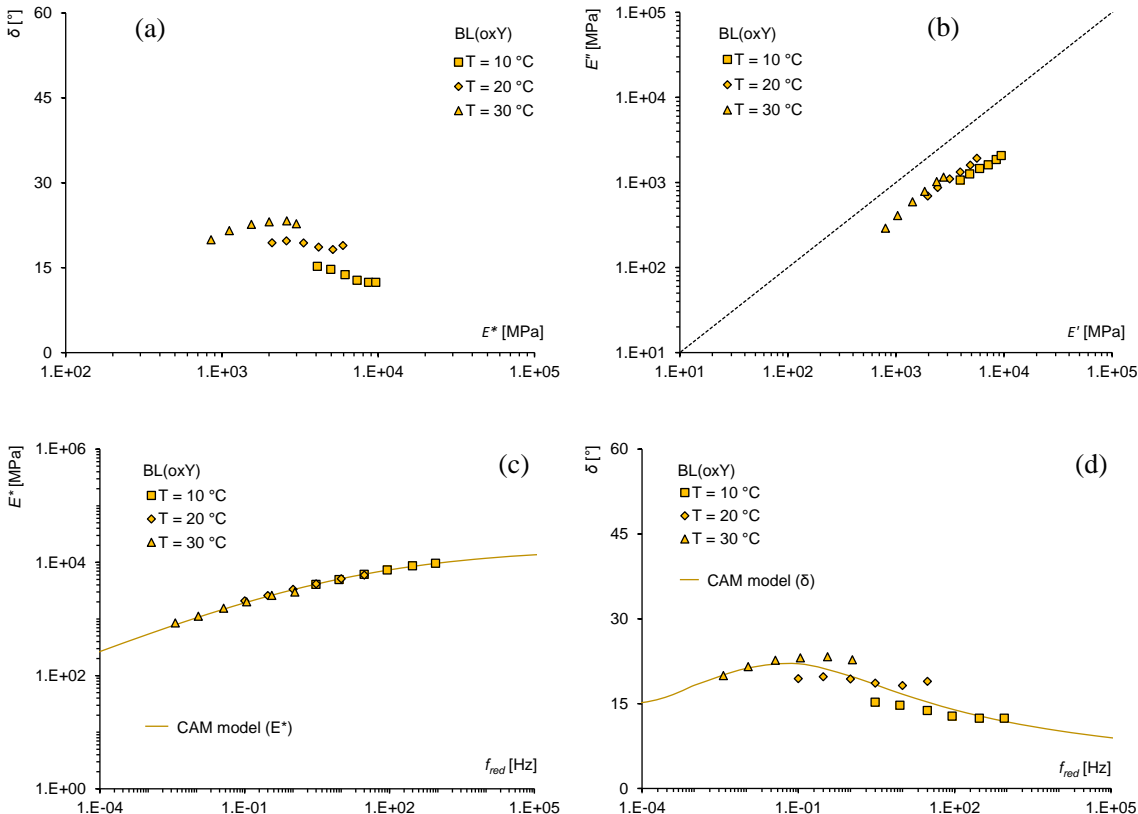


Figure 5.80. Black diagram (a), Cole-Cole plot (b), master curves of E^* (c) and δ (d) of BL(oxY).

Trying to analyze the obtained curves, the consistency of the material thermos-rheological simplicity (and the subsequent validity of the time-temperature superposition principle) was priory discussed. Indeed, although such evaluations were partially affected by the narrow thermal range analyzed and the limited amount of available data (for laboratory constrains, prismatic specimens were tested only at 10, 20 and 30 °C), some interesting information were anyway collected.

Considering the Black spaces' shapes, it is evident that the use of the synthetic resin (S) caused the partial failure of the TTSP regardless the coupling with different aggregate types (curves of various temperature furnished misaligned global trends). Also the presence of oxide pigments showed similar results. However, the misaligned Black curves seem always to tend towards good-looking shapes; in this sense, with respect to the Black curves evinced for binders, at mixture-scale the aggregate contribution attenuated the scattering of the single series. For this reason, the construction of the master curves (shifting of the experimental data in unique representative curves) was anyway proposed and stiffness and phase angle models were employed (a certain reliability was found).

Cole-Cole representation of BL indicated a general elastic behavior of the reference mixture; this was expectable for a conventional wearing-course asphalt concrete at the

intermediate temperature tested (from 10 to 30 °C). Under the same test conditions, S-based mixes started to approach (and crossed in some areas) the equal-slope line and also a viscous-like behavior was detected. Conversely, oxide-pigmented mixes were characterized by Cole-Cole diagrams farer from the bisector, probably in view of the higher stiffness recorded for such a mixtures.

The shape of E^* master curves also indicated a quite different response of the S-based mixes with respect to BL and oxide-colored ones. Whilst the latter drawn a partially-smoothed and aligned curve, the first ones tend to present a s-shaped aspect (within the plotted interval, S-based curves clearly approached the glassy and equilibrium asymptotes). This clearly indicated a greater frequency dependency, at least at the intermediate temperature (reference T is equal to 20 °C) and could be even traduced in higher deformability for the synthetic binder (i.e. the global response already evinced by the S study). In absolute terms, the following Figure 5.81 (comparison of E^* master curve models) indicated always lower stiffness for resin-based samples; in general, using S resin, slightly higher stiffness should be obtained adopting the yellow-Siena marble and coral-pink stone, whereas the utilization of white marble and the limestone seemed to furnish the softer mixtures (see the above-mentioned worse characteristics of aggregates). This could partially threaten the structural integrity of the wearing course layer. On the other hands, oxide-pigmented curves resulted always stiffer than reference BL, without particular significance in the chosen color (it must be remembered that, despite the different pigments, the aggregate used in these cases was always the limestone). For these reasons, considering the limestone presence also in BL, it can be supposed that the relevant stiffening effect was directly provided by the oxides; this totally agreed with previous findings, depicted at the binder-scale, where aggregates were not included.

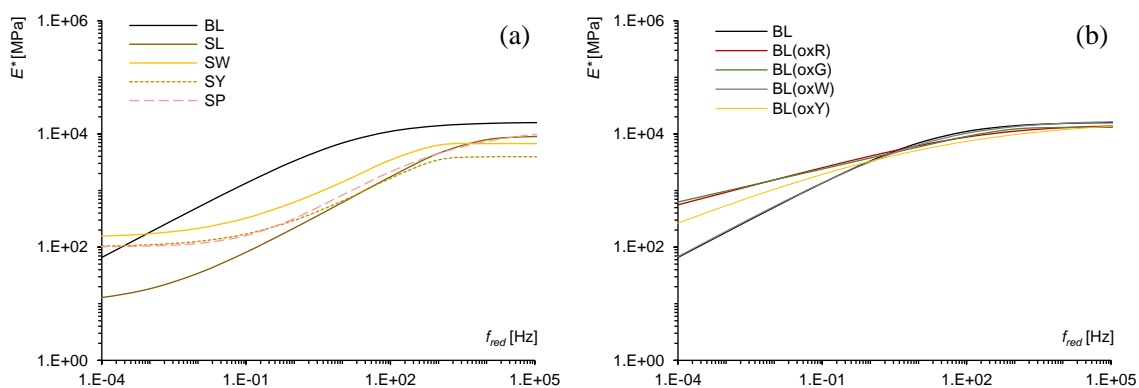


Figure 5.81. Comparison of E^* master curves: BL vs. S-based (a) and oxide-pigmented (b) mixes.

Comparing δ master curve models (Figure 5.82), the above-discussed evincing are again followed. Therefore, interesting concerns were detected analyzing the location of the curves: BL and oxide-colored series presented bell-shapes centered across a location

frequency (f_d) of about 0.1 Hz, whereas S-based ones were always shifted to the right, with f_d greater of about one magnitude order. The fact stated that the transition frequencies from which the phase angles started to decrease (and the materials tend towards the elastic behaviors) were sensibly greater with respect to that of BL and BL(ox-); in this sense, for a defined and probable frequency range, S-based mixtures should present always a predominance of the viscous behavior.

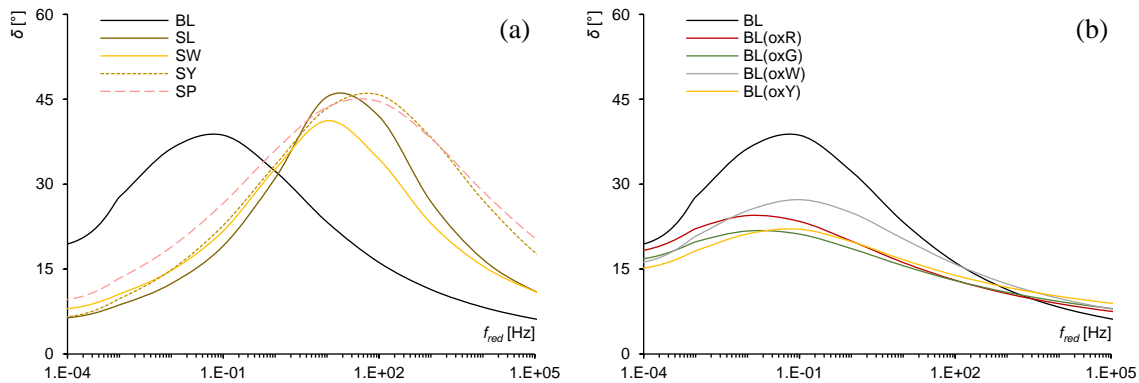


Figure 5.82. Comparison of δ master curves: BL vs. S-based (a) and oxide-pigmented (b) mixes.

Then, it could be also noticed that the stiffness values given by the produced master curves were compatible with those determined through the ITSM tests if, according to many authors, 2 Hz test frequency is assumed in the case of the stiffness modulus impulsive test carried out with a rise-time of 124 ms [5.19, 5.20].

Finally, based on the stiffness findings, some concerns should be surely considered in view of the softer aptitude of the S-based mixes – cause of eventual rutting potential at the higher service temperatures – as well as for what concerning the high rigidity of the oxide-colored ones – the fact can lead to possible embrittlement of the mixture and favour the layer cracking, above all for the arising of fatigue phenomena. Thus, such aspects are following taken into account.

5.3.5.3. Fatigue life

Fatigue resistances of the tested mixtures are here presented and discussed. Experimental tests, executed at different stresses, are shown in Figure 5.83, where the initial stiffness moduli (considered at the 100th cycle) are plotted against the number of cycles before the failure (identified with the typical criterion of the halving of E_{100}). Under this assumptions, S-based mixes furnished noticeable greater fatigue resistances in comparison with the reference BL (at a given E_{100} value, they requested a sensibly higher number of cycles to reach the conventional failure). This was also testified by the A parameters of the fatigue laws reported in Table 5.31. B parameters, representative of the fatigue-line slopes, suggested quite higher inclination of S-based curves, thus they indicated a lightly higher

susceptibility to the stiffness variation, i.e. a slightly greater stress-strain dependency (in line with previous findings). More specifically, SW exhibited the greater fatigue resistance among S-based mixes; in this sense, its lowest stiffness pushed towards this direction (it is widely accepted that softness is one of the crucial parameter able to enhance the fatigue life of the mixtures preventing their excessive embrittlement). Alternatively, SL, SP and SY curves were located intermediately between BL and SW ones, while their slopes were very closed to that of the other S-based solution. On the contrary, oxide-pigmented mixes were characterized by fatigue lines located in the proximity of the reference BL; depending on the pigment, mixes owned lower or higher resistance (overall, results can be considered comparable to BL). Instead, smaller line slopes were always identified (regardless the color, *B* parameters were quite similar – see Table 5.31).

The obtained fatigue-law reliabilities seemed to be more than acceptable, certifying small variability among the different tests replicates. Surely, it should be stressed that, in general, stress-controlled fatigue tests shall be dedicated to the study of thick layers with structural functions (typically, base/sub-base courses) rather than thin wearing courses, which, in a bound system, should suffer deformation induced by the “structural” layers (in a certain manner, the stress-mode could account the fatigue resistances without a strict simulation of that occurring in the field).

However, the obtained estimations of fatigue resistances were considered suitable since all the findings accorded with that expected by the stiffness analysis (hierarchically, stiffer behavior tent to give lower fatigue resistance). Finally, despite the appreciable stiffness, the comparable fatigue lives obtained for BL(ox-) mixes (with respect to BL) must be highlighted (probably, this was ascribable to their higher elasticity, able to comply with the applied stresses and avoid the cracking).

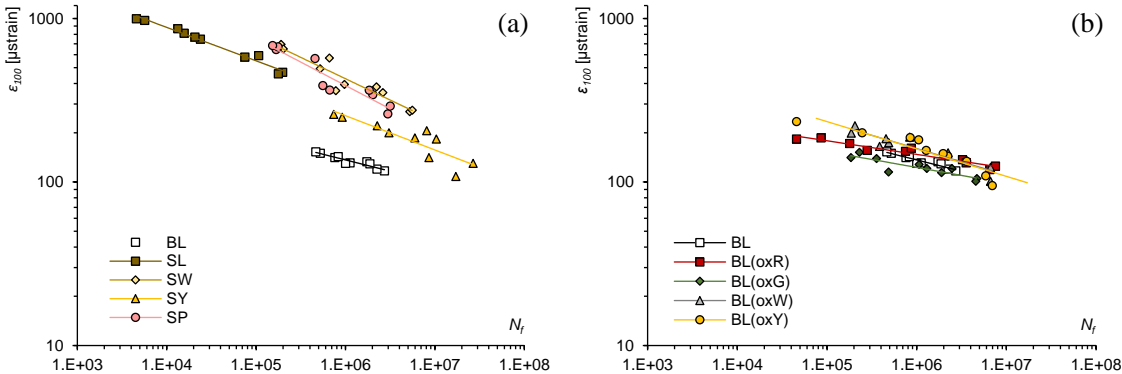


Figure 5.83. Fatigue curves (failure plotted against initial strain): BL vs. S-based (a) and oxide-pigmented (b) mixtures.

Table 5.31. Fatigue results: law parameters and stress related to 10^6 cycles (σ_6).

Mixture	A	B	R ²	σ_6
	[-]	[-]	[-]	[MPa]
BL	915	0.138	0.90	0.659
SL	5799	0.204	0.98	0.198
SW	15694	0.261	0.89	0.348
SY	4596	0.209	0.76	0.453
SP	20308	0.286	0.90	0.320
BL(oxR)	466	0.083	0.93	0.638
BL(oxG)	473	0.098	0.77	0.644
BL(oxW)	1500	0.162	0.86	0.644
BL(oxY)	1609	0.167	0.85	0.652

5.3.5.4. Rutting resistance

Rutting resistance is one of the crucial aspects concerning the wearing courses since it represents the ability of the surfaces to resist against the permanent deformations developed at high in-service temperature (as verified, surface mixtures could reach above 70 °C during hot summer). In this purpose, RLA results are presented in Figure 5.84, where the cumulative axial strain ε_n is given as a function of the creep cycle's number applied to the tested samples. Table 5.32 reports the final axial strain, the creep rate and the creep modulus. Although a limited stiffness was recorded for all the S-based mixes, they were characterized by comparable, even lower rutting potentials with respect to the reference BL for the applied stress – see Figure 5.84a (widely according to literature, poor stiffness generally corresponds to materials more prone to accumulate permanent deformations) [5.21].

Among all the S-based solutions, once again SW (synthetic resin with white marble) gave slightly worse performance probably because of the lithic skeleton characteristics. Moreover, also the lower creep rates of S-based mixtures indicated a good ability to resist against rutting (creep modulus of S-based mixes resulted quite higher with respect to that of BL). Such findings should be also read considering the effective performance of the materials at temperature of 40 °C (the RLA test temperature). In this perspective, with particular focus on the frequency of 0.5 Hz (the RLA test frequency), the hypothetical E^* and δ master curves, shifted at the reference temperature of 40 °C, should give S-based moduli comparable with that of BL and S-based phase angles sensibly lower, indicating a probable elasticity able to limit the aptitude to rutting. Concerning oxide-pigmented solutions, as expected, BL(ox-) mixes demonstrated sensibly greater rutting potential with respect to BL in view of their higher stiffness (definitely lower cumulative axial strains and creep rates, higher creep moduli). In this case, BL(oxY) showed the better performance; overall, the slightly different responses between BL(oxR), BL(oxG), BL(oxW) and BL(oxY) were probably due to the peculiar volumetric characteristics and the structural properties of the single mix.

Globally, it is worth noting that, as demonstrated by the thermal evaluation, the different materials subjected to the same heat energy in the field would attain different temperatures; thus, since the clear or colored mixtures would achieve lower temperatures than the reference black surface of BL (under the same climatic conditions), an even enhanced rutting resistance should be expected both for S-based and oxide pigmented mixtures.

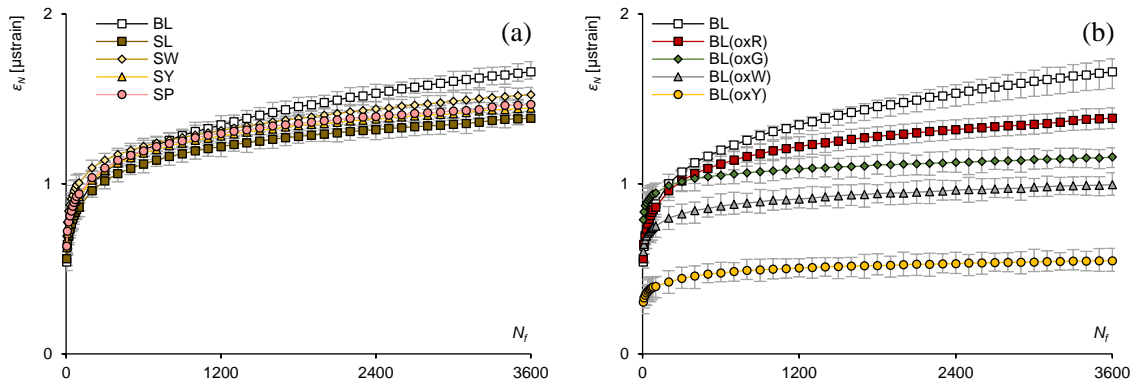


Figure 5.84. RLA tests results: BL vs. S-based (a) and oxide-pigmented (b) mixtures.

Table 5.32. RLA test results: final axial strain, creep rate and creep modulus of mixtures.

Mixture	u_n (at 3600 cycles) [%]	f_c [$\mu\text{strain}/\text{cycle}$]	E_n [MPa]
BL	1.659	1.136	6.027
SL	1.386	0.595	7.213
SW	1.525	0.773	6.559
SY	1.446	0.569	6.917
SP	1.467	0.622	6.817
BL(oxR)	1.386	0.595	7.213
BL(oxG)	1.158	0.258	8.633
BL(oxW)	0.995	0.293	10.046
BL(oxY)	0.548	0.160	18.262

5.3.5.5. Surface characteristics

Surface results of painted (surface-treated) mixtures are following discussed. First, mean texture depth was analyzed trying to evaluate the superficial mixture smoothness for safety and comfort purposes (adherence phenomena and noise emissions). Results reported in Table 5.33 indicate that, as supposed, the application of the surface treatments partially lowered the reference *MTD*; no significant correspondence between the recorded values and the applied color was found, whereas mortar paints seemed to furnish quite smoother surfaces with respect to resins. Permeability P was then evaluated in order to establish possible criticalities due to the presence of stagnant water films on pavement surfaces which can compromise the driving safety (visibility, sliding and aquaplaning concerns are well-

known). Results reported in Table 5.33 were highly scattered probably because of the empirical nature of the experimental test. However, a general increase of the flow time was detected with the surface treatment presence (without particular patterns related to the color or the paint type). Finally, skid resistance was analyzed in order to assess the capability of the surface in guaranteeing adequate adherence (at least comparable with those obtained for a conventional asphalt concrete for wearing course) – see Table 5.34. *PTVs* determined for BL(m-) and BL(s-) mixtures were perfectly in line with the reference one (BL), again without particular recognizable patterns connected to treatment color or nature (the marginal differences were ascribed to the experimental variability). Overall, such results were generally greater than the minimums required from typical technical specifications for wearing courses (as examples, the most restrictive specifications request *MTD* greater than 0.6 and *PTV* higher than 55). As far as the above-described results should vary as a function of the applied paint dosage, some fluctuations should be expected depending on the utilized quantities; otherwise, since the dosages were selected within the ranges suggested by the producers, consideration were considered reliable. Moreover, resins-mortars comparison was considered suitable in view of the identical quantities applied in the two cases.

Table 5.33. Mean texture depth and permeability results for surface-treated mixtures.

Mixture	MTD				P [s]			
	Rep_1	Rep_2	Rep3	MTD _{mean}	Rep_1	Rep_2	Rep_3	P _{mean}
BL	1.070	1.033	1.039	1.048	121	78	77	92
BL(rR)	0.882	0.859	0.859	0.867	393	1080	1080	851
BL(rG)	0.835	0.862	0.901	0.866	400	314	450	388
BL(rY)	0.882	0.930	0.905	0.906	148	258	265	223
BL(rB)	0.757	0.722	0.722	0.734	2160	2160	5400	3240
BL(mR)	0.615	0.615	0.623	0.618	843	609	483	645
BL(mG)	0.670	0.649	0.687	0.669	727	579	613	640
BL(mY)	0.722	0.729	0.722	0.724	247	254	273	258
BL(mB)	0.581	0.576	0.574	0.577	489	626	480	532

Table 5.34. Pendulum test values for surface-treated mixtures.

Mixture	PTV [-]										PTV _{mean}
	Rep_1	Rep_2	Rep3	Rep_4	Rep_5	Rep_6	Rep_7	Rep_8	Rep_9	Rep_10	
BL	75	75	70	80	75	90	80	85	85	75	75
BL(rR)	73	76	76	80	70	87	78	85	85	73	76
BL(rG)	70	75	74	76	70	85	79	90	78	70	75
BL(rY)	70	76	76	75	73	85	83	87	85	70	76
BL(rB)	65	73	75	78	73	83	81	80	80	65	73
BL(mR)	68	70	76	80	70	80	80	80	80	68	70
BL(mG)	63	68	73	80	71	83	82	78	80	63	68
BL(mY)	60	70	74	75	68	83	82	75	87	60	70
BL(mB)	60	72	73	73	68	80	79	78	85	60	72

5.3.5.6. Durability

First, durability was evaluated considering the ITSR results. In this regard, Table 5.35 presents the results obtained for the different mixes (cylindrical 150-mm specimens) tested at 25 °C in dry and wet conditions. As evident, all the selected mixtures exhibited satisfactory ITSR value (ITSR greater than 0.7 are generally considered acceptable [5.22]). Resin-based specimens had the greater moisture resistance since ITSR approached the unity, regardless the aggregate type). According to strength findings (see paragraph 5.3.5.1), oxide-pigmented materials tend to own quite higher tensile strength with respect to black samples, whereas resin-based ones once again demonstrated substantial lower strength. The effect of the aggregate or the color seems to be negligible (same mix types showed similar ITS results).

Table 5.35. Water sensitivity expressed in ITSR.

Mixture	Dry				Wet				ITSR
	d [mm]	h [mm]	P [kN]	ITS [MPa]	d [mm]	h [mm]	P [kN]	ITS [MPa]	
BL	149.54	48.82	7.913	0.690	149.63	48.82	7.087	0.618	0.895
SL	149.96	48.61	3.447	0.301	149.67	48.61	2.991	0.262	0.869
SW	149.64	49.44	2.975	0.256	149.03	49.44	2.874	0.248	0.970
SY	149.64	49.50	3.071	0.264	150.26	49.50	2.837	0.243	0.920
SP	149.65	49.94	2.829	0.241	149.65	49.94	2.575	0.219	0.910
BL(oxR)	149.49	48.89	12.214	1.064	149.91	48.89	9.256	0.804	0.756
BL(oxG)	149.87	49.01	12.946	1.122	148.36	49.01	10.308	0.902	0.804
BL(oxW)	149.58	48.63	11.553	1.011	150.95	48.63	9.443	0.819	0.810
BL(oxY)	149.47	49.02	12.557	1.091	149.67	49.02	10.191	0.884	0.811

As anticipated, the durability of the surface-treated mixtures was evaluated subjecting their surface to an accelerated deterioration (repetition of 100 skid tests). Indeed, the selected procedure was not based on specific standard indications. Otherwise, the use of pendulum tests (without the wetting of the surfaces) produced friction phenomena that could be considered useful to produce tangential stress on pavement and threaten the treatment functionality. Moreover, comparing the various mixtures, eventual different responses were assessed (namely as a function of the treatment type – resin or mortar, in addition to the color). The applied DIP quantified the residual covered percentage after such process; in this perspective, Figure 5.85 reports an example of the obtained results (photographic acquisition). Results concerning the different mixes are reported in the following Tables 5.36 and 5.37, where numerical details of the elaborations and residual coverages are given. Based on the data, resin-treatments resulted highly affected by the abrasion (effective loss near 93-96%), whereas mortar ones presented greater resistance in this sense (mean loss about 0.5%). Thus, also considering the equal dosage of the two treatments, r- was majorly able to prevent the color loss (at least for what regarding the friction effects). Really, a

deeper understanding of the in-field durability should be obtained monitoring real-scale applications (with adequate timing) since the possible color loss should be influenced by several concomitant factors – such as for examples the atmospheric agents, the possible intrinsic variation of the paint color, the effect of dirt and dust – and should depend by various aspects (traffic intensity, typology, weather and climate, etc.).

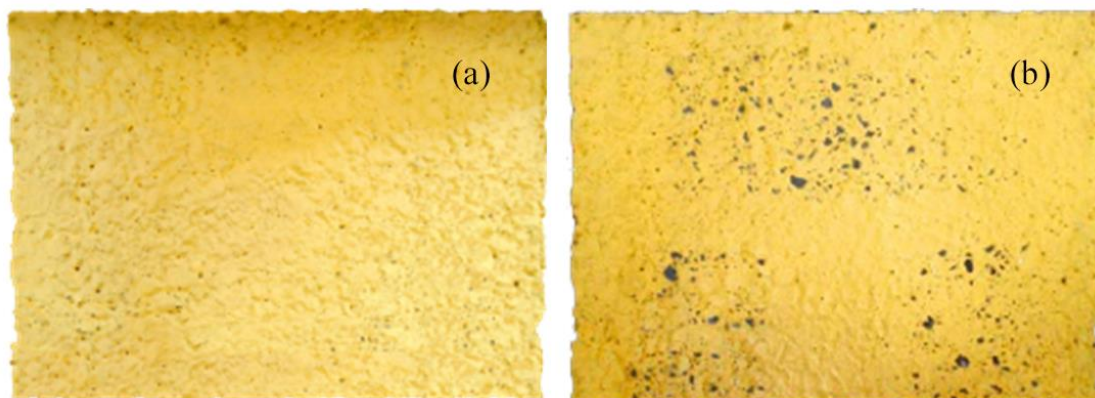


Figure 5.85. Example of DIP: evaluation of residual coating before (a) and after (b) abrasion – BL(rY) mixture.

Table 5.36. Resistance to abrasion for r- surface-treated mixtures.

			BL(rR)	BL(rG)	BL(rY)	BL(rB)
Initial	Total sample:	[pixel]	13644563	12656899	13265465	14066556
	Residual coating:	[pixel]	13500121	12530898	13193669	13690049
	Exposed portion:	[pixel]	144442	126001	71796	376507
	Residual percentage:	[%]	98.94	99.00	99.46	97.32
Final	Residual coating:	[pixel]	13151296	11858956	12364654	13162665
	Exposed portion:	[pixel]	493267	797943	900811	903891
	Residual percentage:	[%]	96.38	93.70	93.21	93.57
Effective loss due to abrasion:		[%]	2.58	5.36	6.28	3.85

Table 5.37. Resistance to abrasion for m- surface-treated mixtures.

			BL(mR)	BL(mG)	BL(mY)	BL(mB)
Initial	Total sample:	[pixel]	12564566	12956566	13564656	13846654
	Residual coating:	[pixel]	11996077	12259732	13319979	12935689
	Exposed portion:	[pixel]	568489	696834	244677	910965
	Residual percentage:	[%]	95.48	94.62	98.20	93.42
Final	Residual coating:	[pixel]	11932048	12191655	13254955	12876559
	Exposed portion:	[pixel]	632518	764911	309701	970095
	Residual percentage:	[%]	94.97	94.10	97.72	92.99
Effective loss due to abrasion:		[%]	0.53	0.56	0.49	0.46

In conclusion, for what regarding the resistance to fuel spillages (evaluated through a brushing procedure on surface-treated mixtures), the following Figures 5.86–5.89 illustrate some representative pictures of the obtained slabs. As evident, the painted surfaces were unable to resist against the fuel action, at least under the test conditions set; after the treatment, the portions exposed to the fuel were characterized by the stripping of the applied paints (regardless the use of resin or mortar) and the concrete surface start to be damaged. Then, the weighting of the loss masses was not carried out because of the complete failure of the surfaces.

For this reason, the surface treatments applied to the slabs were considered useless to prevent the damages caused by fuel spillages.

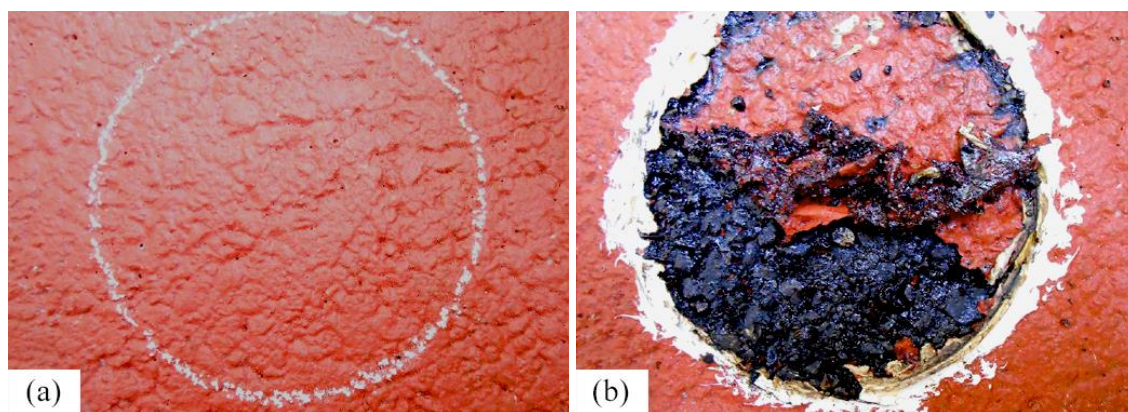


Figure 5.86. Results of fuel resistance: BL(rR) mixture before (a) and after (b) the treatment.

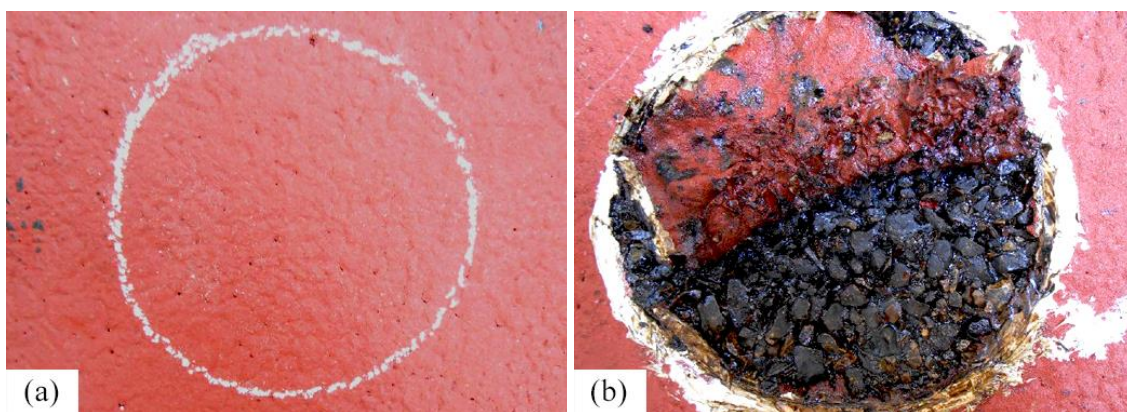


Figure 5.87. Results of fuel resistance: BL(mR) mixture before (a) and after (b) the treatment.

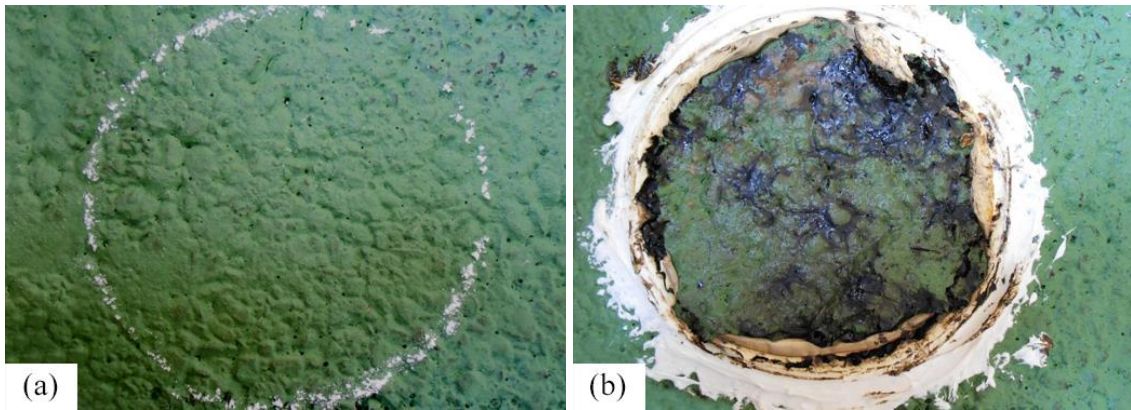


Figure 5.88. Results of fuel resistance: BL(rG) mixture before (a) and after (b) the treatment.

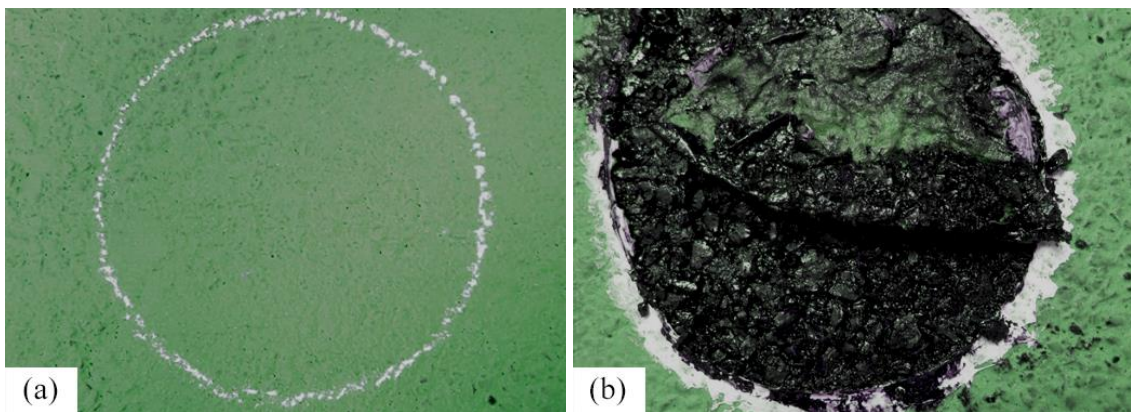


Figure 5.89. Results of fuel resistance: BL(mG) mixture before (a) and after (b) the treatment.

Chapter 6

Outlines and Discussion

The present Chapter aims at discussing the main results deduced by the chromatic evaluation, the thermal analysis and the mechanical characterization performed on the studied materials.

6.1. Thermal correlations

The existence of possible correlations between the chromaticity and the thermal performance of materials is following assessed.

6.1.1. Chromatic-thermal correlations

The earlier steps of the evaluation dealt with the existence of eventual relationships between the colors and the radiative properties of the materials; such prospective correlations were made in order to verify the possibility of estimating the field thermal responses of a given material based on an effortless and timesaving assessment of its chromatic characteristics. In this perspective, it is worth considering that such thermal behavior should be influenced by the combined effects mainly of the emissivity, the albedo and the thermal conductivity of the mixtures. Really, it must be remembered that the albedo was already calculated starting from the chromatic peculiarities of the surface (it was already linked to the lightness value). In other hands, the emissivity resulted an intrinsic characteristic of this kind of road mixtures and slightly varied around 0.9 [2.16]. Therefore, the assessment was performed only considering the values of the thermal conductivity of the mixtures. To this aim, Figure 6.1 reports the k value for each mix as a function of the three color parameters used to

describe the surface color (hue H , saturation S and lightness L). As it can be noticed, experimental data did not evidence clear correlations between the chromatic characteristics and the corresponding thermal conductivity; this could suggest to address the attention to a coupled (overall) evaluation of chromatic and radiative properties in order to achieve a sound estimation of the thermal response of the studied material.

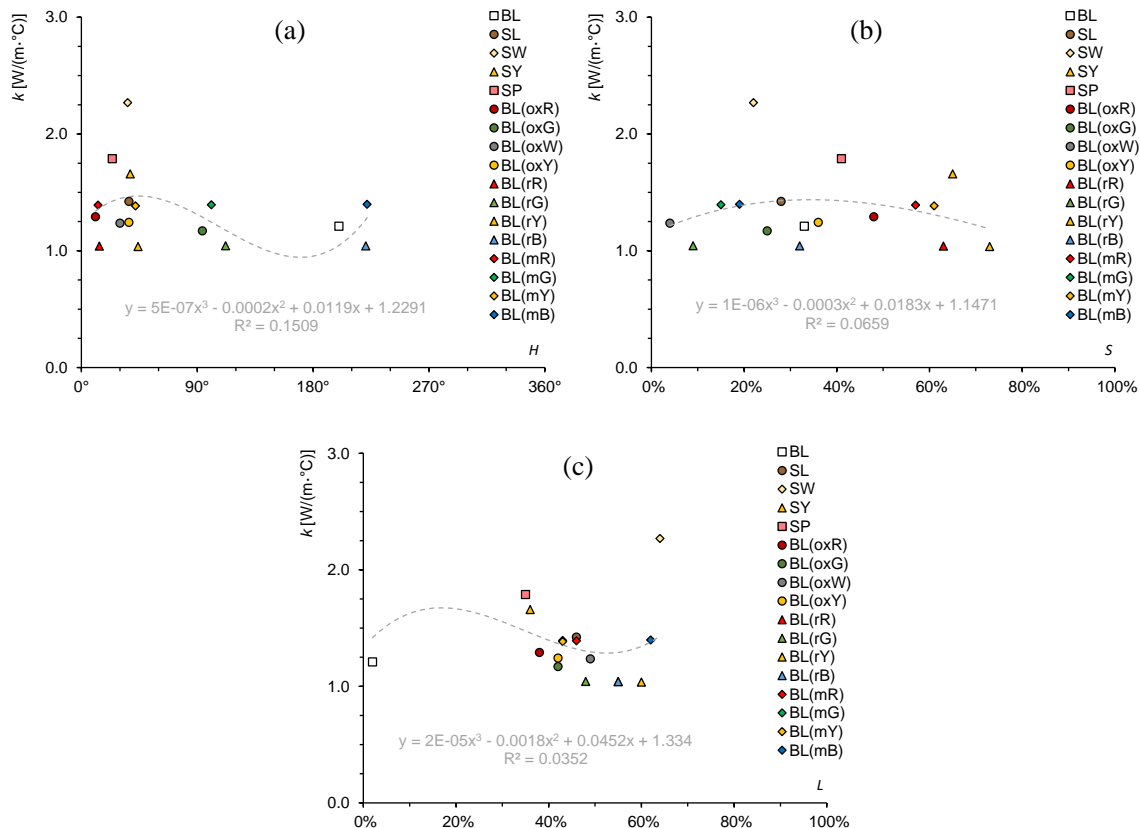


Figure 6.1. Correlation between conductivity and hue (a), saturation (b) and lightness (c).

6.1.2. Thermal responses

The further steps were moved with the objective to investigate the influence of the thermal properties of the tested materials on the heat flow balance, whose background theory have been previously illustrated (see Chapter 2). Therefore, in-service pavement's thermal responses were estimated calculating the values of the net rates of heat flow under the environmental conditions recorded during the experimental survey campaign described above. In this perspective, the following Tables 6.1, 6.2 and the Figure 6.2 show the results obtained for the tested materials, reporting the details used to determine the q_{net} , along with the values of each component of the heat flow balance. The calculations were carried out properly taking into account the above-mentioned sign's convention (positive sign for absorbed rates and negative one for released rates).

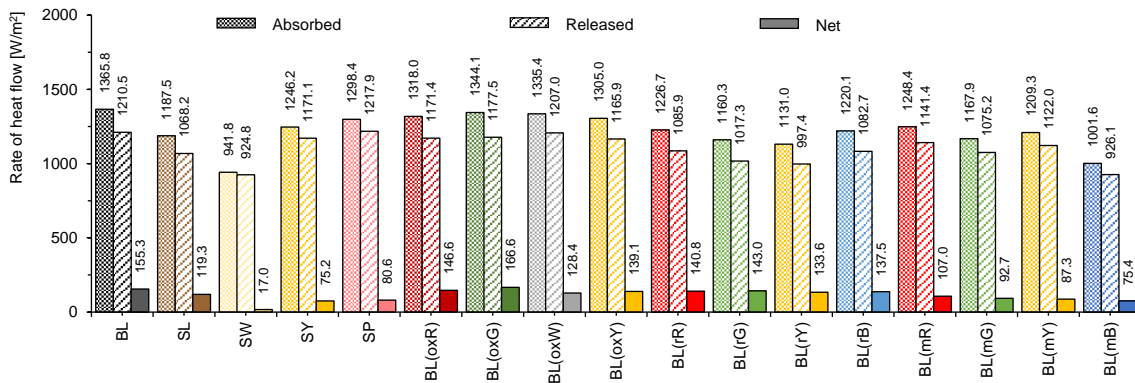
Table 6.1. Details used for the heat flow balance calculation.

Wind speed [m/s]	Vapor pressure [mmHg]	z [°]	τ_a [-]
1.833	40	20	0.78

Table 6.2. Single components of the heat flow balance.

Mixture	$q_{\text{sun}}^{\downarrow}$ [W/m ²]	$q_{\text{cnv}}^{\uparrow}$ [W/m ²]	$q_{\text{cnd}}^{\uparrow}$ [W/m ²]	q_{em}^{\uparrow} [W/m ²]
BL	970.98	430.23	23.74	756.57
SL	792.66	295.16	99.61	673.43
SW	546.92	215.96	90.76	618.06
SY	851.37	340.12	132.72	698.23
SP	903.56	371.51	125.23	721.12
BL(oxR)	923.13	358.74	77.46	735.23
BL(oxG)	949.23	377.22	74.94	725.32
BL(oxW)	940.53	388.56	76.69	741.77
BL(oxY)	910.09	344.43	96.95	724.47
BL(rR)	831.80	334.68	41.64	709.57
BL(rG)	765.47	280.96	73.01	663.34
BL(rY)	736.12	257.60	78.81	660.96
BL(rB)	825.28	314.25	81.28	687.13
BL(mR)	853.55	356.92	58.46	726.05
BL(mG)	773.08	292.25	111.60	671.36
BL(mY)	814.40	316.73	116.34	688.92
BL(mB)	606.72	239.91	44.77	641.47

$q_{\text{atm}}^{\downarrow}$ constant for each case (394.86 W/m²)

**Figure 6.2.** Absorbed, released and net rates of heat flow calculated.

As example, results clearly showed the effectiveness of resin-based samples (i.e. mixtures prepared using the clear synthetic binder) in reducing both the absorbed (from solar radiation) and the released heat energy, leading to a noticeably lower net rate of heat flow for such materials. The most effective result in terms of q_{net} reduction was obtained in the case of SW (mixture prepared with transparent resin and white marble). Thus, in the case of these materials, such findings suggested a strong decrease of the temperatures for the pavement surface and the surrounding environment (leading to a noticeable UHI reduction)

when exposed to a given solar radiation with respect to the reference “black” solution. On the other hands, the colored bituminous mixtures prepared with the oxide pigments did not seem characterized by significant differences with respect to the reference material, suggesting a limited aptitude in reducing temperatures under the specific investigated test conditions. Similar considerations could be drawn in the case of surface-treated mixtures, even if, in some specific cases, mortar-colored ones tent to present slightly lower q_{net} values.

As far as the connection between the absorbed/released rates of heat flow and the temperatures reached by the surfaces is concerned, a deeper analysis was provided trying to establish a mathematical relationship among the resulting q_{net} and the thermal responses of the mixtures. In this regard, Figure 6.3 reports the difference (ΔT_{ref-i}) between the maximum temperature achieved during the outdoor monitoring by the reference BL sample (ref) with respect to the corresponding temperature of the generic clear/colored mix (i) as a function of the corresponding differences in the net rates of heat flow (Δq_{net_ref-i}). Considering all the samples, results seemed unable to outline a certain correlation between the rates of heat flow and the corresponding reduction of the pavement surface temperatures.

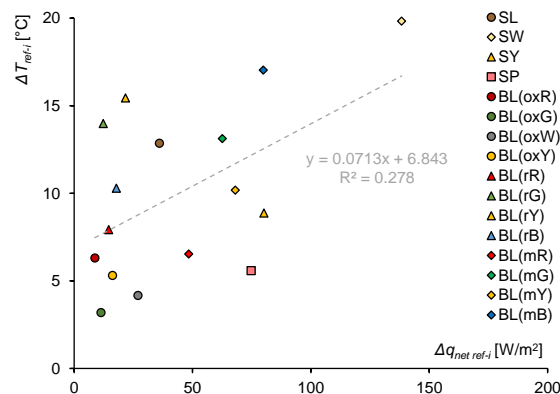


Figure 6.3. Gradients (from reference BL) of temperatures vs. net rates of heat flow.

Further plots of the same results were also proposed grouping the samples of the same typology; this was done supposing that the inconsistency of mathematical law could be ascribed to the different nature of the mixtures (a global plots of all samples – which includes materials of different type – could be considered only partially reliable). Therefore, the following Figure 6.4 illustrates the same elaborations for resin-based mixes (Figure 6.4.a), oxide-pigmented slabs (Figure 6.4.b), surface-treated (resin) concretes (Figure 6.4.c) and surface-treated (mortar) ones (Figure 6.4.d). As evident, also in this case only poor correlations were found, except for the mixtures treated on the surface with mortars – see Figure 6.4.d (coefficient of determination R^2 equal to 0.8109). Thus, the nature of the slabs effectively seems to discriminate the validity of such a relation (possible data scattering connected to the test conditions were limited since all materials were contemporary monitored, thus under the same environmental situation).

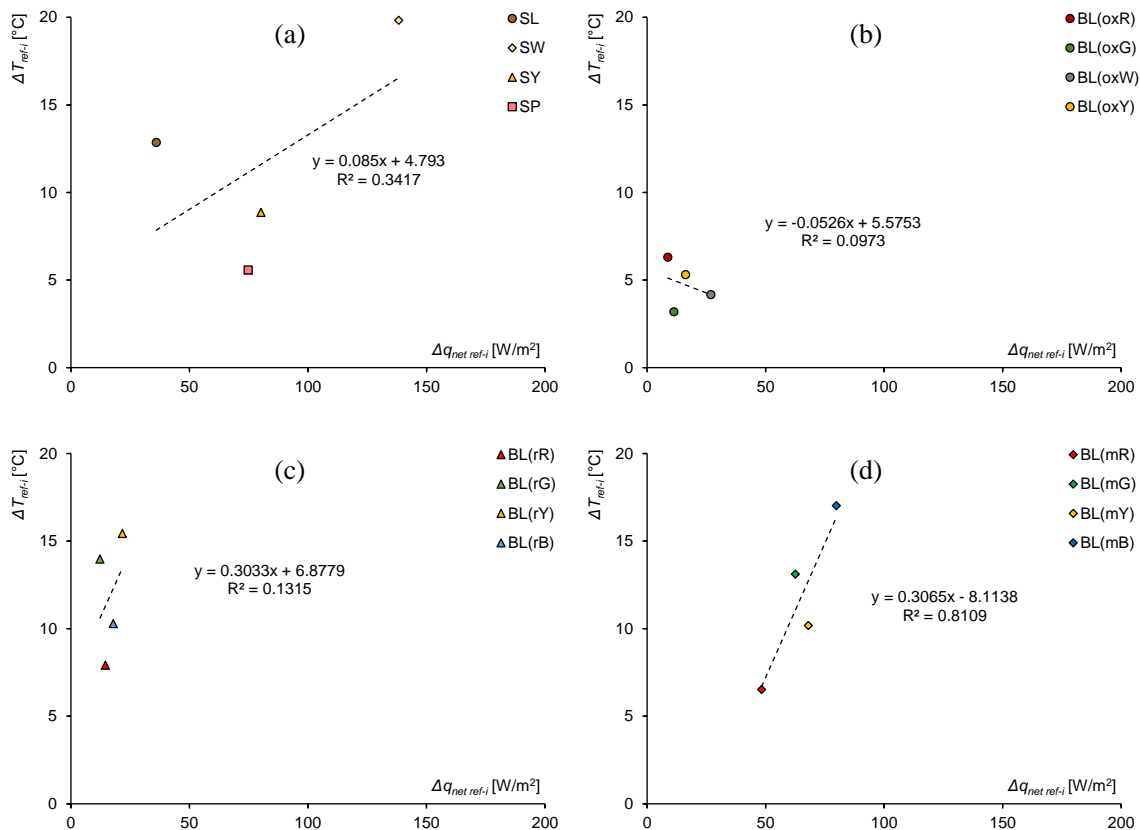


Figure 6.4. Gradients (from reference BL) of temperatures vs. net rate of heat flow (grouped by mixture typology).

The direct estimation of the net rate of heat flow based on the radiative properties of the mixtures was also investigated since such a method could be really advantageous – the thermal performance of mixtures, which request extended monitoring, would be estimated just starting from simple analysis of the radiative properties. Thus, Figure 6.5 tries to link the calculated q_{net} values with the combined effect of the albedos ρ and the thermal conductivities k (the almost-constant emissivities were again neglected). Effectively, a good fit was found with a linear combination of the independent variables (coefficient of determination R^2 equal to 0.926). Equation 6.1 reports the fitting law selected to relate the parameters. With respect to the equation, the fitting parameters a , b , c and d are equal to -148.3 , -407.6 , $+178.8$ and $+353.0$, respectively.

Indeed, the law validity/reliability should be evaluated considering that the proposed energetic balance is governed by specific environmental/boundary conditions. Therefore, further calibration steps could be implemented to determine suitable equations applicable to different monitoring scenarios (varying the incident radiation, the atmospheric scattering, the geometric exposure, the weather conditions, etc.). These concerns will be partially investigated in the following sections, within which some environmental scenarios will be set up to examine the results of the energetic balance.

However, please remember that, based on the background theory, the “prepared” scenarios will be only partially able to predict the thermal responses of the mixtures since the in-field reached temperature is a dependent variable and will be only estimated/inputted.

As a conclusion, please also note that a more precise estimation could also suppose the extension of the sample database (crucial concern for possible future research steps).

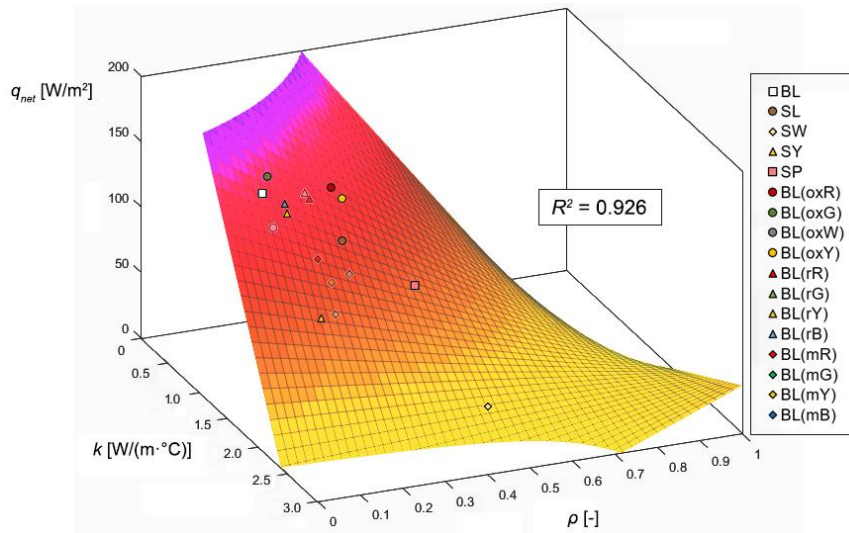


Figure 6.5. Plot of q_{net} vs. k , ρ (mathematical fitting).

$$q_{net} = a \cdot k + b \cdot \rho + c \cdot k \cdot \rho + d \quad (6.1)$$

6.2. Numerical computation

As anticipated, the section aims at proposing a numerical computation with the objective to extend the findings collected during the experimental activity to a wider domain of urban scenarios.

6.2.1. Alternative scenarios

The energetic balance of the road surfaces was alternatively computed introducing different variables regarding the external conditions and the environment. Combining such variables, distinct scenarios were created and treated as self-standing entities.

To this scope, the first independent variable was referred to the solar rate of heat flow parameter; in particular, the transmission coefficient for unit air mass τ_a was alternatively set up equal to 0.81, 0.71 or 0.62, exemplifying the conditions of “sunny day”, “half-cloudy day” or “cloudy day”, respectively. Such expedient could also synthesize a partially

obstructed irradiation, simulated with scenarios owing sky view factors lower than the unity. For what regarding the atmospheric rate of heat flow, the dual action of the air temperature and the vapor within the air was considered. Thus, three values for T_{air} (20, 25 or 30 °C) were introduced and were combined with three values of vapor pressure v , located in a probable range deduced by previous Figure 2.13 (v equal to 30, 35 or 40 mmHg). The air temperature influenced also the convective component of the energetic balance. However, the convective rate of heat flow was also managed considering three distinct wind speeds, typical of three standardized situation: “low wind”, with U equal to 1.39 m/s (5 km/h), “moderate wind”, with U equal to 2.78 m/s (10 km/h) or “significant wind”, with U equal to 4.17 m/s (15 km/h). The last variable of the computation regarded the emitted rate of heat flow and the conductive one since they were both linked to the temperatures reached by the pavement surfaces. As anticipated, the strict evaluation of such an aspect presupposed ad-hoc monitoring which was not possible. For this reason, T_{surf} was calibrated based on the trends of temperature recorded during the outside experimental activity and was discretized through three distinct situations that was linked to the ambient temperature. In this manner, three sets of surface temperatures were obtained (for each mixture) to represent a pavement when monitored during a day with “low”, “intermediate” or “normal” temperature for the summer season. When conductive transfer was calculated, the thermal gradients between the surface and the pavement bottom were not varied, supposing that the intrinsic conductivity of the mixtures governed this transfer, rather than the external conditions.

Combining all the described variables, 24 probable scenarios were constructed. As a summary, the following Tables 6.3–6.5 present the peculiarities of each scenario (scenario description and input parameters utilized for the energetic balance).

Table 6.3. Computation scenarios: description.

Scenario	Description
1	Sunny day with normal temperature for summer season and low wind speed
2	Sunny day with intermediate temperature for summer season and moderate wind speed
3	Sunny day with intermediate temperature for summer season and significant wind speed
4	Sunny day with normal temperature for summer season and low wind speed
5	Sunny day with normal temperature for summer season and moderate wind speed
6	Sunny day with intermediate temperature for summer season and significant wind speed
7	Half-cloudy day with intermediate temperature for summer season and low wind speed
8	Half-cloudy day with low temperature for summer season and moderate wind speed
9	Half-cloudy day with low temperature for summer season and significant wind speed
10	Half-cloudy day with normal temperature for summer season and low wind speed
11	Half-cloudy day with intermediate temperature for summer season and moderate wind speed
12	Half-cloudy day with intermediate temperature for summer season and significant wind speed
13	Half-cloudy day with normal temperature for summer season and low wind speed
14	Half-cloudy day with normal temperature for summer season and moderate wind speed
15	Half-cloudy day with intermediate temperature for summer season and significant wind speed

Scenario	Description
16	Cloudy day with low temperature for summer season and low wind speed
17	Cloudy day with low temperature for summer season and moderate wind speed
18	Cloudy day with low temperature for summer season and significant wind speed
19	Cloudy day with intermediate temperature for summer season and low wind speed
20	Cloudy day with low temperature for summer season and moderate wind speed
21	Cloudy day with low temperature for summer season and significant wind speed
22	Cloudy day with intermediate temperature for summer season and low wind speed
23	Cloudy day with intermediate temperature for summer season and moderate wind speed
24	Cloudy day with intermediate temperature for summer season and significant wind speed

Table 6.4. Computation scenarios: combination of parameters.

Scenario	τ_a [-]			T_{air} [°C]			U [km/h]			T_{surf} [°C]		
	0.81	0.71	0.62	20	25	30	5	10	15	Low	Int.	Norm.
1	✓	✗	✗	✗	✓	✗	✓	✗	✗	✗	✗	✓
2	✓	✗	✗	✗	✓	✗	✗	✓	✗	✗	✓	✗
3	✓	✗	✗	✗	✓	✗	✗	✗	✓	✗	✓	✗
4	✓	✗	✗	✗	✗	✓	✓	✗	✗	✗	✗	✓
5	✓	✗	✗	✗	✗	✓	✗	✓	✗	✗	✗	✓
6	✓	✗	✗	✗	✗	✓	✗	✗	✓	✗	✓	✗
7	✗	✓	✗	✓	✗	✗	✓	✗	✗	✗	✓	✗
8	✗	✓	✗	✓	✗	✗	✗	✓	✗	✓	✗	✗
9	✗	✓	✗	✓	✗	✗	✗	✗	✓	✓	✗	✗
10	✗	✓	✗	✗	✓	✗	✓	✗	✗	✗	✗	✓
11	✗	✓	✗	✗	✓	✗	✗	✓	✗	✗	✓	✗
12	✗	✓	✗	✗	✓	✗	✗	✗	✓	✗	✓	✗
13	✗	✓	✗	✗	✗	✓	✓	✗	✗	✗	✗	✓
14	✗	✓	✗	✗	✗	✓	✗	✓	✗	✗	✗	✓
15	✗	✓	✗	✗	✗	✓	✗	✗	✓	✗	✓	✗
16	✗	✗	✓	✓	✗	✗	✓	✗	✗	✓	✗	✗
17	✗	✗	✓	✓	✗	✗	✗	✓	✗	✓	✗	✗
18	✗	✗	✓	✓	✗	✗	✗	✗	✓	✓	✗	✗
19	✗	✗	✓	✗	✓	✗	✓	✗	✗	✗	✓	✗
20	✗	✗	✓	✗	✓	✗	✗	✓	✗	✓	✗	✗
21	✗	✗	✓	✗	✓	✗	✗	✗	✓	✓	✗	✗
22	✗	✗	✓	✗	✗	✓	✓	✗	✗	✗	✓	✗
23	✗	✗	✓	✗	✗	✓	✗	✓	✗	✗	✓	✗
24	✗	✗	✓	✗	✗	✓	✗	✗	✓	✗	✓	✗

Table 6.5. Scenario's parameters.

Scenario	Parameters
1	$\tau_a = 0.81$; $T_{air} = 25$ °C; $U = 5$ km/h; T_{surf} : normal
2	$\tau_a = 0.81$; $T_{air} = 25$ °C; $U = 10$ km/h; T_{surf} : intermediate
3	$\tau_a = 0.81$; $T_{air} = 25$ °C; $U = 15$ km/h; T_{surf} : intermediate
4	$\tau_a = 0.81$; $T_{air} = 30$ °C; $U = 5$ km/h; T_{surf} : normal
5	$\tau_a = 0.81$; $T_{air} = 30$ °C; $U = 10$ km/h; T_{surf} : normal
6	$\tau_a = 0.81$; $T_{air} = 30$ °C; $U = 15$ km/h; T_{surf} : intermediate
7	$\tau_a = 0.71$; $T_{air} = 20$ °C; $U = 5$ km/h; T_{surf} : intermediate
8	$\tau_a = 0.71$; $T_{air} = 20$ °C; $U = 10$ km/h; T_{surf} : low
9	$\tau_a = 0.71$; $T_{air} = 20$ °C; $U = 15$ km/h; T_{surf} : low
10	$\tau_a = 0.71$; $T_{air} = 25$ °C; $U = 5$ km/h; T_{surf} : normal
11	$\tau_a = 0.71$; $T_{air} = 25$ °C; $U = 10$ km/h; T_{surf} : intermediate
12	$\tau_a = 0.71$; $T_{air} = 25$ °C; $U = 15$ km/h; T_{surf} : intermediate
13	$\tau_a = 0.71$; $T_{air} = 30$ °C; $U = 5$ km/h; T_{surf} : normal
14	$\tau_a = 0.71$; $T_{air} = 30$ °C; $U = 10$ km/h; T_{surf} : normal
15	$\tau_a = 0.71$; $T_{air} = 30$ °C; $U = 15$ km/h; T_{surf} : intermediate
16	$\tau_a = 0.62$; $T_{air} = 20$ °C; $U = 5$ km/h; T_{surf} : low
17	$\tau_a = 0.62$; $T_{air} = 20$ °C; $U = 10$ km/h; T_{surf} : low
18	$\tau_a = 0.62$; $T_{air} = 20$ °C; $U = 15$ km/h; T_{surf} : low
19	$\tau_a = 0.62$; $T_{air} = 25$ °C; $U = 5$ km/h; T_{surf} : intermediate
20	$\tau_a = 0.62$; $T_{air} = 25$ °C; $U = 10$ km/h; T_{surf} : low
21	$\tau_a = 0.62$; $T_{air} = 25$ °C; $U = 15$ km/h; T_{surf} : low
22	$\tau_a = 0.62$; $T_{air} = 30$ °C; $U = 5$ km/h; T_{surf} : intermediate
23	$\tau_a = 0.62$; $T_{air} = 30$ °C; $U = 10$ km/h; T_{surf} : intermediate
24	$\tau_a = 0.62$; $T_{air} = 30$ °C; $U = 15$ km/h; T_{surf} : intermediate

The main results of the proposed computation are following presented; Tables 6.6, 6.7 and 6.8 show for each mixture and scenario the obtained incoming, outgoing and net rates of heat flow, respectively.

First, it is evident that the mixture typology affects the incoming radiations (see Table 6.6); therefore, for any given scenario, q_{in} was always the maximum for the black concrete and, being linked to the albedo, was progressively reduced for the oxide-pigmented solutions, the surface-treated mixes and the resin-based ones. In the latter case (when transparent binder was adopted), the role of the aggregate was crucial in determining the incoming radiation (the lower q_{in} was recorded in the case of SW mix, i.e. in correspondence with the solution with the maximum albedo value).

The outgoing component of the energetic balance furnished quite variable results depending on the scenario and the mixture types. Mainly, no evident trends could be early recognized neither for the solution technique nor for the surface color; in this case, only surface-treated slabs (resin-type) seemed to release slightly lower energy with respect to the reference BL.

The final net rates of heat flow tend to confirm the hierarchic responses of the mixtures according to the findings already evinced by the outside monitoring activity and objectivized with the energetic balance elaborated based on the experimental data. Thus, within almost all the scenarios, the effectiveness of resin-based samples (above all of SW) in reducing the net rate of heat flow was confirmed; this suggested a useful decrease of temperatures for the clear pavement surface and the surrounding environment, thus the subsequent mitigation of the UHI phenomenon under various scenarios typical of the summer season.

As already mentioned, the suitability of the proposed computation could be also extended considering that the management of the incident radiations, as well as the wind blowing on pavement and the humidity presence can synthesize multiple situation properly realized within the urban environment. Here, the ground-level surfaces are surrounded by buildings and structures that partially obstruct the direct solar effect but also concentrate the heat and compromise the energy release. In this sense, further improvements of the research could be aimed at establishing the relation between the adopted parameters and the presence of obstacles (the SVF affects the outgoing radiations, free to propagate in the pavement proximity or eventually intercepted by obstacles). In this perspective, the evaluation of real-scale trial sections and in-situ monitoring of the thermal responses of different road pavements should be strongly useful.

Table 6.6. Computation results: incoming rate of heat flow for each mix and scenario.

Scenario	q_{in} [W/m ²]															
	BL	SL	SW	SY	SP	BL(oxR)	BL(oxG)	BL(oxW)	BL(oxY)	BL(rR)	BL(rG)	BL(rY)	BL(mR)	BL(mG)	BL(mY)	BL(mB)
1	1354	1168	913	1229	1284	1304	1331	1322	1290	1209	1140	1110	1232	1148	1191	975
2	1354	1168	913	1229	1284	1304	1331	1322	1290	1209	1140	1110	1232	1148	1191	975
3	1354	1168	913	1229	1284	1304	1331	1322	1290	1209	1140	1110	1232	1148	1191	975
4	1378	1192	937	1253	1308	1328	1355	1346	1314	1233	1164	1134	1256	1172	1215	999
5	1378	1192	937	1253	1308	1328	1355	1346	1314	1233	1164	1134	1256	1172	1215	999
9	1378	1192	937	1253	1308	1328	1355	1346	1314	1233	1164	1134	1256	1172	1215	999
7	1206	1044	820	1097	1145	1163	1186	1178	1151	1079	1019	992	1099	1026	1064	875
8	1206	1044	820	1097	1145	1163	1186	1178	1151	1079	1019	992	1099	1026	1064	875
6	1206	1044	820	1097	1145	1163	1186	1178	1151	1079	1019	992	1099	1026	1064	875
10	1229	1067	843	1120	1168	1186	1209	1201	1174	1102	1042	1015	1122	1049	1087	898
11	1229	1067	843	1120	1168	1186	1209	1201	1174	1102	1042	1015	1122	1049	1087	898
12	1229	1067	843	1120	1168	1186	1209	1201	1174	1102	1042	1015	1122	1049	1087	898
13	1253	1091	867	1144	1192	1210	1233	1225	1198	1126	1066	1039	1146	1073	1111	922
14	1253	1091	867	1144	1192	1210	1233	1225	1198	1126	1066	1039	1146	1073	1111	922
15	1253	1091	867	1144	1192	1210	1233	1225	1198	1126	1066	1039	1146	1073	1111	922
16	1094	952	757	999	1041	1056	1077	1070	1046	983	931	907	1001	937	970	805
17	1094	952	757	999	1041	1056	1077	1070	1046	983	931	907	1001	937	970	805
18	1094	952	757	999	1041	1056	1077	1070	1046	983	931	907	1001	937	970	805
19	1117	975	780	1022	1063	1079	1100	1093	1069	1006	954	930	1024	960	993	828
20	1117	975	780	1022	1063	1079	1100	1093	1069	1006	954	930	1024	960	993	828
21	1117	975	780	1022	1063	1079	1100	1093	1069	1006	954	930	1024	960	993	828
22	1140	999	803	1045	1087	1102	1123	1116	1092	1030	977	954	1047	983	1016	851
23	1140	999	803	1045	1087	1102	1123	1116	1092	1030	977	954	1047	983	1016	851
24	1140	999	803	1045	1087	1102	1123	1116	1092	1030	977	954	1047	983	1016	851

Table 6.7. Computation results: outgoing rate of heat flow for each mix and scenario.

Scenario	$q_{out} [W/m^2]$																
	BL	SL	SW	SY	SP	BL(oxR)	BL(oxG)	BL(oxW)	BL(oxY)	BL(rR)	BL(rG)	BL(rY)	BL(rB)	BL(mR)	BL(mG)	BL(mY)	BL(mB)
1	982	871	747	964	1003	956	961	986	954	877	823	807	880	927	879	919	741
2	1032	873	721	982	1032	979	992	1021	972	893	820	795	889	951	879	929	724
3	1148	943	765	1068	1128	1071	1090	1123	1059	977	886	853	966	1042	949	1007	775
4	935	825	702	917	956	909	914	939	907	831	778	761	834	881	832	873	696
5	1071	908	754	1018	1069	1017	1030	1059	1010	930	855	830	925	988	914	965	757
6	1061	858	681	981	1041	985	1003	1036	973	890	801	768	880	955	863	921	691
7	944	836	715	928	966	918	924	949	916	841	789	773	845	890	844	884	708
8	995	839	690	947	996	943	956	984	936	858	787	762	855	915	846	895	691
9	1111	910	734	1033	1092	1034	1054	1086	1023	941	853	820	932	1006	915	972	743
10	982	871	747	964	1003	956	961	986	954	877	823	807	880	927	879	919	741
11	1032	873	721	982	1032	979	992	1021	972	893	820	795	889	951	879	929	724
12	1148	943	765	1068	1128	1071	1090	1123	1059	977	886	853	966	1042	949	1007	775
13	935	825	702	917	956	909	914	939	907	831	778	761	834	881	832	873	696
14	1071	908	754	1018	1069	1017	1030	1059	1010	930	855	830	925	988	914	965	757
15	1061	858	681	981	1041	985	1003	1036	973	890	801	768	880	955	863	921	691
16	860	757	639	847	884	835	842	866	835	760	711	695	765	808	765	804	631
17	995	839	690	947	996	943	956	984	936	858	787	762	855	915	846	895	691
18	1111	910	734	1033	1092	1034	1054	1086	1023	941	853	820	932	1006	915	972	743
19	897	790	670	881	919	871	877	902	870	794	743	727	799	843	798	837	663
20	926	772	625	880	928	875	888	916	869	790	721	696	788	847	779	827	626
21	1023	824	650	947	1006	948	967	999	937	855	768	735	846	919	830	886	659
22	850	745	627	835	873	825	831	855	824	749	698	683	753	797	753	792	619
23	963	806	656	914	964	911	924	953	904	825	754	729	822	883	812	861	658
24	1061	858	681	981	1041	985	1003	1036	973	890	801	768	880	955	863	921	691

Table 6.8. Computation results: net rate of heat flow for each mix and scenario.

Scenario	$q_{\text{net}} \text{ [W/m}^2\text{]}$												
	BL	SL	SW	SY	SP	BL(oxR)	BL(oxG)	BL(oxW)	BL(oxY)	BL(oxR)	BL(oxG)	BL(oxY)	BL(oxR)
1	371	298	166	266	281	348	370	336	337	332	317	303	322
2	321	296	192	248	252	325	339	301	318	316	320	315	313
3	205	225	148	162	155	233	241	199	231	232	254	257	236
4	443	368	235	336	352	419	441	407	407	402	387	372	392
5	306	284	183	235	238	311	325	287	305	303	309	304	301
6	317	335	256	272	266	343	352	310	341	343	363	366	346
7	262	208	105	169	179	245	262	230	234	239	230	220	229
8	211	205	130	150	149	220	230	194	214	222	232	230	218
9	96	134	86	65	53	128	132	92	128	138	166	173	142
10	247	196	96	157	165	230	248	215	220	225	219	208	216
11	197	194	122	138	136	206	217	180	202	210	222	220	207
12	81	123	78	53	39	114	119	78	114	126	156	162	130
13	318	266	165	227	236	301	319	286	291	296	288	278	286
14	182	183	113	126	123	192	204	166	188	197	211	210	196
15	192	233	186	163	150	225	230	189	225	236	265	271	240
16	234	195	118	152	157	221	235	204	211	224	220	213	213
17	99	113	67	52	44	113	121	85	109	126	143	145	123
18	-16	43	23	-34	-52	22	23	-16	23	42	78	88	47
19	221	185	110	141	144	208	223	191	199	212	210	203	202
20	191	203	155	142	135	204	212	177	200	216	233	235	213
21	94	151	130	75	58	131	132	94	132	151	186	196	155
22	291	254	177	210	214	277	292	261	268	281	279	271	271
23	177	193	147	131	123	191	199	163	188	205	223	225	203
24	80	141	123	64	45	118	120	80	119	139	176	186	144

6.2.2. Mitigation efficacy

In order to evaluate the mitigation efficacy that could be obtained using the studied pavements, further aspects regarding the energetic balance obtained from the experimental data and the computation activity are following discussed.

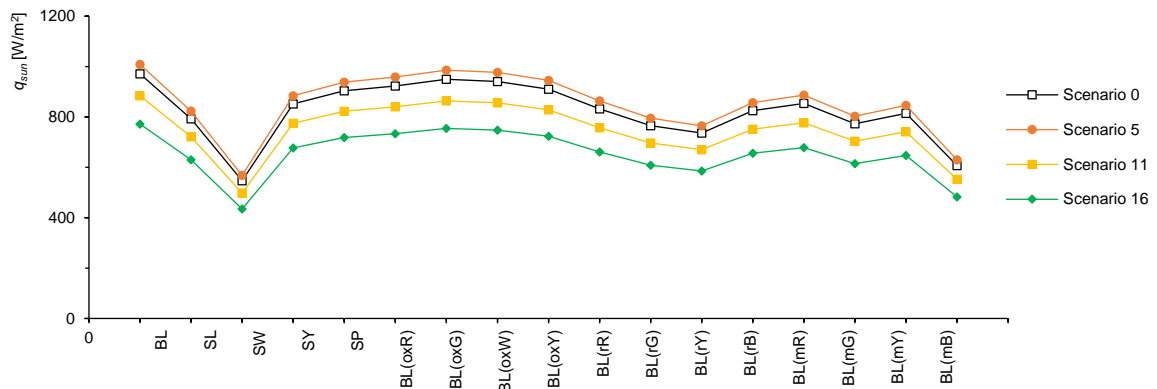
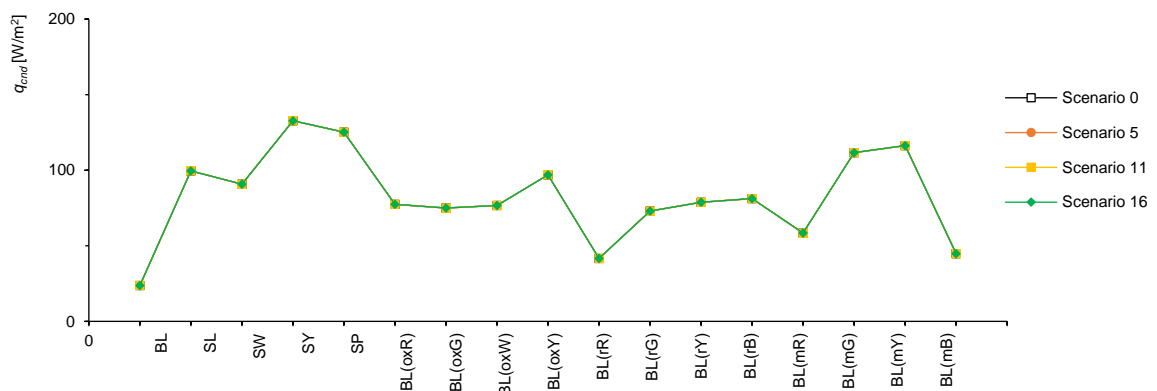
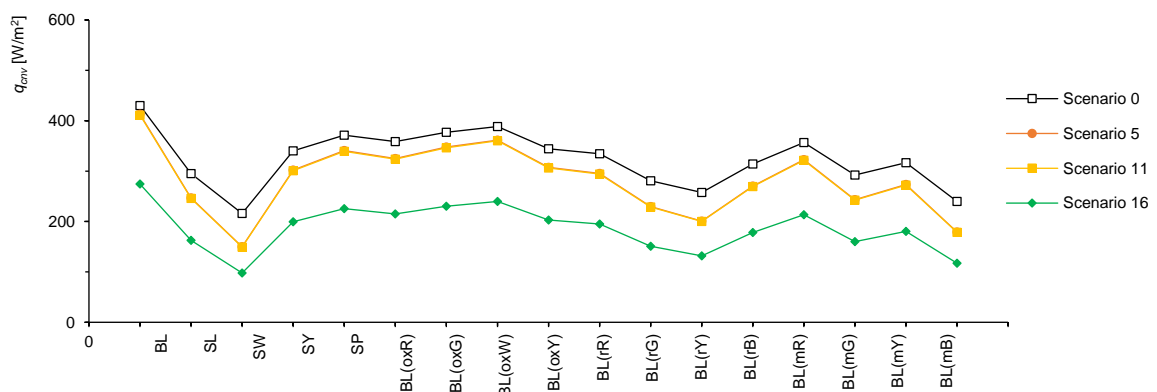
Initially, the reliability of the numerical elaboration was analyzed, since some input scenarios produced incomprehensible/improper results in terms of final rates of heat flow. Generally, this was realized in all that cases characterized by greater q_{net} for the clearer solutions with respect to the reference black BL (this was considered improbable for the explained theory and the results verified though monitoring). Analyzing Table 6.8, a deeper view suggested that the scenarios which tent to produce such concerns were characterized by common input variables: mainly, at least scenarios 9, 12, 15, 18, 21 and 24 resulted in unfitting rates' values since they were set up with a significant wind speed value (15 km/h). In analogy, scenarios from 18 to 24 started to present improbable q_{net} results, which were obtained when the transmission coefficient for unit air mass τ_a was set equal to 0.62, i.e. in the case of cloudy-sky hypothesis. All these considerations seem to suggest that the theory underneath the rate balance could be considered reliable only under specific environmental conditions that, in this case, are commonly an example of a good-wheatear summer day (sky substantially clear or only partially cloudy, low or only moderate wind speed and standard air humidity for the season).

Really, it is also expected that, without such summerly external conditions, the effectiveness of the clear or color solutions in preventing the UHI concerns could be attenuated because of the predominance of the external conditions in the process. In this regard, it is worth noting also that the proposed analysis should be strongly influenced by the location that affects the solar radiation characteristics. Otherwise, regardless such a hypothesis, no additional consideration can be drawn based on the proposed theory and the available data in the research project.

Dealing with the probable results, three selected scenarios was joined to the real one (the experimental environment) in order to numerically evaluate the efficacy of the different mixtures in mitigating the UHI phenomenon. The elaboration was done also with the purpose to identify the crucial role of the above-mentioned external variables that govern the whole complex heat transfer processes. The following Table 6.9 recalls the parameters recorded in the real experimental environment (hereafter named Scenario 0) and those for some scenarios that was chosen as representative cases (which furnished probable results), i.e. the Scenarios 5, 11 and 16. Figures 6.6–6.10 summarize the obtained rates of heat flow in such instances. In particular, q_{sun} , q_{cnd} , q_{cnv} , q_{em} and q_{net} are plotted, whereas q_{atm} is omitted since it is constant for each mixture (395 W/m² for Scenario 0, 369 W/m² for Scenario 5, 345 W/m² for Scenario 11 and 322 W/m² for Scenario 16).

Table 6.9. Parameters of the selected scenarios.

Scenario	Parameters
0 (real)	$\tau_a = 0.78$; $T_{\text{air}} = 35 \text{ }^\circ\text{C}$; $U = 6.59 \text{ km/h}$; T_{surf} : measured
5	$\tau_a = 0.81$; $T_{\text{air}} = 30 \text{ }^\circ\text{C}$; $U = 10 \text{ km/h}$; T_{surf} : normal
11	$\tau_a = 0.71$; $T_{\text{air}} = 25 \text{ }^\circ\text{C}$; $U = 10 \text{ km/h}$; T_{surf} : intermediate
16	$\tau_a = 0.62$; $T_{\text{air}} = 20 \text{ }^\circ\text{C}$; $U = 5 \text{ km/h}$; T_{surf} : low

**Figure 6.6.** Plot of q_{sun} for each mixture and selected scenario.**Figure 6.7.** Plot of q_{cnd} for each mixture and selected scenario.**Figure 6.8.** Plot of q_{env} for each mixture and selected scenario.

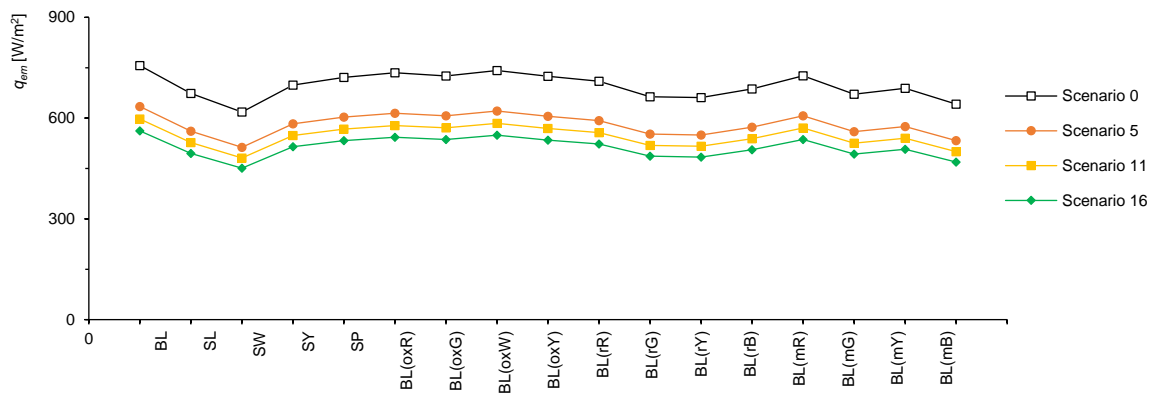


Figure 6.9. Plot of q_{em} for each mixture and selected scenario.

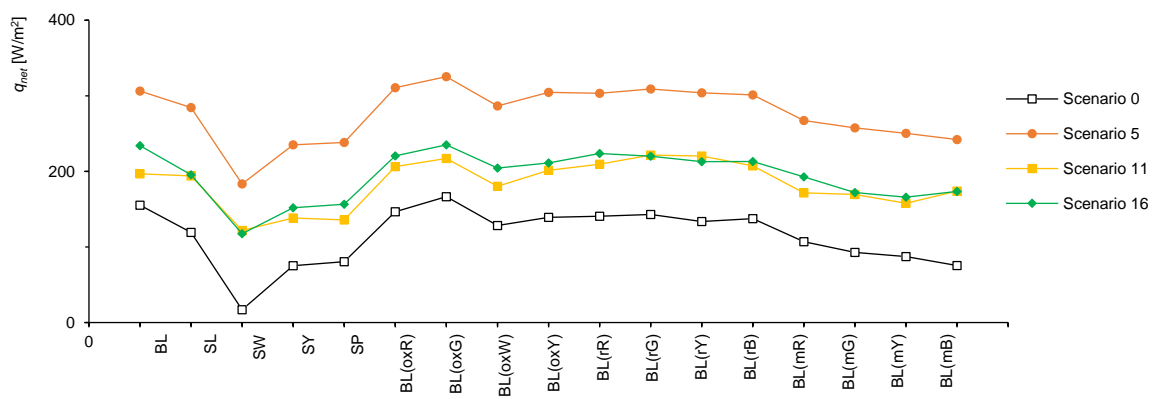


Figure 6.10. Plot of q_{net} for each mixture and selected scenario.

Based on the proposed plots, the efficacy of the resin-based mixtures (above all that of the SW one) is again clear (regardless the selected scenario). Promising results were obtained coupling the transparent binders also with yellow or pink aggregates, as well as in the case of surface-treated concretes painted with mortars (BL(mB) was the most promising one).

However, for each selected scenario, the mitigation efficacy was also numerically evaluated as percentage of reduction in the final q_{net} with respect to that of the reference BL. Such results are presented in the following Table 6.10. As observed, the experimental scenario (Scenario 0) produced the highest reductions in q_{net} with respect to BL (thus, the greater reduction of the surface temperatures can be hypothesized); then, such benefits were attenuated progressively increasing the cloudiness and the wind speed or reducing the air temperature.

Table 6.10. Mitigation efficacy: q_{net} reduction with respect to reference BL.

Mixture	q_{net} reduction (reference BL)			
	Scenario 0	Scenario 5	Scenario 11	Scenario 16
SL	-23%	-7%	-1%	-17%
SW	-89%	-40%	-38%	-50%
SY	-52%	-23%	-30%	-35%
SP	-48%	-22%	-31%	-33%
BL(oxR)	-6%	1%	5%	-6%
BL(oxG)	7%	6%	10%	0%
BL(oxW)	-17%	-6%	-8%	-13%
BL(oxY)	-10%	-1%	2%	-10%
BL(rR)	-9%	-1%	6%	-4%
BL(rG)	-8%	1%	13%	-6%
BL(rY)	-14%	-1%	12%	-9%
BL(rB)	-11%	-2%	5%	-9%
BL(mR)	-31%	-13%	-13%	-18%
BL(mG)	-40%	-16%	-14%	-27%
BL(mY)	-44%	-18%	-20%	-29%
BL(mB)	-51%	-21%	-12%	-26%

In general, this finding could be read as a key outcome: in fact, since the effectiveness of the clearer solutions in mitigating the UHI phenomena seemed to be even boosted in presence of intense heat, their utilization can be strongly suggested within the most warm urban areas where, due to location and climate, city conformation, activities, etc., the UHI phenomena are the most severe. Based on the experimental data, it must be also remembered that such solutions demonstrated also the ability to maintain their efficacy during the cooling in the late afternoon; e.g. the analyzed cooling rates demonstrated that clear/colored mixtures not only reached lower maximum temperatures but were also able to attenuate the heat release (see paragraph 5.3.4.2).

Trying to define the effective role of the test environment, the final data processing was finalized to identify possible relationships between the radiative properties of the materials and the resulting thermal responses under the different scenarios, based on the elaboration already proposed in paragraph 6.1.2. Therefore, the Equation 6.1 was again utilized to fit the computed data and determine the a , b , c and d coefficients. Results reported in Table 6.11 seem to capably show good-reliable fits obtained with the above-proposed law (coefficients of determination R^2 always greater than 0.8). The representation of such coefficients (see Figure 6.11) gave also interesting information about the scenarios. In general, a coefficients (Figure 6.11.a) resulted almost constant regardless the test environment. Conversely, b were deeply affected by the wind velocity (Figure 6.11.b demonstrated consistent b trends, with R^2 always greater than 0.88, if obtained data are grouped at the same wind speed level). Remembering the formulation presented in Equation

6.1, such concerns seem to demonstrate that the conductivity k (linked to a coefficient) influences the final thermal responses of mixtures independently on the environmental settings, whereas the albedo role was significantly conditioned by the external states. Similarly to b , c coefficients furnished quasi-constant values if represented grouping the scenarios with the same wind velocity (see Figure 6.11.c); this could be expected since c regards the $k \cdot \rho$ multiple terms of the proposed equation. Also concerning d , the wind speed seems to discriminate the fitting parameters (deleting some outliers, acceptable coefficients of determination for each wind level are obtained – see Figure 6.11.d).

Really, the produced relationships could be effectively utilized to predict the thermal responses of the mixtures (expressed in term of net rate of heat flow) starting from the radiative properties of each materials (in particular the thermal conductivity k and the albedo ρ) and implementing some conditions referred to the environment. In particular, the curves proposed in Figure 6.11 can be used to determine the law coefficients knowing the wind speed (line selection) and other external conditions such as the cloudiness, the air and surface temperatures and the vapor pressure (position within the same “equal-wind” line).

Table 6.11. Fitting parameters of Equation 6.1 (radiative properties vs. thermal responses).

Scenario	Fitting coefficient				R ²
	a	b	c	d	
1	-148.0	-407.3	178.2	352.7	0.924
2	-150.3	-607.1	198.4	584.6	0.963
3	-150.5	-373.1	169.6	525.6	0.914
4	-150.2	-150.5	142.6	400.0	0.816
5	-150.1	-614.6	198.6	656.4	0.964
6	-149.8	-352.6	166.8	508.5	0.907
7	-149.9	-158.9	142.4	511.7	0.821
8	-151.0	-487.0	201.0	462.7	0.926
9	-151.1	-253.8	172.3	402.6	0.875
10	-150.8	-32.2	145.4	277.5	0.819
11	-150.3	-467.7	198.4	445.1	0.937
12	-150.5	-233.7	169.6	386.2	0.868
13	-150.2	-11.1	142.6	260.6	0.819
14	-150.1	-475.2	198.6	517.0	0.938
15	-149.8	-213.2	166.8	369.1	0.861
16	-149.9	-19.5	142.4	372.3	0.819
17	-151.4	-387.8	203.8	423.6	0.909
18	-151.1	-128.3	172.3	277.1	0.855
19	-150.8	93.3	145.4	152.1	0.862
20	-150.8	-369.0	201.2	407.9	0.904
21	-150.7	-136.7	172.1	368.9	0.856
22	-150.5	84.4	145.2	262.5	0.861
23	-150.4	-377.4	201.0	478.4	0.907
24	-150.1	-116.7	169.4	353.2	0.855

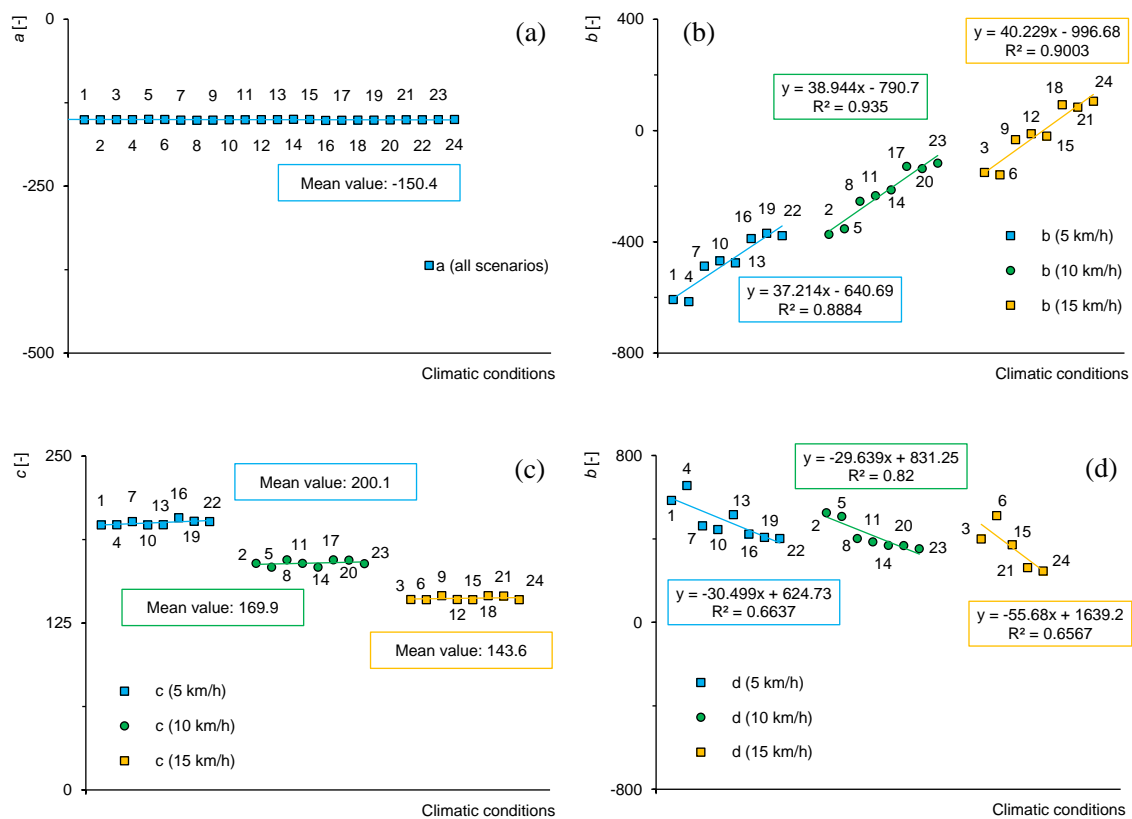


Figure 6.11. Representation of a (a), b (b), c (c) and d (d) coefficients for the different scenarios.

6.3. Multi-scale performance of materials

The present section aims at summarizing the main mechanical performance evinced studying the materials at different analysis scales (i.e. of the binders, their corresponding mastics, the loose blends and the mixtures) trying to discuss about their suitability in manufacturing wearing courses for road pavements.

Basing on the results obtained at binder-scale, the following consideration can be fixed.

Bitumen **B**, representing a conventional unmodified binder with a 50/70 penetration grade, consisted in a standard bitumen for paving and assumed the traditional black color. Their mechanical properties (considered as reference for comparison purposes) indicated a common Newtonian behavior, with viscosity compatible with mixing and compaction operations at the commonly-employed operational temperatures (160–155 °C and 150–155 °C respectively). B showed a thermo-rheologically simple behavior (relaxation mechanisms and stress magnitudes at all time owning the same temperature dependencies). It exhibited a prevalent viscous behavior above the temperature of about 16–22 °C (in the range of frequency between 0.01 and 100 rad/s). Stiffness and elasticity incremented lowering the

temperature and increasing the test frequency. Fatigue resistance resulted comparable to that of similar paving bitumens, with critical strain, corresponding to failure at 10^6 cycles, equal about to 0.196%. Rutting potential substantially manifested at temperatures greater than 56 °C (absence of elastic recovery and development of permanent deformations).

Binder **S** consisted in a synthetic resin with binding properties similar to those of a traditional bitumen; it was characterized by a yellowish color able to exalt the color of the aggregate composing the mixtures (S was considered a transparent binder for clear pavement concretes). Its original color was only partially influenced by the aging, since only small chromatic variations due to oxidizing were identified after the paving operations (mixing and compaction). Given its transparent nature, S color was deeply influenced by that of fillers when mixed with them to obtain mastics. Resin behavior exemplified that of a Newtonian fluid. Its dynamic viscosity was appreciable greater than those the reference bitumen; this fact determined a slight increase of the temperatures required for the mixing and compaction procedures. From the mechanical point of view, S was softer than B; thus, some attentions in the design of S-based mixtures were suggested in order to ensure adequate structural strength. Moreover, S performance strongly depended on the temperature: at lower and higher T (between 4÷16 and 58÷76 °C, respectively), it tent to become more elastic increasing the frequency, whereas at intermediate ones (16÷58 °C) a transition towards the opposite tendency was detected (trend similar to that of B). Overall, a prevalent viscous behavior was found. The lower stiffness guaranteed better fatigue resistance with respect to reference B (with strain corresponding to failure at 10^6 cycles equal to 0.340%), but was partially responsible also of greater rutting potential at the higher temperatures.

B-OX-R and **B-OX-G** were binders made with the bitumen B and some oxide-pigments able to color the blends (and then, the final mixtures). Such pigments were mixed with B with a 1:1 weight ratio basing on the suggested dosage for the mixtures. In particular, B-OX-R oxide was based on iron compounds and conferred a reddish color to the binders; B-OX-G one was composed by chromium and produced a greenish bitumen. Globally, these products tent to exhibit very similar behaviors regardless the selected color. Therefore, such technology led to high-viscosity materials (η greater up to one order of magnitude with respect to B or S), even able to compromise the realization of some viscosity tests because of equipment limits. Otherwise, this was not considered an obstacle for mixing and compaction procedures of concretes since the pigment blending occurred at mixture-scale (furtherly, mixture prepared with B-OX-R or B-OX-G were manufactured without particular issues in such phases). Then, the B-OX bitumens demonstrated typical non-Newtonian pseudo-plastic behaviors, with viscosities decreasing under the shear strain (in fact, efficacy of the oxide's dispersion during blending with bitumen depended on the stirring intensity applied to the compounds). Mechanical analysis indicated sensibly higher

stiffness, as well as smaller temperature and frequency dependencies with respect to B and S. In general, an elastic character strongly prevailed up to 70 °C (phase angle always lower than 45°). All these findings expressed promising structural strength at binder-scale, but also suggested to hypothesize eventual lack of resistance at the low-range temperature (at low in-service T , excessive hardness is considered dangerous for the binder integrity against the thermal cracking). However, such stiffness resulted crucial to fully recover the permanent deformations at the highest temperatures (strain accumulated by B-OX samples was practically null up to 70 °C). Given the chromaticity of the solutions (which will influence the final color of the mixtures), additional evaluations (also regarding the rheological and mechanical performance) should consider the temperature effectively reached by the in-field pavements.

In the case of **mastics**, when B was added with fillers, greater stiffness was found, thus the rutting potential was mitigated; the use of steel slags (as an example of hard, rough and angular aggregate) provided greater hardness to mastics with respect to traditional filler (limestone), determining also improvements in permanent deformation resistance.

Satisfactory rutting resistances were found in the case of S-based mastics; as in the case of B, the harder steel slag provided lower strain accumulations. Thus, in order to face the possible problems related to the high-temperature integrity of pavements manufactured with the resin, the use of hard, high-quality aggregate could be supposed; however, it has to be remembered that particular colorations of aggregate (as example the dark-grey/black of steel slag) could partially compromise the original functioning of S (the obtaining of clear pavements). This must be also considered thinking that the benefits connected to the use of clearer materials are not related only to thermal and heat concerns, but can also affect the thermal loads suffered by the visco-elastic and thermal-dependent materials which constituted the pavements (it was demonstrated that the clearer solutions reached lower temperatures when expose to solar radiations).

Analyzing the **loose blends**, all the selected binders exhibited satisfactory stripping resistance when combined with aggregates of various nature (residual coverage after AST always greater than 87%). This fact was considered an early indicator of a low water sensitivity of the analyzed bitumen-aggregate systems (substantially, adhesion problems were prevented). In particular, S resin tent to produce the higher residual binder coverages after boiling (even greater than those recorded for the reference bitumen-limestone loose blend). The modification of the black bitumen with the oxide pigments produced more evident stripping, otherwise it did not threaten the functioning of the bitumen-aggregate blend.

Dealing with mixture-scale, the mechanical assessment furnished indications consistent with those evinced at binders and mastic-scale.

Reference mixture BL produced with conventional (unmodified) bitumen and limestone aggregate was analyzed as comparison purposes. Substantially, its behavior was perfectly in line with similar conventional asphalt concretes for wearing courses owing analog granulometric distributions and binder type/content. Mainly, all the obtained results seemed to comply with the common technical specifications for this kind of road mixture.

Resin-based mixtures were obtained using the synthetic transparent resin S and using different aggregates. In general, they exhibited lower strengths with respect to the reference BL (even one third): this agreed with findings evinced at binder-scale (tensile strengths were not influenced by the aggregate typology, thus the main actor seemed to be really the binder). S-based mixtures presented also lower stiffness with respect to BL. The worst stiffness results were recorded when S was mixed with a white marble (probably because of the poorer characteristics of such aggregate). Limestone, yellow-Siena marble and coral-pink stone aggregates gave slightly higher stiffness to the mixes with respect to the marble-based one (otherwise stiffness was still lower with respect to reference BL). The previously-identified higher deformability of the synthetic binder seemed also to produced greater frequency dependency at mixture scale (at least at the intermediate in-service temperatures). Concerning the fatigue resistance, the lower stiffness was beneficial and seemed to delay the cracking risk (the softer SW – synthetic resin with white marble – had the higher fatigue resistance). Surprisingly, for what regarding the rutting potential (crucial at high in-service temperatures), S-based mixes were characterized by comparable or even better resistances with respect to the reference BL. Moreover, also lower creep rate values indicated a general ability to resist against the permanent deformations. Among all the S-based solutions, synthetic resin with white marble gave slightly worse performance probably because of the combined effect of the soft binder and characteristics of the lithic skeleton. Water sensitivity tests at mixture-scale confirmed the indications collected treating blends; moisture resistance of all S-based mixes was even higher than those of BL, certifying the good affinity of S with the four selected aggregates (limestone, white marble, yellow-Siena marble and coral-pink stone).

The **oxide-pigmented mixes** were produced coloring the black bitumen (used also for the reference BL mix) with specific oxides diffused during the mixing phases; considering the peculiarities of such technology, these mixtures were classified as “fully-colored” since the pigments were dispersed inside all their matrix. Basing on the mechanical responses, oxide pigments seemed to be responsible of better tensile strength (ITS almost twice with respect to reference BL) and high stiffness, both in the case of ITSM and 4PB tests (the responsibility of oxides was certified since the aggregate used was always limestone, i.e.

the same one of the reference mix). Moreover, this totally agreed with findings obtained at the binder-scale (where aggregates were not included). In general, non-significant differences were recorded depending on the pigment's color. Then, the above-mentioned stiffness only partially threatened the resistance to fatigue cracking at intermediate temperatures because coupled also to a great elastic aptitude of such mixes. Therefore, colored mixes owned comparable fatigue resistances with respect to that of BL. For what concerning the rutting resistance, the recorded stiffness seemed able to limit the permanent deformations (definitely lower cumulative axial strains/creep rates and higher creep moduli were found with repeated load axial tests carried out at high in-service temperatures). Also in the case of oxide-pigmented mixes, more than acceptable water sensitivities were found (in this sense, pigments seem to did not affects the bitumen-limestone affinity).

The surface-treated mixtures were realized using alternatively some resins or mortars in form of paints. As expected, the application of paintings partially reduced the mean texture depths and the horizontal permeability of the surfaces, whereas it did not affect the skid resistance (PTV of varnished slabs very similar to that of the reference BL. Mainly, mortar paints seemed to furnish quite smoother surfaces with respect to resins. In the case of the permeability and the skid performance, no particular patterns were recognized basing on the surface treatment nature of color. The durability (assessed only in the laboratory) seemed to be slightly higher for the mortar paints. Finally, neither mortars nor resins demonstrated to be fuel-resistant.

6.4. Discussion

Final discussion was finalized to hypothesize the possible suitability of the studied solutions basing on the information collected through the chromatic and thermal analysis and considering the mechanical responses achieved within the laboratory.

Overall, the use of the transparent synthetic resin could be suggested to produce clear road pavements effectively useful to strong mitigate the temperatures in the road surface proximity. Given the chromatic results, its combination with particularly valuable aggregates can be promoted to produce clearer wearing courses and to boost the recorded thermal benefits. In synthesis, considering also the mechanical properties evinced for the resin-based mixtures, their laying could be moreover promoted for low-trafficked roads as well as for traffic-free/pedestrian zones or cycle tracks (some doubts could reasonably raise in view of quite poor strength and stiffness). Really, the latter applications (pedestrian zones/cycle tracks) should guarantee the maximization of the achievable thermal benefits in view of the involved users (pedestrians and cyclist are considered the more vulnerable categories for what regarding the heat concerns and the UHI impacts). Further, the limitation of heavy and intense traffics should partially prevent that durability concerns which can be

probably expected in the case of clear/valuable pavements. Similar considerations could even regard some economical/monetary aspects; vehicular traffic limitation can contribute to preserve the greater investments which could be supposed using this kind of road surfaces (moreover employing high valuable aggregate in combination with the clear binder) and could attenuate the wide-diffused scepticism commonly demonstrated by local road contractors. From the technical point of view, such strategy can also avoid possible issues related to the compatibility of the resin-based mixtures with the traditional existing courses – in the case of milling and road maintenance/rehabilitation or with the deeper bituminous layers in the case of new constructions (adequate interlayer connections at the interfaces should be designed, moreover putting in contacts synthetic-based materials with bituminous mixes).

Asphalt mixtures colored with oxide pigments can be adopted for UHI mitigation purposes even if with only partial efficacy; probably, with the objective to exalt the heat mitigation, smarter applications of such technology could be adopted thinking to apply it in combination with other mitigation strategies, as well as with an integrated urban management able to optimize the urban textures and the spaces and avoid the heat concentration. However, given their chromatic properties, they could be surely applied with landscape preservation targets. Oppositely to the synthetic-based solutions, such mixtures exhibited high mechanical performance making them suitable for heavy-trafficked networks, as well as for punctual applications with particular safety purposes (intersections, high-sloped junctions, low-visible sections, etc.). In this sense, adequate surface characteristics (in terms of texture and skid resistance) and low water sensitivity are equally important to comply with satisfactory safety standards. Moreover, their bituminous nature could promote the design of capable interlayer connections to limit possible slippage problems due to poor interfaces (when installing the solution to bituminous supports). However, the evinced concerns about the possible brittleness and subsequent fatigue cracking phenomena, as well as the high stiffness eventually expected at the low in-service temperatures cannot be neglected. For these reasons, their use could be restricted in the case of rigid winter climates or high-temperature-swing environments.

Also surface-varnished bituminous mixtures can be utilized as UHI mitigation strategies, even if their thermal efficiency is strictly related to the adopted color and paint types (significant mitigation effects were obtained in the case of clearer surface with varnished mortars). Otherwise, some doubts related to the solution's durability can be awaited: regardless the promising durability results obtained in the laboratory, dirtying and darkening effects due to atmospheric agents and traffic (in driveway installations) are likely plausible. In this perspective, it is worth noting that the most effective solutions (the clearer paints) should be also more prone to suffer such deteriorations.

In general, all the studied alternatives can be thought rather suitable also because they can be achieved assuming low-significant precautions for what regarding the production and construction requirements, at least with respect to the standard paving procedures used in the case of conventional materials and structures. More specifically, possible concerns related to the production plants and the paving equipment, as well as to the paving temperatures, the accessory materials and the construction phases, must be taken into account while globally analyzing the involved paving process.

In detail, the use of synthetic resin as bitumen substitution should imply only the correct management of the production plants since a worse chromatic yield could be eventually supposed if producing the final mixtures through non-treated, dirt plant lines. The fact can be considered also for the utilization of clear/valuable aggregate that, if dirty, can partially lose their chromatic efficiency. From the construction point of view, particular cares should be followed, especially for the same concept related to the initial status and the degree of cleanliness of the paving machineries. In terms of mixing and compaction temperatures, just small variations have been suggested by experimental findings. Construction phases can be considered the same utilized for bituminous layers, even adopting bituminous tack coats (in form of emulsion) between the clear wearing course and the existing black surfaces. In this perspective, negligible interlayer problems have been faced studying in-service resin-based pavements, even the possible lower chemical affinity between synthetic and bitumen-based courses [6.1]. Such a compatibility is assumed also positive if taking into account the hypothetical recycling of reclaimed asphalt pavements within new-constructed clear wearing courses. Obviously, this environmental-friendly technique can improve the sustainability of the pavements [6.2, 6.3] but could also lead to a darker final aspect of the surface that can partly compromise the pavement thermal effectiveness.

In the case of oxide-pigmented mixtures, no particular requests in terms of mixing and compaction temperatures seemed to be needed. Despite the different viscosity and the presumed modifications in the flow behaviors observed at binder-scale (with respect to the bitumen), no criticalities were faced during mixture-scale production (at the same temperature, a different viscosity can influence compaction, thus the final volumetric properties of mixes [6.4]). Therefore, experimental tests certified the easiness of using the oxide pellets to color the mixtures, which can be simply added to the mix-design during the blending phases. Clearly, no affinity problems with the existing pavement structures must be supposed since, practically, oxide-pigmented mixes maintained their original bituminous nature.

As evident, the application of surface-treatments (resins and mortars), imply a supplementary construction phase with respect to conventional paving but can be realized with simple and wide diffused spraying practices. This, employing usual spraying

equipment generally utilized in the field. From the technical point of view, requirements must be checked at surface scale (wearing courses must ensure adequate standard for permeability, skid and roughness in order to comply safety and functionality reference specifications). Except for the surface, it is thought that the proposed technique does not affect the mechanical and structural properties of the pavements.

In conclusion, it could be said that the use of such innovative technologies for the production of thermal-optimized road wearing courses should be part of an innovative paving approach which must consider the pavements as working mechanisms inserted in the overall urban system, as long as entities that need suitable managing practices (adequate installation, periodical cleaning, ordinary maintenance, ad-hoc rehabilitation, etc.). This would be the way to achieve that environmental sustainability needed when treating the UHI problems, notwithstanding the probable higher monetary costs and investments involved in the process that, in general, are the main reasons of the contractor's distrust.

Chapter 7

Further Aspects

The present Chapter proposes some discussion points about the use of thermal-optimized pavements not only directly connected to the already-reported thermal aspects. First, some arguments related to the infrastructure-landscape integration, the road safety and the night and tunnel lighting are analyzed. Then, some points regarding the human concerns are introduced talking about the thermal and visual comforts. Finally, some guidelines for the production of thermal-optimized roads are proposed.

7.1. Thermal-optimized roads: related aspects

7.1.1. Infrastructure-landscape integration

Since road construction represents a core sector and pavements are widely diffused (they cover large areas in the territorial texture), a growing attention is actually paid to the implementation of new materials for road surfaces able to promote the landscape preservation and the infrastructure-landscape integration [6.1, 7.1]. In this sense, it is widely recognized that clear or colored surfaces are preferred with respect to conventional dark-colored solutions for aesthetic purposes, as well as to promote the quality of the environment it-self [7.2].

A widespread use of clear and colored pavements has been recently encouraged also in different urban spaces. Unlike traditional “black” pavements, the design of appropriate colored and visible pavements has been a key factor for the road wearing courses also in

monumental valuable contexts, where the aesthetic and the appearance of the finished layers represent essential characteristics. Researches in such a field for different urban and peri-urban spaces (streets, squares, preferential and specialized routes, parks, etc.) are constantly evolving, even in response to the increasing and more conscious demand for functional products capable of finding the right balance between performance and environmental safeguard [7.3]. In turn, in the most recent years, the use of such roads started to be promoted also by the public administrations in view of enhancing the aesthetic value of architectural and monumental urban areas [7.4, 7.5].

For instance, Figure 7.1 illustrates an example of a red block pavement placed in the proximity of a monumental valuable area located in the city of Siena, in Italy (Piazza del Campo square).



Figure 7.1. Piazza del Campo square (Siena, Italy): example of red block pavement.

In analogy, these installations are suitable to preserve high-valuable landscapes situated in natural areas generally located in the proximity of rural zones, natural landscapes, lakes, mountain contexts, etc. Effectively, clear/colored solutions demonstrated to promote the road integration in such environments as much as some specific road design patterns able to ensure adequate and homogeneous geometric layouts [7.2]. In this perspective, Figure 7.2 shows an application of a colored asphalt pavement in a naturalistic context in Texas. Figures 7.3 and 7.4 depict a red and a clear road located in Utah and Japan, respectively.



Figure 7.2. Colored asphalt pavement in a naturalistic context in Texas.



Figure 7.3. Red road pavements located in Utah.



Figure 7.4. Clear road pavements located in Japan.

7.1.2. Traffic calming and road safety

Colored road pavements are already employed as traffic calming measures. Mainly, their use is finalized to the pedestrians and cyclist protection. Colored and textured pavement treatments, together with devices, signs and pavement markings, are able to provide visual cues about the traffic-calmed areas; in other situations (along the roadways) they alert motorists to the need for alertness, much as conspicuous materials increase bicyclist and pedestrian visibility. Similarly, the variation from conventional black asphalts or grey concretes associated by most people as “automobile territory” signals to drivers and motorists that they are crossing a “different” area (e.g. residential), which is generally expected to assign greater priority to cyclists and pedestrians. Furthermore, the color (and also the texture) of the street surfaces is an important aspect of the attractiveness of many residential zones [7.6]. Not surprisingly, this is leading many local administrations to adopt such strategies (the great sensibility and attention towards pedestrian and cyclists is a strong incentive). An example of a residential area delimited by colored pavements is presented in Figure 7.5.



Figure 7.5. Residential driveway made with red asphalt concrete.

Whit analogous scopes, the installation of colored surfaces has been more and more sponsored in the case of re-paving of new design of walking and cycling paths manly to increase the track's visibility and force its separation from the trafficked spaces of road reserved to motorized vehicles [7.7]. As examples, Figures 7.6 and 7.7 present two case of colored cycling track.



Figure 7.6. Colored cycling track: example of blue asphalt concrete.



Figure 7.7. Colored cycling track: example of green texturized pavement.

Additionally, the easiness involved in paving operations of color pavements (e.g. the simple surface painting) promotes their localized use in specific road sections for which important safety concerns are requested. This is the case of the pedestrian crossings realized with colored/painted wearing courses in order to capture the driver's attention and enhance the pedestrian visibility [7.8]. An example of such application is presented in the following Figure 7.8.



Figure 7.8. Example of red-painted pedestrian crossing.

With respect to the pedestrian crossings, it can be also noticed that, despite a general lack of standardized design guidelines, for instances shapes, colors, visibility, etc. (see the Italian regulations), colored pavements are more and more utilized in the urban context since they have demonstrated great efficacy for safety purposes. As an example, the Chicago Department of Transportation evaluated colored crosswalk at 100 elementary school zone crosswalks [7.9]. Initially, no statistically significant reductions in the proportion of speeding drivers at the locations were found, otherwise several studies found statistically significant reduction in pedestrian collisions at high-visibility crosswalk locations [7.10, 7.11] and increase in the proportion of pedestrians who looked for vehicles before crossing [7.12]. Analogous safety considerations can be even drawn for what regarding the assignment of priority to particular traffic categories (e.g. taxis, buses, emergency vehicles, etc.) [7.4]. Figures 7.9 and 7.10 properly depict two examples of such use.



Figure 7.9. Colored pavement to assign priority to emergency vehicles.



Figure 7.10. Colored pavement to assign priority to taxis and busses.

7.1.3. Night and tunnel lighting

Further aspects concerning the use of clear road pavements have been also related to the illumination of roads that is required during the night-time. An interesting application of the principle was successfully done by Bocci et al. in a tunnel located in the Northern Italy [6.1]. Authors evaluated in the field and in the laboratory the possible use of the technology in terms of pavement photometric performance. A dense graded clear asphalt mixture for wearing course was produced using a clear aggregates and transparent binder and was subjected to luminance and reflection tests. The luminance was used to indicate the emission or reflection from flat surfaces and was determined by an extremely accurate luminance meter composed by sophisticate optics and electronics. The nightly and daily visibility were measured by a retro-reflectometer with an observation angles of 2.29° (that simulates the position of a driver at a sighting distance of 30 m with eyes height of 1.2 m from the pavement) and 1.24° (condition of a driver using dipped headlights at 0.65 m from the pavement, at a sighting distance of 30 m with eyes height of 1.2 m). Main results indicated higher photometric properties in the case of clear mixture (if compared with a conventional black asphalt concrete). According to other authors, a high reflectance was assumed as a clear indicator of a more visible road surface for the eye of the observer [7.13]; in turn, a more efficient road lighting, presupposing optimized installations and luminance distributions was considered possible. Nevertheless, such results were suitable to achieve cost-saving energy management for what concerning the illumination of the road tunnel. Figure 7.11 illustrates the obtained pavement (installed inside the studied tunnel).



Figure 7.11. Black asphalt concrete (left) vs. clear mixture (right) paved in the tunnel [6.1].

Similar findings were certified also by Fotios et al. [7.14] through the development of a specific technical report which investigated the effect of pavement materials on road lighting performance.

7.2. Thermal-optimized roads: human concerns

7.2.1. Thermal comfort

The thematic of thermal comfort interesting human beings is one of the most significant facets involved in the UHI phenomenon. As already explained in Chapter 1, serious heat repercussions properly regard the human health and affect the human feeling about the topic.

The study of the thermal comfort dates back to the concept of effective temperature which was early investigated by Houghten and Yaglou in 1923 [7.15] considering factors as the air temperature, the relative environmental humidity and the wind speed. Later, other authors proposed to include also the solar radiation [7.16], as well as the human body evapotranspiration mechanisms indicative of the metabolism work and the clothing [7.17]. Furtherly, the indexes defined by ISO 7730 standard started to be widely diffused in the field (six factors including both physical and human quantities were adopted). Höppe proposed also an index based on the energy balance of the human body [7.18, 7.19]. In other cases, the Wind Chill Index is commonly used, particularly in cold regions [7.20], and the Wet Bulb Globe Temperature [7.21] and Heat Index are utilized for the prevention of heat disorders. For what said, an appropriate evaluation of the thermal properties interesting people can be considered as important as the study of the environmental physical quantities treated in the previous sections. In this perspective, an accepted literature theory suggested to quantitatively determine the “human thermal load”, i.e. a mathematical indicator based on various physiological responses of persons on the pavement [7.22–7.25]. Indeed, no specific scientific assessments in this direction will be presented in this dissertation; however, interesting conclusions could be evinced specifically analyzing such an approach.

According to the above-mentioned theory, a thermal equilibrium condition is reached by humans surrounded by the urban environment. Human body interacts with the environment based on the heat balance equation following proposed (Equation 7.1).

$$M + R_{net} = W + C + E \quad (7.1)$$

where: M represents the metabolic rate expressed in W/m^2 and calculated on the body surface, the O_2 intake and the CO_2 production; W is the mechanical workload (W/m^2), i.e. the external work done by the human body; R_{net} is net solar and infrared radiation received by the person and transmitted from body (expressed in W/m^2); C is the sensible heat loss exchanged by the respiration and due to the gradients between the average skin temperature and the air one (W/m^2); E is the latent heat loss due to perspiration, exhalation and insensible perspiration (W/m^2). When the heat dissipated by the body is insufficient, a hot sensation is

suffered by people or, vice versa, the person feels cool with an excessive thermal exchange. In any case, a non-neutral level involves a thermal load applied to the human body that can be accounted with the F_{load} parameter (Equation 7.2) based on the previous heat balance relation.

$$F_{load} = M - W + R_{net} - C - E \quad (7.2)$$

where F_{load} is again expressed in W/m^2 . Given the nature of such parameter, it is evident that, in addition to the physiological terms, also the physical/environmental quantities (see R_{net} variable) cover a crucial role (namely the temperature, the humidity, the amount of radiation and the airflow). The following Figure 7.12 gives a graphical schematization of the described thermal balance

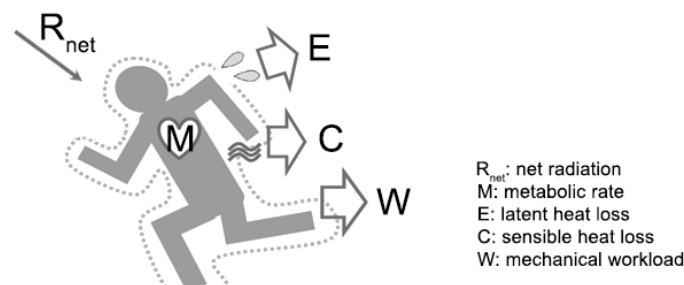


Figure 7.12. Thermal balance: heat exchange between the human body and the environment.

As mentioned, such R_{net} parameter depends also on the radiations received by the body, then it is linked to the previously-defined q_{sun} , q_{atm} and q_{em} quantities (the solar, atmospheric and emitted radiation, respectively). Thus, the beneficial use of cool pavements can be numerically accounted referring the pavement heat transfer balance (see Chapter 2) with the proposed exchange transfer theory. In this regard, Figure 7.13 proposed and adapted scheme of the global het balance.

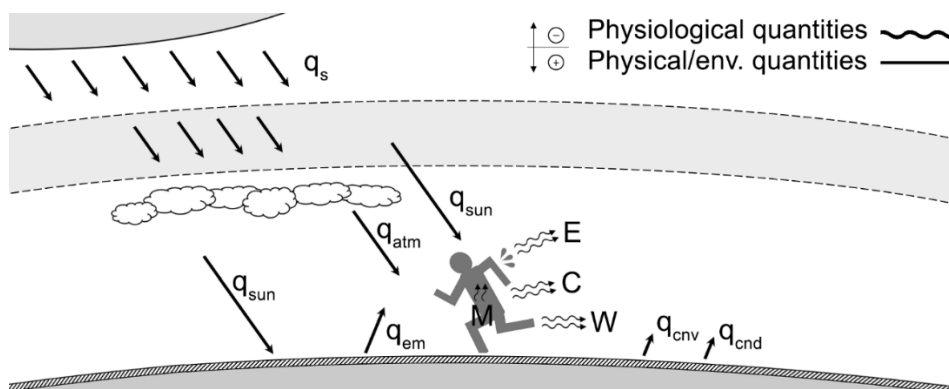


Figure 7.13. Adapted thermal balance: human-environment heat exchange.

For instance, according to literature [7.26], the air temperature is assumed as a crucial parameter to evaluate the influence of the environment in the human thermal load. Based on the example proposed in Table 7.1 (extracted by the cited research), the air temperature role is evident in determining such an aspect linked to the concept of human thermal comfort. Namely, depending on the human activity, sensible and latent heats (C and E , respectively) presented in the Table deeply change as a function of T_{amb} (see the differences between the 20 and 28 °C situations).

Table 7.1. Physiological parameters vs. different air temperature sets (extracted from [7.26]).

Degree of Activity	Average metabolic rate [W]	Air temperature [°C]					
		28		24		20	
		Heat [W]					
		Sens.	Lat.	Sens.	Lat.	Sens.	Lat.
Seated at rest	100	50	50	67	33	79	21
Seated, very light work	120	50	70	70	50	84	36
Office work	130	50	80	70	60	86	44
Standing, walking slowly	130	50	80	70	60	86	44
Walking, seated	150	53	97	76	74	90	60
Moderate work	160	55	105	80	80	98	62
Light bench work	220	55	165	85	135	115	105
Moderate dancing	250	62	188	94	156	125	125
Fast walking	300	80	220	110	190	145	155
Heavy work	430	132	298	154	276	188	242

On the basis of the following Figure 7.14, the physiological responses of human body are again presented as a function of the heat thermal stress of the environment [7.27]: once more, this indicates the importance in reducing the urban temperatures to enhance the perceived comfort.

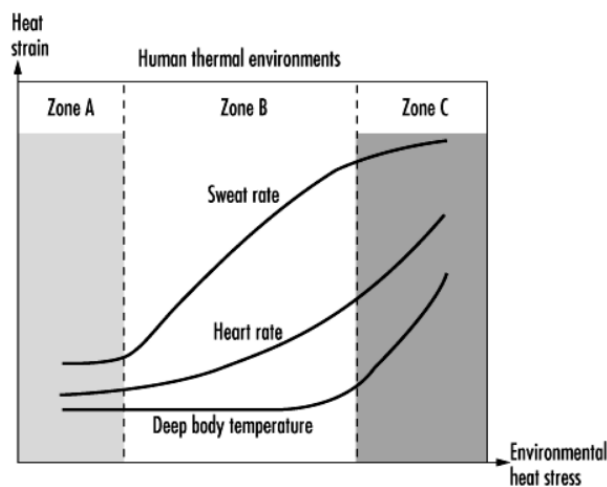


Figure 7.14. Heat “strain” vs. environmental heat stress [7.27].

Similarly, Hashida et al. [7.28] related the human thermal load (and the subsequent thermal sensation) to different ambient sets considering the T_{amb} and also the air humidity, the wind speed and the solar radiation (a parking lot and a forest were assumed to represent various environmental scenarios). Figure 7.15 presents the results obtained in the study.

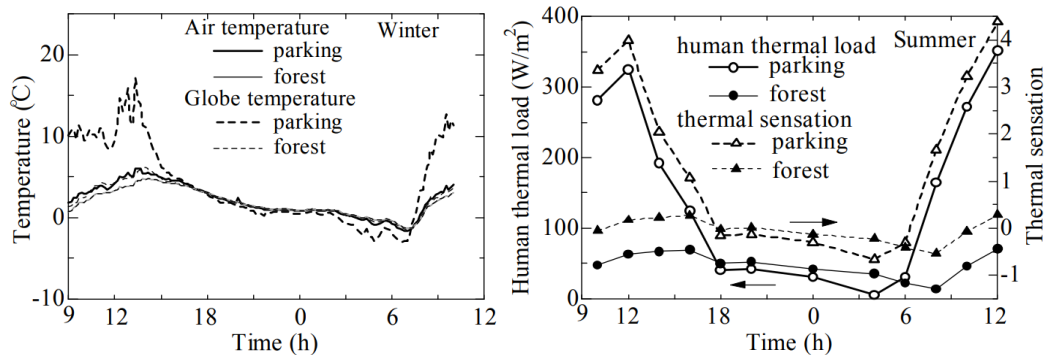


Figure 7.15. Air temperature evolution (left) and obtained physiological quantities (right) [7.28].

7.2.2. Visual comfort

The visual comfort property interesting the urban environment is of immediate impact on humans. In this respect, they could suffer the visual fatigue and dazzling which are surely bad for health but can have also repercussions on safe driving [7.29]. In this context, glare is the condition of vision in which there is discomfort or a reduction in the ability to see details or objects, caused by an unsuitable distribution or range of luminance, or by extreme contrasts [7.30]. Disability glare is defined as a type of glare which impairs the vision and can be caused by scattering of light inside the eye because of the imperfect transparency of the optical components of the eye and to a lesser extent by diffuse light passing through the scleral wall or the iris [7.31]. Discomfort glare is the glare that causes discomfort without necessarily impairing the vision of objects. Veiling glare is defined as the reflection-associated contrast-reduction due to which, the contrast of the visual target falls below the required value, causing difficulty in visibility or readability of the target [7.32].

According to literature, the human eye can encounter a wide range of luminances, from 0.000001 cd/m^2 (very dark night) to 10000 cd/m^2 (sunlit beach) [7.33]. The state of adaptation of the human eye dictates the spectral sensitivity because at different luminances different photoreceptors (rods and cones) are activated (see Figure 4.4 at Chapter 4). In general, three defined states of the spectral sensitivity of the human eye are present: they are photopic vision, scotopic vision and mesopic vision [7.34]. In the luminous environment, the human eye acts adaptively and the visual perception changes accordingly. In order to fully understand the relationship between the complex luminous environment

and the human visual discomfort perception, wide specific literature has been developed over time [7.35–7.38].

In the case of the urban context, it is easy to understand the importance of such topics, above all adopting alternative paving solutions which, in general, are obtained using colored and clear materials. Moreover, the above-mentioned safety implications must be also taken into account, specifically when alternative clear pavements are flanked to conventional paving materials (commonly dark) and significant contrasting colors can influence the human view. An example of an optical study applied to cool road pavements was proposed by Xie et al. [7.39], who studied the effect of near-infrared reflective pigments on the optical properties of some colored pavements. In particular, they analyzed different paving alternatives using the reflectance parameter (some experimental results are presented in Figure 7.16).

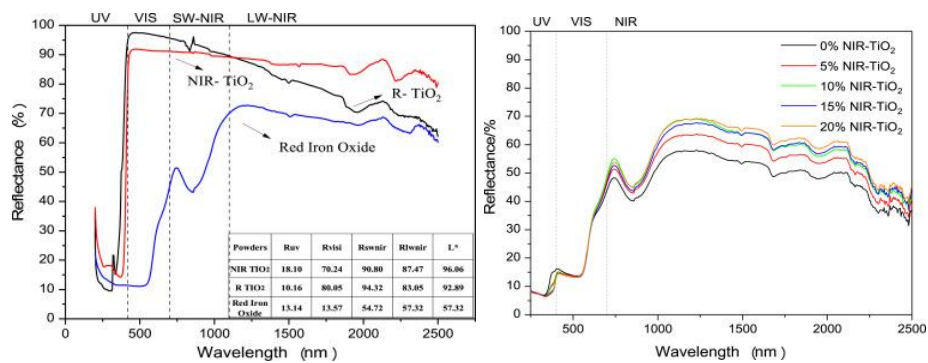


Figure 7.16. Reflectance and visual properties of different kinds of pavements [7.39].

Indeed, no extensive specific literature can be cited about the topic of the visual comfort applied to road pavements. This is probably ascribable to the still low diffusion and application of clear and color pavements in large urban spaces, as well as to the heat-related problems actually investigated when involving these structures. Principally, few publications about visual comfort and visual-health implications are moreover focused on the above-cited safety topics: as an example, some research efforts were spent to link the sun glare to the road safety level in presence of the sun glare based on statistical observation intersection crashes occurred at road intersections [7.29]. For instance, other studies regarded the visual aspects connected to the tunnels (glare problems at entrance and exit of dark/artificial-enlightened environments are well known). In this regard, Cantisani et al., in 2018, concluded some studies about the natural lighting of road pre-tunnels and proposed a methodology to assess the luminance related to pavement [7.40].

Therefore, given the substantial lack of specific literature, the topic should be of great interest in the future in order to fully characterize the overall pavement performance when using thermal-optimized solutions to mitigate the UHI phenomena. Based on this thematic, possible strategies to integrate clear or colored structures in the urban context could concern

adequate installations useful to limit the discomforts due to clear colors and the high contrasts with the remaining urban textures (e.g. gradual changing of pavement color/properties able to indulge the adaptations of the human eye to the new luminance situations).

Not least, definite focus should be addressed to the study of adequate paintings for the horizontal markings since, reasonably, the use of innovative clear/colored road pavements should imply the adaptation of street signs' colors (also technical and legislative standards should move precise steps in this direction).

7.3. Guidelines for thermal-optimized roads

The present paragraph gives a final summary of the main radiative properties of road materials which have been demonstrated to influence the final thermal performance of the in-service road pavements.

The **emissivity** influences the long-wave radiation emitted by the materials as a function of their temperature. High emissivity values correspond to good emitters of radiation and to a ready release of the absorbed energy. Several studies worldwide have been performed to understand the impact of the emissivity on the thermal performance of materials used in the urban environment; principal findings always indicated that the emissivity has a crucial role in affecting the surface temperature of the materials during the night period (a strict correlation between the average nocturnal surface temperature and the corresponding material emissivity has been certified). Generally, it is also reported that the role of emissivity is quite important when the reflectivity of the materials is reduced while, for high albedo values, the relative increase of the emissivity offers minor advantages regarding the cooling potentiality (as obvious, its effects must be always considered in combination with the other radiative quantities). The emissivity of paving materials has been also verified to narrowly vary between 0.90–0.97, being mainly linked to the aggregate matrix which composes the pavements' mixtures (regardless the use of asphaltic binder or cement). For this reason, the main strategies to obtain tangible effects in the reduction of UHI concerns are not generally focused on the variation of such parameter.

The **albedo** is the reflectivity of the material which, together with the spectral and broadband absorptivity, determines the amount of solar radiation absorbed or reflected by the pavement. The albedo is mainly determined by the color of the material surface, but also by its roughness. In general, light colors present a lower absorptivity to the visual spectrum of solar radiation, while, the specific absorptivity to the infrared part of the radiation is quite independent of the perceived color (absorptivity of solar radiation is also affected by the

roughness of the surface). On the contrary, light surfaces are usually characterized by high albedo values. Overall, numerous studies demonstrated strong correlations between the color of pavement materials, their surface temperatures and the sensible heat released. Globally, significant temperature differences have been measured between pavements of different color, even of the same typology. For these reasons, numerous researches to increase the reflectivity of the paving materials have been carried out and reported. Technological solutions usually aim at increasing the albedo of light colored or white pavements, by increasing their spectral reflectance in the visible part of the solar radiation. Most of the existing techniques are applicable to asphalts, concretes and other types of pavements: as examples, the use of conventional cements, the use of concrete additives, the application of white topping and ultra-thin white topping, the use of roller compacted concrete pavement, the utilization of light aggregates in asphalt concrete surfaces, the use of chip or sand seals with light aggregates, the utilization of color pigments and seals and the use of colorless and reflective synthetic binders, the painting of the surfaces with a light color, the use of sand/shot blasting and abrading binder surfaces, the production of resin-based pavements, etc. Depending on the selected technique, new construction or maintenance/rehabilitation of existing pavements can be achieved.

Thermal **conductivity** and thermal **capacity** are the main additional parameters that affect the thermal performance of the in-service pavements. High thermal conductivities of paving surfaces seem to contribute to fasten the heat transfer from the pavements to the ground and vice versa. During day-time (when the temperature of the pavements is higher than that of the ground) heat moves towards the bottom, while, during night-time, the inverse flow is generally observed. Therefore, materials with higher conductivity present lower average maximum and higher average minimum temperatures. Thus, the inclusion in paving mixture of specific components, as long as the design of specific voids' contents, could be managed to achieve structures able to boost such heat transmissions. Globally, the addition of ingredients of high thermal capacity or materials of latent heat storage can be supposed in order to increase the thermal storage capacity of the surfaces. This should contribute to reduce the surface temperatures during the day-time but also to decrease the sensible heat release to the atmosphere. Such concerns must be studied also in view of the heat transfer developed by convection to and from the pavements surface and the surrounding environment (the temperature difference between the ambient air and the surface of the pavement). Heat convection may be free or forced or both, depending on the wind speed and the temperature gradients.

Other effective strategies could involve also permeable pavements, within which the water is allowed to pass to the soil through the materials voids/pores. It evaporates when the temperature of the material increases, contributing to cooler pavement surface. The degree of evaporation is a function of the moisture content in the material and the atmosphere and

highly depends on the temperature of the pavement. Higher moisture contents and increased watering were verified to be able to keep the surface of the pavements cooler. In general, dry permeable pavements present a higher surface temperature than the non-permeable equivalents. Otherwise, some experimental investigations showed poor correlations between the surface temperature and the permeability, above all in the case of water-retaining concrete block pavements. Summarily, permeable pavements seem to be more suitable for warm and humid climates, where rain water is mainly used to cool down the surface of the pavements. Waste water may be also used as the evaporative source. In the case of dry climates, where the availability of water is a problem, permeable pavements may not be a properly suitable. When the target is to increase the permeability of the surfaces, permeable, porous, pervious or water retaining materials are utilized. The water must flow through the material through a series of pores or connected holes. In porous materials holes are available in the material mass but are not necessarily connected. In general, permeable, porous or pervious pavements present a lower albedo than the impermeable alternatives, and higher convective fluxes to the atmosphere because of their higher effective surface area created by the increased void's content.

Finally, other solutions and structures can be designed to produce thermal-optimized/oriented road pavements. Some examples are represented by the above-introduced asphalt solar collectors, usually realized establishing a circulation of a fluid in the mass of the pavement to remove the heat excess or creating a circulation of underground water in the pavement mass. Considering the urban texture which contains the road spaces, the management of shading of the paved areas (e.g. using natural or artificial solar control devices) should be also considered since the shaded surfaces present lower temperatures as the absorbed direct solar radiation is concretely reduced. Solar shading devices may be natural (trees and plants) or artificial and should allow the infrared radiation emitted by the pavements to escape in the atmosphere (radiative cooling of the pavements surfaces).

Overall, as already mentioned, at given environmental conditions (air temperature, solar radiation, humidity, wind, etc.), pavements realized using clear or colored binders should achieve distinctly lower in-service temperatures than traditional dark solutions mainly thanks to their chromatic and radiative properties [5.9]. Surely, such a fact could open interesting perspectives dealing with the topic of pavement structural performance and the subsequent durability concerns due to the lower temperatures reached. In this sense, future research studies can be planned to quantify the thermal responsibility with respect to the materials mechanical properties. As experimentally observed, the lower temperature involved with the use of cool pavements contributes to give promising results at higher in-service temperatures but, at the present stage of the research, the strict definition of the structure in-field durability is not still available. Just a few literature studies early attempted

to establish correlations between the thermal and mechanical characteristics of pavements evaluating also their durability, above all dealing with the internal structure responses. As example, the influence of non-linear temperature gradients was evaluated at long-term to predict the mechanical parameters of asphalt pavements considering the oxidative aging due to exposure under field conditions. In this case, it was demonstrated that, despite being often neglected in mechanistic modeling, temperature is a key parameter for accurate prediction of the distribution of stresses and strains in pavement system. In particular, the thermal analysis revealed that the surface temperature of the pavement and the atmospheric one were strongly correlated, while that inside the pavement structure decreased with depth. The thermal variations within the pavement structure, particularly in the asphalt layer, were non-linear and caused variation of stiffness modulus as a function of depth [7.41]. Another recent study proposed an innovative long-term aging model based on a morphology-kinetics approach. It considered the influence of the temperature with the purpose to predict the field-aged viscosity of a pavement bituminous binder and it was able to accurately estimate the long-term aging performance at the mixture-scale [7.42]. Similarly, temperature effects in asphalt pavements were studied to evaluate changes in the material viscoelastic properties proposing a thermo-mechanical numerical simulations to understand the combined effect of thermal variations and vehicular loads. The produced finite element model gave very encouraging results and indicated that more accurate modeling of the mechanical behavior of such complex pavement materials can be obtained when multiple physical phenomena were simultaneously included in the computation [7.43]. Furtherly, rutting behavior of different pavement structures was studied as a function of the temperature, especially during summer, under heavy traffic loads. Tests were conducted to specifically determine the cause and the source of the rutting at each asphalt pavement layer by surveying the permanent deformations at various depths. Mechanical analysis showed that the shear stress in the middle asphalt-course layer was the highest in magnitude under load or temperature and impacted the most rutting development [7.44].

In general, it is clear that all the reported studies cannot be separated from extended in-field tests, observations and validations: thus, these specific aspects could be deepened at the future steps of the research, when moving the mechanical analysis at field-scale. Coupling the obtainable results with the already-proposed thermal monitoring, the collected information will be useful to enlarge the experimental findings to various cooling pavements for the mitigation of the UHI phenomenon.

7.4. Preliminary cost estimation

A cost estimation of the studied paving solutions is hereafter proposed with the objective to give a preliminary order of magnitude of the involved financial aspects.

Really, it must stressed that a comprehensive analysis should account the costs of the paving technologies but also all the connected savings/drawbacks interesting the urban environment. As analyzed, in fact, the large variety of fields involved in UHI phenomena would surely cause non-negligible repercussions in many factors, equally related to positive concerns (monetary savings for urban cooling, environmental sustainability, pollution and emission reductions, human health preservation, etc.) or negative facets (expansiveness of pavement solutions, maintenance need, etc.). For what said, it is evident that a careful financial balance should be carried out at least with a quite large scale of study; probably, also a long-term monitoring of pavement structures, but also of the surrounding environments, should be promoted to obtain reliable indications. Moreover, the possible computation should include also aspects that can be difficulty monetized (health, comfort, etc.). Given this introduction, it is clear that the actual state of the research is not sufficient to draw a comprehensive financial analysis of the proposed cool pavements. Otherwise, some preliminary estimations about the production/construction costs themselves are following given together with some literature statements that tried to enlarge the pavement cost-related aspects to a wider view.

With respect to the costs of studied materials, the production of resin-based pavements and the related construction can produce a global increase of costs estimated of about three-four times (in comparison to the bitumen, the only synthetic transparent resin is about twice expansive – the cost increase has to be imputed to the plants and laying concerns). Really, the complete analysis must be integrated considering the possible use of valuable and more expansive aggregates: namely, with reference to the utilized lithic matrix, white and yellow marble, or coral-pink stone aggregate, can produce a 15-20% cost increment with respect to the limestone solution for what regarding the final price of the selected constituents. On the contrary, given the great efficacy in reducing the urban temperature of such technology, tangible savings should be achieved with respect to the overall energy balance of the city areas (consumption of for air cooling, artificial lighting, etc.).

The production of oxide-colored pavements reasonably involves cost variations only connected to the pigment additions within asphalt mixtures (mixing and construction temperatures are not altered – construction equipment does not change). Therefore, a 90-100% increment of cost with respect to the unit has to be added to the financial computation. In this case, no further costs should be accounted for what regarding the plants and equipment.

Also dealing with the cases of surface-treatments, quasi-negligible operational costs can be considered (relatively easy and quick varnishing of the finished surfaces). Just few efforts must be addressed to prepare the existing surfaces to take the paintings (e.g. cleaning). Numerically, a preliminary estimation can suppose a 25-30% increment of the cost for the application of the studied mortar and resin treatments. Substantially, the selected color does

not influence the construction costs but, as stated by experimental findings, this could lead to appreciable differences in the final pavement responses, thus in the overall system finance.

In summary, the general idea about pavement costs indicates that more expansive solutions are associated to clear wearing course used to replace the dark asphalt surfaces, moreover in presence of light aggregates. Indeed, some literature contributions reported the use of clear aggregates for resurfacing as a cost-effective option [7.45]. More advanced researches tried also to consider the hypothetical variation of the characteristics and the thermal performance of the materials during their in-service life since it is quite recognized that pavement radiative properties can be progressively modified by the effect of aging [7.46]. As example, the surface albedo of bituminous pavements is reported to increase over time because of the progressive discoloring of the primitive black aspect and the progressive aggregate exposition [7.47]. In turn, light concrete surfaces have been reported to suffer a continuous darkening after the construction, initially due to the cement hydration processes, then to the natural dirtying of the in-service clear surfaces [7.48]. By linking the thermal performance of paving materials simply to the albedo, some literature estimations tried to compute the possible costs of some road maintenance interventions performed with bituminous and cement materials [1.77]. The calculations were firstly referred to a standard urban road in good structural conditions that needed the rehabilitation of the upper layer only. The related results are presented in Table 7.2 and are associated only to the material and construction costs (costs about the road “bed” preparation were neglected). In the second case (see Table 7.3), interventions were more drastic, thus they were intended as repair of the entire pavement depth. In this perspective, please note that the reported costs are actualized at the beginning of the 90’s [7.49–7.54]. Effectively, the significant differences about the costs presented for the solutions in the Tables 7.2 and 7.3 with respect to those identified for the studied materials must be read considering the novelty of the tested technologies, which request new construction approaches. For instance, an analog situation was encountered at the early stage of production of polymer-modified bitumen – actually, its price is completely comparable to that of the conventional non-modified one).

Table 7.2. Cost estimations for paved surfaces – upper layer rehabilitation (extracted from [1.77]).

Paving material	Average cost [\$ /m ² (€ /m ²)]	Estimated albedo		Expected life [years]
		New [-]	Weathered [-]	
Regular asphalt (≈ 2.5 cm)	2.3 (2.11)	0.05–0.10	0.15–0.20	3–5
Asphalt + light aggregates (≈ 2.5 cm)	2.6 (2.38)	0.05–0.10	0.30–0.40	3–5
Regular chip seal (≈ 1.3 cm)	1.2 (1.10)	0.15–0.20	0.15–0.20	3–5
White cheap seal (≈ 1.3 cm)	1.5 (1.37)	0.40–0.50	0.30–0.40	3–5
Regular slurry seal (≈ 1.0 cm)	1.2 (1.10)	0.05–0.10	0.15–0.20	3–5

Table 7.3. Cost estimations for paved surfaces – full-depth rehabilitation (extracted from [1.77]).

Paving material	Average cost [\$/m ² (€/m ²)]	Estimated albedo		Expected life [years]
		New [-]	Weathered [-]	
Regular asphalt (≈ 18.0 cm)	16.4 (15.02)	0.05–0.10	0.15–0.20	20–25
Asphalt + light aggregates (≈ 18.0 cm)	16.7 (15.29)	0.05–0.10	0.30–0.40	20–25
Regular whitetopping (≈ 13.0 cm)	16.4 (15.02)	0.35–0.40	0.25–0.30	20–25
Whitetopping (white conc.) (≈ 13.0 cm)	18.9 (17.31)	0.70–0.80	0.40–0.60	20–25

Conclusions

The present dissertation aimed at analyzing the role of the road pavements with respect to the phenomenon of the Urban Heat Island, i.e. the mechanism developed within the urban context for which the temperature is higher with respect to the surrounding sub-urban/rural regions. Given the growing consciousness about the topic of the environmental sustainability and the possible repercussions of the phenomenon linked to the human health, the thematic is of extreme actuality, also considering that increasing temperature trends due to global warming have been estimated for the next future.

In particular, the first Chapter introduced the UHI concepts, contextualizing the problem and describing the main characteristics of the phenomenon. A brief historical background was proposed, then, the functions of the road pavement in UHI were analyzed.

The second Chapter presented the main theoretical approaches needed to study the heat transfer mechanisms, giving a preliminary knowledge about the physic of the radiations and the heat theory. The radiative properties and the thermal characteristics of the real objects, as well as the properties of the solar and atmospheric radiations, were dealt to evaluate some aspects related to the urban micro-climate. Then, heating processes and transmission mechanisms were studied with reference to the road pavement system.

The third Chapter gave also a brief literature review based on some scientific experiences made to design thermal-optimized structures able to mitigate the UHI concerns and manage the heat interesting the road pavements. Small-scale laboratory and real-scale in-field applications were considered.

The fourth Chapter described the core activity presented in the dissertation; an extensive experimental protocol developed at various analysis scale (in the laboratory and in the external environment) was planned to carry out a comprehensive review of different solutions for the production thermal-optimized road pavements.

The fifth Chapter presented the main results of the experimentation. A multi-scale approach was utilized to characterize the selected materials (resin-based, oxide-pigmented bituminous and surface-painted concretes). Chromatic analysis at binder, mastic and mixture-scale were developed to find the influence of material chromaticity. Thermal assessments at mixture-scale were performed to calculate the radiative properties of the solutions, their thermal responses in the laboratory and their real thermal performance (by mean of thermographic monitoring) in the outside scenarios. Then, an extended mechanical characterization was done at binder, mastic, loose-blend and mixture-scale to define the solution's suitability as effective paving materials (in order to comply acceptable structural, functional and safety standards).

The sixth Chapter aimed at deepening several aspects emerged from the experimental results. The existence of correlations between the chromatic, radiative and thermal properties of the selected mixtures were investigated. Then, the mitigation efficacy of the tested pavements was evaluated. Based on some experimental findings, a numerical approach was also applied to estimate the materials' thermal behaviors under several external conditions; extending the experimental assumptions to additional hypothetic scenarios, such aspects were studied proposing possible methods to determine the thermal responses only as a function of the environmental characteristics and the basic radiative properties of the mixtures.

The seventh Chapter was finalized to introduce further aspects involved with the use of thermal-optimized structures but not directly related to the heat concerns. Thus, some considerations about the infrastructure integration in the landscapes, the road safety and lighting were done. Then, some concepts related to the human comfort (mainly, the thermal and the visual ones) were proposed to evaluate the influence of the road system. As a conclusive summary, some guidelines to obtain effective thermal-optimized road pavements were finally stated resuming the main radiative properties of road materials (critical in determining the thermal responses) and the strategies to limit the UHI issues.

Going back over the principal findings deduced from the dissertation, some conclusions are hereafter summarized:

-
- Given their extensive use and the large areas covered by the road pavements, their crucial role in determining the UHI phenomena was certified.
 - Successful literature experiences were worldwide documented. Several solutions able to produce thermal-optimized surface were produced designing different structures; moreover, suitable pavements were also designed to manage the heat concentration in paving layers (energy harvesting systems able to convert the heat in renewable energy, winter appliances to prevent the issues connected to the cold climates).
 - Suitable small-scale experimental protocols were proposed to simulate and monitor the heating phenomena interesting the real in-service pavements (laboratory evaluation of the reached temperatures and the heat released by surfaces).
 - Resin-based mixtures (produced with synthetic transparent binder substituting the conventional black bitumen) allowed sensible mitigation of the surface temperatures. In combination with valuable clear aggregates (exalted by the transparent nature of binder), summerly temperature reductions up to about 19 °C were verified. Their mechanical characteristics suggested a proper use in low-trafficked/pedestrian/cycling zones or with temperate climates (low stiffness allowed improvements in their fatigue life but could cause also possible criticalities for what regarding the high-temperature rutting resistance, even the lower reached temperatures).
 - Oxide-pigmented mixtures (produced coloring the black bitumen with pelletized oxide pigments) guaranteed an appreciable temperature mitigation (up to about 6 °C). Their excellent mechanical performance suggested a possible structural use (the higher stiffness than conventional bituminous mixture allowed their application even in high-trafficked areas). No critical constrains were found with respect to the fatigue and rutting concerns.
 - The application of surface paintings to conventional black bituminous mixtures (in form of resins or mortars) allowed temperature reductions even up to 17 °C mainly depending on the selected color (clear tonalities were those majorly predisposed to the heat mitigation). Their utilization partially affected only the surface characteristics of the asphalt concretes; otherwise, acceptable safety standards were always complied (even with higher application dosages).
 - In general, except for some painted solutions, the radiative properties of the surfaces seemed the effective parameters linked to the mitigation efficiency, rather than the surface colors.

-
- Promising correlations were found to link the radiative properties of the materials to their real thermal responses (a linear combination of the albedo and the thermal conductivity fitted the experimental results with high accuracy).
 - It was possible to extend the determined findings to further environmental scenarios starting from the material radiative properties (mainly albedo and conductivity) and considering some crucial environmental variables such as the wind speed. In this sense, some graphical schemes were produced to determine the fitting coefficients to apply to the above-mentioned linear combination in order to estimate the material responses under wider boundary conditions.
 - Numerous applications of clear/colored road pavements were also documented. The main purpose aimed at preserving/enhancing the aesthetic characteristics and the appearance of the surfaces in monumental valuable contexts, as well as in natural/rural environments.
 - An extensive use of clear/colored surfaces is going to be more and more promoted in the cities thanks to the high efficacy in increasing the user's safety. In fact, they are able to provide visual cues about traffic-calmed areas, forcing the separation from the trafficked spaces of road reserved to motorized vehicles, thus protecting vulnerable users such as pedestrian and cyclists; extensive use are growing on walking and cycling paths to increase the visibility and in reserved lanes which need special emergency or functional priorities.
 - A direct relationship between the road surfaces and the human perceived comfort was certified. Thermal loads applied to the human body immersed in the urban environment resulted directly affected by the solar incidence but also by the infrared radiation emitted by the pavement. The role of clear materials in causing visual glare and optical discomfort is quite documented, otherwise specific literature is not developed enough (probably because of the quite recent diffusion of such technologies).
 - Possible guidelines to design thermal-optimized pavements suggested to manage the albedo and the conductivity parameters. Albedo (representative of the aptitude to reflect the radiations) should be increased adopting alternative materials or clearer surfaces (albedo linked also to material color). The absorbed solar radiation is also affected by the surface roughness. Higher thermal conductivity seems to contribute to fasten the heat transfer from the pavements to the ground and vice versa, thus lower average maximum and higher average minimum temperatures are generally obtained. Emissivity (i.e. long-wave radiation emitted by the materials as a function of their temperature) is scarcely influent when dealing with paving materials (it narrowly varies between 0.90–0.97, being mainly linked to the aggregate matrix which composes the pavements' mixtures).
-

Recommendations for Future Works

As a conclusion, some possible points for the future improvement of the research have been also considered.

Principally, the extension of the studied materials should be able to increase the experimental database collected during tests. As examples, additional aggregates could be included (even with recycling/waste-reuse purposes) and other binder typologies could be analyzed (for instance, decolored or bituminous bio-binders). In turn, a polymer-modified bitumen can be utilized to produce a supplementary reference material (black polymer-modified bituminous mixture).

Considering the experimental protocol, the external monitoring could be extended to collect more data and introduce alternative environmental scenarios (wind, shade, irrigation, etc.). With respect to the laboratory monitoring, improvements in the artificial lamps used to simulate the solar radiation could be proposed (even the acceptable reliability obtained inside, more realistic heating should be attempted, above all for the intensity and the emission spectrum of the artificial lights).

Furtherly, real-scale applications of the selected technologies should be promoted to validate the collected results. Trial sections and real pavements should be also useful to give all the missing indications not replicable at small-scale: in this sense, some examples can regard the real in-service durability (color deterioration, dirt and tire effects, etc.), the effective mechanical performance, the real thermal responses (also considering that the road systems is part of the complex urban texture), as well as some aspects related to the operational paving phases and the maintenance and rehabilitation needed in the future. From the thermal point of view, real-scale laying should also permit the instrumentation to collect thermal data inside the pavement layers and define their real thermal states (strongly related to UHI concerns, but also to the stresses which affect the mechanical resistance of mixtures).

Bibliography

- 1.1 Environmental Protection Agency (2017). Learn about heat islands. United States. Available at: <https://www.epa.gov/heat-islands/learn-about-heat-islands>.
- 1.2 Hulley, M.E. (2012). The urban heat island effect: causes and potential solutions. *Metropolitan Sustainability*, 2012: 79–98.
- 1.3 Yang, L., Qian, F., Song, D.X., Zheng, K.J. (2016). Research on urban heat-island effect. *Procedia Engineering*, 69: 11–18.
- 1.4 Kim, Y., Baik, J. (2004). Daily maximum urban heat island intensity in large cities of Korea. *Theoretical and Applied Climatology*, 79: 151–164.
- 1.5 Manabe, S., Wetherald, R.T. (1980). On the distribution of climate change resulting from an increase in CO₂ content of the atmosphere. *Journal of the Atmospheric Sciences*, 37: 99–117.
- 1.6 Madden, R.A., Ramanathan, V. (1980). Detecting climate change due to increasing carbon dioxide. *Science*, 209(4458): 763–768.
- 1.7 World Health Organization (2009). Climate change exposures, chronic diseases and mental health in urban populations: a threat to health security, particularly for the poor and disadvantaged. Japan.
- 1.8 European Environment Agency (2018). National climate change vulnerability and risk assessments in Europe. Report No. 1/2018, Luxemburg.
- 1.9 Intergovernmental Panel on Climate Change (2013). Climate change 2013: the physical science basis. Cambridge University Press, Cambridge, United States.
- 1.10 Intergovernmental Panel on Climate Change (2007). Climate change 2007: the physical science basis. Cambridge University Press, Cambridge, United States.
- 1.11 Fischer, E.M., Schar, C. (2010). Consistent geographical patterns of changes in high-impact European heatwaves. *Nature Geoscience*, 3: 398–403.
- 1.12 Hayhoe, K., Cayan, D., Field, C.B., Frumhoff, P.C., Maurer, E.P., Miller, N.L., Moser, S.C., Schneider, S.H., Cahill, K.N., Cleland, E.E., Dale, L., Drapek, R., Hanemann, R.M., Kalkstein, L.S., Lenihan, J., Lunch, C.K., Neilson, R.P., Sheridan, S.C., Verville, J.H. (2004). Emission pathways, climate change and impacts on California. *Proceedings of the National Academy of Sciences*, 101(34): 12422–12427.
- 1.13 United Nations (1998). Kyoto protocol to the United Nations framework convention on climate change. Japan.
- 1.14 United Nations (2015). Paris Agreement. France..
- 1.15 Environmental Protection Agency (2008). Reducing urban heat islands: compendium of strategies - Urban heat island basics. United States.
- 1.16 Kandya, A., Mohan, M. (2018). Mitigating the urban heat island effect through building envelope modifications. *Renewable and Sustainable Energy Reviews*, 164: 266–277.

-
- 1.17 Hu, Y., White, M., Ding, W. (2016). An urban form experiment on urban heat island effect in high density area. *Procedia Engineering*, 169: 166–174.
- 1.18 Higashiyama, H., Sano, M., Nakanishi, F., Takahashi, O., Tsukuma, S. (2016). Field measurements of road surface temperature of several asphalt pavements with temperature rise reducing function. *Case Studies in Construction Materials*, 4: 73–80.
- 1.19 Coseo, P., Larsen, L. (2015). Cooling the heat island in compact urban environments: the effectiveness of Chicago’s green alley program. *Procedia Engineering*, 118: 691–710.
- 1.20 Wang, Y., Berardi, U., Akbari, H. (2015). The urban heat island effect in the city of Toronto. *Procedia Engineering*, 118: 137–144.
- 1.21 Duarte, F., Ferreira, A. (2016). Energy harvesting on road pavements: state of the art. *Proceedings of the Institution of Civil Engineers - Energy*, 169(2): 79–90.
- 1.22 Howard, L. (1818). *The climate of London: deduced from meteorological observations*. London, United Kingdom.
- 1.23 Callendar, G.S. (1938). The artificial production of carbon dioxide and its influence on climate. *Quarterly Journal of Royal Meteorological Society*, 64: 223–240.
- 1.24 Fleming, J.R. (2007). The Callendar effect. *American Meteorological Society*.
- 1.25 Chandler, T. (1965). *The climate of London*. London, United Kingdom.
- 1.26 Oke, T.R. (1967). City size and the urban heat island. *Atmospheric Environment*, 7(8): 769–779.
- 1.27 Barata, M., Ligeti, E., De Simone, G., Dickinson, T., Jack, D., Penney, J., Rahman, M., Zimmerman, R. (2011). *Climate change and human health in cities*. Cambridge University Press, Cambridge, United Kingdom.
- 1.28 Xu, H.Q., Chen, B.Q. (2004). Remote sensing of the urban heat island and its changes in Xiamen City of SE China. *Journal of Environmental Sciences*, 16(2): 276–281.
- 1.29 Stone B. Jr. (2007). Urban and rural temperature trends in proximity to large US cities. *International Journal of Climatology*, 27: 1801–1808.
- 1.30 Wilby, R.L. (2003). Past and projected trends in London’s urban heat island. *Weather*, 58(7): 251–260.
- 1.31 Gaffin, S.R. et al. (2008). Variations in New York city’s urban heat island strength over time and space. *Theoretical and Applied Climatology*, 94: 1–11.
- 1.32 Voogt, J.A., Oke, T.R. (2003). Thermal remote sensing of urban climates. *Remote Sensing of Environment*. 86: 370–384.
- 1.33 Cui, Y., Xu, X., Dong, J., Qin, Y. (2016). Influence of urbanization factors on surface urban heat island intensity: a comparison of countries at different developmental phases. *Sustainability* 8: 706.
- 1.34 Heidl, M., Hammerle, A., Tappeiner, U., Leitinger, G. (2015). Determinants of urban–rural land surface temperature differences – a landscape scale perspective. *Landscape and Urban Planning*, 134: 33–42.
-

-
- 1.35 Imhoff, M.L., Zhang, P., Wolfe, R.E., Bounoua, L. (2010). Remote sensing of the urban heat island effect across biomes in the continental USA. *Remote Sensing of Environment*, 114: 504–513.
- 1.36 Du, H., Wang, D., Wang, Y., Zhao, X., Qin, F., Jiang, H., et al. (2016). Influences of land cover types, meteorological conditions, anthropogenic heat and urban area on surface urban heat island in the Yangtze River Delta Urban Agglomeration. *Science of the Total Environment*, 574: 461–470.
- 1.37 Weng, Q. (2009). Thermal infrared remote sensing for urban climate and environmental studies: methods, applications, and trends. *Journal of Photogrammetry and Remote Sensing*, 64(4): 335–344..
- 1.38 Choi, Y.Y., Suh, M.S., Park, K.H. (2014). Assessment of surface urban heat islands over three megacities in East Asia using land surface temperature data retrieved from COMS. *Remote Sensing*, 6(6): 5852–5867.
- 1.39 Sobrino, J., Oltra-Carrió, R., Sòria, G., Jiménez-Muñoz, J.C., Franch, B., Hidalgo, V., Paganini, M. (2013). Evaluation of the surface urban heat island effect in the city of Madrid by thermal remote sensing. *International Journal of Remote Sensing*, 34(9-10): 3177–3192.
- 1.40 Peng, S., Piao, S., Ciais, P., Friedlingstein, P., Oettle, C., Bréon, F.M. et al. (2012). Surface urban heat island across 419 global big cities. *Environmental Science & Technology*, 46(2): 696–703.
- 1.41 Li, X., Zhou, Y., Asrar, G.R., Imhoff, M., Li, X. (2017). The surface urban heat island response to urban expansion: a panel analysis for the conterminous United States. *Science of the Total Environment*, 605–606: 426–435.
- 1.42 Liu, K., Su, H., Zhang, L., Yang, H., Zhang, R., Li, R. (2015). Analysis of the urban heat island effect in Shijiazhuang, China using satellite and airborne data. *International Journal of Remote Sensing*, 7(4): 4804–4833.
- 1.43 Jason, S., Christopher, J.K. (2015). Urban climate effects on extreme temperatures in Madison, Wisconsin, USA. *Environmental Research Letters*, 10.
- 1.44 Smoliak, B.V., Snyder, P.K., Twine, T.E., Mykleby, P.M., Hertel, W.F. (2015). ense network observations of the twin cities canopy-layer urban heat island”, *Journal of Applied Meteorology and Climatology*, 54: 1899–1917.
- 1.45 Morris, C., Simmonds, I., Plummer, N. (2001). Quantification of the influences of wind and cloud on the nocturnal urban heat island of a large city. *Journal of Applied Meteorology and Climatology*, 40: 169–182.
- 1.46 Schatz, J., Kucharik, C.J. (2014). Seasonality of the urban heat island effect in Madison, Wisconsin. *Journal of Applied Meteorology and Climatology*, 53: 2371–2386.
- 1.47 Zhao, C., Fu, G., Liu, X., Fu, F. (2011). Urban planning indicators, morphology and climate indicators: a case study for a north-south transect of Beijing, China. *Building and Environment*, 46: 1174–1183.
- 1.48 Givoni, B. (1989). Urban design in different climates. *World Meteorological Organization*, WMO/TD No.346.
- 1.49 Santamouris, M. (2001). Energy and climate in the urban built environment. James and James, London, United Kingdom.
-

-
- 1.50 Oke, T.R. (1984). Towards a prescription for the greater use of climatic principles in settlement planning. *Energy Buildings*, 7: 1–10.
- 1.51 Mills, G. (1999). Urban climatology and urban design. *Proceedings of the International Congress of Biometeorology and International Conference on Urban Climatology*, 8-12 November 1999, Sydney, Australia.
- 1.52 Perry, A.H., Symons, L.J. (1991). Highway Meteorology. CRC Press, Boca Raton, Florida.
- 1.53 Johnson, G.T., Watson, I.D. (1984). The determination of view-factors in urban canyons. *Journal of Applied Meteorology and Climatology*, 23: 329–335.
- 1.54 Watson, I.D., Johnson, G.T. (1987). Graphical estimation of sky view-factors in urban environments. *International Journal of Climatology*, 7: 193–197.
- 1.55 Yamashita, S. (1986). On relationships between heat island and sky view factor in the cities of Tama river basin, Japan. *Atmospheric Environment*, 20(4): 681–685.
- 1.56 Liang, J., Gong, J., Sun, J., Liu, J. (2017). A customizable framework for computing sky view factor from large-scale 3D city models. *Energy Buildings*, 149: 38–44.
- 1.57 Yang, J., Wong, M.S., Menenti, M., Nichol, J., Voogt, J., Krayenhoff, E.S., Chan, P.W. (2016). Development of an improved urban emissivity model based on sky view factor for retrieving effective emissivity and surface temperature over urban areas. *Journal of Photogrammetry and Remote Sensing*, 122: 30–40.
- 1.58 Middel, A., Lukasczyk, J., Maciejewski, R., Demuzere, M., Roth, M. (2018). Sky View Factor footprints for urban climate modeling. *Urban Climate*, 25: 120–134.
- 1.59 Joshi, K.K., Kono, T. (2009). Optimization of floor area ratio regulation in a growing city. *Regional Science and Urban Economics*, 39(4): 502–511.
- 1.60 Environmental Protection Agency (2010). Heat island impacts. United States. Available at: <http://www.epa.gov/heatisd/>. September 2010.
- 1.61 Collier, C.G. (2006). The impact of urban areas on weather. *Quarterly Journal of the Royal Meteorological Society*, 132: 1–25.
- 1.62 Fatogoma, O., Jacko, R.B. (2002). A model to estimate mixing height and its effects on ozone modeling. *Atmospheric Environment*, 36: 3699–3708.
- 1.63 Fan, H., Sailor, D.J. (2005). Modeling the impacts of anthropogenic heating on the urban climate of Philadelphia: a comparison of implementations in two PBL schemes. *Atmospheric Environment*, 39: 73–84.
- 1.64 Chen, W., Kuze, H., Uchiyama, A., Suzuki, Y., Takeuchi, N. (2001). One-year observation of urban mixed layer characteristics at Tsukuba, Japan using a micro pulse lidar. *Atmospheric Environment*, 35: 4273–4280.
- 1.65 Lin, C.Y., Chen, F., Huang, J.C., Chen, W.C., Liou, Y.A., Chen, W.N., Liu, S.C. (2008). Urban heat island effect and its impact on boundary layer development and land–sea circulation over northern Taiwan. *Atmospheric Environment*, 42(22): 5635–5649.
- 1.66 Environmental Protection Agency (2008). Heat Island Compendium. United States. Available at: <https://www.epa.gov/heat-islands/heat-island-compendium>.
-

-
- 1.67 Eurosense (2011). Thermo for Ghent city goes public!. Available at: http://www.eurosense.com/documents/offices/belgium/news-archive/thermo_gent.xml?lang=en-gb.
- 1.68 University of Illinois (2017). The global ledger of heat energy. Available at: https://www.e-education.psu.edu/meteo3/11_p11.html.
- 1.69 Patra, S., Sahoo, S., Mishra, P., Mahapatra, S.C. (2018). Impacts of urbanization on land use /cover changes and its probable implications on local climate and groundwater level. *Journal of Urban Management*, 7(2): 70–84.
- 1.70 O’Toole, J.C., Cruz, R.T., Singh, T.N. (1979). Leaf rolling and transpiration. *Plant Science Letters*, 16(1): 111–114.
- 1.71 Gkatsopoulos, P. (2017). A methodology for calculating cooling from vegetation evapotranspiration for use in urban space microclimate simulations. *Procedia Environmental Sciences*, 38: 477–484.
- 1.72 Santamouris, M. (2003). Understanding the microclimate. *Proceedings of 2003 Bioclimatic Architecture in Office Buildings Conference*, Athens, Greece.
- 1.73 Grimmond, C.S.B., Oke, T.R. (1999). Evapotranspiration rates in urban areas. *Proceedings of Impacts of Urban Growth on Surface Water and Groundwater Quality 1999*, 259: 235–243.
- 1.74 Chandler, T.J. (1976). Urban climatology and its relevance to urban design. WMO Tech. Note 149, Geneva, Switzerland.
- 1.75 Environmental Protection Agency (2017). Urban heat island basics – Reducing urban heat islands: compendium of strategies. United States. Available at: <https://www.epa.gov/heat-islands/heat-island-compendium>.
- 1.76 Bonan, G.B. (2002). Ecological climatology: concept and applications. Massachusetts, MA; Cambridge University Press.
- 1.77 Taha, H., Sailor, D.J., Akbari, H. (1992). High-albedo materials for reducing building cooling energy use. *US. Department of Energy Office of Scientific and Technical Information*, Lawrence Berkeley Lab., California, United States.
- 1.78 Ciocia, C., Marinetti, S. (2012). In-situ emissivity measurement of construction materials. *Proceedings of the 11th International Conference on Quantitative InfraRed Thermography*, 11–14 June 2012, Naples. Italy.
- 1.79 Christen, A., Vogt., R. (2004). Energy and radiation balance of a central European city. *International Journal of Climatology*, 24(11): 1395–1421.
- 1.80 Synnefa, A., Dandou, A., Santamouris, M., Tombrou, M., Soulakellis, N. (2008). On the use of cool materials as a heat island mitigation strategy. *Journal of Applied Meteorology and Climatology*, 47: 2846–2856.
- 1.81 Fachinotti, A., Carnielo, E., Zinzi, M. (n.a.). Impact of cool materials on urban heat islands and on buildings comfort and energy consumption. Available at: https://ases.conference-services.net/resources/252/2859/pdf/SOLAR2012_0176_full%20paper.pdf.
- 1.82 Sharma, A., Conry, P., Fernando, H.J.S., Hamlet, A.F., Hellmann, J.J., Chen, F. (2016). Green and cool roofs to mitigate urban heat island effects in the Chicago metropolitan area: evaluation with a regional climate model. *Environmental Research Letters*, 11: 1–15.
-

-
- 1.84 Greenequity (2015). Mitigating UHI: cool roof. Available at: <https://faezehforghanifard.wordpress.com/2015/06/07/mitigating-uhi-cool-roof/>.
- 1.85 Lee, J.S., Kim, J.T., Lee, M.G. (2013). Mitigation of urban heat island effect and greenroofs. *Indoee and Built Environment*, 23(1): 62–69.
- 1.86 Qin, Y. (2015). A review on the development of cool pavements to mitigate urban heat island effect. *Renewable and Sustainable Energy Reviews*, 450: 445–459.
- 1.87 Chang, H.T. (2016). A temporal and spatial analysis of urban heat island in basin city utilizing remote sensing techniques. *The International Archives of the Photogrammetry, Remote Sensing and Spatial Information Sciences*, XLI(B2): 165–170.
- 1.88 Zhou, B., Rybski, D., Kropp, J.P. (2017). The role of city size and urban form in the surface urban heat island. *Scientific Reports*, 7(1): 1–9.
- 1.89 Shashua-Bar, L., Tzamir, Y., Hoffman, M.E. (2004). Thermal effects of building geometry and spacing on the urban canopy layer microclimate in a hot-humid climate in summer. *International Journal of Climatology*, 24(13): 1729–1742.
- 1.90 Rajagopalan, P., Lim, K.C., Jamei, E. (2014). “Urban heat island and wind flow characteristics of a tropical city”. *Solar Energy*, 107: 159–170.
- 1.91 Sailor, D.J., Fan, H. (2002). Modeling the diurnal variability of effective albedo for cities. *Atmospheric Environment*, 36(4): 713–725.
- 1.92 Robaa, S.M. (2011). Effect of urbanization and industrialization processes on outdoor thermal human comfort in Egypt. *Atmospheric and Climate Sciences*, 1(3): 100–112.
- 1.93 Simscale (2017). Wind Comfort in Urban Areas (webinar). Available at: <https://www.simscale.com/wind-comfort-webinar/>.
- 1.94 Chung, D.H.J., Hien, W.N., Jusuf, S.K. (2015). Anthropogenic heat contribution to air temperature increase at pedestrian height in Singapore’s high density Central Business District (CBD). *Proceedings of the 9th International Conference on Urban Climate jointly with the 12th Symposium on the Urban Environment*, 20-24 June 2015, Toulouse, France.
- 1.95 Voogt, J. (2002). Urban heat island. *Encyclopedia of Global Environmental Change*, Volume 3, John Wiley and Sons, United States.
- 1.96 Shahmohamadi, P., Che-Ani, A.I., Maulud, K.N.A., Tawil, N.M., Abdullah, N.A.G. (2011). The impact of anthropogenic heat on formation of urban heat island and energy consumption balance. *Urban Studies Research*, 2011: 1–9.
- 1.97 Flanner, M.G. (2009). Integrating anthropogenic heat flux with global climate models. *Geophysical Research Letters*, 36.
- 1.98 Maharani, Y.N., Lee, S., Lee, Y.K. (2009). Topographical effects on wind speed over various terrains: a case study for Korean peninsula. *Proceedings of the 7th Asia-Pacific Conference on Wind Engineering*, 8-12 Novemebr 2009, Taipei, Taiwan.
- 1.99 Enete, I.C., Awuh, M.E., Amawa, S. (2014). Assessment of health related impacts of urban heat island (UHI) in Douala Metropolis, Cameroon. *International Journal of Environmental Protection and Policy*, 2(1): 35–40.
-

-
- 1.100 Intergovernmental Panel on Climate Change (2001). *Climate change 2001: the scientific basis*. Cambridge University Press, Cambridge, United States.
- 1.101 Villanueva, K., Badland, H., Hooper, P., Koohsari, M.J., Mavoa, S., Davern, M., Roberts, R., Goldfeld, S., Giles-Corti, B. (2015). Developing indicators of public open space to promote health and wellbeing in communities. *Applied Geography*, 57: 112–119.
- 1.102 Environmental Protection Agency (2016). *Climate change indicators in the United States: heat-related deaths*. United States.
- 1.103 World Health Organization (2017). Data and statistics. Available at: <http://www.euro.who.int/en/health-topics/environment-and-health/Climate-change/data-and-statistics>.
- 1.104 World Health Organization (2000). *Climate change and human health: impact and adaptation*. Geneva, Switzerland.
- 1.105 Kiehl, J.T., Trenberth, K.E. (1997). Earth's annual global mean energy budget. *Bulletin of the American Meteorological Society*, 78(2): 197–208.
- 1.106 Zillman, J., Sherwood, S. (2017). The enhanced greenhouse effect. *Australian Academy of Science*, Available at: <https://www.science.org.au/curious/earth-environment/enhanced-greenhouse-effect>.
- 1.107 Perera, M., Sanford, T. (2011). Climate change and your health. *Union of Concerned Scientists*. Available at: https://www.nrcm.org/wp-content/uploads/2013/09/UCS_climate_health_impact6.1.11.pdf.
- 1.108 Ravillious, K. (2014). The seven countries driving global warming. *New Scientists*, 221(2952): 1–12.
- 1.109 European Commission (2017). GHG (CO₂, CH₄, N₂O, F-gases) emission time series 1990-2012 per capita for world countries. Emission Database for Global Atmospheric Research. Available at: http://edgar.jrc.ec.europa.eu/overview.php?v=GHGts_pc1990-2012.
- 1.110 Zipper, S.C., Schatz, J., Singh, A., Kucharik, C.J., Townsend, P.A., Loheide, S.P. (2016). Urban heat island impacts on plant phenology: intra-urban variability and response to land cover. *Environmental Research Letters*, 11: 1–12.
- 1.111 Caissie, D. (20069). The thermal regime of rivers: a review. *Freshwater Biology*, 51(8): 1389–1406.
- 1.112 McDonnell, M.J., Pickett, S.T., Groffman, P., Bohlen, P., Pouyat, R.V., Zipperer, W.C., Parmelee, R.W., Carreiro, M.M., Medley, K. (1997). Ecosystem processes along an urban-to-rural gradient. *Urban Ecosystems*, 1(1): 21–36.
- 1.113 n.d. (2014). Ask a biologist. *Arizona State University*, Arizona, United States. Available at: <https://askabiologist.asu.edu/plosable/where-are-insects>.
- 1.114 Tryjanowski, P., Sparks, T.H., Kuźniak, S., Czechowski, P., Jerzak, L. (2013). Bird migration advances more strongly in urban environments. *PLoS One*, 5(8): 1–6.
- 1.115 Canadian Geographic. (2016). Stunning map predicts how wildlife will move to adapt to climate change. The Royal Canadian Geographical Society. Available at: <https://www.canadiangeographic.ca/article/stunning-map-predicts-how-wildlife-will-move-adapt-climate-change>
-

-
- 1.116 Taha, H., Akbari, H., Rosenfeld, A., Huang, J. (1988). Residential cooling loads and the urban heat island – the effects of albedo. *Building and Environment*, 20(4): 271–283.
- 1.117 Akbari, H. (2005). Energy saving potentials and air quality benefits of urban heat island mitigation. *Proceedings of 1st International Conference on Passive and Low Energy Cooling for the Built Environment*, 17-24 May 2005, Athens, Greece.
- 1.118 Isaac, M., Van Vuuren, D.P. (2009). Modeling global residential sector energy demand for heating and air conditioning in the context of climate change. *Energy Policy*, 37(2): 507–521.
- 1.119 Calm, J.M. (2002). Emissions and environmental impacts from air-conditioning and refrigeration systems. *International Journal of Refrigeration*, 25(3): 293–305.
- 1.120 Environmental Protection Agency (2017). Heat island impacts. United States. Available at: <https://www.epa.gov/heat-islands/heat-island-impacts#energy>.
- 1.121 Ürge-Vorsatza, D., Cabeza, L.F., Serrano, S., Barreneche, C., Petrichenko, K. (2015). Heating and cooling energy trends and drivers in buildings. *Renewable and Sustainable Energy Reviews*, 41: 85–98.
- 1.122 Halipah, I.S., Ibrahim N., Wahid, J., Goh, N.A., Koesmeri, D., Nawi, M. (2018). The impact of road pavement on urban heat island (UHI) phenomenon. *International Journal of Technology*, 9(8): 1597–1608.
- 1.123 Roesler, J., Sen, S. (2016). Impact of pavements on the urban heat island. University of Urbana-Champaign, Illinois, United States.
- 1.124 Stempihar, J.J., Pourshmas-Manzouri, T., Kaloush, K.E., Rodezno, M.C. (2012). Porous asphalt pavement temperature effects for urban heat island analysis. *Transportation Research Record*, 2293(1): 123–130.
- 1.125 Quattrochi, D.A., Ridd, M.K. (1994). Measurement and analysis of thermal energy responses from discrete urban surfaces using remote sensing data. *International Journal of Remote Sensing*, 15(10): 1991–2022.
- 1.126 Streutker, D.R. (2003). Satellite-measured growth of the urban heat island of Houston, Texas. *Remote Sensing of Environment*, 85: 282–289.
- 1.127 Streutker, D.R. (2002). A remote sensing study of the urban heat island of Houston, Texas. *International Journal of Remote Sensing*, 23: 2595–2608.
- 1.128 Carnahan, W.H., Larson, R.C. (1990). An analysis of an urban heat sink. *Remote Sensing of Environment*, 33: 65–71.
- 1.129 Voogt, J.A, Oke, T.R. (1997). Complete urban surface temperatures. *Journal of Applied Meteorology*, 36(9): 1117–1132.
- 1.130 Roth, M., Oke, T.R., Emery, W.J. (1989). Satellite-derived urban heat islands from three coastal cities and the utilization of such data in urban climatology. *International Journal of Remote Sensing*, 10: 1699–1720.
- 1.131 Asaeda, T., Thanh, C., Wake, A. (1996). Heat storage of pavement and its effect on the lower atmosphere. *Atmospheric Environment*, 30(3) :413–427.
- 1.132 Doll, D., Ching, J.K.S., Kaneshiro, J. (1985). Parameterization of subsurface heating for soil and concrete using net radiation data. *Boundary-Layer Meteorology*, 32: 351–372.
-

-
- 1.133 Torbjörn, G., Jörgen, B., Green, C. (2001). Road climate in cities: a study of the Stockholm area, South-East Sweden. *Meteorological Applications*, 8: 481–489.
- 1.134 Gui, J. et al. (2007). Impact of pavement thermophysical properties on surface temperatures. *Journal of Materials in Civil Engineering*, 19(8): 683–690.
- 1.135 Pourshams-Manzouri, T. (2013). Pavement Temperature Effects on Overall Urban Heat Island. Master Degree Thesis, Arizona State University, Arizona, United States.
- 1.136 Buettner, K., Kern, D. (1965). The determination of infrared emissivities of terrestrial surfaces. *Journal of Geophysical Research*, 70: 1329–1337.
- 1.137 Combs, A.C., Weickmann, H.K., Mader, C., Tebo, A. (1965). Application of infrared radiometers to meteorology. *Journal of Applied Meteorology*, 4: 253–262.
- 1.138 Rubio, E., Caselles, V., Coll, C., Valour, E., Sospedra, F. (2003). Thermal infrared emissivities of natural surfaces: improvements on the experimental set-up and new measurements. *International Journal of Remote Sensing*, 24: 5379–5390.
- 1.139 Lee, K.W.K., Kohm, S. (2014). Cool pavements. *Green Energy and Technology*, 204: 439–453.
- 1.140 Levinson, R., Akbari, H., Konopacki, S., Bretz, S. (2002). Inclusion of cool roofs in nonresidential Title 24 prescriptive requirements. Lawrence Berkeley National, California, United States.
- 1.141 Li, H., Harvey, J.T., Holland, T.J., Kayhanian, M. (2013). The use of reflective and permeable pavements as a potential practice for heat island mitigation and stormwater management. *Environmental Research Letters*, 8(1): 1–14.
- 1.142 Tran, N., Powell, B., Marks, H., West, R., Kvasnak, A. (2009). Strategies for design and construction of high-reflectance asphalt pavements. *Transportation Research Record*, 2098: 124–130.
- 1.143 Liu, Y., Li, T., Peng, H. (2018). A new structure of permeable pavement for mitigating urban heat island. *Science of the Total Environment*, 634: 1119–1125.
- 1.144 Haselbach, L. (2009). Pervious concrete and mitigation of the urban heat island effect. *Proceedings of the Transportation Research Board Annual Meeting*, Washington, DC, United States.
- 1.145 Mallick, R.B., Chen, B.L., Bhowmick, S. (2009). Harvesting energy from asphalt pavements and reducing the heat island effect. *International Journal of Sustainable Engineering*, 2(3): 214–228.
- 1.146 Sasaki, K., Horikawa, D., Goto, K. (2015). Consideration of thermoelectric power generation by using hot spring thermal energy or industrial waste heat. *Journal of Electronic Materials*, 44(1): 391–398.
- 1.147 Loughner, C.P., Allen, D.J., Zhang, D.L., Pickering, K.E., Dickerson, R.R., Landry, L. (2012). Roles of urban tree canopy and buildings in urban heat island effects: parameterization and preliminary results. *Journal of Applied Meteorology and Climatology*, 51: 1775–1792.
- 2.1 Maxwell, J.C. (1865). A dynamical theory of the electromagnetic field. *Philosophical Transaction*, 155: 459–512.
-

-
- 2.2 Hertz, H. (1971). Über sehr schnelle elektrische Schwingungen. Four papers with an introduction and an afterword by Gustav Her. *Geest und Portig (Ostwalds Klassiker)*, Leipzig, Germany.
- 2.3 Planck, M. (1901). On the Law of the Energy Distribution in the Normal Spectrum. *Annals of Physics*, 4: 553.
- 2.4 Stefan Boltzaman libro Stefan, J. (1879). Über die beziehung der wärmestrahlung und der temperatur”. *Sitzungsberichte der Kaiserlichen Akademie der Wissenschaften, Mathematische-Naturwissenschaftliche Classe Abteilung II*, 79: 391–428.
- 2.5 Wien, W. (1897). On the division of energy in the emission-spectrum of a black body. *Philosophical Magazine. Series 5*. 43(262): 214–220.
- 2.6 Kirchhoff, G. (1860). Ueber das verhältniss zwischen dem emissionsvermögen und dem absorptionsvermögen der körper für wärme and licht. *Annalen der Physik und Chemie*. 109(2): 275–301.
- 2.7 Solaimanian, M., Kennedy, T.W. (1993). Predicting maximum pavement surface temperature using maximum air temperature and hourly solar radiation. *Transportation Research Record*, 1417: 1–11.
- 2.8 Brown, A.I., Marco., S.M. (1951). Introduction to heat transfer. 2nd ed. McGraw Hill Book Company, Inc., New York, United States.
- 2.9 Agenzia Nazionale Nuove Tecnologie, Energia Sviluppo Economico Sostenibile – ENEA (2013). Atlante italiano della radiazione solare (Solar radiation Italian Atlas). Available at: <http://www.solaritaly.enea.it> (accessed on 23, March, 2019)
- 2.10 Dempsey, B.J., Thompson, M.R. (1970). A heat transfer model for evaluating frost action and temperature-related effects in multilayered pavement systems. *Highway Research Record*, 342: 39–56.
- 2.11 Parsons, R., Bewick, S. (2011). Introduction Chemistry. *CK-12 Foundation*, California, United States.
- 2.12 Katzschner, L. (2006). Microclimatic thermal comfort analysis in cities for urban planning and open space design. *Proceedings of Comfort and Energy Use in Buildings - Getting it Right*, 27–30 April 2006, Windsor Great Park, United Kingdom.
- 2.13 Grosso, M., Peretti, G., Piardi S., Scudo G. (2005). Progettazione ecocompatibile dell'architettura. *Sistemi Editoriali*, Naples, Italy
- 2.14 Santamouris, M. (2014). On the energy impact of urban heat island and global warming on buildings. *Energy and Buildings*, 82: 100–113.
- 2.15 Highter, W.H., Wall, D.J. (1984). Thermal properties of some asphaltic concrete mixes. *Transportation Research Record*, 968: 38–45.
- 2.16 Shen, J., Zhang, Y., Xing, T. (2018). The study on the measurement accuracy of non-steady state temperature field under different emissivity using infrared thermal image. *Infrared Physics & Technology*, 94: 207–213.
- 2.17 Lillesand, D.T., Kiefer, R.W., Chipman, J. (2015). Remote sensing and image interpretation. *Wiley*, New Jersey, United States.
-

-
- 2.18 Kanakiya R.S., Singh S.K., Mehta P.M. (2015). Urban Canyon modelling: a need for the design of future Indian cities. *International Research Journal of Environment Sciences*, 4(7): 86–95.
- 2.19 Asimakopoulos, D.N., Assimakopoulos, V.D., Chrisomallidou, N., Klitsikas, N., Mangold, D., Micheal, P., Santamouris, M., Tsangrassoulis, A. (2001). Energy and climate in the urban built environment. James & James, London, United Kingdom.
- 2.20 Doulos, L., Santamouris, M., Livada, I. (2004). Passive cooling of outdoor urban spaces. The role of materials. *Solar Energy*, 77(2): 231–249.
- 3.1 Alawi, M.H., Helal, M.M. (2014). A mathematical model for the distribution of heat through pavement layers in Makkah roads. *Journal of King Saud University - Engineering Sciences*, 26(1): 41–48.
- 3.2 Davies, T.W. (1985). Transient conduction in a plate with counteracting convection and thermal radiation at the boundary. *Applied Mathematical Modelling*, 9(5): 337–340.
- 3.3 Pasetto, M., Moro, L., Nosandoni, R. (2003). Analisi teorica del comportamento termico i regime transitorio delle pavimentazioni flessibili al variare delle condizioni climatiche”, *XIII Convegno Nazionale S.I.I.V*, Padova 30–31 October, 2003.
- 3.4 Kevern, J., Wang, K., Suleiman M., Schaefer, V.R. (2006). Pervious concrete construction: methods and quality control. NRMCA concrete technology forum: focus on pervious concrete. Nashville, TN, 1–14.
- 3.5 Kevern, J., Wang, K., Suleiman, M.T., Schaefer, V.R. (2005). Mix design development for pervious concrete in cold weather climates. Iowa State University, Iowa. 1–11.
- 3.6 Qin, Y., Yang, H., Deng, Z., He, J. (2015). Water permeability of pervious concrete is dependent on the applied pressure and testing methods. *Advances in Materials Science and Engineering*, 2015: 1–6.
- 3.7 Roseen, R., Ballestero, T., Houle, J., Avellaneda, P., Briggs, J., Fowler, G. (2009). Seasonal performance variations for storm-water management systems in cold climate conditions. *Journal of Environmental Engineering*, 135: 128–137.
- 3.8 Asaeda, T., Ca, V.T. (2000). Characteristics of permeable pavement during hot summer weather and impact on the thermal environment. *Building and Environment*, 35: 363–375.
- 3.9 Lynn, B.H., Carlson, T.N., Rosenzweig, C., Goldberg, R., Druyan, L., Cox, J. (2009). A modification to the NOAA LSM to simulate heat mitigation strategies in the New York City metropolitan area. *Journal of Applied Meteorology and Climatology*, 48: 199–216.
- 3.10 Haselbach, L., Boyer, M., Kevern, J.T., Schaefer, V.R. (2011). Cyclic heat island impacts on traditional versus pervious concrete pavement systems. *Transportation Research Record*, 2240: 107–115.
- 3.11 Kevern, J.T., Schaefer, V.R., Wang, K. (2009). Temperature behavior of pervious concrete systems. *Transportation Research Record*, 2098: 94–101.
- 3.12 Gedafa, D.S., Hossain, M., Romanoschi, S.A. (2014). Perpetual pavement temperature prediction model. *Road Materials and Pavement Design*, 15(1): 55–65.
- 3.13 Wang, T.H., Su, L.J., Zhai, J.Y. (2014). A case study on diurnal and seasonal variation in pavement temperature. *International Journal of Pavement Engineering*, 15(5): 402–408.
-

-
- 3.14 Zhu, B. (2013). Thermal stresses and temperature control of mass concrete. 1st Edition, Elsevier.
- 3.15 Hendel, M., Colombert, M., Diab, Y., Royon L. (2015). An analysis of pavement heat flux to optimize the water efficiency of a pavement-watering method. *Applied Thermal Engineering*, 78: 658–669.
- 3.16 Hendel, M., Royon, L. (2015). The effect of pavement-watering on subsurface pavement temperatures. *Urban Climate*, 14(4): 650–654.
- 3.17 Dumais, S., Doré, G. (2016). An albedo based model for the calculation of pavement surface temperatures in permafrost regions. *Cold Regions Science and Technology*, 123: 44–52.
- 3.18 Marceau, M.L., VanGeem, M.G. (2007). Solar reflectance of concretes for LEED sustainable sites credit: heat island effect Illinois. Portland Cement Association, Stokie. Serial no. 2982.
- 3.19 Levinson, R., Akbari H. (2002). Effects of composition and exposure on the solar reflectance of Portland cement concrete. *Cement and Concrete Research*, 32: 1679–1698.
- 3.20 Boriboonsomsin, K., Reza, F. (2007). Mix design and benefit evaluation of high solar reflectance concrete for pavements. *Transportation Research Record*, 2011: 11–20.
- 3.21 Marceau, N.L., Vangeem, M.G. (2008). Solar reflectance values for concrete: intrinsic material properties can minimize the heat island effect. *Concrete International*, 2008: 52–58.
- 3.22 Higashiyama, H., Sano, M., Inaoka, N., Nakanishi, F., Takahashi, O., Tsukuma S. (2016). Development of water absorption asphalt pavement having surface temperature rise reducing function and verification by field tests. *Case Studies in Construction Materials*, 4: 73–80.
- 3.23 Cuculic, M., Deluka-Tibljias, A., Babic, S. (2014). Urban pavement surfaces heating - influencing parameters. *Proceedings of 3rd International Conference on Road and Rail Infrastructure*, CETRA 2014. 28–30 April, 2014, Split, Croatia.
- 3.24 Stroup-Gardiner, A., Law, M., Nesmith, C. (2000). Using infrared thermography to detect and measure segregation in hot mix asphalt pavements. *International Journal of Pavement Engineering*, 1(4): 265–284.
- 3.25 Giuliani, F. (2000). Indagine teorico-sperimentale sulla trasmissione del calore nel conglomerato bituminoso. *X Convegno Nazionale S.I.I.V.*, 26–28 October, 2000, Catania, Italy.
- 3.26 Xu, Q., Solaimanian, M. (2010). Modeling temperature distribution and thermal property of asphalt concrete for laboratory testing applications. *Construction and Building Materials*, 24(4): 487–497.
- 3.27 Guangxi, W., Xiong, B.Y. (2012). Thermal energy harvesting system to harvest thermal energy across pavement structure. *International Journal of Pavement Research and Technology*, 5(5): 311–316.
- 3.28 Di Maria, V., Rahman, M., Collins, P., Dondi, G., Sangiorgi, C. (2013). Urban heat island effect: thermal response from different types of exposed paved surfaces. *International Journal of Pavement Research and Technology*, 6(4): 412–422.
- 3.29 Synnefa, A., Karlessi, T., Gaitani, N., Santamouris, M., Assimakopoulos, D.N., Papakatsikas, C. (2011). Experimental testing of cool colored thin layer asphalt and estimation of its potential to improve the urban microclimate. *Building and Environment*, 46: 38–44.
-

-
- 3.30 Yinfei, D., Shengyue, W., Jian, Z. (2015). Cooling asphalt pavement by a highly oriented heat conduction structure. *Energy and Building*, 102: 187–196.
- 3.31 Yinfei, D., Qin, S., Shengyue, W. (2015). Bidirectional heat induced structure of asphalt pavement for reducing pavement temperature. *Applied Thermal Engineering*, 75: 298–306.
- 3.32 Hassn, A., Chiarelli, A., Dawson, A., Garcia, A. (2016). Thermal properties of asphalt pavements under dry and wet conditions. *Materials and Design*, 91: 432–439.
- 3.33 Chiarelli, A., Dawson, A.R., García, A. (2017). Field evaluation of the effects of air convection in energy harvesting asphalt pavements. *Sustainable Energy Technologies and Assessments*, 21: 50–58.
- 3.34 Dawson, A.R., Dehdezi, P.K., Hall, M.R., Wang, J., Isola, R. (2012). Enhancing thermal properties of asphalt materials for heat storage and transfer applications. *Road Materials and Pavement Design*, 13(4): 784–803.
- 3.35 Bobes-Jesus, V., Pascual-Muñoz, P., Castro-Fresno, D., Rodriguez-Hernandez, J. (2013). Asphalt solar collectors: a literature review. *Applied Energy*, 102: 962–970.
- 3.36 Guldentops, G., Nejad, A.M., Vuyec, C., Van den Berghc, W., Rahbara, N. (2016). Performance of a pavement solar energy collector: model development and validation. *Applied Energy*, 163: 180–189.
- 3.37 Yinfei, D., Shengyue, W. (2015). Oriented heat release in asphalt pavement induced by high-thermal-conductivity rods. *Applied Thermal Engineering*, 90: 424–431.
- 3.38 Obika, B., Freer-Hewish, R.J., Fookes, P.G. (1989). Soluble salt damage to thin bituminous road and runway surfaces. *Quarterly Journal of Engineering Geology and Hydrogeology*, 22: 59–73.
- 3.39 Chen, M., Wu, S., Wang, H., Zhang, J. (2011). Study of ice and snow melting process on conductive asphalt solar collector. *Solar Energy Materials & Solar Cells*, 95: 3241–3250.
- 3.40 Giuliani, F. (2001). Studio sperimentale sulle pavimentazioni stradali riscaldate. XI Convegno S.I.I.V., 28–30 November, 2001, Verona, Italy.
- 3.41 Khan, A., Mrawir, D., Hildebrand, E.E. (2009). Use of lightweight aggregate to mitigate frost damage in flexible pavements. *International Journal of Pavement Engineering*, 10(5): 329–339.
- 4.1 Smith, T., Guild, J. (1931). The C.I.E. colorimetric standards and their use. *Transactions of the Optical Society*, 33(3): 73–134.
- 4.2 Strangor, C. (2012). Eye anatomy. Illustration from *Beginning Psychology*, 1.0: 1–817.
- 4.3 Berk, T., Kaufman, A., Brownston, L. (1982). A human factors study of color notation systems for computer graphics. *Communications of the ACM*, 25(8): 547–550.
- 4.4 Schwarz, M.W., Cowan, W.B., Beatty, J.C. (1987). An experimental comparison of RGB, YIQ, LAB, HSV, and opponent color models. *ACM Transactions on Graphics*, 6(2): 123–158.
- 4.5 Prado, R.T.A., Ferreira F.L. (2005). Measurement of albedo and analysis of its influence the surface temperature of building roof materials. *Energy and Buildings*, 37: 295–300.
- 4.6 Gomes, C.C., Preto, S. (2015). Should the light be static or dynamic?. *Procedia Manufacturing*, 3: 4635–4642.
-

-
- 4.7 Yasar, E., Erdogan, Y., Güneyli, H. (2008). Determination of the thermal conductivity from physico-mechanical properties. *Bulletin of Engineering Geology and the Environment*, 67(2): 219–225.
- 4.8 Ahmad, L., Kanth, R.H., Parvaze, S., Mahdi, S.S. (2017). Experimental agrometeorology: a practical manual. Springer, Cham, Switzerland.
- 4.9 Coutinho, P.P., Branco, V.C., Soares, J.B. (2010). Multiscale approach for characterization of asphaltic materials designed in Brazil and Spain. *Proceedings of the 11th International Conference on Asphalt Pavements – ISAP*, 1: 1–10, Japan.
- 4.10 Underwood B.S. (2015). Multiscale modeling approach for asphalt concrete and its implications on oxidative aging. *Advances in Asphalt Materials, Road and Pavement Construction*. 2015: 273–302.
- 4.11 Yusoff, M.d., Izzi, N. (2012). Modelling the linear viscoelastic rheological properties of bituminous binders. PhD thesis, University of Nottingham, Nottingham, United Kingdom.
- 4.12 Anderson, D.A., Christensen, D.W., Bahia B.U. et al. (1994). Binder characterization, vol. 3: physical properties, *SHARP-A-369*, National Research Council, Washington, DC, United States.
- 4.13 Marasteanu, M.O., Anderson, D.A. (2000). Establishing linear viscoelastic conditions for asphalt binders. *Transportation Research Record*, 1728: 1–6.
- 4.14 Roylance, D. (2001). Engineering viscoelasticity. Department of Materials Science and Engineering, Massachusetts Institute of Technology, Cambridge, Massachusetts, United States.
- 4.15 Rowe, G.M., Sharrock, M.J. (2011). Alternate shift factor relationship for describing temperature dependency of viscoelastic behavior of asphalt materials. *Transportation Research Record*, 2207(1): 125– 135.
- 4.16 Williams, M.L., Landel, R.F., Ferry, J.D. (1955). The temperature dependence of relaxation mechanisms in amorphous polymers and other glass-forming liquids. *Journal of the American Chemical Society*, 77(14): 3701–3707.
- 4.17 Mezger, T. (2014). The rheology handbook- Fourth edition. *Vincentz Network GmbH Co*, Hanover, Germany.
- 4.18 National Cooperative Highway Research Program (2001). Characterization of modified asphalt binders in Superpave mix design. NCHRP-Report-459, Washington, DC, United States.
- 4.19 Hintz, C., Velasquez, R., Bahia, U.H., (2011). Modification and validation of the linear amplitude sweep test for binder fatigue specification. *Transportation Research Record*, 2207: 99–106.
- 4.20 Botella, R., Pérez-Jiménez, F.E., Miró, R. (2012). Application of a strain sweep test to assess fatigue behaviour of asphalt binders. *Construction and Building Materials*, 36: 906–912.
- 4.21 Liao, M.C., Chen, J.S., Tsou, K.W. (2011). Fatigue characteristics of bitumen-filler mastics and asphalt mixtures. *Journal of Materials in Civil Engineering*, 24(7): 916–923.
- 4.22 Al-Haddad, A. (2015). Fatigue evaluation of Iraqui asphalt binders based on the dissipated energy and viscoelastic continuum damage (VECD) approaches. *Journal of Civil Engineering and Construction Technology*, 6(3), 27–50.
-

-
- 4.23 National Research Council, Transportation Research Board (1998). Development in Asphalt Binder Specifications. *Transportation research e-circulars*.
- 4.24 Pereira, A., Micaelo, R., Quesada, L., Cicade, M.T. (2016). Evaluation of different methods for the estimation of the bitumen fatigue life with DSR testing. *8th RILEM International Symposium on Testing and Characterization of Sustainable and Innovative Bituminous Materials*, RILEM Bookseries, Springer, 11: 1017–1028.
- 4.25 Kim, Y., Lee, H.J., Little, D.N., Kim, Y.R. (2006). A simple testing method to evaluate fatigue fracture and damage performance of asphalt mixtures. *Journal of Association of Asphalt Paving Technologists*, 75: 755–788.
- 4.26 Kim, Y.R., Little, D.N. (1990). One-dimensional constitutive modeling of asphalt concrete. *Journal of Engineering Mechanics*, 116(4): 751–772.
- 4.27 Schapery, R.A. (1984). Correspondence principles and a generalized J-integral for large deformation and fracture analysis of viscoelastic media. *International Journal of Fracture*, 25(3): 195–223.
- 4.28 Roberts, F.L., Kandhal, P.S., Brown, E.R., Lee, D.Y., Kennedy, T.W. (1996). Hot mix asphalt materials, mixture design and construction - Second edition. National Asphalt Pavement Association Research and Education Foundation, Lanham, United States.
- 4.29 Bocci, M., Colagrande, S. (1993). The adhesiveness of modified road bitumens. *Proceedings of 5th Eurobitume Congress*, Stockholm, Sweden, 317–321.
- 4.30 Behairy, A.E. (1993). Laboratory evaluation of resistance to moisture damage in asphalt mixtures. *Ain Shams Engineering Journal*, 4(3): 351–363.
- 5.1 Yildirim, Y., Solaimanian, M., Kennedy, T.W. (2000). Mixing and compaction temperatures for hot mix asphalt concrete. Technical Report 1250-5, Center for Transportation Research, The University of Texas at Austin, Austin, Texas, TX, United States.
- 5.2 Airey, G., Mohammed, M.H. (2008). Rheological properties of polyacrylates as synthetic road binders. *Rheologica Acta*, 47(7): 751–763.
- 5.3 Planche, J.P., Lesueur, D., Hines, M. (1996). valuation of elastomer modified bitumens using SHRP binder specifications”. *Proceedings of 1st Eurasphalt and Eurobitume Conference*, 1–17, Strasbourg, France.
- 5.4 Pasetto, M., Baliello, A., Giacomello, G., Pasquini, E. (2016). Rheological characterization of warm-modified asphalt mastics containing electric arc furnace steel. *Advances in Materials Science and Engineering*, 2016, Article ID 9535940, 11 pages.
- 5.5 Grabowski, W., Wilanowicz, J. (2008). The structure of mineral fillers and their stiffening properties in filler-bitumen mastics. *Materials and Structures*, 41(4): 793–804.
- 5.6 Partl, M., Bahia, U.H., Canestrari, F., De La Roche, C., Di Benedetto, H., Piber, H., Sybilski, D. (2013). Bituminous Binder Fatigue Testing – State-Of-The-Art-Report. *Advances in Interlaboratory Testing and Evaluation of Bituminous Materials*, Springer Netherlands, Netherlands.
- 5.7 Zaniwski, J.P., Nallamothu, S.H. (2003). Evaluation of binder grades on rutting performance. Asphalt Technology Program, Department of Civil and Environmental Engineering, Morgantown, West Virginia, WV, United States.
-

-
- 5.8 Brasileiro, L., Moreno-Navarro, F., Tauste-Martinez, R., Matos, J., Rubio-Gamez, C. (2019). Reclaimed polymers as asphalt binder modifiers for more sustainable roads: a review. *Sustainability*, 11(646): 1–20.
- 5.9 Pasetto, M., Pasquini, E., Giacomello, G., Baliello, A. (2019). Innovative pavement surfaces as Urban Heat Islands mitigation strategy: chromatic, thermal and mechanical characterization of clear/colored mixtures. *Road Materials and Pavement Design*, 2019: 1–23.
- 5.10 Shen, J., Zhang, Y., Xing, T. (2018). The study on the measurement accuracy of non-steady state temperature field under different emissivity using infrared thermal image. *Infrared Physics & Technology*, 94: 207–213.
- 5.11 Bai, B.C, Park, D.W., Vo, H.V., Dessouky, S., Im, J.S. (2015). Thermal properties of asphalt mixtures modified with conductive fillers. *Journal of Nanomaterials*, 2015: 1–6.
- 5.12 Mirzanamadi, R., Johansson, P., Grammatikos, S.A. (2018). Thermal properties of asphalt concrete: a numerical and experimental. *Construction and Building Materials*, 158: 774–785.
- 5.13 Ahmedzade, P., Sengoz, B. (2009). Evaluation of steel slag coarse aggregate in hot mix asphalt concrete. *Journal of Hazardous Materials*, 165: 300–305.
- 5.14 Behnood, A., Ameri, M. (2012). Experimental investigation of stone matrix asphalt mixtures containing steel slag. *Scientia Iranica Sharif University of Technology*, 19(5): 1214–1219.
- 5.15 Noureldin, A.S., MacDaniel, R.S. (1990). Evaluation of surface mixtures of steel slag and asphalt. *Transportation Research Record*, 1269: 133–149.
- 5.16 Ameri, M., Hesami, S., Goli, H. (2013). Laboratory evaluation of warm mix asphalt mixtures containing electric arc furnace (EAF) steel slag. *Construction and Building Materials*, 49: 611–617.
- 5.17 Islam, M.R., Hossain, M.I., Tarefder, R.A. (2015). A study of asphalt aging using Indirect Tensile Strength test. *Construction and Building Materials*, 95: 218–223.
- 5.18 Pasetto, M., Baldo, N. (2011). Mix design and performance analysis of asphalt concretes with electric arc furnace slag. *Construction and Building Materials*, 25: 3458–3468.
- 5.19 Pasetto, M., Baldo, N. (2010). Experimental evaluation of high performance base course and road base asphalt concrete with electric arc furnace steel slags. *Journal of Hazardous Materials*, 181(1-3): 938-948.
- 5.20 Pasetto, M., Pasquini, E., Giacomello, G., Baliello, A. (2018). Preliminary investigation of mechanical and functional properties of coloured asphalt pavement surfaces. *Road and Rail Infrastructure V - Proceedings of the 5th International Conference on Road and Rail Infrastructure (CETRA2018)*, 519–525.
- 5.21 Safiuddin, M., Tighe, S., Uzarowski, L. (2012). Evaluation of stiffness to predict rutting Resistance of hot mix asphalt: a Canadian case study. *The Baltic Journal of Road and Bridge Engineering*, 9(4): 283–296.
- 5.22 Pasetto, M., Pasquini, E., Giacomello, G., Baliello, A. (2017). Warm chemical additive to improve water resistance of asphalt mixtures containing steel slags: a multi-scale approach. *The International Journal of Pavement Engineering & Asphalt Technology*, 18(2): 26–39.
-

-
- 6.1 Bocci, M., Grilli, A., Cardone, F., Virgili, A. (2012). Clear asphalt mixture for wearing course in tunnels: experimental application in the province of Bolzano. *Procedia - Social and Behavioral Sciences*, 53: 115–124.
- 6.2 Pasetto, M., Baliello, A., Giacomello, G., Pasquini, E. (2019). Cold recycling of reclaimed asphalt: analysis of alternative procedures. *Proceedings of the 7th International Conference on Bituminous Mixtures and Pavements, June 12-14, 2019, Thessaloniki, Greece*.
- 6.3 Sabouri, M. (2020). Viscosity criteria and methodology for estimating the optimum compaction temperatures of polymer modified asphalt binders in hot mix asphalt design. *Construction and Building Materials*, 235, 117545.
- 6.4 Geng, H., Li, L., Han, H. (2016). Evaluation of performance-based mix design for asphalt mixtures containing Reclaimed Asphalt Pavement (RAP). *Construction and Building Materials*, 128, 308–314.
- 7.1 Pierard, N., De Visscher, J., Vansteenkiste, S., Vanelstraete, A. (2016). Coloured asphalt pavements: mix design and laboratory performance testing. *Proceedings of the 8th RILEM International Symposium on Testing and Characterization of Sustainable and Innovative Bituminous Materials*, 11: 283–294.
- 7.2 Sebastián, J.B. (2013). Road design for landscape integration. Available at: https://www.researchgate.net/publication/292503399_Road_design_for_landscape_integration.
- 7.3 Ando, R., Inagaki, T., Mimura, Y. (2011). Does colored pavement make non-signalized intersections safer? A case study in Japan. *Procedia - Social and Behavioral Sciences*, 20(6): 741–751.
- 7.4 Kawther, K. (2018). Colored asphalt and street print are decorating paving in public spaces. *MATEC Web of Conferences*, 162.
- 7.5 Sicard, D., Bonvalot, F., Bonnet, G. (1997). Le Choix des Revêtements Colorés À Base de Bitume Ou de Résine Pour la Voirie Urbaine. Dossier CERTU No. 73. Centre d'études sur les réseaux, les transports, l'urbanisme et les constructions publiques Laboratoire Régional de l'Ouest Parisien, France.
- 7.6 n.d. (2019) FHWA course on bicycle and pedestrian transportation. Lesson 11: Traffic calming. Available at: https://safety.fhwa.dot.gov/ped_bike/univcourse/pdf/swless11.pdf
- 7.7 Tukiran, J., Ariffin, J., Ghani, A.N.A. (2016). Comparison on colored coating for asphalt and concrete pavement based on thermal performance and cooling effect. *Jurnal Teknologi*, 78. 63–70.
- 7.8 Cuculić, M., Babić, S., Deluka-Tibljaš, A., Šurdonja, S. (2012). Pavement surfaces in urban areas. *Proceedings of the 2nd Interantional Conference on Road and Rail Structures, CETRA 2012, 7–9 May 2012, Dubrovnik, Croatia*.
- 7.9 Monsere, C.M., Figliozzi, M., Kothuri, S., Razmpa, A., Hazel, D.R. (2016). Safety effectiveness of pedestrian crossing enhancements. Civil and Environmental Engineering Faculty, 2016.
- Publications and Presentations
- 7.10 Fotios, S., Boyce, P., Ellis, C. (2005). The effect of pavement material on road lighting performance. Department for Transport on behalf of the UK Lighting Board, 2005.
-

-
- 7.11 Engineering ToolBox (2004). metabolic heat gain from persons. Available at: https://www.engineeringtoolbox.com/metabolic-heat-persons-d_706.html
- 7.12 n.d. (1998). Physiological responses to the thermal environment. Chapter 42: Heat and cold. *Encyclopaedia of Occupational Health and Safety 4th Edition*. Available at: <http://www.ilocis.org/documents/chpt42e.htm>
- 7.13 Hashida, S., Shimazaki, Y., Yoshida, A., (2014). Field investigation on thermal environment and human thermal sensation in premises woods in urban area. *Journal of Heat Island Institute International*, 9(2): 127–132.
- 7.14 Xie, N., Li, H., Zhao, W., Zhang, C., Yang, B., Zhang, H., Zhang, Y. (2019). Optical and durability performance of near-infrared reflective coatings for cool pavement: laboratorial investigation. *Building and Environment*, 163: 2–11.
- 7.15 Sudeshna, M., (2014). Sun glare and road safety: an empirical investigation of intersection crashes. *Safety Science*, 70: 246–254.
- 7.16 Cantisani, G., D’Andrea, A., Moretti, L. (2018). Natural lighting of road pre-tunnels: a methodology to assess the luminance on the pavement – Part II. *Tunnelling and Underground Space Technology*, 73: 37–47.
- 7.17 M. Collins, M., Brown, B., Bowman, K., Carkeet, A. (1990) Workstation variables and visual discomfort associated with VDTs. *Applied Ergonomics*, 21(2): 157–161.
- 7.18 Yoshimoto, S., Jiang, F., Takeuchi, T., Wilkins, A.J., Webster, M.A. (2019) Adaptation and visual discomfort from flicker. *Vision Research*, 160: 99–107.
- 7.19 Penacchio, O., Wilkins, A.J. (2015). Visual discomfort and the spatial distribution of Fourier energy. *Vision Research*, 108: 1–7.
- 7.20 Wilkins, A.J. (1985). Discomfort and visual displays. *Displays* 6(2): 101–103.
- 7.21 Feldman, M., Manzi J.G., Mitman, M. (2010). An empirical Bayesian evaluation of the safety effects of high-visibility school (yellow) crosswalks in San Francisco. *Transportation Research Record*, 2198: 8–14.
- 7.22 Chen, L., Chen, C., Ewing, R., McKnight, C., Srinivasan, R., Roe, M. (2013). Safety countermeasures and crash reduction in New York City - Experience and lessons learned. *Accident Analysis and Prevention*, 50: 312–322.
- 7.23 Pulugurtha, S.S., Vasudevan, V., Nambisan, S.S., Dangeti, M.R. (2012). Evaluating the effectiveness on infrastructure-based countermeasures on pedestrian safety.” *Transportation Research Record*, 2299: 100–109.
- 7.24 Wilken, D., Ananthanarayanan, B., Hasson, P., Lutkevich, P.J., Watson, C., Burkett, K., Arens, J., Havard, J., Unick, J. (2001). European road lighting technologies. Report FHWA-PL-01-034, Federal Highway Administration, U.S. Department of Transportation, United States.
- 7.25 Houghten, F.C., Yaglou, C.P. (1923). Determining lines of equal comfort. *Transactions of American Society of Heating Ventilating Engineers*, 29,: 163–175.
- 7.26 Vernon, H.M, Warner, C.G. (1932). The influence of the humidity of the air on capacity for work at high temperature. *Journal of Hygiene*, 32(3): 431–462.
-

-
- 7.27 Gagge, A.P., Stolwijk, J.A.J., Nishi, Y. (1971). An effective temperature scale based on a simple model of human physiological regulatory response. *ASHRAE Transactions*, 77(1): 247–262.
- 7.28 Höppe, P. (1999). The physiological equivalent temperature – a universal index for the biometeorological assessment of the thermal environment. *International Journal of Biometeorology*, 43: 71–75.
- 7.29 Matzarakis, A., Mayer, H., Iziomon, M.G. (1999). Applications of a universal thermal index: physiological equivalent temperature. *International Journal of Biometeorology*, 43: 76–84.
- 7.30 Siple, P.A., Passel, C.F. (1945). Measurements of dry atmospheric cooling in sub-freezing temperatures. *Proceedings of the American Philosophical Society*, 89: 177–199.
- 7.31 Yaglou, C.P., Minard, C.D. (1957). Control of casualties at military training centers. *AMA Archives of Industrial Health*, 16: 302–316.
- 7.32 Shimazaki, Y., Yoshida, A., Suzuki, A., Kawabata, T., Imai, T., Kinoshita, S. (2001). Application of human thermal load into unsteady condition for improving outdoor thermal comfort. *Building and Environment*, 46(8): 1716–1724.
- 7.33 Nitta, J., Shimazaki, Y., Aoki, M., Kamidouzono, K., Sakoi, T., Satsumoto, Y. (2017). Experimental evaluation on cooling effects of water retaining pavement on human. *Proceedings of 8th Japanese-German meeting on urban climatology*, Osaka, Japan, 25–29 March, 217–222.
- 7.34 Aoki, M., Shimazaki, Y., Nitta, J., Kamidouzono, K. (2017). Improving effects of water retaining pavement on human thermal environment. Verification based on human physiological responses. *Proceedings of the 4th international symposium on asphalt pavements & environment*, Tokyo, Japan, 20–21 November, 1–15.
- 7.35 Aoki, M., Nakamura, T., Shimazaki, Y. (2018). Experimental investigation of the effect of waterretentive sidewalk block pavement on improving human thermal environment. *Proceedings of 12th international conference on concrete block pavement*, Seoul, South Korea, 16–19 October, 150–160.
- 7.36 CIE (1987). International lighting vocabulary: Bureau Central de la Commission Electrotechnique Internationale. Switzerland
- 7.37 CIE (2002). CIE collection on glare. Commission Internationale de l'Éclairage. Austria.
- 7.38 Moghbel, N. (2012). New model for VDT associated visual comfort in office spaces. Ph.D. Thesis. Verlag nicht ermittelbar.
- 7.39 Wördenweber, B., Wallaschek, J., Boyce, P., Hoffman, D. (2007). Automotive lighting and human vision. Springer.
- 7.40 Boyce, P.R. (2008). Lighting for driving: roads, vehicles, signs, and signals. CRC Press.
- 7.41 Assogba, O.C., Tan, Y., Zhou, X., Zhang, C., Anato, J.N. (2020). Numerical investigation of the mechanical response of semi-rigid base asphalt pavement under traffic load and nonlinear temperature gradient effect. *Construction and Building Materials*, 235: 117406.
- 7.42 Zhang, D., Birgisson, B., Luo, X., Onifade, I. (2019). A new long-term aging model for asphalt pavements using morphology-kinetics based approach. *Construction and Building Materials*, 229: 117032.
-

-
- 7.43 Souza, F.V., Castro, L.S. (2012). Effect of temperature on the mechanical response of thermo-viscoelastic asphalt pavements. *Construction and Building Materials*, 30: 574–582.
- 7.44 Zhang, Q.S., Chen, Y.L., Li, X.L. (2009). Rutting in asphalt pavement under heavy load and high temperature. *Geotechnical Special Publication*, 190: 39–48.
- 7.45 Shuler, S. (1991). Director of Research, Asphalt Institute, Executive Offices and Research Center, Reseach Park Drive, Lexington, Kentucky 40512-4052. Personal communication.
- 7.46 Alleman, J., Heitzman, M. (2019). Quantifying pavement albedo. NCAT Report 19-09, U.S. Department of Transportation. National Center for Asphalt Technology, Auburn University, AL, United States.
- 7.47 Chen, J., Chu, R., Wang, H., Zhang, L., Chen, X., Du, Y. (2019). Alleviating urban heat island effect using high-conductivity permeable concrete pavement. *Journal of Cleaner Production*, 237: 117722.
- 7.48 Richard, C., Dore, G., Lemieux, C., Bilodeau, J. P., Haure-Touzé, J. (2015). Albedo of pavement surfacing materials: In situ measurements. *Cold Regions Engineering: Developing and Maintaining Resilient Infrastructure*, 181–192.
- 7.49 Means R.S. Company Inc. (1989). Building Construction Cost Data, 2nd Western Annual Edition.
- 7.50 Reese, R. (1989). California Department of Transportation, Office of Transportation Laboratory, 5900 Folsom Blvd., Sacramento, CA 95819. Personal communication with P. Martien.
- 7.51 Threlkeld, J.L. (1970). Thermal Environmental Engineering, Second Edition, Prentice-Hall, Englewood Hills, New Jersey.
- 7.52 Oke, T.R. (1987). Boundary Layer Climates, Second Edition, Methuen, London.
- 7.53 Griggs, E.I., Sharp, T.R., MacDonald, J.M. (1989). Guide for estimating differences in building heating and cooling energy due to changes in solar reflectance of a low-sloped roof. Oak Ridge National Laboratory Report ORNL-6527.
- 7.54 Reagan, J.A., Acklam, D.M. (1979). Solar reflectivity of common building materials and its influence on the roof heat gain of typical Southwestern U.S.A. residences. *Energy and Buildings*, 2: 237–248.
